Gas Phase Generation and Deposition of Size-Selected Metal Clusters

by

AHMED ABDELA

A thesis submitted to the
University of Birmingham
for the degree of
DOCTOR OF PHILOSOPHY

Nanoscale Physics Research Laboratory
School of Physics and Astronomy
College of Engineering and Physical Sciences
University of Birmingham
July 2013

Abstract

Size-selected metal clusters have various potential applications in technology. This thesis presents modifications to and optimisations of a cluster beam source, one application being the generation of large area graphite tape samples bearing size-selected palladium cluster catalysts for model catalysis under realistic conditions.

Alignment of the nozzle to the first skimmer, together with enlargement of the entrance and exit apertures of the mass filter increased the cluster beam current almost two-fold. A new analysis of the mass resolution obtained from the novel Lateral Time-of-Flight (LTOF) mass filter employed in the source is also given. The standard expression for the mass resolution ($R = m/\Delta m$), lateral displacement over real exit aperture size ($R = x/b_{rea}$), is only valid for a beam focused perfectly at the *virtual aperture*, otherwise the mass resolution is the lateral displacement over the *effective exit aperture*. The effective exit aperture is the convolution of the real exit aperture and the virtual aperture, giving a size relationship of $a_{eff}^2 = b_{rea}^2 + c_{vir}^2$.

The overall improvements have enabled several further breakthroughs in the use of size-selected clusters. Most notably, size-selected Pd clusters have been used as "mass standards" to determine both the size and shape of industrial Pd catalysts when using the high angle annular dark field scanning transmission electron microscope (HAADF-STEM) as a quantitative electron probe. Size-selected metal clusters have also assisted in the calibration of HAADF-STEM (Z-contrast) imaging, while the degree of pinning of Pd clusters on graphite was found to affect the degree of sintering under realistic catalytic reaction conditions when oxidising methane.

A major modification to the cluster source enabled coating of clusters in a new way. The impact of Pd_{561}, Pd_{55} and Pd_4 clusters (1, 1.5 and 1 keV) on a thin material film evaporated onto a solid argon matrix led to deposition of large, 5-40 nm diameter, irregularly shaped particles. Furthermore, Pd_{923} and Pd_{2000} clusters, with both 0.5 and 1.5 keV impact energies, have been coated in-flight by impact on the thin film/solid matrix, as verified from the increase in diameters of the deposited particles and the detection of Pd signal by electron energy loss spectroscopy (EELS).

MoS_2 nano pillar catalyst samples were etched using size-selected metal etch masks. Catalyst samples of *ordered* MoS_2 nano pillars were fabricated using nano sphere lithography (NSL) and a novel way to apply nano spheres was developed. Different etch recipes were used to obtain nano pillars with different diameters and heights; these recipes were also applied to reference MoS_2 samples without etch masks. Generally, the reference catalyst samples, with their roughened surfaces, showed higher hydrogen evolution reaction (HER) activity than their corresponding ordered MoS_2 nano pillar catalyst samples.

For Family & Friends

ACKNOWLEDGEMENTS

I would like to thank my supervisor Prof. Richard E. Palmer for his encouragement and advice and for giving me the opportunity to learn so much. I want to especially thank Dr. Sung Jin Park, Dr. Jedsada Manyam, Dr. Andreas Frommhold, Dr. Vahideh Habibpour, Dr. Zhiwei Wang and Dr. Feng Yin for constructive assistance and discussions. I am also very grateful to the Nanoscale Physics Research Laboratory group for creating a stimulating and attractive scientific and social atmosphere. Mr. Gary Walsh deserves thanks for his efforts and assistance to solve different issues regarding the cluster source. Thanks go also to Mr. Stephen Brookes and the guys in the workshop for their help in constructing parts for the cluster source. Special thanks go to our external collaborators; Dr. Anders B. Laursen and Prof. Ib Chorkendorff from Technical University of Denmark, and Dr. Sungsik Lee and Dr. Stefan Vajda from Argonne National Laboratory.

PAPERS

Published Papers

1. Z. W. Wang, Z. Y. Li, S. J. Park, **A. Abdela**, D. Tang, R. E. Palmer, *Quantitative Z-contrast imaging in the scanning transmission electron microscope with size-selected clusters*, *Phys. Rev. B* **84**, 073408 (2011).

2. F. Yin, S. Lee, **A. Abdela**, S. Vajda, R. E. Palmer, *Communication: Suppression of sintering of size-selected Pd clusters under realistic reaction conditions for catalysis*, *J. Chem. Phys.* **134**, 141101 (2011).

3. D. Pearmain, S. J. Park, Z. W. Wang, **A. Abdela**, R. E. Palmer and Z. Y. Li, *Size and shape of industrial Pd catalyst particles using size-selected clusters as mass standards*, *Appl. Phys. Lett.* **102**, 163103 (2013).

Papers in Preparation

- Fabrication of MoS_2 nanopillars.
- In-flight coating of size-selected clusters.

CONTENTS

ABBREVIATIONS

AFM	**A**tomic **F**orce **M**icroscopy/**M**icroscope
amu	**a**tomic **m**ass **u**nit
CV	**C**yclic **V**oltammetry
DC	**D**irect **C**urrent
EELS	**E**lectron **E**nergy **L**oss **S**pectroscopy/**S**pectrometer
HAADF	**H**igh **A**ngle **A**nnular **D**ark **F**ield
HOPG	**H**ighly **O**rdered **P**yrolytic **G**raphite
HV	**H**igh **V**acuum
ICP	**I**nductively **C**oupled **P**lasma
LTOF-MS	**L**ateral **T**ime **O**f **F**light **M**ass **S**elector
NC	**N**atural **C**rystal
NHE	**N**ormal **H**ydrogen **E**lectrode
NS	**N**ano **S**phere(s)
NSL	**N**ano **S**phere **L**ithography
RF	**R**adio **F**requency
RHE	**R**eversible **H**ydrogen **E**lectrode
RT	**R**oom **T**emperature
SCA	**S**pherical **C**luster **A**pproximation
sccm	**s**tandard **c**ubic **c**enti**m**etre
SCE	**S**aturated **C**alomel **E**lectrode
SEM	**S**canning **E**lectron **M**icroscopy/**M**icroscope
STEM	**S**canning **T**ransmission **E**lectron **M**icroscopy/**M**icroscope
STM	**S**canning **T**unnelling **M**icroscopy/**M**icroscope
TPR	**T**emperature **P**rogrammed **R**eaction
UHV	**U**ltra **H**igh **V**acuum

CHAPTER

ONE

INTRODUCTION AND BACKGROUND

Man has always been fascinated by the world surrounding him, seeking to search beyond the current boundaries of knowledge. One frontier area of scientific research is nanotechnology, of which cluster science forms a part. This chapter serves to set the stage for the new results to follow and gently engage the reader with the work presented in this thesis.

1.1 Thesis Overview

The work presented in this thesis focuses on the gas phase generation and deposition of size-selected metal clusters and the work underpinning it, i.e. the optimisation and modification of the cluster source in the Nanoscale Physics Research Laboratory (NPRL) at the University of Birmingham (UoB), Birmingham, UK. The versatility of size-selected clusters and important role they play in different experimental usage is demonstrated. Clusters were deposited on substrates and characterised to study their morphology, in order to gain insights into the fundamental science and explore technological applications.

Clusters, due to their narrow size distribution, were used to characterise unknown nano particles. They were also deposited on substrates and used as catalysts in realistic catalytic reaction conditions. Moreover, size-selected metal clusters have been coated in-flight with a secondary metal in order to generate bimetallic clusters through a novel technique. They have also been deposited onto MoS_2 substrates to act as masks when fabricating non-ordered nano pillars, through plasma etching.

Further development, through nano fabrication, of MoS_2 nano pillars by nano sphere lithography (NSL) is also detailed in this thesis. The work also presented here is the cyclic voltammetry (CV) measurements of the hydrogen evolution reaction (HER) using the fabricated MoS_2 nano pillar catalyst samples, which was conducted in the Center for Individual Nanoparticle Functionality (CINF) at the Technical University of Denmark (DTU), Kongens Lungby (Copenhagen), Denmark.

This thesis consists of five chapters. This chapter provides a comprehensive overview of the background & theory of cluster science, nano fabrication and catalysis. The second chapter covers the experimental equipment used, as well as the experimental techniques employed. In the third chapter, cluster source modifications and optimisations are presented as well as some of the cluster deposition work and results. Chapter Four details the work and results of the in-flight coating method for bimetallic cluster generation. The results from nano fabrication work making MoS_2 nanostructured catalysts and the results from catalytic measurements of these novel catalysts are covered in Chapter Five.

1.2 Nanoscience

Nanoscience is an interdisciplinary field connecting several disciplines together, including physics, chemistry, biology and engineering. This growing field deals with materials and phenomena taking place at the nanoscale (1 nanometre = 10^{-9} m); the range of size

considered runs from 100 nm down to the atom. There are two approaches when making structures at the nanoscale: the Top-Down and Bottom-Up methods. The Top-Down approach, mostly, uses conventional lithography-etching techniques, where one starts out with a bulk material and "sculpts" one's way down to the nanoscale. Top-Down is widely used in research and industry today. In contrast, the Bottom-Up approach reaches the nanoscale by building structures atom-by-atom and molecule-by-molecule.

1.2.1 Clusters

Clusters are small multi-atom or multi-molecule particles. They bridge the world of atoms to that of bulk matter, acting as intermediary stages. Properties of clusters are size dependent and can differ wildly from those of bulk matter and single atoms [1]. Clusters can be produced by chemical or physical methods. Clusters can, e.g., be made through the inverse micelle technique, which is based on colloidal chemistry [2]. Plasma ion sputtering and condensation, is another method, which is a physical approach to cluster production [3]. Physical cluster production methods are incorporated into cluster sources that form beams. Beams of clusters can be used to realise the Bottom-Up construction approach, as they are powerful and versatile tools to control and deposit clusters [4, 5]. Cluster beams can be used to study cluster properties and/or to deposit or implant clusters on/in substrates, define patterns and permit the construction of devices.

1.2.2 Applications of Clusters

Cluster science can be applied in different areas, e.g. cluster beams can be used to sputter, etch and smooth surfaces [5–7]. Apart from refining surfaces, they can be used to grow smooth dense films [6]. When using cluster beams to nanostructure surfaces it is possible to build different kinds of devices having unique optical, magnetic, electric and catalytic

properties.

Porous silicon nanocluster films can be used as light emitters in optoelectronics [6, 8] and films of magnetic clusters are important for the advances in high density information storage [9]. The electronics industry utilises semiconductors when realising advanced devices, and it is therefore possible that semiconductor clusters can be used in future electronic devices, such as sensors for measuring both physical properties and the detection of single molecules [6, 10]. Metal clusters deposited on oxide (SiO_2) and lamellar (graphite) supports can be used as catalysts in industry to speed up chemical reactions [11]. One envisages also that one potential application for metal clusters (Pd_n) pinned on graphite is hydrogen storage [12], which is highly topical in relevance to fuel cells.

1.3 Cluster Physics

1.3.1 Atomic Clusters

The individual atom is one of two extreme ends of matter, at the other end of matter we find the bulk. Both can be characterised by their electronic properties, discrete energy states and bands of energy states, respectively [7]. In between these two extremes we find aggregates of individual atoms, clusters, which have totally different properties when compared to the extremes of matter [13]. The properties of clusters are tied to the number of constituents, which can range from 2 to 10^{6-7} particles [14].

Clusters can be formed from most elements in the periodic table. They can contain identical particles or two or more species. In contrast to clusters, molecules have limited number of atoms, defined chemical composition and unique spatial structures [3]. Moreover, any elements or indeed molecules may make up a cluster as long as the cluster has more than two constituents and has properties that have not yet reached their bulk character.

It is possible to estimate the size of clusters by approximating the packing of hard spheres into a spherical volume. Despite it being an approximation, it gives a rather reasonable mapping of cluster sizes to diameters, fraction of surface atoms etc. for larger clusters. The model assumes a cluster consisting of N atoms having following volume

$$V_c = NV_a, \tag{1.1}$$

where V_a is the volume of a single bulk atom. The expression 1.1 can be expressed in terms of atomic (R_a) and cluster radii (R_c)

$$\frac{4\pi}{3}R_c^3 = N\frac{4\pi}{3}R_a^3, \tag{1.2}$$

which simplifies to

$$R_c = N^{1/3}R_a. \tag{1.3}$$

The cluster diameter (D_c) is then

$$D_c = 2R_c = N^{1/3}2R_a. \tag{1.4}$$

In the same manner, the surface area of the cluster (S_c) is related to the surface area of the atom (S_a) by

$$S_c = 4\pi R_c^2 = 4\pi\left(N^{1/3}R_a\right)^2 = N^{2/3}S_a. \tag{1.5}$$

Many properties, as well as catalytic properties, of clusters depend on the ratio (F_s) of surface atoms (N_s) to cluster atoms (N). The number of surface atoms (N_s) can be ob-

tained by dividing the cluster surface area by the cross sectional area of a single bulk atom (A_a) in the large cluster limit. The ratio for pseudo-spherical clusters (e.g. icosahedral) is [14]

$$F_s = \frac{N_s}{N} = \left(\frac{4\pi N^{2/3} R_a^2}{\pi R_a^2}\right)/N = \frac{4N^{2/3}}{N} = 4N^{-1/3}. \tag{1.6}$$

Determining structures of small objects is a difficult experimental task and clusters are not an exception to this rule. The field of solid state science was aided by the long-range translational periodicity of crystalline materials, which made it possible to observe their structure by x-ray diffraction techniques [15]. Clusters lack long-range translational periodicity but they show geometric and/or electronic shell periodicity. During a cluster's early evolution it changes its geometric structure whenever an atom is added till a certain point. At this point, most types of clusters prefer a symmetry corresponding to one of the five Platonic solids or the two Kepler solids, see Figure 1.1 [15, 16].

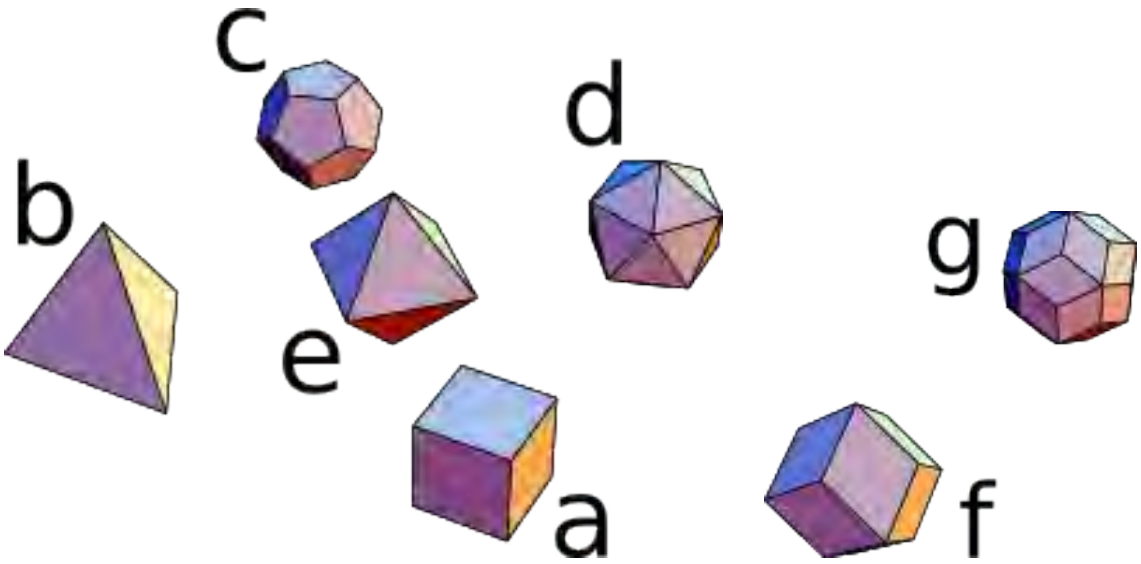

Figure 1.1: The five *Platonic Solids* (a) *cube* (b) *tetrahedron* (c) *pentagonal dodecahedron* (d) *icosahedron* and (e) *octahedron*. Kepler's two solids (f) *rhombic dodecahedron* and (g) *rhombic triacontahedron*.

In most cases of further cluster growth, concentric atomic layers (geometric shells of

atoms) are added to the "static" cluster core, thus preserving the original symmetry and giving rise to a *shell periodicity*. Due to this fact one can, occasionally, deduce the structure of an unknown cluster.

Some metal clusters also show electronic shell structure, analogous to the *nuclear shell model* in nuclear physics. *The Jellium Model* is employed; a sphere of uniform positive charge density has valence electrons filling the energy levels, following the Pauli principle. In the same manner as closed geometric shells signal stability, filled electronic shells result in a more stable structure. These stable geometric and electronic configurations show up as peak intensity in mass spectra and are called *"magic numbers"*, see Figure 1.2 [17–20].

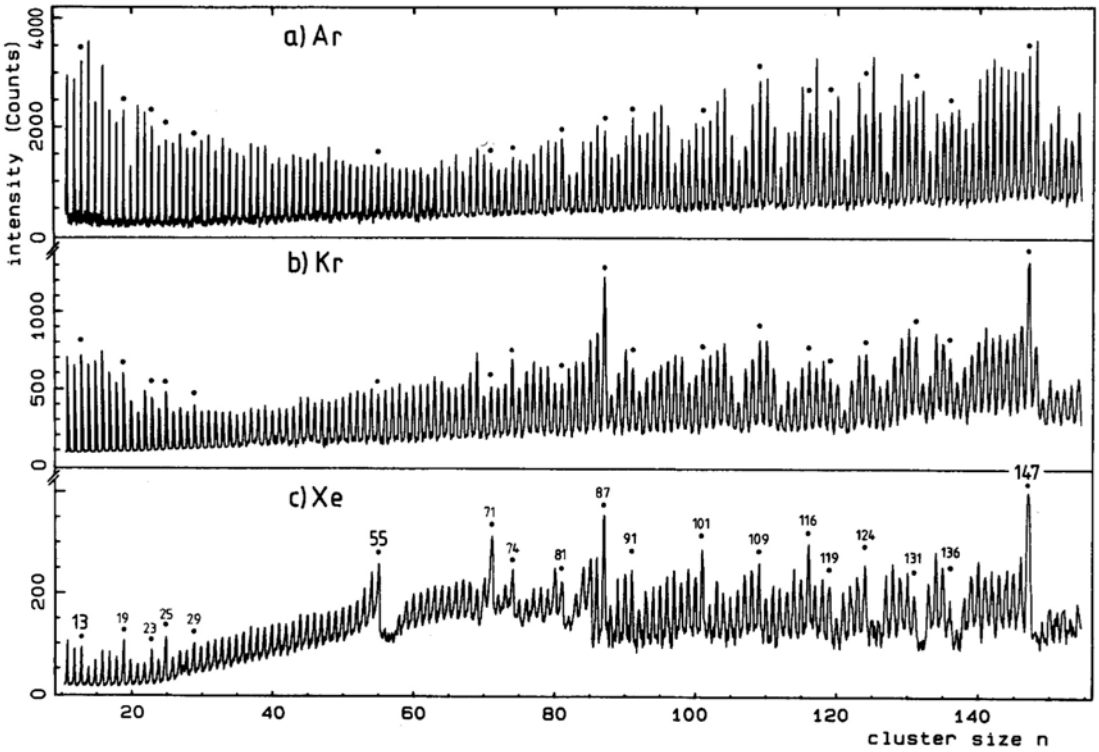

Figure 1.2: Mass spectra of rare gas clusters showing relative abundance of different cluster sizes. Magic numbers corresponding to filled shells or subshells of icosahedra are marked. (a) Mass spectrum of argon clusters, (b) krypton clusters and (c) xenon clusters. (Adapted from [17].)

Clusters have a large surface to volume ratio and therefore share many properties of bulk

surfaces. It is expected that in order to lower their energy, the atoms at the cluster surface undergoes reconstruction and possibly change the shape of the cluster. The large surface to volume ratio also means that clusters can act efficiently as catalysts.

The key parameter, which controls virtually all properties of a cluster is the number of atoms in that cluster. While observing the discrete development atom-by-atom, a single atom to the bulk, one can see the evolution of physical properties from "quantised" to "quasi-continuous" to "continuous". For example clusters having different sizes have different melting points. Close to the melting point the core of the cluster can be solid while the surface layer is liquid. Other parameters such as ionisation potential, magnetic and optical properties are also dependent on cluster sizes. For metal clusters, the ionisation potential increases with decreasing cluster sizes, and a bandgap appears (contrary to metal bulk) which increases in size. This implies that metal clusters becomes semiconducting and finally isolating for smaller cluster sizes [14, 21–23]. This in turn allows the tailoring of devices with certain electronic and optical properties by selecting appropriate sizes. Magnetic properties also get altered with cluster size, the magnetic moment per atom increases with decrease of number of atoms for transition metal clusters [24, 25].

Metal Clusters

Three main different types of metal clusters exist, namely clusters from the s-block metals, from the sp-metals and from the transition metals. These metal categories have different properties, which are also observed in the respective cluster types. For s-block metals, the s valence orbitals contribute to the metallic non-directional and delocalised bonding. The bonding has more covalent character for sp-metals, since the directional p-orbitals also contribute to the bonding. For transition metals, the d valence orbitals contribute to the bonding, which is more covalent and directional.

Different models exist to describe the bonding of metal clusters and their different proper-

ties [14]. The simplest model is a classical electrostatic model, where a uniform conducting sphere approximates the metal cluster. The Liquid Drop Model (LDM) can explain several properties of metal clusters as a function of cluster size. The ionization energy and electron affinity of metal cluster as a function of size is explained very well with the LDM. The prediction is that the ionisation energy (ionisation potential) will decrease with increasing cluster sizes. Less energy is required to remove an electron from a large cluster compared to a small cluster finally reaching the bulk work-function value. The electron affinity should increase for increasing cluster sizes (more energy is released when adding an electron to a large cluster compared to a small cluster) and finally reach the bulk work-function. The LDM breaks down for small metal clusters, because it does not take into account quantum size effects (QSEs).

Where the LDM fails to explain the behaviour of IPs and EAs of small alkali metal clusters because of QSEs, the Jellium Model provides an explanation. The Jellium model was originally used to explain atomic nuclei stability and structure and its applicability over such a wide length scale shows its vast unifying strength. The Spherical Jellium Model depicts the metal cluster as a sphere having a uniform positive charge and being filled with an electron gas. An electron would "feel" the mean field potential of the ionic cores, while it moves under the constraint of the sphere. The attractive potential imposes boundary conditions which gives rise to quantisation of the electron energy levels. Clusters having several thousands of atoms show electronic shell structure with this quantum mechanical model.

The Schrödinger equation for the electron, solved for the Jellium model, is valid for the alkali and noble metals (copper, silver and gold). This being due to their non-localised valence electrons having s-wave character. Yet another condition is that the model applies only for molten clusters, which should be the case for alkali metal clusters as they have low melting points in the bulk, with a melting point decreasing with cluster size.

The appearance of magic numbers can either depend on electronic or geometric structure, as mentioned earlier in section 1.3.1. Clusters can adopt different types of geometric structures, such as icosahedra, decahedra, cuboctahedra and rhombic dodecahedra. These polyhedra can be built up by adding more concentric shells, where a closed shell marks a more stable structure and the total number of atoms making up the cluster structure, the corresponding magic number. The equation

$$n(K) = \frac{1}{3}\left(10K^3 + 15K^2 + 11K + 3\right), \tag{1.7}$$

gives the number of atoms n making up the cluster having K number of closed concentric shells (i.e., magic numbers) and is valid for icosahedra, decahedra and cuboctahedra. In order to distinguish which particular cluster structure one has, a closer look needs to be taken from the fine structure of the mass spectra to distinguish magic numbers linked to filling of sub-shells, i.e. filling of the different structures' faces. These are different for the three different polyhedra and can therefore be used to distinguish the final shape. The magic numbers n for a rhombic dodecahedron having K shells, are given by

$$n(K) = 4K^3 + 6K^2 + 4K + 1. \tag{1.8}$$

The icosahedron is a Platonic solid and has the highest symmetry of all discrete point groups [15]. Its geometry allows atoms to be closely packed but only up to certain cluster sizes, where it undergoes a structural phase transition when reaching the bulk.

The first shell is constructed upon a single atom by 12 equally spaced (from the centre atom and from each other) atoms, summing up to a total of 13 atoms in the cluster. The evolution from the dimer towards this structure gives new geometrical structures in each step, see Figure 1.3a. However, starting from the 13 atom cluster, the icosahedral core is preserved and further growth takes place by adding shells. Thus, adding a second shell

containing 42 atoms will give a total of 55 atoms and a third 147 and so on according to formula 1.7 first highlighted by Mackay [26].

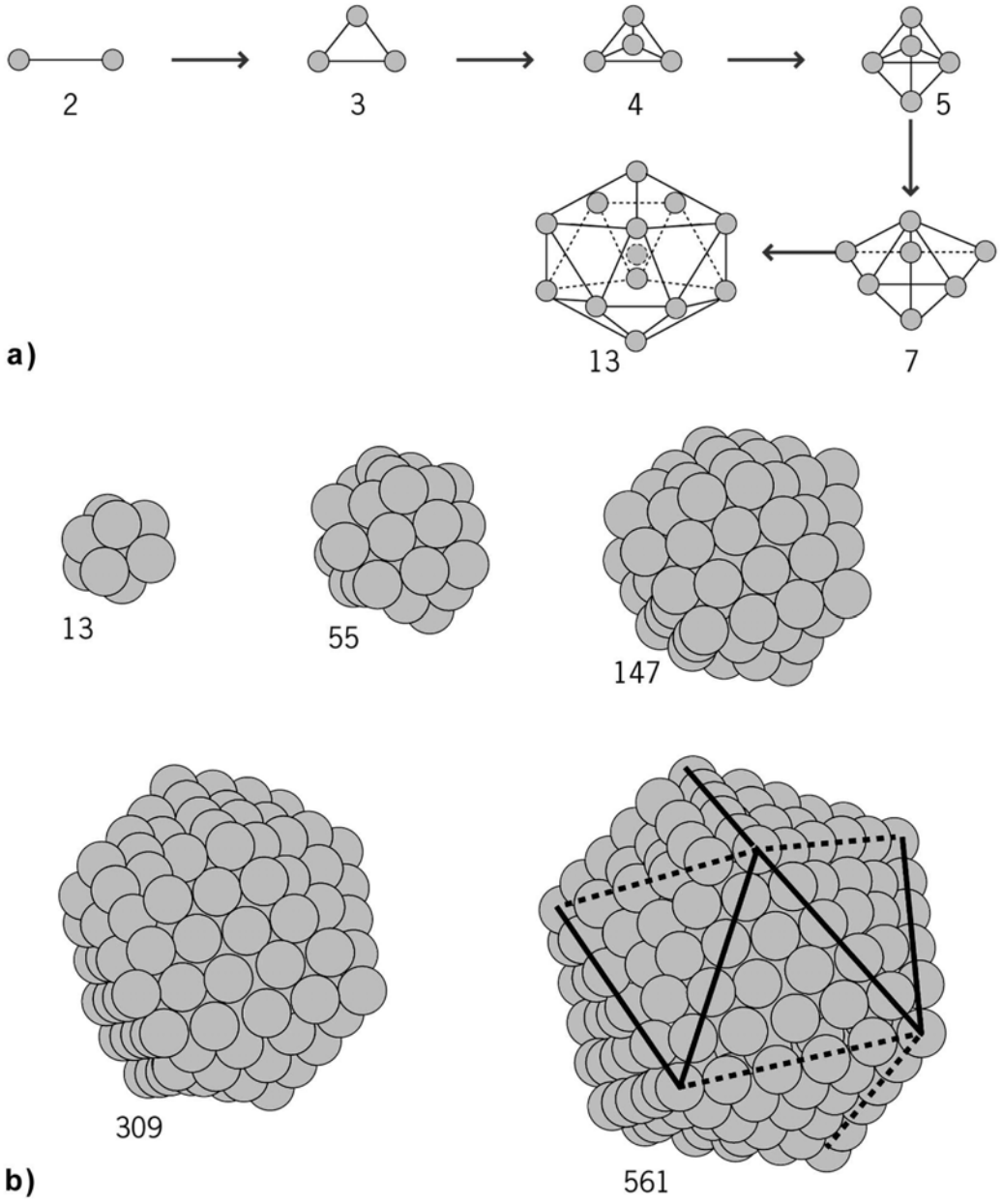

Figure 1.3: (a) Depicts the first evolutionary steps, by additional atoms, from the dimer (2 atoms) until reaching the first icosahedral structure (13 atoms). (b) Structure of the first five Mackay icosahedra (magic numbers). The intermediary stages (filling of subshells, solid faces), which also can be found from mass spectra (see Figure 1.2), exist but are not illustrated. (Adapted from [14].)

Geometric shell structure dominates the mass spectra of transition metal clusters having sizes down to tens of atoms. This is largely due to narrow bands on each atom, from the partially filled set of five tightly bound valence *d* orbitals, having high density of electronic states, hence small energy level separations.

In this work, some extra focus has been placed on clusters from palladium (Pd) even though clusters of both copper (Cu) and gold (Au) have been produced and used. Palladium belongs to the group of transition metals. The atomic number (Z) and radius of palladium is 46 and 0.14 nm, respectively and it forms a face-centered-cubic (fcc) structure as a bulk material [27]. The importance and focus of Pd (bulk and clusters) in catalysis and increased interest in relevant research, partly guided the choice of this element. Moreover, a higher flux of clusters and greater stability of the cluster source was experienced when working with Pd compared to Cu and Au. It also helped that a higher contrast of Pd, compared to Cu, improved characterisation in HAADF-STEM, especially when also working with Au.

The structure of palladium clusters has been studied experimentally and theoretically. The structure and stability of palladium clusters (up to Pd_{55}) using density functional theory were investigated by Zhang *et al.* [28]. Comparisons of several isomers (1D, 2D and 3D) were performed for $Pd_{\leqslant 13}$ and a few selected structures at sizes Pd_{19} and Pd_{55} were also explored. They found that icosahedral structures are favoured over both cuboctahedral and decahedral structures for Pd_{13} and Pd_{55} and that, from the tetramer up, the lowest-lying isomers are 3D. For Pd_{13}, the cuboctahedron is more stable than the icosahedron according to density functional calculations by Watari and Ohnishi [29], which is contrary to the results above.

Few results exist for larger cluster sizes [22] due to the computationally expensive calculations associated with larger systems. Kumar and Kawazoe found that the lowest energy for both Pd_{55} and Pd_{147} belonged to slightly distorted icosahedral structures, when

comparing icosahedron with cuboctahedron and Ino-decahedron clusters for the above-mentioned sizes [30]. A perfect icosahedron at size Pd_{55} was found to have a higher energy than a distorted icosahedron (Jahn-Teller) by Nava *et al.* [31]. They also found that sizes Pd_{147} and Pd_{309} have icosahedral and cuboctahedral structures, which are very close in energy. However, the icosahedra had lower energy for Pd_{147} and for Pd_{309} the cuboctahedral structure was more stable. To the contrary, Barreteau *et al.* found that the icosahedron is still lower in energy than the cuboctahedron for Pd_{309}, but not for Pd_{561}, by using tight-binding calculations [32].

Icosahedral structure for Pd_{55} was also found through global optimisation studies using the Sutton–Chen potential [33] for sizes up to Pd_{100}, yielding the same results for palladium as silver. This result is also confirmed by Massen *et al.* in the optimisation of the Gupta potential [34]. Experimentally, icosahedral structures of small palladium particles were found by high-resolution electron microscopy (HRTEM) by Penisson and Renou [35]. Transmission electron microscopy investigation of thiol-passivated palladium nanoparticles was performed by Jose-Yacaman *et al.* [36]. Clusters ranging from 1–5 nm in diameter and a variety of structures from icosahedral, to fcc, to decahedral as well as amorphous structures were observed. Even quite large icosahedral clusters were found, which the authors suggested is due to kinetic trapping effects.

1.3.2 Cluster Formation

Clusters are seldom created spontaneously in equilibrium conditions and so certain criteria have to be fulfilled in order for clusters to be produced. The formation of dimers, through a three-atom collision, is possible when the local thermal energy of the gas is lower than the dimer binding energy. The requirement of preserving both momentum and energy necessitates the interaction of three atoms in the nucleation process, equation 1.9.

$$A + A + A \longrightarrow A + A_2 \tag{1.9}$$

The excess energy is transformed to the third atom, thus maintaining the dimer stability. The introduction of a cold inert carrier gas can further enhance the efficiency of cluster nucleation and cooling of larger clusters. Collisions between clusters and the cold inert atoms removes the excess internal energy as kinetic energy.

After the nucleation step initial growth is commenced by adding of atoms one at a time. When the concentration of clusters increases further, growth will take place by the coalescence of small clusters into bigger clusters. During the growth process, heat builds up and the competition between growth and evaporation of the cluster makes them unstable. This is why it is desirable to cool the clusters with the cold gas. Another approach to cooling is by adiabatic gas expansion which is performed in a supersonic nozzle source.

Cluster Ionisation

In order to exercise control over the cluster beam, all clusters are charged so that electrostatic lenses can be used for beam manipulation. Since the properties of clusters change with size, it is crucial to filter the cluster beam in order to obtain clusters with a specific desired size.

Ionisation of clusters can be achieved in different ways, e.g. by electric discharge, electron transfer photoionisation or electron impact. Corona discharges are used to positively charge clusters in the stagnation chamber, prior to expansion, in supersonic nozzle sources. The use of a laser allows the fine-tuning of photon energy, used in the ionisation process, avoiding cluster fragmentation and determining the ionisation energy of the cluster. By using an electron gun or thermal electrons from a heated wire one can knock away electrons from clusters and, hence, create positive ions, but the likelihood of frag-

mentation is large. To create negatively charged clusters one can use (valence) electron transfer from electropositive alkali metal atoms in the vapour phase, or more preferably, capture of low energy electrons, which is a more clean and versatile method.

Charged clusters are inherently formed in the generation process (due to the plasma) in electric discharge sources, sputtering sources and laser ablation sources.

Mass Selection/Detection

The mass selector/detector in a cluster source has a dual function. It analyses the cluster sizes in the beam and it acts as a mass filter. These are two very important functions for understanding, characterising and developing cluster sources as well as for experiments utilising them. There are different routes one can take to achieve mass selection of clusters from a cluster source, of which the main three are presented below.

The Wien Velocity Filter utilises a magnetic field to deflect the clusters in a beam according to their charge and velocity. An additional force balancing, perpendicular, electric field is applied. Only one charge/velocity ratio is balanced in the filter and thus allowed to pass, while the other clusters get deflected. The intensity of the size-selected beam is high, as the selection process operates continuously. However, the mass resolution drops with increasing mass, as the cluster velocity is inversely proportional to the square root of the mass ($v_c \propto 1/\sqrt{m}$), rendering the filter effective only for small clusters. The filter, being compact and not deflecting the transmitted, size-selected beam, can easily be installed into existing cluster sources.

Four cylindrical rods placed as the parallel edges in a cube make up the *Quadrupole Mass Filter*. A bias of $V = \pm(V_{dc} + V_{ac} sin(\omega t))$ is applied to the rods, with every other rod having opposite and equal voltage. Cluster ions assume a helical trajectory inside the quadrupole and only one charge to mass ratio is transmitted, thus enabling size-selection. The filter is continuous, thus having high intensity, but unfortunately both transmittance and reso-

lution decreases with increasing mass. The filter is only effective for small clusters and because low beam energy operation is used, the filter experiences space-charge problems.

Time of Flight Mass Spectrometry (TOF-MS), and in particular a linear configuration, which initially was proposed by Wiley and McLaren 1955 [37], enables very good discrimination of cluster masses. The idea is to accelerate charged particles using equal kinetic energy and track their time of arrival at a detector. The particles will arrive at different times due to their different masses.

The linear TOF spectrometer has three main regions. In the initial region, clusters are ionised by electron or photon impact and extracted towards the second region by an electric field. In the second region the cluster ions get their final acceleration towards the detector. The final region does not have an electric field so the cluster ions move with a velocity proportional to the square root of their charge to mass ratio. An ion detector sits at the end of the region and registers the arrival time of each cluster ion with a current pulse.

The main disadvantage of previous TOF spectrometers was their limited resolution. The ions formed in the ionisation region are located in different positions and have different kinetic energies. These ever-present distributions limit the overall resolution. The Wiley-McLaren configuration introduces a second accelerating region, and thus two new parameters, namely the length of the second region and the ratio of the second and first regions' electric fields. A proper choice of these parameters compensates for the initial space and kinetic energy distributions and an increase in resolution is achieved.

The novel lateral TOF-MS, used in the NPRL cluster source, is described in section 2.1.3.

1.3.3 Cluster Sources

The production of clusters started out as an unwanted process. In the latter half of the 1950s, researchers were focusing on producing high-intensity molecular beams. Clustering of the molecules produced artefacts and decreased the intensity of the molecular beams. The group of Becker was among the first to produce clusters purposefully in experiments in 1956 [38]. Today, cluster science is an independent, mature field and several means of cluster production and manipulation exist.

There are different types of cluster sources, each suited for different experimental purposes and with each producing different cluster size distributions. There is a wide range of source types, such as sputtering sources, gas aggregation sources and laser ablation sources [14]. Despite these different cluster production techniques, the generation of clusters goes through the same stages: *vaporisation*, where particles are produced in the gas phase; *nucleation*, where particles are initially condensed and form the nucleus of a cluster; *growth*, where other particles are added to the nucleus; *coalescence*, where small clusters merge to form bigger ones; and particle *evaporation* where particles are lost [7].

The *Supersonic (Free Jet) Nozzle Source* lets a gas expand, adiabatically, from a relatively high pressure stagnation chamber through a small nozzle and into a vacuum, thus forming a supersonic beam. The source creates clusters from low-boiling metals (mercury) and inert gases, molecules and clusters from alkali metals with the additional use of an inert carrier gas. It is a continuous source with an intense beam and generates clusters having a wide size distribution. The *Laser Vaporization - Flow Condensation Source* is a pulsed source utilising a pulsed high power laser, which ablates the surface of a rotating target (rod). The ablated atoms and small clusters, which are ionised in the process, start clustering when interacting with a pulse of inert gas and then undergo supersonic jet expansion. This process can generate clusters containing several hundreds of atoms from any metal, silicon and carbon. This type of source uses expensive high power lasers, but is otherwise

versatile with stable and intense beam. The special family of sputtering sources include the *Pulsed-Arc Cluster Ion Source (PACIS)* which uses electrical discharge to vapourise cluster material, *Ion Sputtering Source* that generates small clusters with a single charge by ion gun sputtering of high-melting material and refractory metal targets, and finally *Magnetron Sputtering Source* which has been used in this work and will be explained in Chapter 2.

1.3.4 Clusters on Surfaces

Cluster beam sources can be used for the deposition of clusters onto surfaces, thereby structuring surfaces at the nanoscale. There are different kinetic energy regimes used to deposit clusters onto surfaces. These energy regimes are classified according to what interactions take place between the cluster and the surface after impact. The main aim is to understand the deposition and implantation of clusters on substrates and study the properties [39]. There are two energy regimes giving rise to specific cluster-surface impact phenomena, the low-energy deposition and the energetic interaction regimes. When the binding energy of the cluster atoms is greater than the kinetic energy per atom, the deposition process is considered to be low energy and the clusters land "softly" on the substrate surface. They do not fragment upon impact, but their structure can distort. Deposited clusters can coalesce or agglomerate together to form larger structures due to their high surface diffusive mobility [7]. Low energetic deposition is, for this reason, deployed when growing porous films and producing special surface reliefs.

The other end of the energy scale is the energetic interaction regime, for which the binding energy of the individual cluster atoms is smaller than the kinetic energy per atom. During impact these high energy clusters can break up and by increasing the energy the cluster can be implanted [40, 41].

Pinning is a special case between the two energy regimes where some atoms of the surface

are displaced during energetic cluster impact and some of the cluster atoms are implanted in the vacant positions [12, 42–46]. The clusters maintain their structure and do not diffuse on the surface.

The pinning energy and the energy regime, in which the morphology/shape (height and diameter) of the cluster can be controlled, belong to the energy interval between the two regimes described above [47].

For the work presented in this thesis, the main interest was on the pinning energy regime, but both higher and lower energies have been used extensively too. For the most part, the main task has been to avoid aggregation and try to have as dense coverage as possible yet maintain monodispersed clusters.

1.3.5 Bimetallic Clusters

The easiest way to synthesise nanoparticles, and to do so in large quantities, is by chemical preparation techniques, which is also the case for binary (bimetallic) nanoparticles [48]. For any specific application purposes where the properties of the nanoparticles are to be utilised, as has been mentioned, they are quite well linked to their size, the chemical nanoparticle synthesis techniques unfortunately produce particles with a wide size distribution. As if this was not enough, the particles are also covered in organic molecules in order to passivate them and prevent them from aggregating and/or sintering in chemical preparation methods. These passivating ligands can affect the properties of individual particles and thus their overall properties change and affect their usage in specific application purposes. In order to circumvent the property pollution of ligands affecting nanoparticles and also finely tune the nanoparticles' inherit properties, which are linked to their size, one can use physical gas phase preparation techniques and size-selection filters.

There are many benefits to using nanoparticles consisting of more than one element. The

most important benefit is mixing valuable and less valuable materials together to get particles that have similar or better properties than single element nanoparticles, while being much cheaper. That is of course under the assumption that the final synthesised particles will have a core-shell structure, but one could end up with a structure where the nanoparticles are half element A and half element B or where they are mixed to different degrees by their both elements (< nanoalloys).

The addition of an extra element and all the conceivable different structures adds more dimensions to all the possible properties, that the binary nanoparticles can offer. Focusing on metals, as we do, a huge interest has spurred the generation of bimetallic, and even trimetallic, nanoparticles (and clusters) for different relevant applications already using 'unimetallic' nanoparticles (clusters) [49–51]. With the huge interest in these particles, the different techniques in generating them has also created quite some interest. In particular, gas-phase production techniques have become interesting due to the inherit issues with chemical preparation methods mentioned above. Some physical gas-phase techniques are simpler than others and others are more elaborate. As we specialise in clusters and the use of magnetron cluster beam source we have looked into these technologies and found that there are mainly two distinct techniques, namely the use of mixed (two/three metal alloys) targets (or double targets, each with different metal/element) and the subsequent metal/element coating of pre-deposited single metal/element clusters on substrates by, e.g., physical vapour deposition.

Bimetallic Clusters by Coating and Annealing after Pre-Deposition of Supported Clusters

One way of making alloy bimetallic clusters is to coat already deposited clusters by various vapour deposition techniques in-situ. Basically, one would choose the more strongly binding metal to the substrate as the first metal for deposition, forming clusters, which

would act as seed nuclei for further bimetallic cluster formation. In order to allow for diffusion and sintering of adatoms during deposition, the substrate is kept at a high temperature. The less binding metal to the substrate is deposited after the first and subsequently build up bimetallic clusters on the substrate as the final step in the overall process. Core-shell bimetallic clusters can be formed in this way by not only taking into account the interaction of the two metals and the substrate, but also the surface free energies of the metals as well as their miscibility.

Langlois *et al.* have prepared core-shell bimetallic CuAg clusters by this method [52]. Silver and copper are immiscible elements and were therefore chosen to prepare bimetallic core-shell clusters. Silver has a lower surface free energy than copper, which is why copper was first thermally evaporated on amorphous carbon substrate. The substrate was kept at a temperature of 400° C, which assisted in the formation of copper clusters. In the second step, silver was thermally evaporated, while maintaining substrate temperature, to form CuAg core-shell clusters of ~25 nm diameters. That size was achieved by evaporating 6 nm of Cu followed by 3 nm of Ag evaporation (nominal thicknesses).

From the thermodynamics, complete silver shells surrounding the copper cores is expected from the process and this was confirmed by using high resolution transmission electron microscopy (HRTEM) to study the Moiré patterns rising as evidence of core-shell structure as well as using energy filtered transmission electron microscope (EFTEM) results. They reported, however, that small elemental silver clusters were formed as the interaction between the amorphous carbon substrate and the silver was strong enough.

Another interesting result was observed, when already existing platinum clusters on a substrate of $TiO_2(110)$ were deposited with gold at room temperature to yield Au and Pt binary clusters, by Chen *et al.* [53]. STM imaging before and after gold deposition confirmed the formation of alloy clusters, as the cluster density was the same while an increase in cluster size after gold deposition was noticed. Through low energy ion scattering

experiments it was possible to confirm that AuPt (intermixed) alloy clusters were formed after gold deposition and not AuPt core-shell clusters. In the case of the bulk, platinum has a higher surface free energy than gold, thus thermodynamically one would expect that platinum would make up the core while gold would cover the cluster and hence make up the shell. This was not the case, being a perfect example that the bulk surface properties are quite different from the surface properties of nanoclusters.

One important and big drawback with this method is the broad size distribution of the formed binary clusters, but this can, however, be overcome. Previous work done in our group utilised the size-selected clusters, which were subsequently covered with a second metal, to obtain a narrower size-selection [54]. Both Au_{250} and Au_{2000} cluster sizes were used when depositing size-selected clusters, with a hybrid rf magnetron sputtering and condensation cluster beam source equipped with a lateral mass filter, on freshly cleaved highly ordered pyrolitic graphite (HOPG) substrates. The samples were subsequently coated with silver through thermal evaporation in order to form AuAg binary clusters. Computer simulations as well as AFM and STM confirmed the formation of AuAg binary clusters from the deposited size-selected gold clusters and the thermally evaporated and deposited silver atoms. However, the final structure and chemical arrangement of the clusters are yet to be confirmed, but the size distribution is narrow and has maintained/inherited the narrow size distribution of the original size-selected "seed" gold clusters.

Overall, this method is quite effective, and it has been demonstrated that the type of substrate and metals chosen are important when preparing binary clusters. An additional degree of freedom can be achieved by pinning already size-selected clusters so the cluster-substrate effect can be avoided, thus relaxing the constraint of possible metals for the coating step. The other benefit of this introduced technique to the original method is obviously the narrower size-distribution that is possible. Bimetallic clusters through coating

and annealing is one method of a couple of potential routes to make binary clusters. Another popular route is to utilise mixed or dual targets in a plasma sputtering cluster beam source to produce bimetallic clusters.

Bimetallic Clusters by Mixed or Double Targets

The use of double targets (e.g. two magnetron sputter sources) or a mixed target is the most popular physical (cluster beam) technique to create bimetallic (binary) clusters as it is the most straight forward and feasible direction to take if one already have a cluster source. Different physical methods exist to vaporise targets, as e.g. laser ablation, magnetron sputtering and hydrogen (nitrogen) plasma-metal reaction. Laser ablation happens to be the most widely used technique as it is quite versatile and can be applied to a wide type of materials. Usually, binary cluster generation takes place by the use of a single laser beam on a single alloy/mixed target or a double (split) laser beam with each beam vaporising a single element target each. The produced binary plasma is then further mixed and condensed to form clusters, by introducing cool inert gas, which are then deposited onto substrates. The condensed cluster vapour plasma mix can also be allowed to adiabatically expand through a narrow nozzle orifice to form a cluster beam prior to deposition. The quality of the beam can be sublimed further by the use of skimmers for beam collimation prior to its introduction to a size-selection filter from which the beam will exit size-selected before being deposited.

Various types of bimetallic clusters have been formed by the use of a mixed target or dual elemental targets. The majority of binary structures formed have been alloy (mixed) clusters. For most cases, the size distribution as well as the chemical composition have been tunable by the control of the evaporation conditions. An addition of size-selection filter to cluster sources have outputted size-selected binary clusters in beams. Although Lieven's and Wang's groups have studied core-shell bimetallic clusters, in one sense, they were

limited in size due to their inherent structure limitation [55–60]. Both groups have verified the ability of a second metal atom to enter and occupy the centre of cage structures of small metal clusters. Theoretical calculations together with mass abundance spectroscopy (Lieven's group [58–60]) and anion photoelectron spectroscopy (Wang's group [55–57]) proved the structure of this type of core-shell bimetallic clusters. Moreover, due to this cage structure, limitations to the size distribution as well as the element composition are imposed and they were only able to prepare clusters smaller than 100 atoms.

Core-shell clusters of other compositions than metal-metal have also been generated through laser vaporisation, such as metal-semiconductor and metal-oxide, which have not been constrained or confined to only small sizes of clusters. However, the element composition and the size distribution have not been controlled very well for these types of core-shell clusters.

Despite the main advantage of the laser ablation technique for cluster sources being its material versatility, its pulsed operation becomes a drawback when a (huge) continuous flux of material is desired as output. This is where the magnetron sputtering cluster source becomes advantageous with its high throughput and continuous operation. In Sumiyama's group for example, a double target sputtering system is deployed [61]. For metal cluster preparation, one of the targets can be operated in dc glow discharge mode and the other target in rf glow discharge mode, for the preparation of semiconductor and insulator clusters. Both targets can also be operated in tandem by single glow discharge mode to produce binary clusters and a plate can be employed to either separate or join the two target chambers in the system, see Figure 1.4.

Large binary core-shell clusters of Co/Si and Fe/Si, as well as bimetallic alloy clusters of CoPt and CoAl, were prepared with this system. Without the use of the separation plate to divide the target chambers, homogenous nanoalloys of CoAl and CoPt clusters were produced by the use of two metal targets and single (DC) glow discharge mode. In

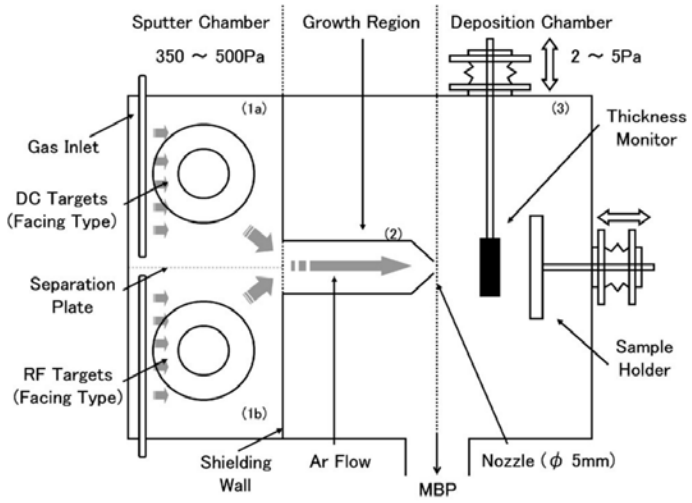

Figure 1.4: Schematics showing the cluster source setup in Sumiyama's group. (Adapted from [61].)

the same way, by using one metal and one semiconductor target and dual glow discharge mode, core-shell Fe/Si and Co/Si clusters were formed. With the plate separating the two chambers, only mixtures of Fe and Si (Co and Si) single clusters resulted, showing the importance of the two material vapours mixing together before condensing to form core-shell and alloy clusters.

A Nanogen 50 system (Mantis Deposition Ltd) was deployed in José-Yacamán's group, which is a commercial uni-target magnetron sputtering cluster source. They were able to generate AuPd alloy clusters by using a AuPd alloy target and tune the size by controlling evaporation conditions. Bimetallic AuPd alloy clusters with diameter sizes 1.1±0.44 nm, 3±0.3 nm and 5±0.07 nm were generated by tuning [62].

All mentioned work clearly shows the possibility of producing nanoalloy (mixed) clusters as well as core-shell clusters with this technique (also with slightly different flavours of vapour generating techniques based on this main technique). However, it is still evident, from previous cited work, that large (core-shell) clusters are still proven a challenge to generate.

Two routes in preparing bimetallic clusters have been presented so far, however, a third

more exotic production technique is to be explored in this thesis and that is, the idea of coating size-selected clusters "in-flight" before deposition onto substrate surfaces.

Bimetallic Clusters by In-Flight Coating

The inspiration of the feasibility to pursue such a coating technique is brought from the work of Harbich's group, involving deposition of size-selected metal clusters in rare-gas matrix films [63–66] and the work of Nepijko *et al.* related to the surface shape of frozen rare-gas films [67]. They use the replica method, where silver atoms are condensed on a freshly made layer of frozen rare gas in order to directly visualize and investigate the pores of the surface. Atomic force microscopy (AFM) and scanning electron microscopy (SEM) were used to characterise the self-supporting metal film replica of the frozen solid rare gas matrix surface structure, which in turn gives an indication of the matrix porosity. Films of Ar, Kr and Xe were investigated through this method where the hills of the replicas represented the pores of the rare gas layers. By varying the condensation times (20, 60 and 300 s) for, e.g., Ar, different layer thicknesses were achieved (150, 500 and 2500 nm) at same condensation temperature (5 K) and resulted in unchanged porosity (for >150 nm). The number of pores are found to increase at temperatures below certain temperatures (20, 35 and 40 K) for the solid rare gases (Ar, Kr and Xe). With increasing temperature, the pore concentration and pore size distribution decreases while the maximum of the distribution increases.

The overall idea, which is explained in more detail in the in-flight coating chapter, is to first condense a solid rare-gas (Ar) matrix film onto a liquid helium cooled TEM Cu mesh grid. Thereafter, a thin film of metal (Au) is evaporated on top of the matrix, which is then ready for the size-selected metal (Pd) cluster beam to travel through and get coated in-flight prior to substrate deposition.

1.4 Nanofabrication

In previous sections you have seen the Bottom-Up approach to nanoscience and nanotechnology and now you will be introduced to the Top-Down method. Bulk materials (conductors, semiconductors and insulators) are shaped in order to form different structures with enhanced properties, which is extrapolated to the making of various devices with important technological applications. One such material, of interest in this thesis, is molybdenum disulphide (MoS_2), which can be used in catalysis. The different tools and processes used in fabrication are also covered in the following sections.

1.4.1 Molybdenum Disulphide

Bulk molybdenum disulphide (MoS_2) is a semiconductor with an indirect band gap of ~1.22 eV [68]. The semiconductor has a lamellar structure, as that of graphite and mica. A hexagonal molybdenum atomic layer is sandwiched between two hexagonal sulphur atomic layers forming a basic trilayer. There are two different structures reflecting the stacking of hexagonal-packed layer planes found in natural MoS_2 crystals (molybdenite), i.e. the $3R$ and $2H$ polytype structures, respectively (see Figure 1.5).

The forces between basal planes (trilayers) are much weaker (van der Waals) than the covalent bonds between molybdenum and sulphur within the basal planes [70]. This allows the basal planes to de-attach and slip on each other, which gives MoS_2 low-friction properties and is thus widely used as a dry solid lubricant (additive) [71, 72]. MoS_2 is also used as a catalyst in hydrogen desulphurisation (HDS) [73, 74]. Other areas of use are in hydrogen storage, shock absorption, rechargeable batteries and photovoltaics [75–77]. Electronics and thermoelectric applications are also successfully benefitting from the material [72, 78]. In this work the main interest of MoS_2 is its use as a catalyst for the hydrogen evolution reaction (HER) [73, 79, 80].

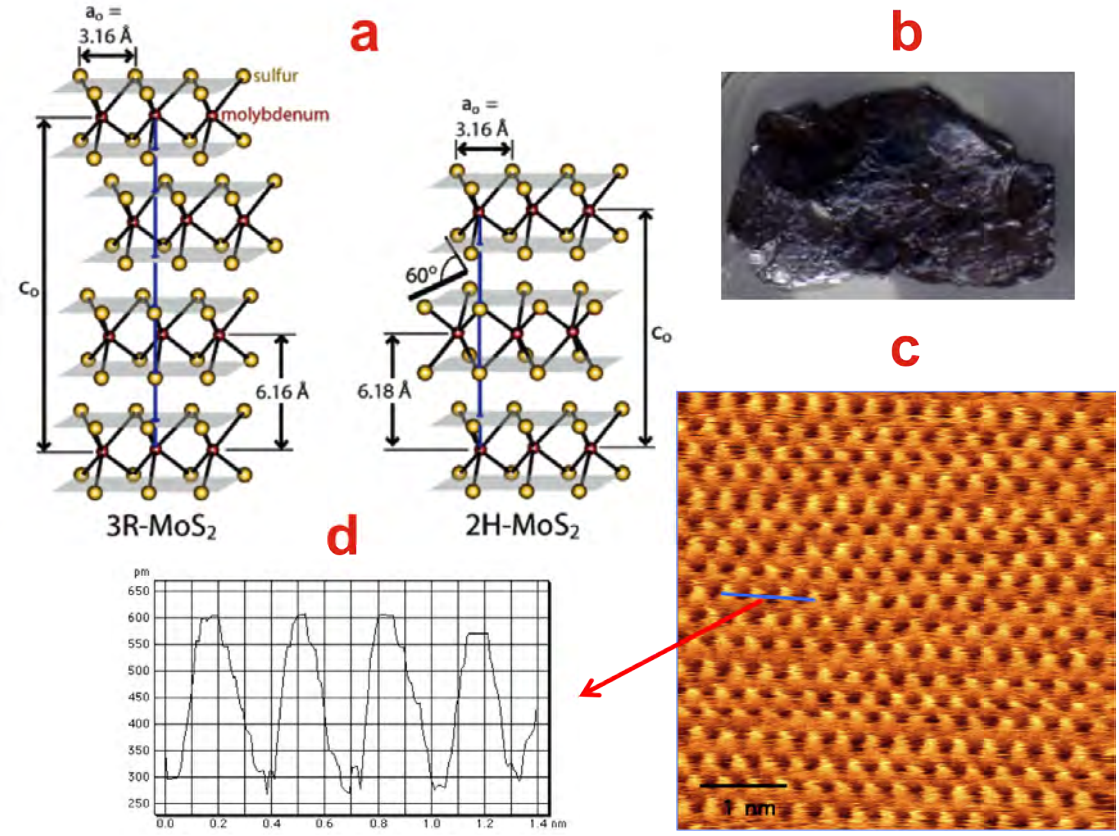

Figure 1.5: MoS_2 has a lamellar structure with each basal plane made up of one hexagonal molybdenum (red in diagram) atomic layer sandwiched between two hexagonal sulphur (yellow in diagram) atomic layers. (a) Schematic diagram depicting the rhombohedral (3R) and hexagonal (2H) structures of bulk MoS_2 natural crystals (Adapted from [69]). (b) Natural bulk MoS_2 (molybdenite) crystal (~10 × 20 mm^2). (c) STM image of cleaved MoS_2 showing atomic resolution (current: 1.1 nA, bias: -0.24 V; 1 nm scale bar). (d) Line profile of the MoS_2 STM image (purple line) depicted in (c), showing ~3.3 Å atomic interspacing.

MoS_2 has been made into many different structures and forms to further enhance and/or change the properties of the bulk material for different applications [71, 85]. All of these new allotropes are in the nano scale, such as 1D clusters [81], fullerene-like particles [83], nanotubes [83], fullerenes (nanooctahedra) [84] and platelets [82] (see Figure 1.6). Nanoplatelets of MoS_2 was found to be good catalysts for HER, with their edges identified as the active sites [80].

Moreover, Wilcoxon *et al.* showed widening of the band gap with the size of highly crystalline MoS_2 nanoparticles (>4 nm) [68, 88], see Figure 1.7. In addition to demon-

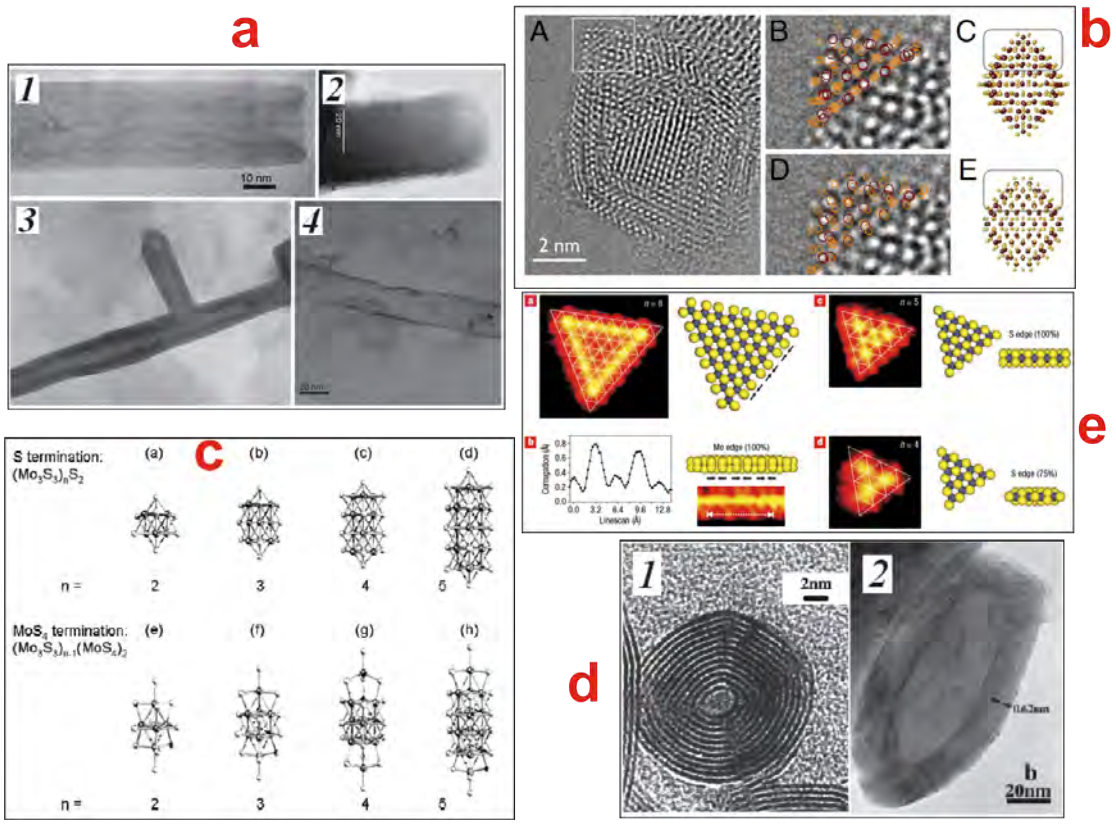

Figure 1.6: Different nano scale allotropes of MoS_2 are (a) nanotubes, (b) fullerenes (nanooctahedra), (c) 1D clusters, (d) fullerene-like particles and (e) platelets (adapted from [81–84]).

strating quantum confinement, smaller non-crystal particles were also produced and pentachlorophenol and phenol was decomposed with good photocatalytic activity [86, 89]. The blueshift of the band gap allows for the tuning of the wavelength of the visible light absorbed by MoS_2 nanoparticles with decreased sizes [87] (see Figure 1.7).

The interest in MoS_2 in this work is to explore another new form of the material, by nanostructuring the bulk through fabrication. The enhanced properties of MoS_2 nanoplatelets in catalysis, compared to the bulk, is a motivation to seek and find a new form of MoS_2 to increase the effect of edge sites in catalysis. Conceptually, nanopillars of MoS_2 are nanoplatelets stacked on top of each other, making it possible to increase the number of edge sites, without being constrained to the 2D nature of a surface. Moreover, solar radiation would drive the evolution of hydrogen through water splitting due to quantum

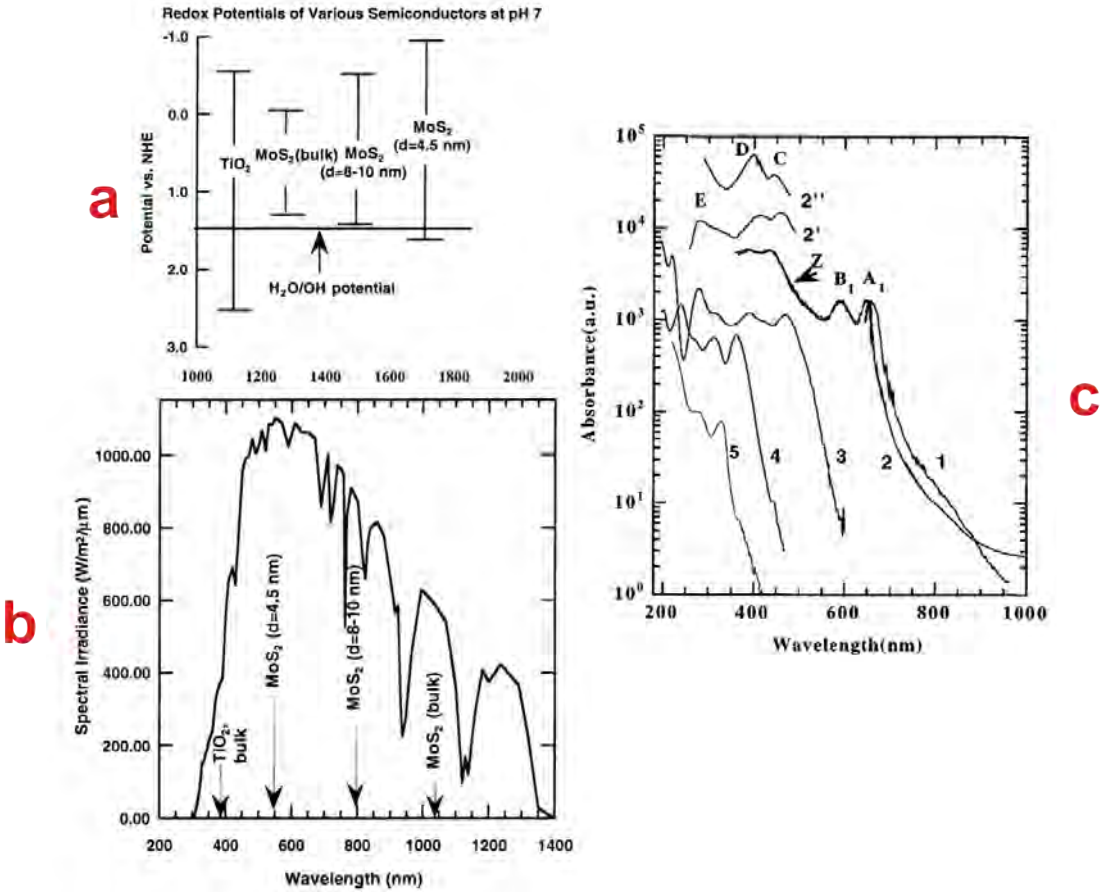

Figure 1.7: (a) The conduction and valence band edge positions vs normal hydrogen electrode (NHE) for MoS_2 with different sizes and bulk TiO_2. The widening of the band gap with decreasing MoS_2 size can be seen. Photogenerated holes can oxidize water and create hydroxyl radicals (oxidizes dissolved organic chemicals) when the valence band edge is higher than +1.2-1.5 V. (b) The absorbance edge of various semiconductors are shown together with the spectral irradiance, of the solar radiation reaching the earth's surface, vs photon wavelength (AM1.5D). The blueshift of the absorbance edge of MoS_2 with reduced size is clearly evident. (c) Optical absorption spectra of (1) synthetic and (2) natural MoS_2 bulk crystals (the latter with various features). (2') & (2") Depict higher resolution of the high energy features. Long wavelength spectra of (3) 4.5 nm, (4) 3.0 nm and (5) 2.5 nm diameter MoS_2 cluster samples are shown for comparison. The features of the curves are blueshifted with decreasing cluster sizes (adapted from [86, 87]).

confinement of the MoS_2 nanopillars.

1.4.2 Lithography

Part of the process of pattern transfer from mask to substrate is called lithography and can be applied through different techniques having various advantages and disadvantages. The most common type in industry is photolithography as it is a parallel process giving high throughput and thus enables mass scaling in production. Other types of lithography are also defined by the radiation used in the process, such as X-ray lithography, electron beam lithography and ion-beam lithography [90].

The process consists of applying a light-sensitive resist on to a substrate and then shining light through a shadow coating mask, which projects the desired pattern onto the resist that gives rise to chemical changes allowing the pattern to be transferred to the resist. The best resolution (smallest feature size) obtained by photolithographic systems is limited by the wavelength of the light used in the process, where UV light has the smallest wavelengths and can achieve sizes as small as a micron [91, 92].

One need to turn to other techniques for better resolution such as electron beam lithography (EBL), which uses a beam of electrons instead of light. In this case a special resist, sensitive to electrons, is used and after exposure to the electron beam either the chemically altered resist areas or the non-exposed areas are removed in the development process by appropriate solvents [93].

The feature size (resolution) achieved of an EBL system depends on the resist, the energy and spot size of the incident electron beam as well as the backscattered electrons and the dose. The clear advantages of electron beam lithography is the greater resolution and the larger pattern flexibility compared to photolithography [94].

Nanosphere Lithography

A Bottom-Up approach to lithography, which (conventionally) is a Top-Down approach to nanotechnology, is the use of Self Assembled Monolayers (SAMs) of spherical micro- or nanoparticles as patterned masks in the lithographic step instead of polymer resists and pattern exposure. This Nanosphere Lithography (NSL) can be used in tandem with conventional lithography, creating a dynamic range to the different feature sizes possible in the fabrication of structures, or solely, giving a boost to the resolution (feature size) of patterns formed.

Micro- and nanometre spheres (e.g. latex polymer or silica) suspended in solution (e.g. water) are typically used in NSL due to their straightforward application and inherent interaction properties to produce the desired final result. The spheres come in many different sizes and materials, making them somewhat versatile depending on specific application requirements. As the suspended spheres are applied to a surface, they start to self assemble to form hexagonally packed monolayers as the solvent (water) evaporates. One of the first uses of this technique was by Fischer and Zingsheim, where they used a monolayer of nanospheres as masks during metal deposition [95]. However, it was Deckman and Dunsmuir who developed the technique by extending its use with etching and deposition, making it a firm tool in the repertoire of micro- and nanofabrication [96]. Hulteen and Van Duyne pioneered the use of bilayers of nanospheres and were the ones to coin the term *"Nanosphere Lithography"* [97]. They also undertook thorough investigations of the deposition patterns formed using NSL. Members in our group have previously also been able to fabricate ordered silicon nanopillars successfully with NSL [98, 99].

NSL is a much less expensive method than conventional lithographic methods, but at the same time, it still retains the advantage of parallel patterning as the latter, speeding up the overall process. Other techniques, that are able to pattern structures at the nano scale, such as direct laser scribing, electron beam lithography and scanning tunnelling

microscopy (scanning probe microscopy) suffer from longer process times as they are operated serially and are much more expensive to deploy compared to NSL. The main two disadvantages of NSL are the limited shapes and coverage. As the pattern shapes depend on either the interstices between the nanospheres as they close-pack (for the smallest features) and the (shrunk) nanospheres themselves (for the largest features), not much can be done in that regime. Unfortunately though, the nanospheres do not close-pack neatly forever to create nice periodic SAMs. When experimentally depositing the nanospheres, large coverage of highly ordered arrays is quite a challenge and for most cases small area sizes are frequently achieved before defects (dislocations, cracks, etc.) start to appear as further out you go from the centre.

Denkov *et al.* described the hexagonal close-packing process of the nanospheres, as the solvent evaporates, in great detail [100]. Through optical observations they found that the basic mechanism pushing the self assembly is convective solvent flux as well as interaction of contact forces between particles and solvent.

As detailed in this thesis, it is the first time NSL is used to nanostructure MoS_2 and this, potentially, for the application of catalysing the production of hydrogen from water with solar energy. The final developed NSL process utilises a simple and neat bench-top setup, streamlining the whole nano patterning procedure.

1.4.3 Etching

After transferring the pattern from mask to resist on a substrate, the substrate needs to be formed according to the pattern through a process called etching. There are mainly two main routes of etching, namely dry and wet etching. Acids in the liquid phase are used to chemically "erode" the materials of interest in wet etching processes. In dry etching both chemical and physical gas phase processes are utilised to form materials. Dry etching (chemical) uses etchant gases from which reactive species are derived, in a

plasma for example, that act as etching agents while ion bombardment is the main agent in the physical counterpart process.

Dry etching is difficult to setup and facilitate from an equipment point of view while wet etching is much more easy. The etching process can be more fine tuned in dry etching, resulting in different etch rates for vertical and lateral features (anisotropic etching), while wet etching, typically, only achieves equal etch rates (isotropic etching). More types of materials can be processed with dry etching (lower selectivity), while wet etching can only process certain materials (higher selectivity) [91, 92].

In this work, a dry etching process was utilised and this will therefore be covered in more detail from now on.

Plasma Etching

In microfabrication, plasma etching is the most used dry etching technique. As described previously, a plasma is a charged gas containing equal amounts of positive and negative charges as well as possible unionised molecules. Different vital steps make up the whole plasma etching process.

The plasma etching process, in a vacuum chamber, starts with the introduction of etchant gases, such as O_2, SF_6 and CF_4 matching the material to be etched. Electrons are made to oscillate, when a radio frequency (RF) power is applied between two electrodes (anode and cathode), and collide with neutral gas molecules to form new ions and electrons, e.g. as in formula 1.10 [101].

$$CF_4 + e^- + A \longrightarrow CF_3^+ + F^* + 2e^- \tag{1.10}$$

Volatile products are formed when the radical F^* react with the substrate, e.g. as in formula 1.11 and then pumped away through an exhaust line.

$$Si + 4F^* \longrightarrow SiF_4 \uparrow \tag{1.11}$$

Reactive Ion Etching

The pressure range in the vacuum chamber varies between 10^{-3}–10^{-1} Torr in reactive ion etching (RIE) to yield different reactions for the etching process. The high RF power generated plasma produces reactive species that goes from a physical sputtering process at pressures lower than 100 mTorr through to a physical-chemical process at a pressure of around 100 mTorr and a chemical etching process at pressures higher than 100 mTorr. When etching by physical sputtering at pressures lower than 100 mTorr, a transfer of momentum takes place between Ar^+ and the surface as it gets bombarded, giving rise to an anisotropic etching. Chemical etching is isotropic and performed by the reactive species produced in the plasma [101].

Due to the change of the etching regimes by the plasma pressure conditions, RIE can be used to dynamically control the etch profile. High pressures, larger than 100 mTorr, give rise to isotropic etching, as the reactive etching species reach all substrate features uniformly, and give high etching rates and selectivity. Low pressures of ∼0.1–1 mTorr result in anisotropic etching, as the collision rate of the ions hitting horizontal substrate features are larger than those hitting vertical features, and result in less selectivity and low etching rates.

Electron Cyclotron Resonance Microwave Plasma Etching

Electron Cyclotron Resonance (ECR) etching is achieved by making the electrons, in an already RF power generated plasma, move in a circular motion by applying a microwave frequency power and a static magnetic field. The electron motion is at the ECR frequency and made to resonate by the magnetic field and microwave frequency power, which gen-

erates a high-density plasma at low pressures. By controlling the gas pressure and the microwave power, the density of the plasma gets fine tuned. The advantage of ECR compared to RIE is that anisotropy and selectivity is higher as well as etch rate, while the RF powers and pressures are small.

Deep Reactive Ion Etching

In order to achieve high-aspect ratio (semiconductor) micro (nano) structures, Deep Reactive Ion Etching (DRIE), which is a highly anisotropic etch process, with a high etch rate, is used. An inductively coupled coil generator, with the power at 13.56 MHz, produces a plasma and an axial RF magnetic field together with an electrostatic field. Coupling the electrons in the plasma with the RF magnetic field creates a low power and low pressure, high-density plasma [101]. The etch rate has been improved by further developments of the technique, which is also applied in order to reduce thermal stress, that can have adverse effects when etching and achieve an anisotropic etch profile by protecting the sidewalls during the process.

DRIE consists of a passivation and an etching step with sulphur hexafluoride (SF_6) [102].

$$SF_6 + e^- \longrightarrow S_xF_y^+ + S_xF_y^* + F^* + 2e^- \tag{1.12}$$

In the first step the radical formation in formula 1.13 takes place. In the second step, a polymer layer is deposited on the substrate in order to passivate it, e.g. by ionizing C_4F_8 to form a polymer (C_xF_y) as following,

$$Si + F^* \longrightarrow SiF_x \text{ (volatile gas)} \tag{1.13}$$

$$C_4F_8 + e^- \longrightarrow CF_x^+ + CF_x^* + F^* + 2e^- \tag{1.14}$$

$$CF_x^* \longrightarrow nCF_2 \text{ (fluorocarbon polymer)} \tag{1.15}$$

In the third step the first step is repeated, but because the SF_6 sputtering removes the polymer on horizontal surfaces while leaving it on the sidewalls (before subsequent etch), an anisotropic etch profile takes form as this two-step cycle is repeated. This process can be run until the desired depth is reached, forming very long vertical sidewalls and high-aspect ratio features.

1.4.4 Thin Film Deposition

In fabrication, many different methods and techniques exist to deposit thin films of different materials onto substrates. Common methods, such as thermal evaporation, pulsed laser ablation(/deposition), sputtering, chemical vapour deposition and Langmuir-Blodgett film deposition are all frequently used in the preparation of thin material films for different purposes. Sputtering has been used to deposit films (metal and semiconductor) in the fabrication work and will be looked into further.

Sputtering

Sputtering is an important thin film deposition technique as it is fairly simple, as well as versatile and flexible. A wide range of materials can be used, such as metals, insulators, alloys and semiconductors, in order to deposit multilayers making up thin films. In contrast to thermal evaporation, the deposited material is not heated nor is the substrate (but could be), but the deposited material layers adhere stronger to the substrate than with thermal

evaporation. Different techniques/derivatives exist even within the sputtering family, such as reactive sputtering, RF sputtering, diode sputtering and direct current (DC) sputtering. The focus here will be RF sputtering, as in the cluster source condensation chamber.

Electromagnetic power with high frequency (13.56 MHz) is generated across a cathode and anode which are set up to allow for non-thermal physical deposition. The target, the material to be used, is mounted onto a magnetron, which acts as the cathode of the electrical circuit, and the substrate to be coated, is placed onto a grounded plate and acts as the anode. Argon gas is introduced into the low pressure ($\sim 1\times10^{-6}$ mbar) chamber and ionised by the applied RF field, igniting the plasma, making the positively charged argon ions accelerate towards the negatively charged cathode and physically sputtering the target material out into vacuum. With a free line of sight (longer mean free path than the cathode-anode separation), the expelled target material atoms/clusters deposit onto the substrate surface to make up islands that connect together to build up monolayers on top of each other, otherwise the atoms/clusters collide with the plasma species or gas molecules if the pressure is too high, preventing them from reaching very far. The film adhesion is therefore improved as the higher energy atoms/clusters reach the substrate surface as the sputter gas pressure is lowered.

The formula for the amount of sputtered material Q from the target is given by,

$$Q = \frac{kVi}{Pd} \tag{1.16}$$

where P is the gas pressure, d is the separation distance between the cathode and anode, k is a constant of proportionality, V is the working voltage and i is the discharge current [103]. By changing the target-sample separation, the voltage or pressure, the amount of sputtered material can be controlled. The mean free path (λ) of the sputtered target particles depend on the gas pressure and their maximum escape energy from the target is set by the voltage applied.

1.5 Microscopy

1.5.1 Scanning Electron Microscopy

When a beam of electrons collide with surface atoms (matter) different types of photons and electrons are emitted from them. Inelastic scattering between impinging accelerated primary electrons and electrons in atoms of first few surface layers (~1-10 nm) of matter gives off low energy (~2-50 eV) secondary electrons (SE). In Scanning Electron Microscopy (SEM), a detector is typically placed 45° relative to the sample surface normal, in order to collect SEs. Primary electrons can also interact with atomic nuclei and scatter elastically, thus producing highly energetic backscattered electrons (BSE). In order to detect BSEs, which have a high scattering angle, the last part of the beam column is fitted with a through lens detector (TLD) above the last aperture. In SEM, emitted BSEs and SEs from the surface atoms are used to obtain information related to atomic weight as well as information linked to high resolution surface topography, respectively, when imaging. After a cycle of raster scanning, the detected scattered electrons for each probe position during scan is converted to the intensity of corresponding pixels on a screen making up a full frame greyscale image [104, 105].

For the SEM to work it has to be housed in a vacuum system and consist of an electron gun, detector(s), apertures (blocking, collimating), electron optics (deflection coils, objective lens, condenser lens) and a sample stage (Figure 1.8). The electron beam can either be aligned to the optical axis or offset to it by a beam blanking aperture, hence be turned on and off. The electron beam can also be translated to any position on the sample surface or raster scan across it with the help of deflection coils. The electromagnetic lenses in the system are generally divided into two different ones, namely the condenser lens and the objective lens. The condenser lens is collimating the electron beam and the objective lens is focusing the beam on the substrate surface, potentially having a final spot size of a

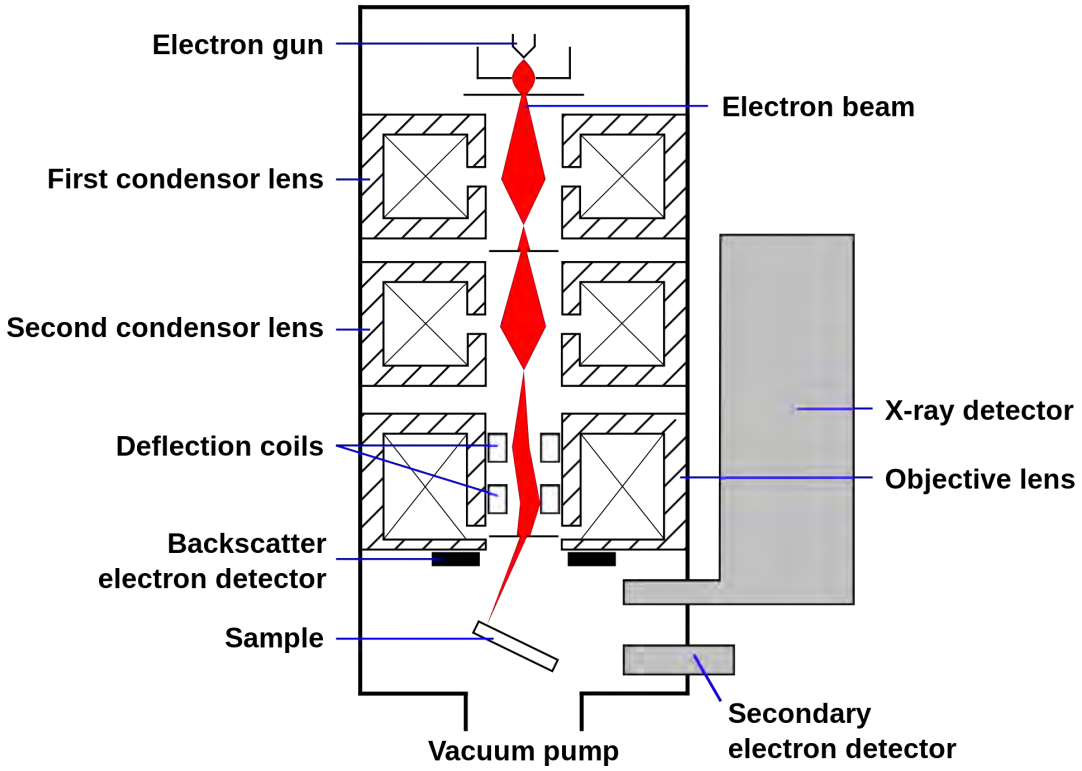

Figure 1.8: This schematic show the inner workings of a Scanning Electron Microscope. From top to bottom we have the electron gun, electron lens optics and detectors. Generated and emitted electrons from the electron gun make up a beam that is collimated and focused by the electron optics system. Secondary electrons and backscattered ones are found by respective detectors and results are displayed on screen. (Adapted from Wikimedia Commons)

couple of nanometers. A common problem that relates to aberration astigmatism, where a beam has different focal points in different perpendicular planes, can be minimised by using a stigmator lens in the system.

SEM is a non-invasive (non-intrusive, non-obtrusive, non-interfering) probing technique, i.e. it doesn't cause any damage to the sample, allowing for high resolution images to be obtained as well as quantitative and qualitative information, which is a clear advantage. The cost of this advantage is the clear disadvantage of the limitation of the types of samples that can be used. Charge is accumulated on the surface of samples of insulating materials, causing distortions to the images detected due to unpredictable deflections of incident and reflected/emitted electrons.

1.5.2 Scanning Tunnelling Microscopy

Scanning tunnelling microscopy (STM) was invented 1981 by Gerd Binnig and Heinrich Rohrer [106]. They won the Nobel Prize in 1986 for this invention. STM is a powerful technique that allows for locally probed and atomically resolved topographical images of surfaces. The STM can also probe the density of states of a material.

The STM takes advantage of two technologies, the first being the quantum mechanical tunnelling effect, which is the fundamental principle the STM is based on, and the second technology is the use of piezoelectric crystals. According to classical mechanics, an object such as a ball can not penetrate a wall, rather it will bounce back. However, according to quantum mechanics, balls (electrons) having lower energy than the wall (barrier) height can penetrate through (tunnel) depending on the width of the wall.

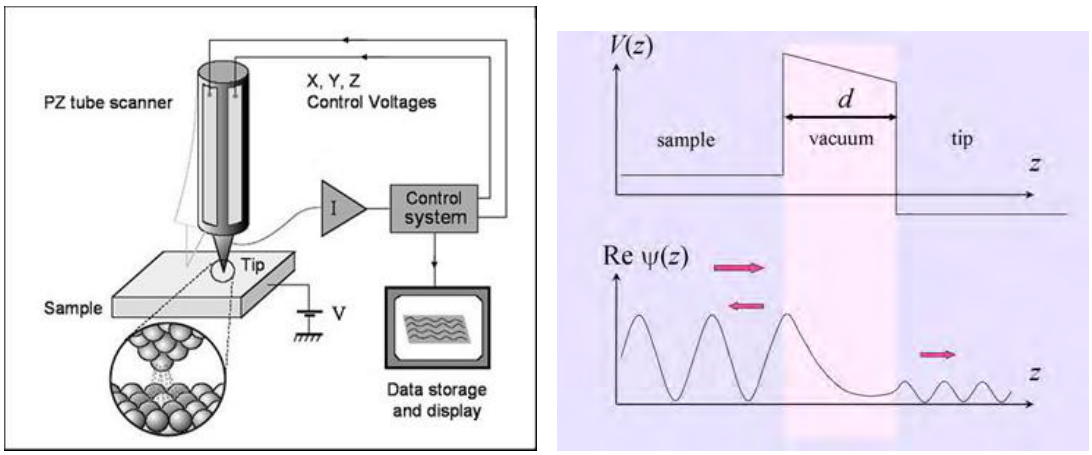

Figure 1.9: (Left) Schematic of the STM showing the piezoelectric tube for translating the tip in the x, y and z-coodinates, the sample bias setting (V), the tunnelling current measurement (I), the feedback control system as well as the display and data storage system. (Right) Diagram of the potential energy of an electron incident from the sample. The electrons are free to move in either electrode and the wave function is an oscillatory function. In the barrier region, the wave function is exponentially decaying and explains the similar dependence of the tunnelling current on barrier width d. (Adapted from [107]).

Tunnelling is achieved by having two metals very close to each other and applying a bias between them (Figure 1.9). In STM, one of the metal sides is the tip (scanning probe) and the other is the sample. The spacing between the tip and the sample affects the tunnelling

current exponentially (gap-current sensitivity: ~0.01 Å). By rastering the tip over a 2D surface and measuring the tunnelling current, a very accurate (spatial resolution: ~1 Å), atomically resolved, 3D surface image can be obtained.

Precise lateral translation of the tip is required, as is true for the vertical translation, in order to get adequate resolution. That is why piezoelectric crystals are used. They work in such a way, that by deforming the crystal an electric potential is generated. The opposite is also true, i.e. by applying a voltage, the crystal would deform (increase/decrease in size).

For current tunnelling, let us look at the one-dimensional case of two metal solids separated by an insulator or vacuum (rectangular) barrier, as is done by Bonnell [108]. For a small separation distance of the metals (z) and an applied bias, a few electrons, having the following wave function

$$\psi(z) = \psi(0)e^{-\kappa z} \tag{1.17}$$

where

$$\kappa = \frac{\sqrt{2m(V-E)}}{\hbar} \tag{1.18}$$

will tunnel. These are the solutions of Schrödinger's equation inside the barrier, m being the electron mass, $\hbar$ Planck's constant, E (eV) the electron energy and V the potential in the barrier [108, 109]. The tunnelling current I is proportional to the probability that an electron will cross the barrier, which is obtained by squaring the absolute value of the electron wave function (probability $P=|\psi|^2=\psi\psi^*=\psi^*\psi$ under Born interpretation, where ψ^* is the complex conjugate of the electron wave function), i.e.

$$I \propto e^{-2\kappa z}. \tag{1.19}$$

The picture is similar for the STM, where one of the metal sides is the tip, the other the sample and the gap between them the vacuum.

1.5.3 Atomic Force Microscopy

Atomic force microscopy (AFM) is another surface probe microscopy (SPM) technique that was invented in 1986, a couple of years after the STM, by Binnig *et al.* [110]. The STM is bound to only measure conductive samples, thus the AFM is more versatile. The similarities between the AFM and STM is that both use piezoelectric crystals for translation of the sample or probe (tip), which is the differing part for both techniques. Instead of measuring the tunnelling current like the STM, the probe of the AFM measures the forces between a tip (at the end of a cantilever) and the surface investigated.

At close proximity, an attractive force exists between tip and sample, but turns repulsive when the gap is further reduced. This change in magnitude of the force due to the tip-sample distance is used to map the topography of the sample surface. The force at play is mainly the van der Waals force, however other forces may also exist, such as the electrostatic force, capillary force etc. [111]. The tip is at the end of a cantilever, which deflects due to the change of the force. The deflections are registered by a laser reflecting off the upside of the cantilever (tip on the downside) and registered by a beam detector, which are then converted into electrical signals, see Figure 1.10. During rastering, the tip can either be in constant contact with the surface (contact mode) or oscillate and not be in constant contact with the surface (non-contact mode) or oscillate and constantly tapping the surface (tapping mode).

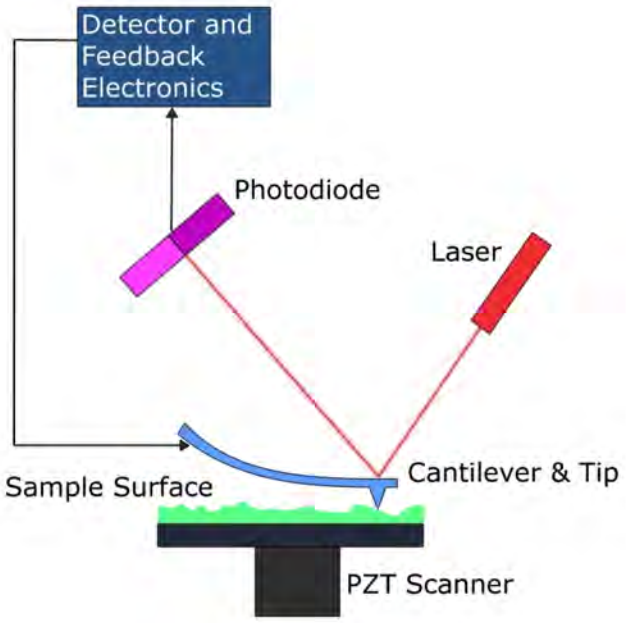

Figure 1.10: Diagram of atomic force microscope, where a laser beam is reflected on the backside of a cantilever and detected by a photodiode, which converts the deflections into electric signals, while the tip or sample is scanned through the surface. The lateral coordinates are linked to the force data in order to produce a topographic image of the sample surface. (Adapted from Wikimedia Commons)

1.5.4 High Angle Annular Dark Field Scanning Transmission Electron Microscopy

A High Angle Annular Dark Field Scanning Transmission Electron Microscope (HAADF-STEM) has been used to achieve the highest resolution images of some of the clusters used in this work.

The first Transmission Electron Microscope, built by Knoll and Ruska, was demonstrated in 1931. The electron microscope broke the resolution barrier of conventional optical microscopes for the first time and for this ground breaking invention, Ruska received the Nobel Prize 54 years later together with the inventors of the scanning tunnelling microscope (STM), Binnig and Rohrer in 1986. In the last 26 years, electron microscopes (TEM/STEM) have improved a lot, with continuous development and advances, and most

recently, aberration corrected microscopes have surfaced, making it much easier to study small particles such as atomic clusters [112, 113].

As electrons have a negative charge, they can be manipulated by both electric and magnetic fields to, e.g., form a beam, which is the basis of electron microscopy. 80-500 keV [114] electron beams are accelerated, deflected and focused by lens optics to transmit through samples in order to image and characterise them by decoding the necessary information from the detected scattered electrons. Different detection techniques can be used to obtain these vital data, one such technique is the HAADF. Electrons can either scatter elastically or inelastically or not scatter at all when transmitting through samples. Knowing what type of scattering different detected electrons have experienced is relevant in order to deduce correct information about the sample interacted with.

Electron inelastic and elastic scattering interactions are when the electrons collide and change their travel directions with and without losing energy, respectively. Another way of categorising the scattering is by referring to it as incoherent and coherent electron scattering. The coherency (or lack thereof) here, is relative to the phase of the incident beam of electrons. For low (scattering) angles, the electrons are in step phase with the incident beam and for high angles, the electrons are out of phase when it comes to elastic electron scattering [115]. This is particularly important for HAADF. These interactions are key in the production of relevant diffraction patterns and images, which are generated subsequently to detection of the electrons.

Abbe's theory describes image formation in a TEM, simplifying it into a single lens microscope and keeping only the objective lens as it mainly determines the resolution (see Figure 1.11). As according to the Figure, a parallel (or nearly parallel) electron beam illuminates the surface of a specimen (thin foil). The crystal lattices of the specimen diffract the electron beam that forms beams moving in several directions. Quantum mechanical diffraction theory, beyond the scope of this work, determines amplitude and phase

changes in the electron wave due to the electron-crystal interaction. To form an image, the objective lens collects the scattered electrons and at the focal point a Fourier transform is produced of the sample. In bright field (BF) imaging, the objective aperture is kept narrow to only allow an area of the projected Fourier spectrum with beams that are narrowly deviated and unscattered through. In dark field (DF) imaging, the narrow central area is instead excluded and only electrons that are highly deviated are considered.

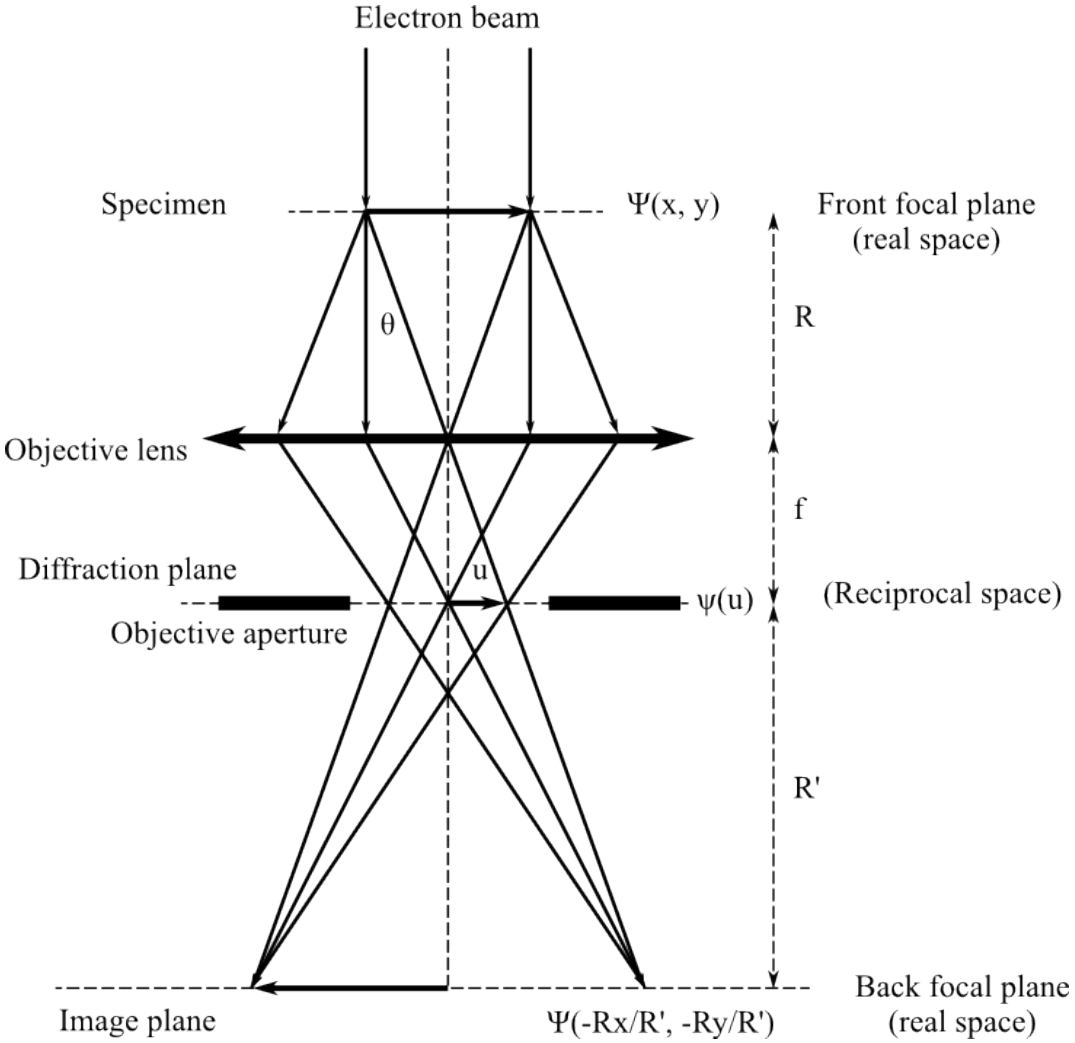

Figure 1.11: Image formation in a one-lens transmission electron microscope is given by Abbe's theory which is for a general optical system in TEM (Adapted from [116].)

At the exit face of the crystal, for high-energy electrons and a thin specimen, the transmitted wave function Ψ(x, y) can be assumed to be made up of a forward scattered wave. In

TEM, the main source of non-linear information transfer is by non-near-axis propagation through the objective lens. In the back focal plane diffracted beams are focused and an ideal thin lens focuses the waves that are transmitted parallel on the axis in the plane. A diffraction pattern is formed by waves leaving the specimen at angle θ with the optic axis (or in the same direction) and joining on the back focal plane at a point. Due to spherical and chromatic aberrations of the lens, these electrons experience a phase shift, which is a function of the scattering angle. The diffraction amplitude is thus modified by

$$\psi'(\mathbf{u}) = \psi(\mathbf{u})A(\mathbf{u}) \tag{1.20}$$

at the back focal plane. $\psi(\mathbf{u})$ is the Fourier transform of $\Psi(\mathbf{r})$ at the exit face of the crystal specimen, $\mathbf{u}$ the reciprocal space vector (related to the scattering angle by $u = 2\sin\theta/\lambda$, where λ is the electron wavelength) and A($\mathbf{u}$) is the lens phase function. The phase modulation introduced by the aberration of the objective lens affects the interference pattern, which is the result of the beams scattered to different angles. This electron image is given by

$$I(\mathbf{r}) = |\psi(\mathbf{r}) \otimes \Im\left[A(\mathbf{u})\right]|^2 \tag{1.21}$$

where $\Im$ indicates taking the inverse Fourier transform and $\otimes$ indicates a convolution calculation. This is to say that the transfer properties of the lens system and the scattering of the electrons with the sample leads to image contrast in TEM micrographs. According to Williams and Carter [115], an analytical expression for the image intensity to the first order is

$$I(\mathbf{r}) \approx 1 + 2\sigma V_p(\mathbf{r}) \otimes \Im\left[\mathrm{Im}\left[A(\mathbf{u})\right]\right] \tag{1.22}$$

when weak scattering is assumed and only thin samples considered, i.e. when weak-phase object approximation (WPOA) is considered. σ is the interaction constant and $V_p(\mathbf{r})$ is the projected potential of the crystal. $\mathrm{Im}\,[A(\mathbf{u})]$ is the transfer function and is denoted with $T(\mathbf{u})$, see references [115, 116] for more details. In the TEM micrograph, the contrast level is described by the transfer function if the sample is a weak-phase object. Bright atoms are visible against a dark background for positive $T(\mathbf{u})$, while they appear dark on a bright background for negative values. No detail are visible when $T(\mathbf{u}) = 0$, for that value of $\mathbf{u}$, in the image.

For TEM, image formation, in short, is done by mathematical operations (Fourier transforms) to the electron wave that is forward scattered as it exits the sample and multiplying the contributions of the lens (its transfer function) and additional mathematical operations (inverse Fourier transforms) to the amplitude (in the back focal plane). Modifications to the lens system makes the image more elaborate. Scattered waves off samples achieve contrast due to their coherent interference. Images of great structural detail can be achieved from small particles, such as atomic clusters, by the TEM. However, as only intensities and not information of phase can be recorded of the exit wave, quantitative interpretation is difficult to achieve from TEM images. By using, e.g., a scanning TEM (STEM), this could be achieved by selecting different types of scattered electrons from a sample.

The difference between TEM and STEM is that for STEM, for each probe position the electron flux scattered for any direction is detected in order to form an image. No refocusing is necessary of scattered electrons from a sample to form an image with STEM. As a matter of fact, the ray diagram of STEM is the reciprocal of the ray diagram of TEM as according to the principle of reciprocity, which states that the amplitude of a wave in point O due to a source at point S is exactly the same as the amplitude of a wave in point S due to a source at point O [116].

In STEM mode, an objective lens and a set of condenser lenses focus the beam to a sharp point. The angle of illumination from the incoming electron beam (incident probe) is limited by an objective aperture, before it reaches the sample and interacts with it, and a set of scanning coils is employed to raster it across the surface. Scattered electrons are collected by detectors after they travel through the sample.

A wave function $\Psi(\mathbf{K})$ can describe the amplitude distribution of the electron beam as it exits the sample. $\mathbf{K}$ is a 2D vector in reciprocal space, where $|\mathbf{K}| = 2\sin(\theta/2)/\lambda$ (λ is the wavelength and θ is the scattering angle of incident electrons). Information about the electron beam-sample interactions is carried as variations of $\psi\mathbf{K}$ when the sample surface is scanned across by the electron probe. Thus, structural information of samples can be extracted from samples if the exit wave function $\psi\mathbf{K}$ can be determined, but to that directly is not possible. Instead, by experimentally collecting scattered or directly transmitted electrons, images of the sample can be formed. Equation Equation (1.23) shows the relationship between $\Psi(\mathbf{K})$ and the image intensity ($I(\mathbf{X})$) as a function of the beam position ($\mathbf{X}$) observed. $\Psi(\mathbf{K}, \mathbf{X})$ is the amplitude function and $D(\mathbf{K})$ is the detector transmission function.

$$I(\mathbf{X}) = \int D(\mathbf{K}) \, |\Psi(\mathbf{K}, \mathbf{X})|^2 \, d\mathbf{K} \tag{1.23}$$

Different detectors are employed in STEM for different type of characterisation of samples being probed. Typical detectors are electron energy loss spectrometer (EELS), bright field (BF) detector, annular dark field (ADF) detector, energy-dispersive X-ray (EDX) detector and high angle annular dark field (HAADF) detector. Many of the cluster-deposited samples referred to within this thesis were imaged with the HAADF detector, which also goes by the name *Z*-contrast imaging. With this detector, it is possible to detect single electrons that travel through the sample and scatter within a span of high angles. This high angle scattering is usually due to electrons colliding with the nucleus of atoms in

the sample being probed (Rutherford scattering of electrons). Actually, the scattering depends on the atomic number (Z) of the scattering atoms in the sample, hence the name Z-contrast imaging, and the intensity of the images shifts with $\sim Z^2$ of the probed sample [117]. Unfortunately, this scattering, which is incoherent for the most cases, does not carry any phase information.

The Rutherford cross-section can be used to approximate the angular distribution of scattering at an angle θ from an atom with atomic number Z

$$\frac{d\sigma(\theta)}{d\Omega} = \frac{e^4 Z^2}{16(E_0)^2 \sin^4 \frac{\theta}{2}} \tag{1.24}$$

where Ω is the solid angle of collection, E_0 the beam energy and σ the scattering cross section of a single atom. For a cluster, the total intensity integrated over the area it occupies can be compared to the total intensity of scattered electrons from the atoms in the cluster. The total intensity I from a cluster is dependent only on the number of atoms N that it consists of and the energy of the electron beam used to probe it, for incoherent scattered electrons at high angles. Hence, for incoherently scattered electrons, one can obtain the size of a cluster by the integrated intensity of its image. However, due to different effects, such as electron channeling and multiple scattering when electrons interact with materials, not all electrons scatter incoherently [118].

1.6 Catalysis

There are different types of catalysis, for example heterogenous, homogenous, enzymatic (biological), electro-, photo- [119] and autocatalysis. Catalysis is, however, mainly branched into either homogeneous or heterogenous catalysis. Organometallic catalysts are used widely in homogeneous catalysis (catalyst and reactants in the same phase). These catalysts are usually dissolved in a solvent with the substrates. Heterogenous cata-

lysts are commonly solids on supports in a gaseous or liquid reaction mixture [120].

Most large-scale industrial and relevant catalytic processes belong to the branch of heterogeneous catalysis. For heterogeneous catalysis, the focus of catalytic reactions is at the surface of the catalyst material and by studying the nature of the highest atomic layers, exposed to the reactants, one can achieve a better understanding of these processes. The efficiency of the reaction is dependent on the surface area of the catalyst, which is maintained by the use of a support/substrate (particle catalysts), its detailed composition and structure [121, 122].

Catalysts increase the rate of chemical reactions, without themselves being consumed, by stabilising intermediate states having lower activation energies and thus create alternative reaction pathways to form products. Catalytic reactions are not different compared to typical chemical reactions when it comes to kinetics. For the rate determining step, the contact frequency of the reactants decides the reaction rate. The amount of catalyst in this, usually, slow step limits the rate. The diffusion of reactants and products to and from the surface respectively can be rate determining in heterogeneous catalysis as well. For homogeneous catalysis, substrate binding and product dissociation are analogous.

Different reactants' adsorption strength, as well as product desorption, does also affect the kinetics of catalytic reactions and can sometimes be the rate limiting steps. Two mechanisms than can occur are the Eley-Rideal kinetic model, where one reactant is adsorbed onto the catalyst and the other reacts with it from the gas phase, and the Langmuir-Hinshelwood mechanism, where both reactants adsorb onto the catalyst and subsequently react to form the product, which then desorbs.

In a typical catalytic reaction scheme the catalyst C forms intermediate(s) XC with reactant(s) X, which yields final product(s) Z and regenerates the catalyst C.

$$X + C \rightarrow XC \tag{1.25}$$

$$Y + XC \rightarrow XYC \tag{1.26}$$

$$XYC \rightarrow CZ \tag{1.27}$$

$$CZ \rightarrow C + Z \tag{1.28}$$

Thus, only a small amount of the catalyst is necessary to increase the rate of the overall reaction.

$$X + Y \rightarrow Z \tag{1.29}$$

Practically however, secondary processes in catalytic reactions can destroy, inhibit or deactivate catalysts even if they are not consumed by the reactions. The ratio between forward and backward rates is not changed by the presence of a catalyst, i.e., catalysts do not affect the chemical equilibrium of a reaction. The measurement of catalytic activity and efficiency is done by the SI derived unit *katal* (mol/s) or Turn Over Number (TON) and the Turn Over Frequency (TOF) (number of reactant molecules converted by the average active site in unit time) [123].

Catalysts are very diverse, but it is possible to make some generalisations. Probably, the most used catalysts are proton acids (reactions with water, e.g. hydrolyses and its reverse). Some graphitic carbon, alumina and zeolites are found to be active as well (multifunctional solids). For redox reactions (hydrogenation and oxidation), transition metals are usually used as catalysts and for reactions involving hydrogen platinum metals are required. An induction period is usual for several catalytic reactions, because the catalysts used are actually precatalysts. They are easier to store and are easily converted

to catalysts in the reaction.

1.6.1 The Catalytic Reaction Process

CO oxidation is a model reaction (e.g. taking place in automobile catalytic converters), which is an adequate example to use in order to illustrate the molecular level processes in product formation, see Figure 1.12.

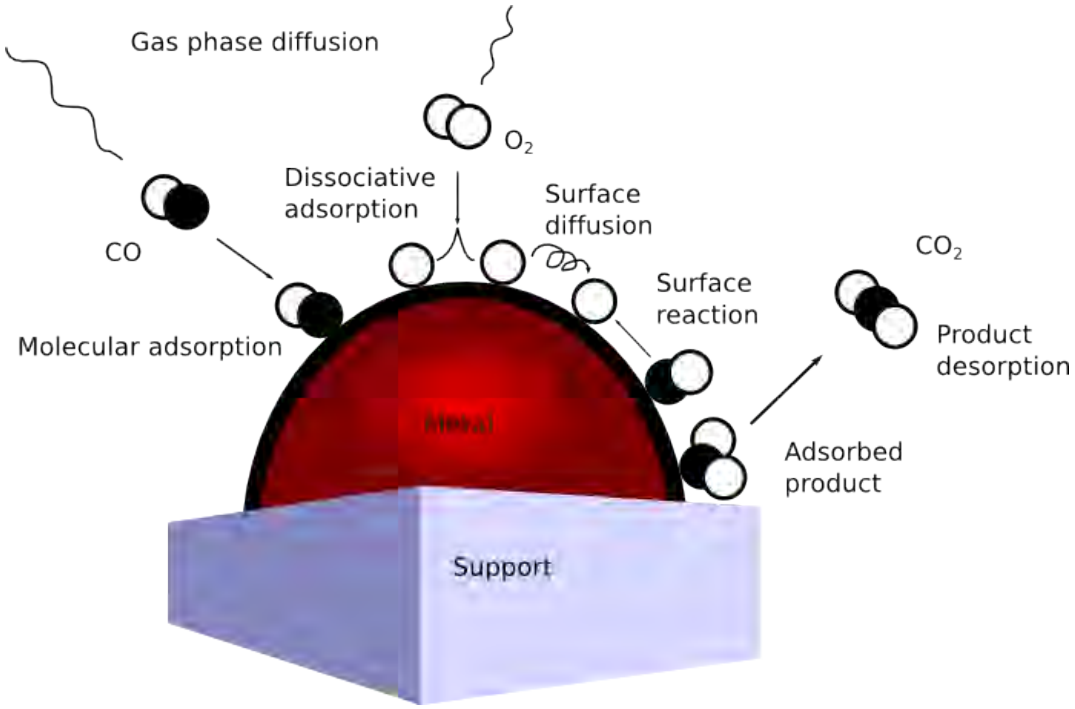

Figure 1.12: Processes at the surface layer during catalytic reaction at the molecular and atomic level. Gas phase diffusion of reactants followed by molecular adsorption or dissociative adsorption takes place initially. Reactants may then diffuse and react on the catalyst surface. Finally, the adsorbed product desorbs (Adapted from [124].)

The different steps in the process are following:

1. Diffusion of reactants (CO and O_2) through the gas (liquid) phase to the catalyst (metal) surface where they may bond (adsorb) and keep their molecular form.

2. The reactants can then diffuse on the surface or even dissociate into atoms (CO does

not dissociate because it has a much higher internal bond strength compared to O_2, 1076 kJ/mol and 500 kJ/mol respectively).

3. Most often the surface reaction step is the rate-limiting one in a catalytic reaction (O atoms react with CO to form adsorbed CO_2).

4. Desorption is the final step, where the bond to the surface is broken and the product (CO_2) enters the gas phase.

In chemical reactions, molecules rearrange their bonds when breaking and making, which requires more energy than in uncatalysed reactions. The catalytic reaction process is favoured by available catalyst bonding sites (so called active sites) which provides a lower energy route.

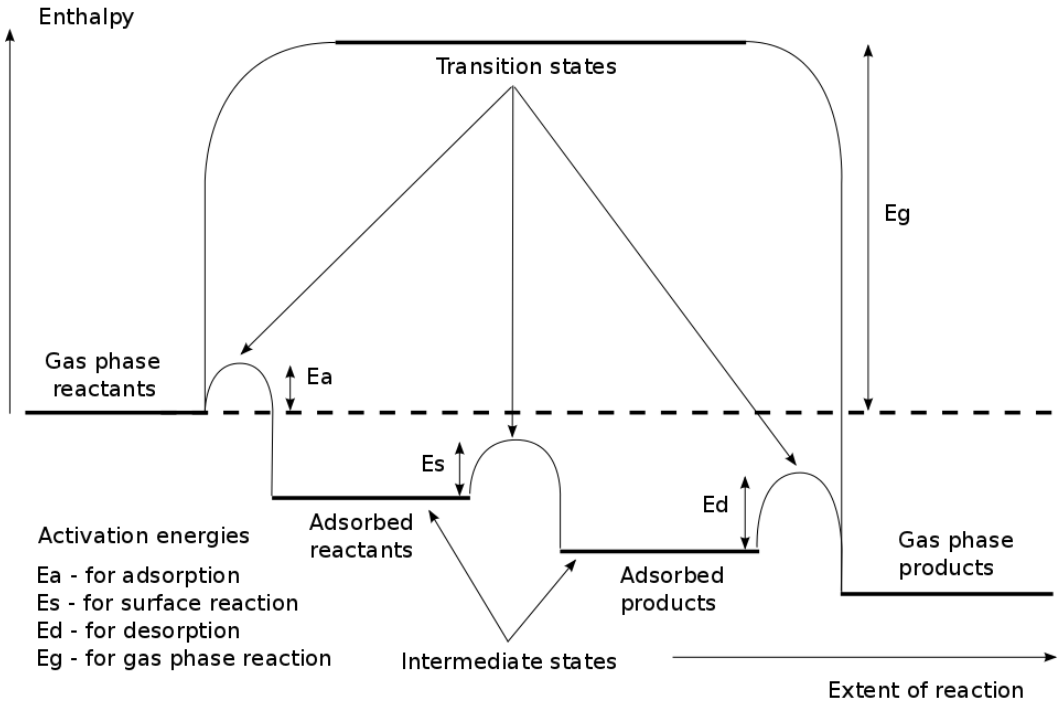

Figure 1.13: A catalytic reaction's simplified energetics. Catalysts provide alternative routes to lower activation energies and different transition states. Slowed and blocked reactions, because of too high kinetic barriers, can therefore be accelerated (Adapted from [124].)

For molecules in the gas phase, a lot of energy is necessary to break bonds before making new ones, resulting in a high reaction activation energy, ΔE_g. In the catalytic process,

the molecules are bonded to the catalyst surface, allowing the intermediates to stabilise, which would otherwise be unstable in the gas phase due to unsatisfied valences. Hence, the activation energies are lower, resulting in a faster reaction, see Figure 1.13.

By providing alternative routes to lower activation energies and different transition states, catalysts enable otherwise slowed or even blocked reactions (due to too high kinetic barriers) [14]. Equilibrium is reached faster but concentrations at equilibrium are not affected [124]. Not only do catalysts increase the reaction rate, they can even reduce the reaction temperature of high temperature reactions and increase selectivity.

The reactants have a distribution of energies with only a few of them with enough high energies to overcome the kinetic barrier and this is rate limiting. By lowering the activation energy more of the lower energy reactants are available to the reaction, thus increasing the rate. This is given by the Arrhenius equation Equation (1.30)

$$k = Ae^{\frac{-E_a}{RT}}, \tag{1.30}$$

where k is the rate constant, A the frequency factor, E_a the activation energy, R the gas constant and T the temperature. Thus, when decreasing the activation energy, E_a, the rate constant, k, increases.

Adsorption of molecules to the catalyst surface is the first step in the catalytic reaction process, as seen in Figure 1.12. Just like condensation on cold surfaces, physisorption is a weak adsorption ($\Delta H_a \sim 20\ kJ/mol$) due to equilibrium between attractive and repulsive forces as the molecule approaches the surface. When the molecule approaches the surface even closer, instead of experiencing attractive Van der Waals forces, it experiences repulsive forces between the outer electronic orbitals of the solid and molecule [124]. Chemisorption is a strong adsorption, involving breaking/weakening and making of reactant bonds to the catalyst surface ($\Delta H_a \sim 40 - 600\ kJ/mol$). Catalysis is possible

due to this process being thermodynamically "downhill" (at least for transition metals).

1.6.2 Support Effects

The main function of supports are to maintain the integrity of the metal phase of catalyst particles, where the reaction is taking place. Without the support, the metal would undergo sintering (fusion of the particles) very rapidly and would therefore lose activity. In sintering, the total surface energy of separated small catalyst particles is minimised by the formation of bigger and fewer particles through fusion. This results in lower surface area and higher average surface coordination, which causes the catalyst to lose its efficiency.

Many effects influence the activity of catalytic systems consisting of highly dispersed, small diameter, precious metal particles on supports (see Figure 1.14). For very small particles ($\leqslant$3 nm), splitting of the conduction band into discrete energy levels, makes them less metallic and could therefore change the surface reactivity and activation energies for all reaction steps involved. Additionally, charge transfer between the support material and catalyst particle, depending on the nature of both the support and catalyst as well as its size/structure, can exist.

Reduced support compounds can diffuse onto the catalyst, which strongly affects the catalytic performance. This happens when metal catalyst nanoparticles are supported on partially reducible oxides (e.g. TiO_2) and is called Strong Metal Support Interaction (SMSI) [124]. Edge atoms of small particles, in contact with both the support and the gas-solid interface, can also be very important as the fraction of the atoms involved can be significant.

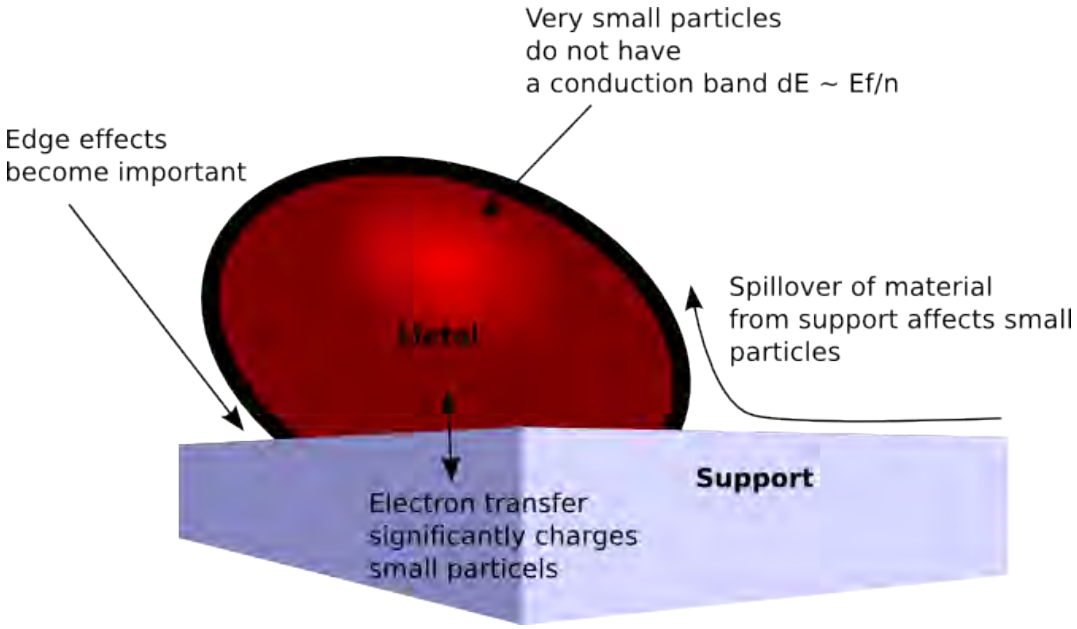

Figure 1.14: Illustrating the different factors affecting the properties of a small metal particle adsorbed on a support material. (Adapted from [124].)

1.6.3 Catalysis by Clusters

Studies in reactivity have focused mainly on transition metals (incompletely filled *d* orbitals) [123]. Interest in these studies arose in order to better understand fundamental processes occurring in heterogeneous catalysis and modelling them. For some reactions, activity depends only on total catalyst surface area, which favours smaller particles, having larger total surface area per mass of catalyst. However, for some other reactions the size and structure of the clusters does affect the catalytic activity. The nature of heterogeneous catalysis is better approximated by reactions of clusters with molecules in an inert carrier gas rather than the use of clean single-crystal metal surfaces under vacuum, which is far from real conditions. The reactivity of clusters depends, just like the reactivity of surfaces of bulk metals, on the arrangement and number of *d* electrons (i.e. on topography and material), and additionally, on the overall geometry and cluster size (number of atoms in the cluster).

Heterogeneous catalysts in modern industry are small metal particles supported on non-

metallic high-surface area substrates. Size-selected cluster catalysts are investigated in search for higher activity, higher selectivity [125], as well as increasing the catalyst lifespan. Several transition metals and complexes of them are used in catalysis. The increased total surface area per mass of metal catalyst yields a higher catalytic activity. Advantages of supported metal clusters are immobilised and stabilised clusters avoiding sintering/aggregation/coalescence as well as easy recovery of catalysts and separation from the reactant/product mixture. Generally, oxides are used as support material, e.g. alumina (Al_2O_3), silica (SiO_2) and titania (TiO_2), but even boron nitride (BN) and carbon is used. Even nanoporous materials are used, such as zeolites.

In recent years, cluster catalysis has been realised both experimentally and theoretically. Xu *et al.* studied redox catalysis of single colloidal Au nanoparticles by single-molecule detection of fluorogenic reactions [126]. Turner *et al.* found that small gold particles (~1.4 nm) from Au_{55} clusters are good catalysts [127]. They are robust and efficient catalysts for selective oxidation of styrene by O_2. Particles with ~2 nm diameter and above did not exhibit any catalytic activity in their experiments and they thought that the altered electronic structure, which is intrinsic for small sized gold nanoparticles, is the reason for their high catalytic activity. Novo *et al.* reported the first instance of direct measurement of catalytic property of only one nanoparticle, using surface plasmon spectroscopy [128]. The reaction studied was the oxidation of ascorbic acid, which was catalysed by gold nanocrystals (~50 nm). Joo *et al.* found that Pt@mSiO_2 nanoparticles maintain their structural configuration up to 750 °C and that they show high catalytic activity for both CO oxidation and ethylene hydrogenation [129]. Colloidal nanoparticle synthesis offers the precise control of the size, shape and composition of nanocatalysts, which, in turn, affects their catalytic activity and selectivity. The ligands that cover and stabilise the nanoparticles are, however, a limiting factor in high-temperature catalytic reactions (several industrially important catalytic processes >300 °C). By using core-shell nanoparticles, Pt metal cores (14 nm) covered by mesoporous silica shells (17 nm) sintering is

prevented, in high-temperature catalytic reactions and access to the catalytically active cores is possible through mesopores (2–3 nm) in the silica shells.

Certain sizes of aluminium cluster anions produce hydrogen gas from water (Al_{16}^-, Al_{17}^- and Al_{18}^-) [130]. Roach *et al.* found that the reactivity of aluminium anion clusters with water distinctively vary with size. Water introduced into a fast-flow reactor under multi-collisional conditions with aluminium cluster anions show products (adducts) of Al anion clusters with one or several adsorbed water molecules with varying intensity for certain cluster sizes. The reactivity is dependent on geometric shell structure and attributed to dissociative chemisorption at specific surface sites. These complementary active sites are made up of pairs of adjacent Al atoms. One of the Al atom acts like a Lewis acid and the second Al atom like a Lewis base. The adsorption of water onto the clusters requires the cleavage of an OH bond, which is done by the two above mentioned surface sites. These surface sites exist due to irregular charge distribution on the cluster surface.

Recently Harding *et al.* showed that the metal oxide support thickness and composition affects the activity of catalysts [131]. Au_{20} clusters on MgO surfaces (with different thicknesses) on Mo(100) were found to have different CO oxidation activity with varying MgO thickness as well as coverage of oxygen surface defects. Both Temperature Programmed Reaction (TPR) measurements and first-principles density functional theory calculations were utilised. CO molecules were found to either adsorb directly to the clusters or bind to the MgO surface close to the clusters. Some cases indicate activated, dissociate adsorption of O_2 at the MgO/cluster periphery interface. An increase in MgO film thickness (from ~1–10 ML) gives rise to a shift of the CO_2 formation peak from ~300 K (two regimes: minor peak at ~180 K and major peak at ~300 K) to ~250 K (one regime, single peak) in TPR spectra. A shift is also observed from ~400 K to ~250 K between defect-rich (two regimes: minor peak at ~200 K and major peak at ~400 K) and defect-poor MgO films (~10 ML).

Experimental and theoretical investigations of the catalytic properties of palladium clusters have also been conducted. Starchevsky *et al.* [132] used Pd_{561} clusters in solution to undergo lower alcohol oxidation around room temperature (293–323 K) yielding a wide range of products. The surrounding ligands were thought to have an essential role in the catalytic process. Density functional theory calculations performed by Huber *et al.* showed that the structure of Pd_{4-9} on MgO is transformed, when reacting with O_2, to crystalline nano-oxide clusters (Pd_xO_y), which are in epitaxy with the MgO. These complexes were found to catalyse CO oxidation better than palladium clusters [133]. Despite this, the most apparent factor determining the catalytic activity of metallic clusters is dependent on the number of reaction sites provided by the structure (determined by N) [134, 135], little experimental data exists linking reaction rates to the size N and shape of (palladium) clusters. Abbet *et al.* investigated the size-dependency of acetylene cyclotrimerisation to form benzene on small Pd_{1-30} clusters supported on MgO(100) [136]. Two main features, high temperature desorption (430 K) of benzene for Pd_{7-30} and low temperature (300 K) desorption for Pd_{1-30}, were observed from temperature programmed reaction experiments. The production of benzene is abruptly increased when going from Pd_7 to Pd_8 (1 benzene per octamer) which is associated with the 430 K benzene production peak. The production of benzene was found to increase with cluster size, reaching an average production of 4–5 benzene molecules for Pd_{30}. Gniewek *et al.* studied Pd catalysts (with different shapes and sizes ranging from 1.9 to 19.8 nm) prepared chemically by reduction methods [137]. They used x-ray diffraction (XRD) and TEM to characterise the cluster diameter and morphology and their catalytic activity was studied by the methoxycarbonylation of iodobenzene. Higher yields of the reaction products were obtained for smaller Pd nanoparticles.

1.6.4 Photoelectrocatalysis

Among the state-of-the-art systems working on achieving stable, cheap, abundant and comparably active catalysts to the precious metal catalysts (especially platinum) are hybrid molybdenum disulphide and reduced graphene oxide catalysts, as well as tandem systems utilising nanostructured semiconductors with co-catalysts such as nano-pillar Si with cubane-like Mo_3S_4 clusters and other similar work [138–142]. A small selection of such relevant work is presented here.

Li *et al.* report on a new hybrid catalyst for hydrogen generation [73]. The hybrid catalyst consists of MoS_2 nanoparticles synthesised on reduced graphene oxide (RGO) through a selective solovthermal method while the RGO sheets were suspended in solution. This resulted in stacked few-layer MoS_2 onto graphene with plenty of edge sites exposed resulting in much better activity in the hydrogen evolution reaction (HER) compared to other molybdenum disulfide catalysts. A small Tafel slope of ~41 mV/decade was obtained indicating that the Volmer-Heyrovsky mechanism steers the HER and that the rate-limiting step being electrochemical desorption of hydrogen.

At a temperature of 200 °C the $(NH_4)_2MoS_4$ precursor was reduced to MoS_2 on graphene oxide and the graphene oxide itself was reduced by hydrazine in a one-step solvothermal reaction in *N*, *N*-dimethylformamide (DMF) solvent. The MoS_2 nanoparticles are found to uniformly decorate the reduced graphene oxide support with the planes parallel mostly, but some particles with folded edges reveal the individual sheets. High-resolution transmission electron microscopy (HR-TEM), X-ray diffraction (XRD), Raman spectroscopy, micro-Raman imaging and X-ray photoelectron spectroscopy (XPS) were used to characterise all the novel attributes of the hybrid catalyst.

A three electrode setup was used to measure the activity of the hybrid catalyst on glassy carbon electrodes in H_2SO_4 solution (0.5 M). For reference purposes a commercial 20 wt% platinum on Vulcan carbon black catalyst was used, as well as coalesced 3D MoS_2 cata-

lysts produced in the same method as the hybrid catalysts, but without the graphene oxide and also reduced graphene oxide solely. The commercial Pt catalyst showed the highest activity with a Tafel slope of ~30 mV/decade with almost no overpotential, while RGO and free MoS_2 (~94 mV/decade) showed little HER activity and the hybrid MoS_2/RGO catalyst showed highest activity compared to other MoS_2 catalysts (even when comparing same high loading of 1 mg/cm^2) with a Tafel slope of ~41 mV/decade and an overpotential of ~0.1 V.

Hou *et al.* show how Mo_3S_4 clusters coupled with p-type silicon pillars makes excellent photocatalysts comparable to Pt [143]. The main motivation of the work was to realise part of a tandem photo-chemical solar cell using silicon pillars as the backbone incorporated into a membrane that permeates protons. The idea is that the silicon pillars are doped so that they act as high-gap photoanodes at one side of the membrane absorbing the blue part of the incident solar light in order to oxidise water into O_2 and protons. At the other side of the membrane are silicon pillars with Mo_3S_4, incomplete cubane-like co-catalyst clusters, adsorbed onto them acting like low-gap photocathodes and absorb the red and infrared band of the incident solar spectrum which reduces the protons moving through the membrane.

The reported work focuses on the solar hydrogen evolution part and the function of the p-silicon pillars as photocathodes excited by the red part of the solar spectrum with the Mo_3S_4 as co-catatlyst. Hydrogen-terminated pillar-structured p-Si(100) and planar p-Si(100) as well as one of each covered with Mo_3S_4 protected with hydrophobic ligands were compared. When dark, almost no current (~0 mA/cm) is observed for all the electrodes when submerged into $HClO_4$ (1.0 mol/l) under electrochemical reaction runs (cyclic voltammetry). When illuminated by a filtered Xe-arc lamp (approx. AM 1.5G and $\lambda \approx$ 620–1050 nm) photoactivity is observed for all samples. An enhancement in the onset of the photocurrent from -0.4 V (U_{RHE}), for bare planar silicon, to +0.15 V, for Mo_3S_4

clusters deposited planar Si is obtained which gives a 8 mA/cm^2 HER current density at U_{RHE} = 0 V (reversible potential). The highly ordered and regular pillar silicon samples with a diameter of 3 μm and a height of 50 μm achieves a limiting current density of 16 mA/cm^2 (12 mA/cm^2 for planar silicon) and a further enhancement of the photoactivity is achieved by deposition of Mo_3S_4 clusters onto pillar silicon giving a HER current density of 9 mA/cm^2 at 0 V.

Polymeric carbon nitride is reported to work as a photocatalyst by Wang *et al.* [119]. They show that the inexpensive and abundant material, in the presence of a sacrificial donor, can produce hydrogen from water under visible-light irradiation. The catalyst was prepared by heating cyanamide to 673–873 K for 4 h. The optical and electronic properties of the material could be finely tuned by the condensation temperature, so that increasing it would give a redshift of the absorption edge and thus a decrease of the semiconductors bandgap. Density-functional-theory calculations suggest that the nitrogen atoms, in the catalyst, act as the preferred oxidation sites for H_2O to form O_2 and the carbon atoms as reduction sites for H^+ to H_2. The chemically and thermally stable photocatalyst showed very fluctuant H_2 activity, but this was rectified by adding a small amount of Pt which increased the activity. Despite the modification, the estimated quantum efficiency is only 0.1 % when system is irradiated by light of wavelengths 420–460 nm.

The electrochemical evolution of H_2 from MoS_2 depend linearly with the nanocatalysts' edge site number, as shown by Jaramillo *et al.* [80]. MoS_2 samples consisting of flat polygons of S-Mo-S trilayers on Au(111) were prepared in Ultra High Vacuum (UHV) in a way that the ratio of terrace and edge sites varied systematically. This was done by annealing the samples at 400°C and 550°C after Physical Vapour Deposition (PVD) of Mo in a H_2S atmosphere. Scanning Tunnelling Microscopy (STM) revealed dispersed triangular nanoplates of MoS_2 with conducting edge states and dominant sulphided termination of the Mo-edges (active site for evolution of H_2) irrespective of annealing temperature, but

where the higher annealing temperature showed larger sizes of the catalysts. The activity of the Hydrogen Evolution Reaction (HER) was measured in an electrochemical cell and by comparing the exchange current density to the edge length of the different samples a linear correlation is evident. It is also evident that higher annealing temperature yields lower exchange current densities.

1.7 Summary

The background of the different areas relevant to the work in this thesis have been covered briefly in this chapter. The main focus is on clusters, which was covered first, followed by nanofabrication, which is relevant to Chapter 5. Next, the different microscopy methods were introduced before going through catalysis at the very end. The coming chapter will cover the experimental equipment and techniques used in this work.

CHAPTER

TWO

EXPERIMENTAL EQUIPMENT AND METHODS

The experimental techniques and methods used in this thesis are outlined in this chapter. A large part of the work was focused on modifications and improvements of the existing RF magnetron cluster ion beam source. This was done in order to reach the goal of a high enough throughput to allow the production of catalytically active samples on a larger scale as well as enabling in-flight coating of clusters to create bimetallic clusters (core-shell, alloy and/or partly coated).

The work based in the clean room involved preparation, fabrication and characterisation of samples of MoS_2, potentially to be used as photocatalysts in the production of hydrogen from water with solar energy. The techniques and methods of the photo-electro characterisation with the setup used, is also outlined, demonstrating the catalytic performance of the samples.

First, the cluster source is covered and secondly, the fabrication equipment. Finally, microscopy and photoelectrochemistry equipment used for characterisation of samples and the preparation of samples are presented.

Throughout this work the cluster ion beam source, built at the Nanoscale Physics Research Laboratory (NPRL) in the University of Birmingham, has been utilised. The magnetron source was developed by a previous PhD student, Simon Carroll [144] (June 1999), and commissioned by his successor, another previous PhD student, Sirapat Pratontep [145] (September 2002). Other students, e.g. Stefano Palomba [146] (March 2007), and post-docs have made changes to and optimised the system since then. The system employs the lateral time-of-flight mass selector (LTOF-MS) designed by von Issendorff and Palmer [147] in 1995 and installed in 1996.

A huge part of this work has also been performed in the well-equipped clean room in the same department (NPRL). Collaboration with the Centre for Individual Nanoparticle Functionality (CINF) at Technical University of Denmark (DTU) has allowed for some work to be done at their laboratories too.

2.1 RF Magnetron Gas Condensation Cluster Ion Beam Source

The cluster source is a true work horse, consisting of several turbo molecular pumps, rotary pumps and many vacuum chambers making it a noisy beast that can produce some of the smallest thinkable structures. Despite this, it also contains delicate parts which enables the formation of a fine beam of nano-sized clusters of atoms that can be used to structure surfaces at the nanoscale.

The advantages of the Birmingham RF magnetron cluster source include, the potential use of a diverse range of materials (even semiconductors and insulators), a large cluster-size range (from 2 to at least ~70 000 atoms) and the inherent ionisation of clusters. Furthermore, the source has a very high transmission, compared to other cluster source techniques, and is equipped with a novel LTOF-MS, which will be introduced later on.

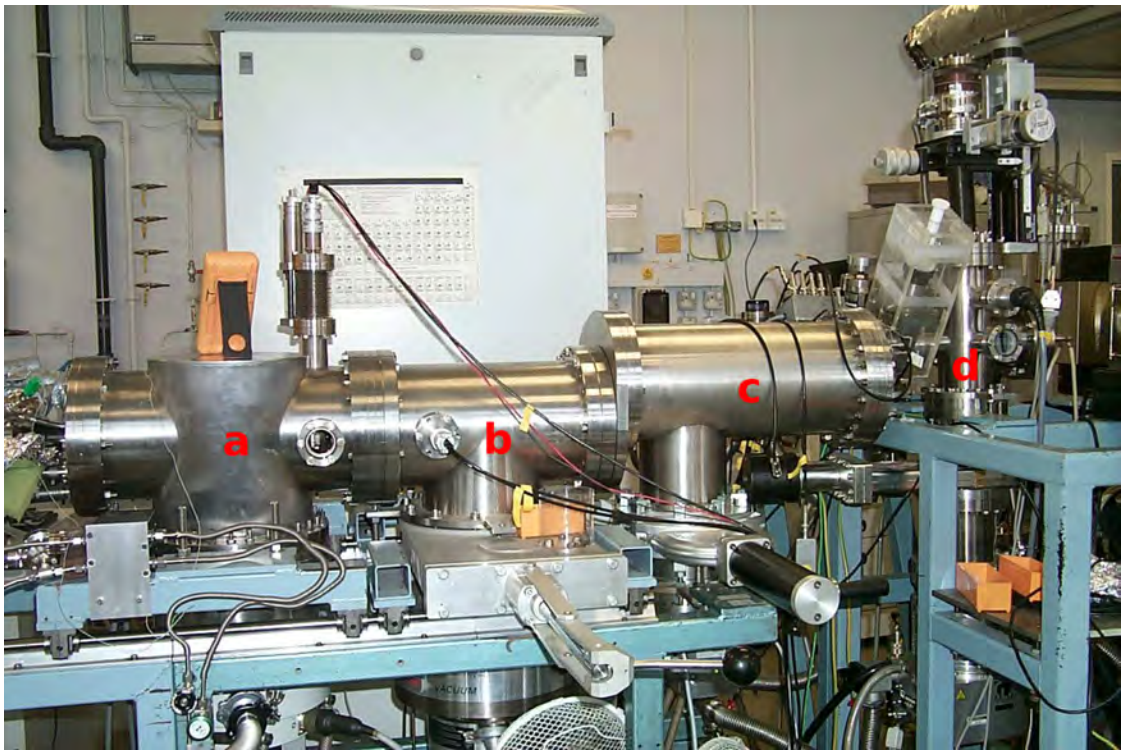

Figure 2.1: Photo showing the cluster source at the Nanoscale Physics Research Laboratory, University of Birmingham. The three main source chambers from left to right are (a) the generation chamber, (b) the ion optics chamber and (c) the lateral time of flight mass selection chamber, which are connected to (d) the deposition chamber.

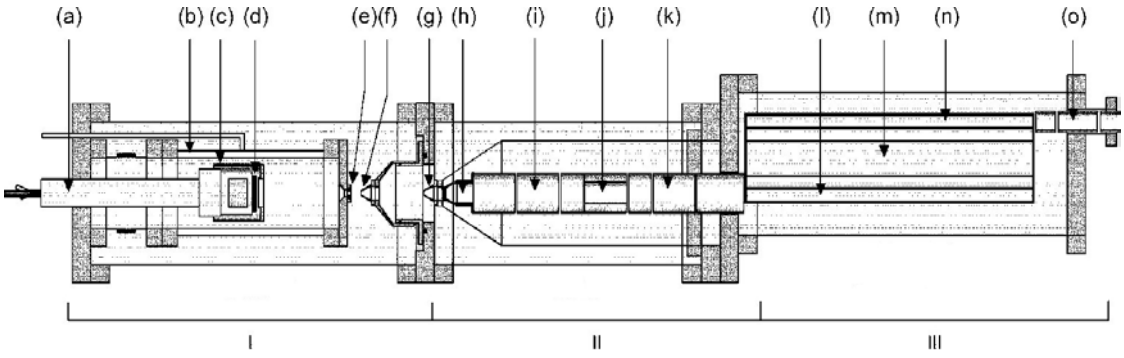

Figure 2.2: Schematics showing the cluster source at the Nanoscale Physics Research Laboratory, University of Birmingham. Schematic of the cluster source, (I) the generation chamber; (II) the ion optics chamber; (III) the lateral time of flight mass selection chamber, showing: (a) magnetron axial mount; (b) liquid nitrogen (lN2) chamber; (c) dark space shield; (d) sputter target; (e) adjustable nozzle; (f) first skimmer; (g) second skimmer; (h) extraction lens; (i) first einzel lens; (j) deflection plates; (k) second einzel lens; (l) LTOF acceleration region; (m) LTOF field-free region; (n) LTOF deceleration region; and (o) third einzel lens. (Adapted from [148].)

2.1.1 Cluster Production Chamber

Clusters are formed in the first chamber of the system, where the magnetron head is installed. The chamber contains a second "inner" chamber, which is double-walled and cooled with liquid nitrogen during operation and reaches a temperature of ~-180 °C. Argon and helium gas with typical pressures of ~0.4 mbar and ~1.0 mbar, respectively, fill the chamber and enable the production of clusters.

A target connected with an RF power ignites a plasma that gives rise to a negative self induced bias on its surface. Ar^+ ions accelerate from the plasma and hit the target giving rise to an expulsion of target atoms and small target clusters ($n \approx 1–10$). To increase the sputtering efficiency, magnets are used to create a magnetic field, which intensifies and confines the plasma. The presence of cold He gas induces nucleation and aggregation of larger clusters from the sputtered target atoms and small clusters by condensation (collision cooling). Decreasing the He pressure prevents growth by aggregation and thus fewer larger clusters are formed.

The produced clusters are ionised due to the presence of the plasma, through either exchange of charge when colliding with Ar^+ ions or energetic electrons in the plasma [144]. Hence, different electrostatic plates can be used to accelerate, deflect and focus the charged cluster particles. The gas flow in the double-walled inner chamber carries the clusters through a nozzle in an adiabatic supersonic expansion that suppresses continued growth of the clusters. The last part of the cluster generation chamber is the first skimmer, which extracts a molecular beam from the expanding mixture.

2.1.2 Ion Optics Chamber

Most ion optics reside in this chamber, which is the middle chamber of the cluster source. The ion optics manipulate the beam much like light is manipulated by optical instruments

like lenses and mirrors, hence the name. The cluster beam can be focused, deflected and accelerated. Small negative bias voltages (cluster beam is positive) are applied to the different lens elements, such as the nozzle (outside the ion optics chamber), first skimmer (outside the ion optics chamber) and second skimmer to give a few examples. The LTOF-MS (outside the ion optics chamber) also uses electrostatic plates for cluster size-selection and an einzel lens after the LTOF-MS is used to refocus the beam. Finally, a negative bias is applied to the sample (residing inside the deposition chamber) in order to control the deposition energy [148].

The ion optics consist of four parts, an extractor lens, a first einzel lens, X-Y deflection plates and a second einzel lens. The different lenses are mounted on teflon parts, which are supported on four rods. The whole piece is fastened on an oval flange, which connects the ion optics chamber with the LTOF-MS chamber.

2.1.3 Lateral Time of Flight Mass Selector Chamber

The unique piece in this cluster source is the LTOF-MS chamber. It uses a novel method of mass selection using a lateral acceleration-deceleration of the beam by short high-voltage pulses. This keeps a high throughput and mass resolution over the whole mass range.

The mass resolution of the mass selector has been improved since its installation. Initially the mass resolution was $m/\Delta m \approx 25$ and was maintained so for at least the first three years. Subsequent changes of the LTOF-MS exit aperture have changed the mass resolution during the years. The mass resolution in this work was $m/\Delta m \approx 19$, see section 3.1.1.

LTOF-MS Schematics

The LTOF-MS is, as mentioned, a lateral acceleration-deceleration mass selector consisting of several parts. The mass selector can be divided into three regions, namely the

acceleration region, the field-free drift region and the deceleration region. The cluster beam goes through the entrance aperture, at the left side (see Figure 2.3), and into the acceleration region and focuses ideally on a rear aperture, at the right side. At the bottom of the acceleration region a short high voltage pulse is applied to the plate, which causes the beam to drift laterally. A part of the beam drifts past the top of the acceleration region and passes by the first grid. It then continues to drift through the field-free drift region and passes through the second grid and into the deceleration region. For clusters with the same charge, the smaller clusters move faster than the larger clusters through the field-free region. A second high voltage pulse, of equal magnitude, is applied to the plate at the top of the deceleration region that halts the vertical motion of the cluster beam. The cluster size which is aligned to the exit aperture, from the vertically dispersed cluster sizes, will form the beam that passes through the exit aperture.

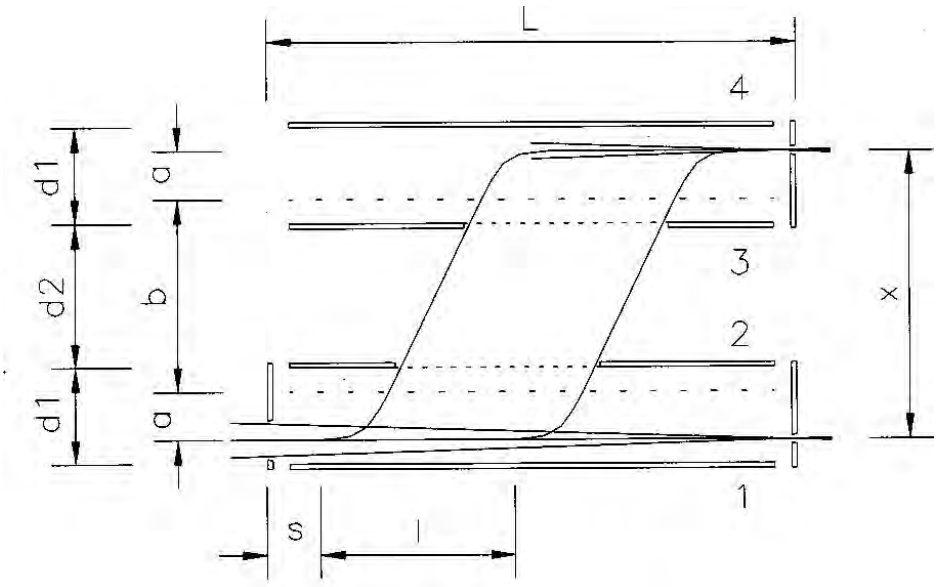

Figure 2.3: Schematic of the novel LTOF-MS incorporated in the RF magnetron sputtering cluster source. Short high voltage pulses are applied to plates one and four to laterally displace a focused cluster ion beam. l length of the cluster ion beam package displacement; x total displacement; a beam offset traversed during the high voltage pulse; b length of the field-free region; $d1/d2$ plate separations; s length of the portion of the ion beam which cannot be used due to field distortion; L total length (Adapted from [147].)

The mass resolution of the LTOF-MS is defined by the exit aperture. By following the

motion of the clusters, a theoretical derivation of the mass resolution can be achieved and which includes the exit aperture slit size. The clusters move from the acceleration region after the end of the short high voltage pulse. According to Carroll [144] the individual clusters experience a vertical acceleration a during the lifetime of the short high voltage pulse by

$$a = \frac{F}{m}, \tag{2.1}$$

where m is the cluster mass and F the force exerted by the electric field. This gives the clusters a vertical drift velocity

$$v = \frac{F\tau_p}{m}, \tag{2.2}$$

τ_p being the pulse time duration. Each cluster crosses the field-free drift region, having a length x, in the time

$$t_x = \frac{xm}{F\tau_p}. \tag{2.3}$$

The vertical separation Δx of two clusters having masses m and $m + \Delta m$ after the first cluster drifts distance x, after time t_x is

$$\Delta x = \frac{F\tau_p}{m} \times \frac{mx}{F\tau_p} - \frac{F\tau_p}{m + \Delta m} \times \frac{mx}{F\tau_p} = x\frac{\Delta m}{m + \Delta m} \tag{2.4}$$

which gives

$$\frac{x}{\Delta x} \approx \frac{m}{\Delta m}. \tag{2.5}$$

One can clearly see the advantage of the LTOF-MS from equation 2.5, which gives a constant mass resolution for the whole mass range if the exit aperture slit size is Δx. For most cases m is not much larger than Δm and equation 2.5 becomes

$$\frac{x}{\Delta x} = \frac{m}{\Delta m} + 1. \tag{2.6}$$

However, Issendorff and Palmer [147] has another derivation with same result as 2.5. The same momentum will be obtained by all ions for a certain length of a high voltage pulse. With the mass and lateral velocity of the ions transmitted by the selector being m_0 and V_{m_0}, respectively, the lateral velocity of an ion having mass m will be

$$V_m = V_{m_0}\frac{m_0}{m}. \tag{2.7}$$

Lateral displacement for said ion is thus

$$x_m = \frac{m_0}{m}x \tag{2.8}$$

where x is the total displacement of the ions transmitted by the selector, see Figure 2.3. In order to get the width of the mass range that is allowed through the exit aperture, Issendorff and Palmer then take the derivative of the displacement with respect to the mass

$$\left.\frac{dx_m}{dm}\right|_{m=m_0} = -\left.\frac{m_0}{m^2}x\right|_{m=m_0} = -\frac{x}{m_0} \tag{2.9}$$

and the range of masses is thus

$$\Delta m = \frac{dm}{dx_m}\Delta x = -\frac{m_0}{x}\Delta x \tag{2.10}$$

and Δx is the full-width-half-maximum of the convolution of the beam profile and exit aperture. The ratio of the lateral displacement and exit slit width thus gives the maximum mass resolution of the selector (compare with 2.5)

$$R = \frac{x}{\Delta x} = \frac{m}{\Delta m}. \tag{2.11}$$

In ordinary TOF-MS the contribution from the initial energy spread of the clusters affect the resolution and is one of the things the Wiley-Mclaren TOF setup tries to solve. However, our LTOF-MS solves this by deflecting the beam laterally. The divergence or convergence of the beam is preserved as the relative velocities of ions with same mass do not change during mass selection, they only gain and lose the same velocity during the lateral displacement process. Therefore, a well focused beam before displacement will remain well focused at the exit aperture after beam displacement, which is necessary for reasonable mass resolutions [147]. The theoretical resolution of the LTOF-MS was initially $m/\Delta m = 40$ [144]. The distance l being fixed and known ($l = 120$ mm) allows us to obtain the slit width employed experimentally $\Delta x = 3$ mm. The measured resolution was found to be $m/\Delta m \approx 25$, which was lower than the theoretical resolution and attributed to imperfect focusing of the beam at the exit aperture, see section 3.1 for further discussion.

2.1.4 Deposition Chamber

The deposition chamber is attached to the exit of the LTOF-MS chamber and supported by its own frame. A turbomolecular pump is connected to the bottom of the chamber and, together with the system's differential pumping, achieves a high vacuum (HV) environment with a base pressure of $\sim 10^{-8}$ mbar and an operating pressure of $\sim 10^{-6}$ mbar. A sample holder is connected at the top of the chamber and can be translated in all three spatial directions, two of them by computer controlled stepper motors. The sample holder

can hold up to twelve 10×5 mm samples. At the right side of the chamber, with respect to the beam propagation direction, a viewport allows crucial instant inspection. The back-side of the deposition chamber is where a tape drive or an evaporator can be mounted. On the left side, a fluid chamber is mounted and to it a load-lock chamber, but they have not been used in this work.

2.2 Fabrication

All fabrication and relevant processing was performed in the well-equipped Nanoscale Physics Research Laboratory (NPRL) clean room. The clean room has all the basic and fundamental equipment such as a wet table for cleaning, de-ionised (DI) water (Purite Neptune, 18.2 MΩ), spin coater, hot plates, scales and various chemicals for different processing. The set of equipment housed in the clean room of particular interest and which was used in this work consists of: an experimental prototype plasma etcher, magnetron sputter coater, tube furnace, scanning electron microscope (e-beam lithography), dicer and profiler.

2.2.1 Plasma Etcher

All (dry) etching was performed with a PlasmaPro NGP80 etcher, equipped with Inductively Coupled Plasma (ICP) technology, which is a high density plasma system, from Oxford Instruments. The RF signal, that is used to generate the plasma, is transmitted through a coil rather than the conventional way with ICP. By decoupling two RF generators, one for the ICP and the other for conventional electrodes, the etcher is able to independently control the ion energy and the plasma density in an advantageous way.

The top part of the plasma chamber is occupied by the antenna coil, which provides for the ICP. An induced electric field from the antenna coil, which generates an RF mag-

netic field, ignites the plasma in the chamber by initially dissociating gas molecules into electrons and ions. These are then accelerated and in a "chain reaction"-like way they dissociate more gas molecules through collisions, thus increasing the density of the plasma rapidly. The sample stage also acts as an electrode and is connected to the other RF generator, which controls the impact energy of the ions by controlling the DC bias [105].

Sulphur hexafluoride (SF_6) was the main etchant gas used in this work, which is commonly used to etch silicon. A fluorine radical and an ion is produced as the etchant is dissociated in the plasma according to formula 2.12.

$$SF_6 + e^- \longrightarrow SF_5^+ + F^* + 2e^- \tag{2.12}$$

When etching, e.g., silicon, a volatile product is gained according to formula 2.13.

$$Si + 4F^* \longrightarrow SiF_4 \tag{2.13}$$

Octafluorobutene (C_4F_8) was also used as it produces a so called passivation layer on surfaces, formed by fluorocarbon molecules derived from plasma ionised C_4F_8. The passivation layer, e.g., enhances the etch resilience of resist masks, as it reduces accelerated ions' harmful impact, despite chemical etching being more forbearing than ion sputtering. However, as ion bombardment is directional, usually passivation layer covered sidewalls are protected while the etching process heads vertically. High aspect ratio structures can easily be fabricated with vertical sidewalls by combining passivation and etching, either alternatively or simultaneously according to the necessary specifications and constraints laid down.

2.2.2 Sputter Coater

All deposited films in the clean room fabrication work were done with an RF magnetron sputter coater, model 306 from Edwards. Samples are mounted with surface, to be deposited, pointing down on a rotatable holder and the vacuum chamber is equipped with three magnetrons in the base of the chamber, making it possible to deposit three different materials without breaking the vacuum and exposing the sample or target(s) to ambient atmospheric pressure. After sample loading, the pressure is brought down to $\sim 5\times10^{-5}$ mbar, before introducing argon gas (1×10^{-2} mbar), to be ignited by applying RF power (<600 W), in order to generate a plasma.

The plasma sputters the -400 V biased target, which expels the material particles towards the grounded sample, ~100 mm above, where they are deposited and slowly build up a thin film. The grounded rotatable sample holder is fitted with a water cooling system keeping the sample cool during deposition. The chamber is also equipped with a shutter in order to better control the deposition purity and exposure time. Before deposition, the sample is blocked by the shutter for a short moment until the contaminated top layers of the target are sputtered away. The shutter is then quickly moved to the side, exposing the sample for deposition until the desired thickness has been achieved and then quickly moved back in order to block any further material deposition. This gives more sharp initial and final deposition times, hence a more accurate deposition time.

Many parameters affect the rate of deposition as well as the morphologies of films deposited. By changing the gas pressure, the bias between target and sample and also the RF power, different results can be obtained. Fine-tuning and optimising these parameters, therefore, allows one to achieve the desired results.

2.2.3 Tube Furnace

The tube furnace, from Carbolite, was used to anneal samples. The furnace have N_2 and O_2 gas supplies fitted and the possibility to fit or switch to other gas types is also available.

2.2.4 Surface Profiler

Most thicknesses were measured with a profiler, a Dektak^{3}ST from Veeco Instruments. Measurements were done by initially placing a sample with the area of interest under the stylus and its diamond fitted tip in contact with the surface at 90°. The profiler then performs a line scan across the sample surface at constant force, recording the vertical displacements of the tip and the position along the scan line to produce a one dimensional topographical profile of the scanned sample surface. Step heights can be measured to high accuracy, with a precision of ~5 nm vertical resolution. One clear disadvantage of the profiler is that it can not be used on all types of surfaces and is restricted to hard enough surfaces to bear the weight of the stylus during scans. Unfortunately, scans of too soft surfaces lead to measurement errors as well as damages to the material.

2.2.5 Nano Sphere Deposition Setup

A bespoke piece of kit was utilised to (form and) deposit the close-packed latex polymer nano spheres onto substrates. The final nano sphere lithography (NSL) process employed, utilises a basic bench-top setup as in Figures 2.4 and 2.5. The setup consists of a standard, off the shelf, glass basin filled with (DI) water. Ordinary tap water might have worked just as well, but in order to insure minimum particle interference with the close-packing process of the nano spheres on the water surface and the subsequent deposition of the hexagonally ordered layer on substrate surfaces, DI water was used. The bottom of the basin was fitted with a flat tilted platform, for the sample holders, which assists in the

deposition process. Blue tack was used to fill the lid of a reasonably sized Petri dish (to make a platform, with glass side facing up and blue tack filled side facing down), making sure no air was trapped inside and attached to the bottom of the glass basin making sure the platform was slightly tilted. Custom-made sample holders were made out of vial screw cap lids, filled with blue tack, once again making sure no air bubbles were trapped inside, which could ruin the nano sphere monolayer at the air-water interface if escaped during deposition. All parts were thoroughly cleaned with ethanol before and after each deposition to get rid of any loose organic material such as nano spheres and particles from the blue tack, with areas already being minimally exposed to the water. Double-sided carbon tape was used to fit samples onto the sample holders, which were then submerged into the water.

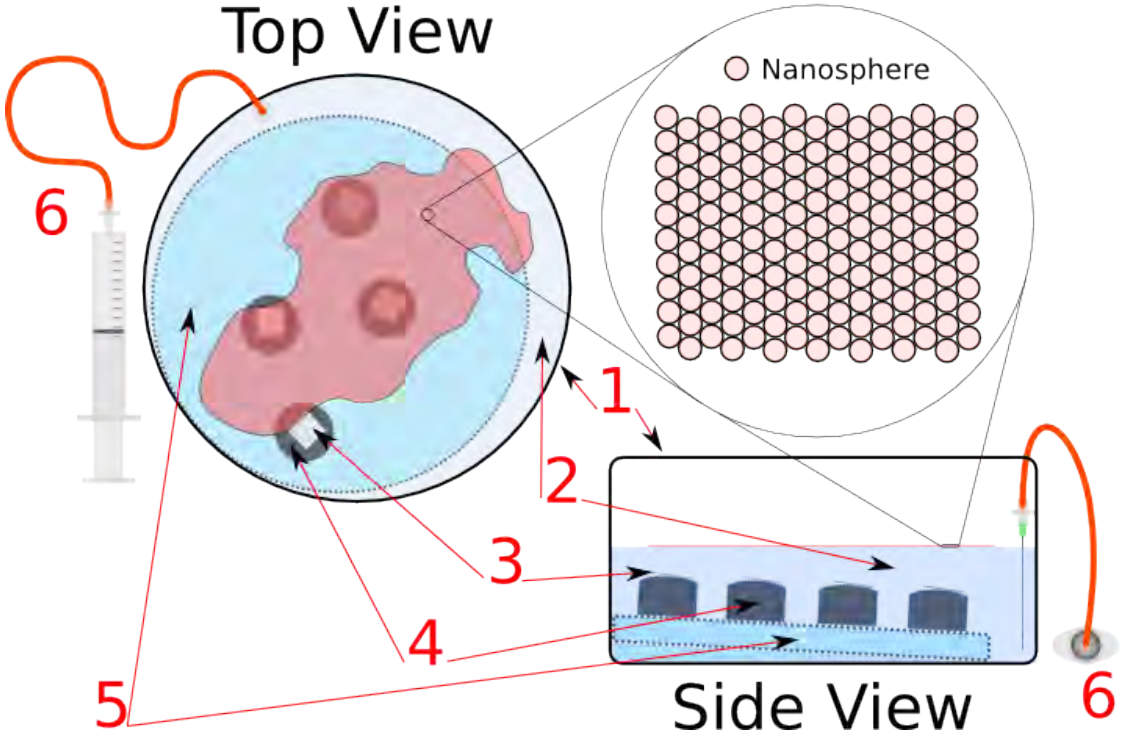

Figure 2.4: Diagram depicting bench-top NSL setup. 1) A glass basin is filled with 2) (DI) water and then 3) samples, fitted onto 4) bespoke holders, are submerged into the water and stand on 5) a tilted platform. 6 A bespoke self-built tool, consisting of a needle, rubber hose and syringe is fitted to the basin, in order to lower the water level through siphoning for nano sphere deposition on the samples.

A prepared diluted solution of suspended nano spheres where spread onto a dry (hydrophilic) pre-cleaned 2×2 cm^2 Si sample, acting as a transfer medium of the nano spheres, by pipette dripping. After the complete spread of the nano sphere solution drop over the entire Si surface, the transfer sample was tilted (45°) and very slowly submerged into the water with tweezers, transferring the nano sphere layer onto the air-water interface. A syringe connected to a rubber hose, which in turn was connected to a needle acted as the siphoning tool used to lower the water surface level (Figure 2.5). The setup was placed on a vibration-free table (air-legs of SEM) and covered with a Petri dish lid during siphoning in order to avoid air currents stirring the close-packed nano sphere monolayer at the air-water interface.

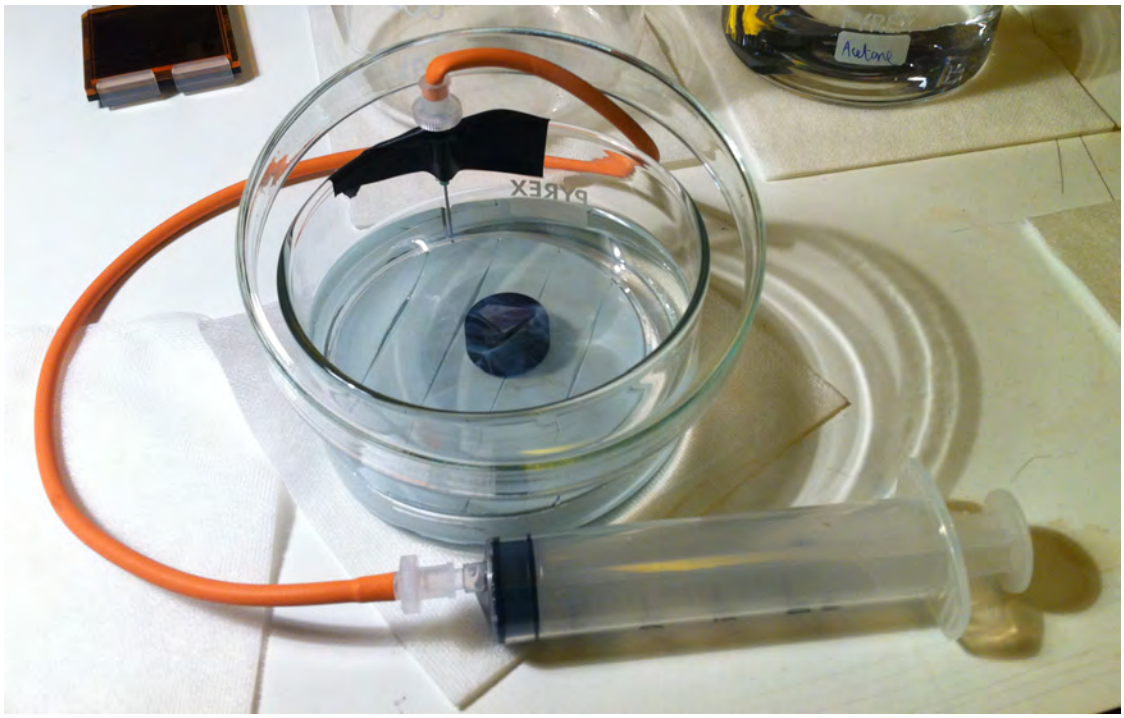

Figure 2.5: Photograph of final bench-top NSL setup. A basin is filled with (DI) water and bespoke sample holders are fitted with samples and then submerged into the water. A bespoke self-built tool, consisting of a needle, rubber hose and syringe is fitted to the basin, in order to lower the water level for nano sphere deposition.

This setup was the most tried out and successful one, achieving good deposition coverage on MoS_2 samples. Other configurations that have been tested will be demonstrated and

discussed in Chapter 5.

2.2.6 Scanning Electron Microscope

An XL 30 SFEG Scanning Electron Microscope from FEI was used in this work when imaging the Si and MoS_2 samples, after fabrication, in order to visualise features at the micro- and nanoscale. The SEM is part of an electron beam lithography (EBL) system made up by another key component, namely an ELPHY Quantum pattern generator from Raith GmbH. Arbitrary patterns can be generated by included computer aided design (CAD) software so that the pattern generator can control resist exposure by electron beam position. The SEM was mainly utilised as it has become an indispensable standard tool to image (fabricated) structures and surfaces at nano resolution (~5-10 nm for our system depending on the beam spot size).

A lanthanum boride (LaB_6) filament, in our system, operating at an accelerating voltage range of 1-30 kV, generates the electrons, which are then emitted from the electron gun via Schottky field emission at UHV ($\sim 10^{-10}$ mbar) and focused/directed by electromagnetic lenses/apertures onto a substrate surface on a sample stage [104, 105]. The electrons travel through the different components of the system along its optical axis.

Samples are loaded into a specimen chamber that goes from slightly above atmospheric pressure (in order to prevent airflow, containing moisture and contaminants, into it while loading samples) to high vacuum (HV) $\sim 10^{-5}$, before connecting with the electron beam column chamber. The impinging electrons on the substrate surface can either backscatter or give rise to secondary electrons. The backscattered electrons are found by a detector located below the objective lens in close proximity to the sample, while the detector for the secondary electrons is mounted at (>)45° relative to the substrate surface normal.

2.3 Scanning Probe Microscopy

Parts of the sample characterisation was performed by utilising a scanning probe microscope (SPM) combining both a scanning tunnelling microscope (STM) and an atomic force microscope (AFM) in one. By swapping/adding a controller and changing probes one can switch between a scanning tunnelling microscope and an atomic force microscope.

2.3.1 Scanning Tunnelling Microscope

For the characterisation of samples, the NanoScope III scanning tunnelling microscope (Digital Instruments)[149] was used. This commercial microscope is an in-air microscope of the single-tube design [109], i.e. the tube piezo scanner is incorporated inside and at the centre of a sturdy metal cylinder. The metal cylinder houses the preamplifier, which is directly connected to the tip, and thereby completes the assembly which is referred to as the scanning head.

The scanning head is placed upon three screws with magnetic, polished spherical ends that are fastened on a base plate, whereupon the sample is placed. The stage on which the sample is placed is free to move laterally by micropositioners with respect to the base plate screws supporting the scanning head. The two front screws are coarse and used to advance the tip very close to the sample surface. The rear screw is actuated by a stepping motor (housed inside the base support) and is used to fine approach and land the tip on the surface.

The whole assembly (head, base and base support) is placed on a vibration-isolation table and is connected to the same NanoScope III control system that controls all of the microscopes manufactured by Digital Instruments. The controller is subsequently connected to a computer with related software, allowing the user to easily control the microscope,

capture images as well as post-process them. The tips used, were mechanically prepared from Pt/Ir (90:10) wire (Advent Research Materials Ltd) with a side cutter.

2.3.2 Atomic Force Microscope

When running the NanoScope III (Digital Instruments) as an atomic force microscope (AFM) an extra controller is connected and a purpose-built stage is used together with a cantilever and laser head in order to probe samples. Tips from Vista probes (T300R) were used with tip radius of ~1-10 nm in tapping mode to image samples.

2.4 High Angle Annular Dark Field Scanning Transmission Electron Microscope

Electron microscopy images presented within this work were all taken with at least one of two STEMs with HAADF detectors present at NPRL by colleagues working with the microscopes [150]. From March 2008 to March 2009, an FEI Tecnai F20 was used by colleagues in imaging samples made by the author. In June 2009, an aberration corrected (C_s corrector) JEOL 2100F replaced the former electron microscope in NPRL. The main difference between the two microscopes is the spherical aberration corrector in the new system, which lays a greater addition to the operational procedures and manual controls to the JEOL system in comparison to the old Tecnai system, even though both systems are basically the same in principle. Moreover, the resolution achieved by the newer system is much higher and enables the study of the 3D atomic structure of nanomaterials.

Inside a column there is an electron source, a sample stage, an illumination stage, a detection section and a magnification stage, which are the five sections, typically, making up a microscope.

2.4.1 Electron Source Section

Highly energetic, bright and coherent electrons are used to illuminate studied samples. Previously, thermionic emission, where materials were heated enough to give electrons more energy than the material work-function, was used to generate electrons. However, Schottky Field Emission Guns (FEGs) achieve much higher beam currents and are used in newer electron microscopes and were fitted in both the Tecnai and JEOL microscopes. In FEGs, a very sharp tungsten tip acts as a cathode and a very high voltage (kV) is applied between it and an anode, which induces an electric field that extracts electrons from the tip. The extracted electrons are then accelerated to 200 kV by a second anode after the first one (acting as an electrostatic lens) and a crossover of the electron beam is produced from their combined electric fields [150].

The two microscopes, both use this type of FEG with the addition of an extra layer of Zirconia Oxide on top of the tungsten cathode to help lower the work-function and thus enhance the extraction of electrons. To help increase the beam current further the sharp tip is also heated, which furthermore makes sure the level of contaminants are low. It is however, the high vacuum environment that ensures a high level of cleanliness of both material surfaces and "empty" (enough) space for electrons to travel freely without colliding.

2.4.2 Illumination Stage Section

All the stigmators, the deflector coils and lenses are part of the illumination stage. All lenses in both microscopes are electromagnetic, with the exception being the electrostatic lens at the gun (1st and 2nd anodes). Each electromagnetic lens is made up of three different parts, namely lens coils, magnetic circuit and cooling system. When an electric current flows in the lens coils a magnetic field is induced with a distribution depending

on the shape of the magnetic alloy containing the electric current coils (i.e. the magnetic circuit). Thus, the magnetic circuit has to be machined very precisely for the electron beam to behave as expected. The cooling system is based on the flow of cold water (precisely regulated temperature and flow rate for minimum perturbation of the stability of the electron beam) around the lens in order to counteract unavoidable heat generated from electric current flow in the coils, which causes instabilities to the steady operation of the electron beam.

Electron optics at the electron gun help emit electrons at the top of the microscope column, the following lenses, in the column, then focus them into a beam. The beam is aligned by the deflection coils to the optical axis and the illumination intensity is set by condenser lenses C_1 and C_2. The incident beam impinges on the sample nearly parallel by the 1st objective lens, together with the two condenser lenses. In order to have a focused beam incident on the sample the 1st objective lens in the Tecnai has to be very strong, which corresponds to the condenser minilens for the JEOL, when in STEM mode [150]. The focused beam is then rasterised across the sample by AC scanning coils, which manipulate the incident electron ray.

Stigmators are used in the column to correct for astigmatism, where asymmetry of the beam are caused by lenses that commonly focus better in one direction. It is thus possible to make elliptical beams more circular with the help of stigmators, which consists of quadrupole setups that, with magnetic field control, focus and defocus the beam with each opposite pairing.

The main difference between the Tecnai and JEOL microscopes, when it comes to the illumination stage, is the addition of the aberration correction in the JEOL unit. The electron beam is effectively divided up into field and axial rays, in the unit's lens configuration, and follow different paths through hexapole lenses, which corrects the C_s coefficient (under and over correction for a number of orders) [150]. The resolution in STEM is much

improved as the beam is converged back with a C_s coefficient that is much lower than when it entered the corrector.

Aberrations affect electrons that travel through lenses at high angles, relative to the optical axis, the most. However, for the on-axis image, their aberrations go unnoticed as the scattering at these high angles are minute. A tableau, which is made by letting the incident beam tilt, through a set of azimuthal angles, around the optical axis, is taken to solve this issue. A standard calibration sample, consisting of gold nanoparticles on an amorphous carbon TEM grid, is used in the alignment process. The change in size and shape of the Au nanoparticles, for different recorded images, are clear signs of aberrations. Corrections to these defects are possible by measuring the values of the aberration (up to the third order).

2.4.3 Sample Stage Section

Sample handling is done by a single tilt sample holder, on which 3 mm TEM grids are fitted. Clusters are deposited onto these TEM grid samples, after which they are placed on the holder that is then inserted into the column chamber. The alignment of samples in regards to the electron beam is ensured by the ability to tilt the sample holder with ease. In order to reduce contamination, the vacuum around it is improved by liquid nitrogen cold fingers cooling the surrounding area.

2.4.4 Magnification Section

For magnification as well as imaging in TEM mode, the projector and intermediate lenses are used. Thus, more electron optics is used to focus the electron beam at this section for TEM mode imaging and diffraction pattern formation, which is formed by the selected area aperture.

2.4.5 Detection Section

When not in use, the ring-shaped high angle annular dark field (HAADF) detector in the Tecnai microscope, can be retracted from the microscope column. The HAADF detector collects the electrons that is scattered at high angles from the sample, and is thus placed above the viewing screen. Single electron detection is the usage it has been optimised for and it consists of a photomultiplier tube, to which a scintillator is optically coupled to. For the JEOL microscope, a JEOL EM-24560 Dark Field Image Observation Device was used, while the HAADF detector for the Tecnai system was a Fischione 3000 [150].

For both microscopes, the electron beam is aligned while viewing a fluorescent screen, which is retractable. In addition, a US 1000 camera is fitted under the viewing screen of the JEOL system. This allows for better more detailed alignment of the beam.

2.4.6 Vacuum System

The presence of a vacuum (the non-existence of particles) inside the microscope is fundamental to the proper electron propagation, the isolation of the electron optics as well as the sample cleanliness. The vacuum system is an integral part of both microscopes and is divided by small apertures into three different sections. The first section is the gun followed by the column and finally the chamber, which are all differentially pumped. The pressure at the gun can typically get as low as 10^{-10} mbar while 10^{-7} mbar can be achieved in the chamber with the use of liquid nitrogen.

2.5 Cyclic Voltammetry Setup

2.5.1 The Cell

The setup was made up by a bespoke H-cell (designed in CINF at DTU [151, 152]) made from pyrex glass and which had two compartments, see Figures 2.6 and 2.7. One of the compartments was for the counter electrode and the other for the photo electrode (working electrode). They were both divided by a barrier of glass frit, which reduce the migration of gases from one compartment to the other to a minimum, but allows the passing of ions. A planar glass window was formed on the photo electrode compartment side in order to minimise diffraction of the incident light. The same compartment was also fitted (taper glass joints) with the reference electrode compartment, through a lapped stopcock, and ended in a Luggin capillary.

A fine pored frit fitted to the end of the Luggin probe made sure that loading an ion-bridge into the compartment would not allow it to diffuse out to the electrolyte and at the same time prevent reference electrode contamination from the electrolyte. Glass lids were used to close each compartment, which fit to each other by standard taper glass joints. Two electrical feedthroughs (with GC-style septa from Supelco) were fitted on each glass lid for electrode connections as well as two gas connections, which could be used for input and output purposes. For purging of the electrolyte (before and during experiments) a bubble tube, to supply Ar and/or H_2 gases, was introduced into the working photo electrode compartment.

2.5.2 Conditions & Parameters

Before use of the cell, it was cleaned with (immersed in) freshly prepared piranha solution (35 % hydrogen peroxide and concentrated sulphuric acid in 1:3 ratio) and subsequently

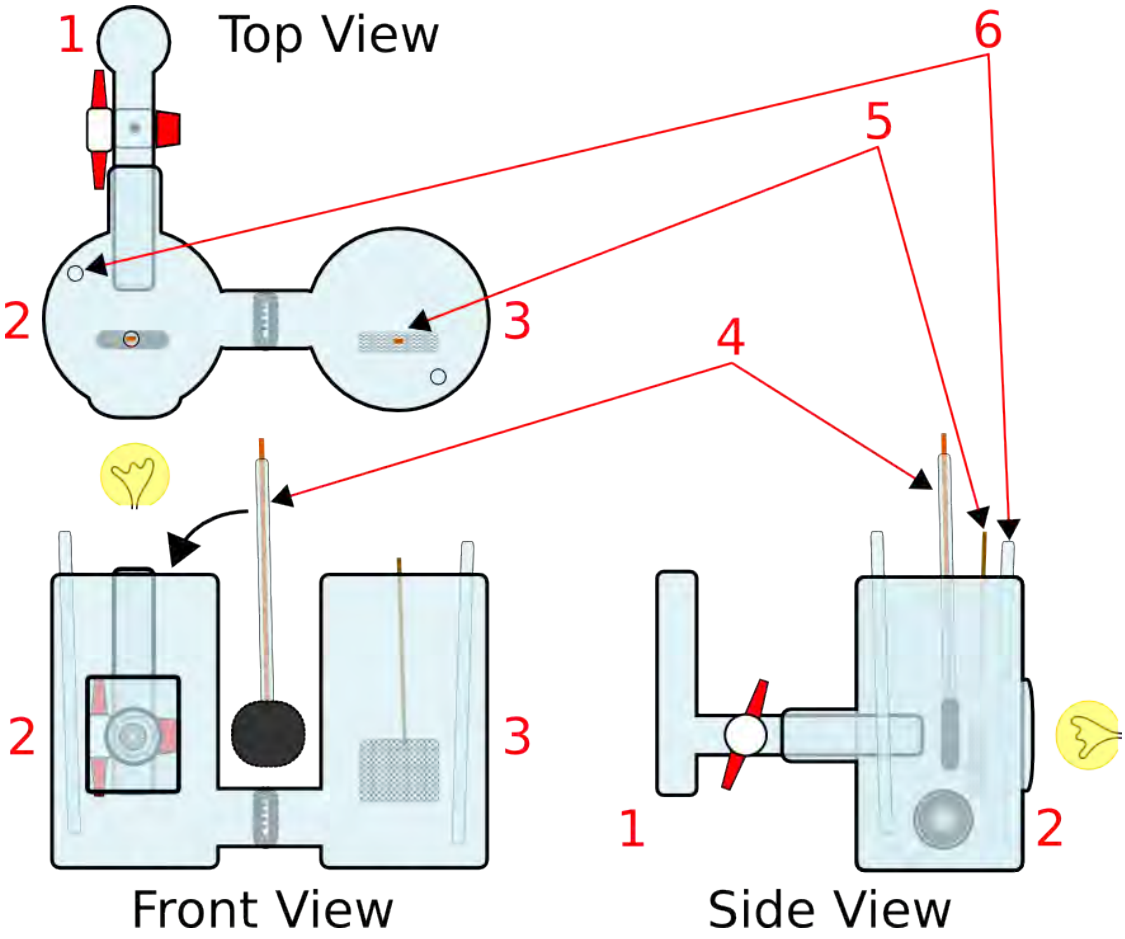

Figure 2.6: The three compartments making up the cell used in the photoelectrochemistry experiments are clearly shown. (1) The reference electrode compartment is directly connected to (2) the photo electrode compartment, which in turn is connected to (3) the counter electrode compartment. (4) Photo electrode, (5) counter electrode and (6) gas feedthroughs are indicated in the schematic diagram. For clarity some non-vital parts (glass lids) have been omitted from the diagram, but which are clearly visible in Figure 2.7.

sonicated for ~30 min in DI water (milliQ 18.2 MΩcm). This was also done with the glassware used for chemical handling in order to dissolve impurities (metal and carbon based).

The cell was filled with electrolyte, 0.1 M perchloric acid at pH 1.0, that was ensured to be enough to immerse all necessary parts for each experiment. A square platinum mesh with dimensions 1.5×1.5 cm and bubbled with H_2 continuously was used as the counter electrode. The reference electrode was a saturated calomel electrode used together with saturated sodium chloride solution as an ion-bridge in the reference electrode compart-

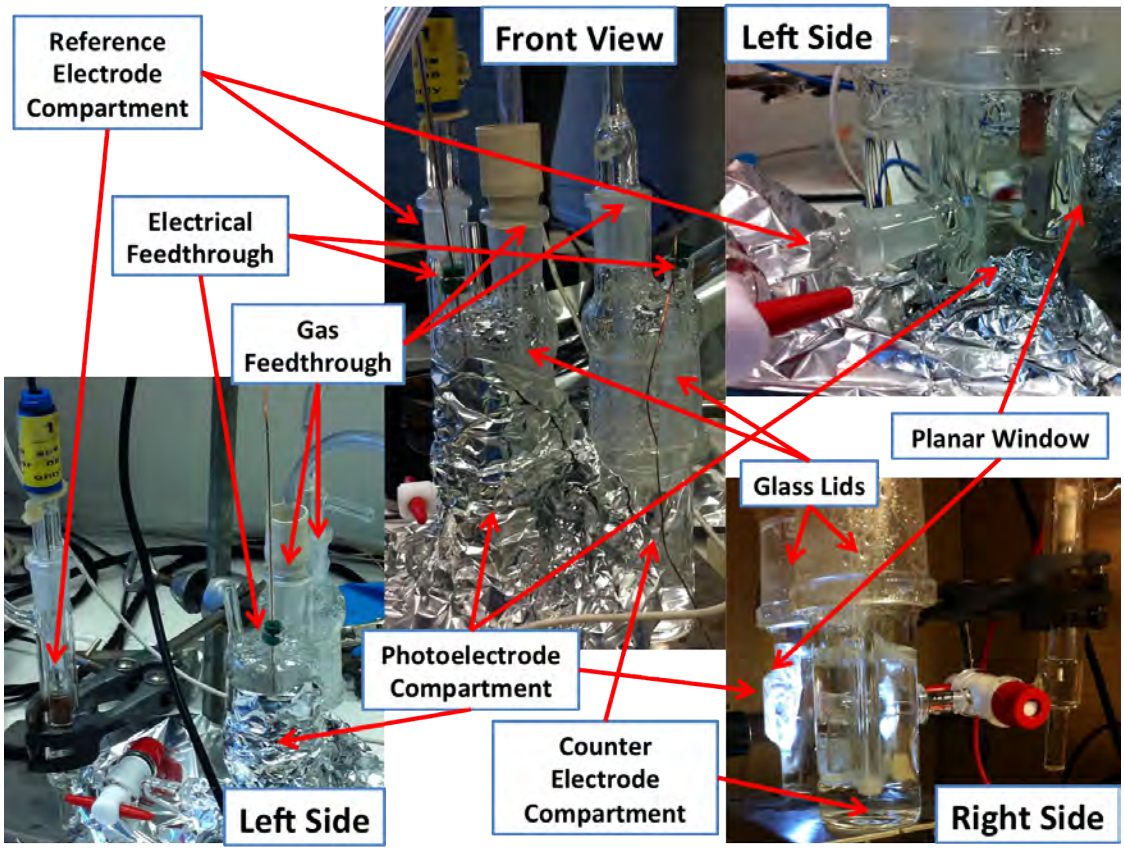

Figure 2.7: The three compartments making up the cell used in the photoelectrochemistry experiments are clearly shown. The reference electrode is inserted into its own compartment, which is directly connected to the photo electrode compartment, which in turn is connected to the counter electrode compartment.

ment.

Before commencing the experiments, introduced Ar gas was bubbled for at least ~30 min in order to purge the electrolyte. The gas was then changed to hydrogen gas and let to bubble for at least ~10 min, in order to saturate the electrolyte, before starting experiments while leaving it bubbling. The septa used for the electrodes ensured a tight seal of the cell avoiding the introduction of oxygen. During electrode exchange, the hydrogen gas was let to purge the electrolyte from any oxygen left in the top part of the compartment for a minute or so.

The working photo electrode compartment was covered with aluminium foil to simulate darkness, while the setup was still being in a lit lab, in order to prevent the effect of light

on the catalytic activity of the tested samples. Photoelectrochemistry experiments are performed while housing the whole cell, together with the light source, inside a cardboard box in a dark lab (lights switched off).

All measurements were done at a scan rate of 5 mV/s, from -0.3 V vs SCE to -0.9 V vs SCE, with the EC-Lab software suite (V10.02 from Bio-Logic), while the data was corrected for in SciDAVis (open source data analysis and visualisation software suite).

2.6 Sample Preparation

Different kind of samples have been used for different parts of this work. Overall, the preparation of all samples in this thesis varies from experiment to experiment and from batch to batch (some slightly and some a lot) and will therefore be covered here.

2.6.1 Carbon Supports

Two types of substrates were used during the course of the initial cluster deposition work, namely graphite tape and highly ordered pyrolytic graphite (HOPG). High purity exfoliated mineral flake graphite is compressed into sheeting form and then cut to make thin graphite tapes, which were supplied by Minseal, Mineral Seal Corporation. The tape was loaded without any processing (as is, from the supplier) into the tape drive in high vacuum (HV).

The HOPG, supplied by Momentive Performance Materials, were cut (with scalpel) and cleaved (with Scotch tape), in air, to ~6-8 pieces (from one supplied 10 × 10 × 2 mm piece) before being loaded to the sample holder into the high vacuum deposition chamber.

After cluster deposition, at room temperature, both types of substrates (graphite tape and HOPG) were exposed to air when taken out of the chamber for imaging/characterisation

with the microscopes (AFM/STM) and when shipped to collaborators (characterisation & catalysis).

2.6.2 Clean Room Samples

A 4 inch silicon wafer (n-type, phosphorous-doped, Si 100), from Rockwood Wafer Reclaim, was diced with Disco DAD321 automatic wafer dicing saw, producing several 1×1 cm^2 square samples that were cleaned (underwent a certain cleaning treatment) before use.

To get rid of particles and dust (after the dicing), the Si square substrates were submerged in isopropanol and acetone in ultrasonic bath for $\sim$ 10 min, subsequently cleaned under the flow of de-ionised water and then dried with the flow of nitrogen gas.

Before each fabrication experiment the Si squares were immersed in Piranha solution (concentrated 95-98 % sulphuric acid, H_2SO_4, Fluka with 30 % hydrogen peroxide, H_2O_2, Riedel-de Haën), in equal parts by volume, for 10 min before being rinsed with DI water and dried with nitrogen gas.

Rough natural crystals of MoS_2, from SPI Supplies, with dimensions of $\sim 14 \times 9$ mm were cleaved and cut, in air, into small pieces of $\sim 3 \times 3$ mm with scalpel and Scotch tape. Samples to be deposited by clusters were used as is and loaded directly to the cluster source sample holder and placed into high vacuum after preparation. After cluster deposition the samples were introduced into the clean room where they were etched and imaged/characterised.

MoS_2 samples for nano sphere deposition were prepared in the clean room. After being cut and cleaved, the samples underwent a Piranha solution bath for $\sim$ 10 min, after which they were rinsed in DI water and dried with nitrogen. Afterwards the samples were ready for nano sphere deposition.

After fabrication, all samples were exposed to air when taken out of the clean room for imaging/characterisation with the microscopes (AFM/STM) and when shipped to collaborators (characterisation/catalysis).

2.6.3 Catalysis Samples

When testing the fabricated catalyst samples all the samples were specially prepared before going through cyclic voltammetry experiments, see Section 5.4.1 on page 241 in Chapter 5 for more details. The samples were adapted into suitable electrodes using copper tape with adhesive backsides for electrical connection and teflon tape for electrical isolation, which could easily be introduced into the photo electrode compartment of the photoelectrochemical cell used in the cyclic voltammetry measurements.

2.7 Summary

Experimental equipment and methods relevant to the work presented in this thesis have been covered in this chapter. The different important parts of the cluster source used to generate size-selected clusters was initially covered. Following the cluster source equipment, the fabrication equipment was presented. The different microscopes, used to characterise all the produced samples, were covered afterwards. At the end, the cyclic voltammetry setup was presented followed by the sample preparation techniques. The first results, covering the cluster source optimisation and modification, will be presented in the coming chapter.

CHAPTER

THREE

CLUSTER SOURCE OPTIMISATION, MODIFICATION AND APPLICATIONS

This chapter covers general source optimisation and modification for various cluster deposition experiments. Optimisations and modifications have been performed to the RF magnetron cluster ion beam source in order to improve the sample deposition efficiency and, initially, to reach the target of producing large-area samples for catalysis experiments. The cluster source developments have been pursued by a process of accumulating detailed, but important, changes. First of all, the change of the LTOF-MS entrance and exit aperture slit sizes will be discussed. Secondly, the alignment issue of nozzle with respect to the first skimmer, will be dealt with. The commissioning of the tape drive and modifications (computer control and changes of spool setup etc.) will also be presented. Finally, the optimisation of the liquid nitrogen cooling process is addressed. The chapter is then rounded off with examples of cluster deposition experiments performed.

3.1 LTOF-MS Apertures

The exchange of the LTOF-MS apertures was made in order to increase the flux of the cluster beam so that the deposition time would decrease. As mentioned in section 2.1.3 the cluster beam is defined by one entrance aperture before the lateral time-of-flight mass selector and one exit aperture at its end. The aperture plates of the LTOF-MS were designed to be easily swapped to different plates with other aperture dimensions/geometries. Unfortunately, the elaborate assembly of the LTOF-MS inside the vacuum chamber makes it cumbersome and a non-trivial process to swap apertures despite the original simplicity of installation (but which a lesson has been drawn from and is improved in the new cluster source). For the current assembly, at least three people are required when swapping the apertures, because the LTOF-MS vacuum chamber needs to be de-attached at two locations. The chamber needs to be detached from the deposition chamber first, and then from the turbo pump in order to slide the chamber back and then dismantle and slide out the end flange to which the LTOF-MS is attached, see Figure 3.1.

The dimension of the entrance slit before the swap was a circular aperture having a diameter of 6 mm. The exit slit was a rectangular aperture having dimension 3.5×10.5 mm. Both slits were exchanged with rectangular apertures having the same dimensions of 5×15 mm. An increase of transmission was expected, theoretically, by the width increase of the entrance and exit apertures. Interesting to note was the discovery of the hybrid nature of the LTOF-MS in terms of slits.

The mass resolution is not easily obtained by geometrical considerations and the assumption of a focused beam. Rather, a real world situation, with a non-perfectly focused beam, needs to be taken into account when considering the mass resolution of the LTOF-MS.

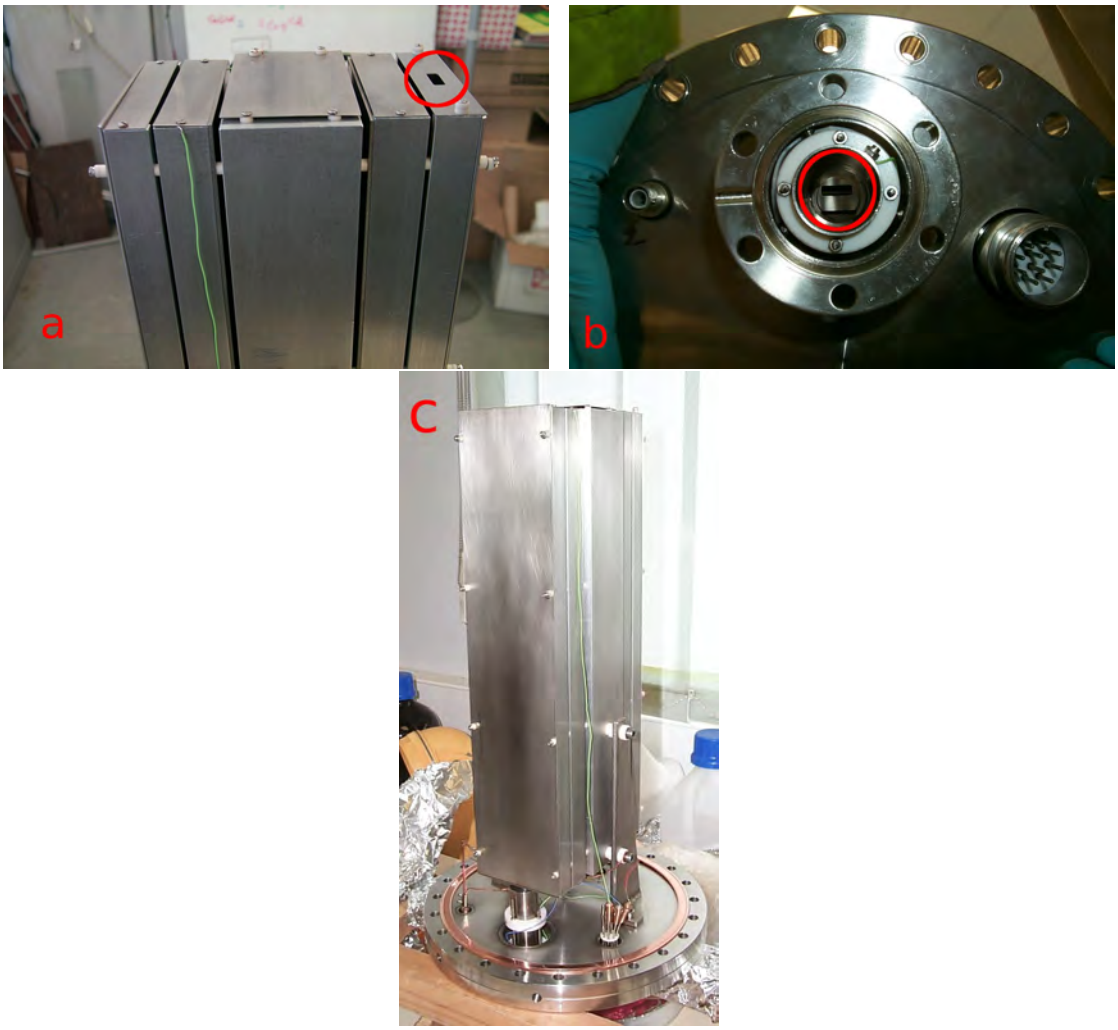

Figure 3.1: (a) The entrance aperture after the swap having dimensions 5×15 mm. (b) The exit aperture after the swap also having dimensions 5×15 mm. (c) Picture showing the LTOF-MS attached to the chamber end-flange in a vertical position (it is situated horizontally when attached to the chamber).

3.1.1 Real Versus Effective Exit Aperture

The mass resolution of the novel LTOF-MS corresponds to the lateral cluster displacement over the vertical exit slit size [147],

$$R = \frac{m}{\Delta m} = \frac{x}{\Delta x}. \tag{3.1}$$

This is theoretically worked out to be the case if the beam converges (is focused) to a

spot at the *"virtual aperture"*, see Figure 3.2. If, however, the beam is defocused at the virtual aperture this relationship cannot be true. Instead an *"effective exit aperture"* can be worked out if the experimental mass resolution can be obtained. If no lateral displacement of the beam takes place, the virtual aperture becomes the real exit aperture and the beam can be detected at that point. One can choose to detect the beam at that point (e.g. for focusing) and then displace the beam laterally, in which case the aperture becomes "virtual". Hence, the effective exit aperture depends on the beam profile at the virtual aperture ("virtual aperture size") and the real exit aperture, which the beam goes through after the lateral displacement.

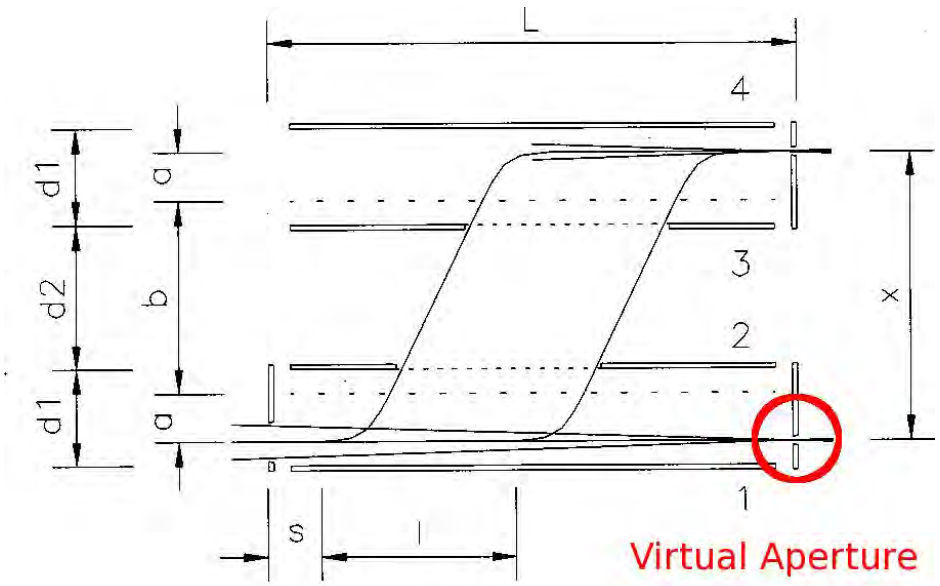

Figure 3.2: Schematic of the novel LTOF-MS incorporated in the RF magnetron sputtering cluster source. Short high voltage pulses are applied to plates one and four to laterally displace a focused cluster ion beam. l length of the cluster ion beam package displacement; x total displacement; a beam offset traversed during the high voltage pulse; b length of the field-free region; $d1/d2$ plate separations; s length of the portion of the ion beam which cannot be used due to field distortion; L total length (Adapted from [147].)

After acquiring mass spectra and obtaining the peak representing the argon monomer, the mass resolution could be calculated by taking the mass value of the maximum of the peak m and dividing by the full-width-half-maximum FWHM Δm [147]. The mass resolution of the system, before the LTOF-MS aperture swap, is worked out to be $m/\Delta m = 27$ from

the mass spectrum in Figure 3.3. However, from the dimensions of the old, 3.5×10.5 mm, rectangular exit aperture we get a mass resolution of $x/\Delta x = 34$. This difference between theoretical and experimental mass resolution does not stop here, but is also evident after the aperture swap. After the aperture swap, the LTOF-MS mass resolution obtained from the mass spectrum was $m/\Delta m = 19$. Once again the mass resolution deviates from the theoretical value, which is expected to be $x/\Delta x = 24$ for the new, 5×15 mm, rectangular exit aperture.

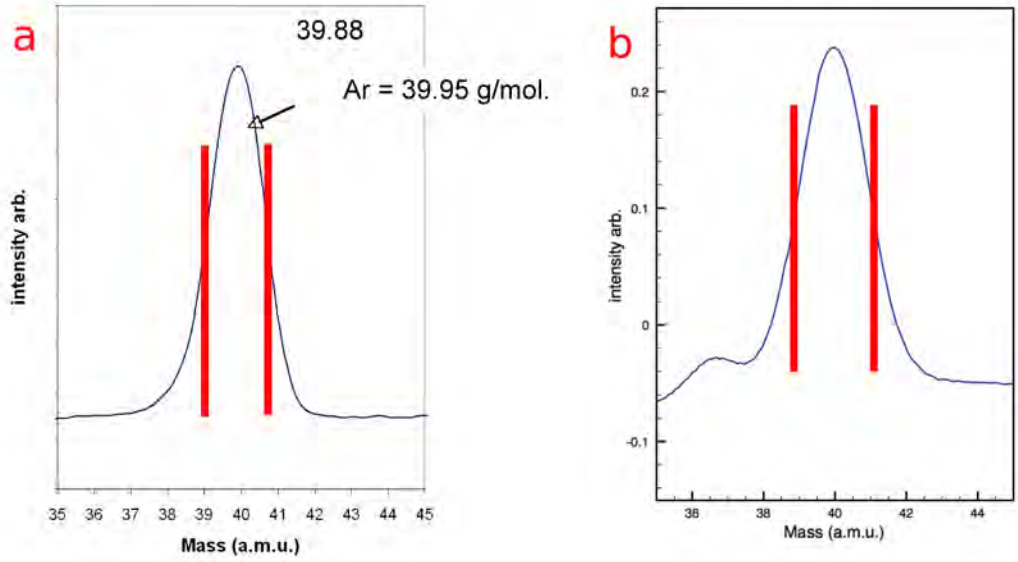

Figure 3.3: (a) Mass spectrum showing the argon monomer peak acquired in order to get the mass resolution of the system and was performed before the aperture swaps. Mass resolution is $m/\Delta m = 27$ (data courtesy of A. Pulisciano, a previous post doc). (b) Mass spectrum of the argon monomer peak acquired after the aperture swap showing a mass resolution of $m/\Delta m = 19$.

As treated by von Issendorff and Palmer [147], the assumption of a focused beam at the virtual aperture cannot be made. It is proven invalid from the experimental data shown above. Δx is referred to being the full-width-half-maximum (FWHM) of the convolution of the exit aperture width and the cluster beam profile. For two gaussian distributions (real exit aperture width and the cluster beam profile at virtual aperture) the standard deviation σ (FWHM $a = 2\sqrt{2\ln 2}\sigma \approx 2.35\sigma$) of the convolution (*"effective exit aperture"*) is given by [153],

$$\sigma_{eff}^2 = \sigma_{rea}^2 + \sigma_{vir}^2, \tag{3.2}$$

thus

$$\Delta x = a_{eff} = \sqrt{b_{rea}^2 + c_{vir}^2}. \tag{3.3}$$

For a focused beam profile at the virtual aperture, $c_{vir} = 0$, the relationship simplifies to the effective aperture being the real aperture and will thus give the maximum mass resolution of the mass selector by the ratio of the lateral displacement and real exit aperture width ($x/\Delta x$), as is mentioned in [147].

The lateral displacement x is fixed and has the value of 120 mm. It is therefore possible to obtain the full-width-half-maximum (FWHM) of the beam profile at the virtual aperture (c_{vir}). By using the experimental values of the mass resolution of the system, before ($m/\Delta m = 27$) and after ($m/\Delta m = 19$) the aperture swap, we can work out the effective aperture sizes using equation 3.1, which gives the values 4.4 mm and 6.3 mm respectively. In the same way we can get the virtual aperture sizes by then using equation 3.3 that will give us 2.7 mm and 3.9 mm, respectively. The virtual aperture sizes are clearly smaller than the 5 mm entrance aperture (6 mm diameter circular entrance aperture before the swap) which confirms that the beam for both cases were convergent but not focused to a point at the virtual aperture.

3.2 Nozzle-Skimmer Alignment

Perfect alignment of the different aperture elements in the source is crucial for a high flux cluster beam. Even the smallest misalignment of any lens element down the beam line could have a considerable effect. The cluster source, which initially had perfectly aligned

lens elements, experienced a sagging of the inner condensation chamber, with time, that gave rise to an obvious misalignment between the nozzle and first skimmer. As a result a needle/shelf of material was deposited under the orifice of the first skimmer, which was actually known by both previous PhD students mainly working with the cluster source [144, 145], see Figure 3.4. A device was even employed in order to scrape the needle residue (when it grew big enough and would interfere with the beam) without the need to break vacuum.

The alignment process was performed in two steps, the first step being aligning only the nozzle (i.e. not the whole inner condensation chamber) with respect to the first skimmer. The second step was to align the whole inner condensation chamber by moving the supporting rods with three teflon washers, see Figure 3.5. The first step was employed because of its ease of implementation and quick feedback, despite the fact that the alignment was not with respect of the plasma (magnetron head) inside the inner condensation chamber. The alignment proved to be efficient, why pursuing the second step was logical in order to see if the alignment of the plasma with respect of the nozzle and first skimmer gave a different (i.e. better) result. An even ring distribution of residue, which is concentric to the orifice is observed on the skimmer after alignment, see Figure 3.4. An additional benefit of the alignment is the longer operation time between servicing of the generation chamber, where the chamber is vented and cleaned. Before alignment the chamber was cleaned approximately once a month. This was after normal usage of three deposition sessions a week. The chamber was cleaned approximately once every two months after the alignment.

The contribution of both the slit change and the alignment of the nozzle with respect to the first skimmer improved the cluster beam current almost two-fold for cluster sizes (Pd_{55} and Pd_{309}) relevant to high-area samples for catalysis experiments, see Figure 3.6.

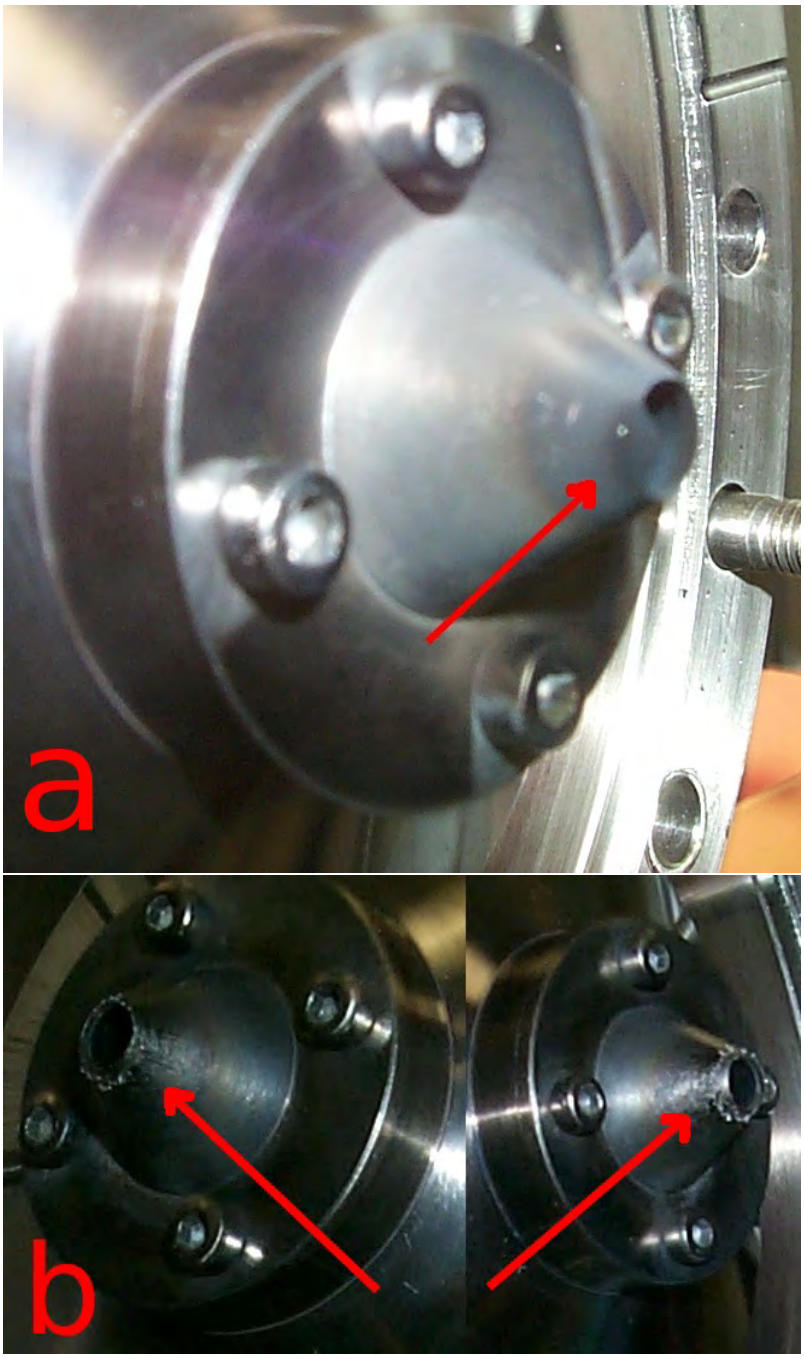

Figure 3.4: (a) Picture before the nozzle-skimmer alignment showing the needle residue (here) grown out from the left side of the first skimmer orifice. (b). Picture after the alignment showing the even distribution of residue as a ring on the skimmer, concentric to the orifice. This reduced down-time of the system considerably.

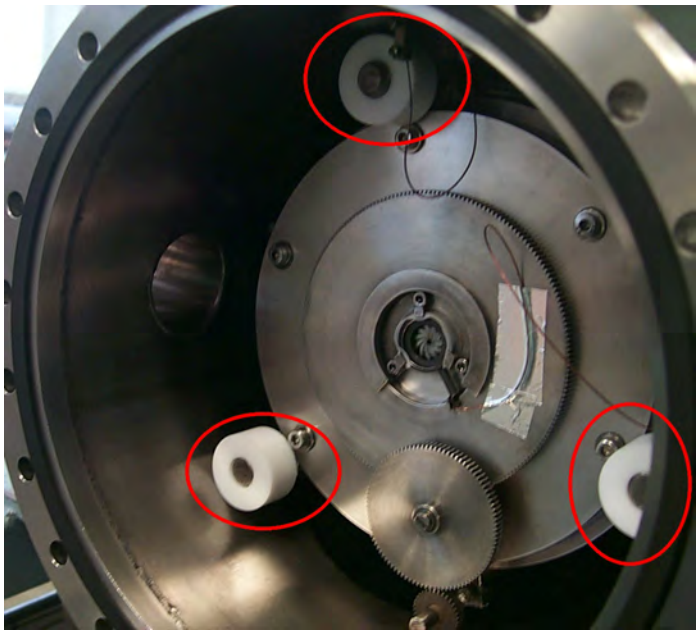

Figure 3.5: Teflon washers fitted to supporting rods in order to align inner chamber with respect to the first skimmer. The nozzle (variable iris diaphragm) is situated in the middle of the inner condensation chamber end flange.

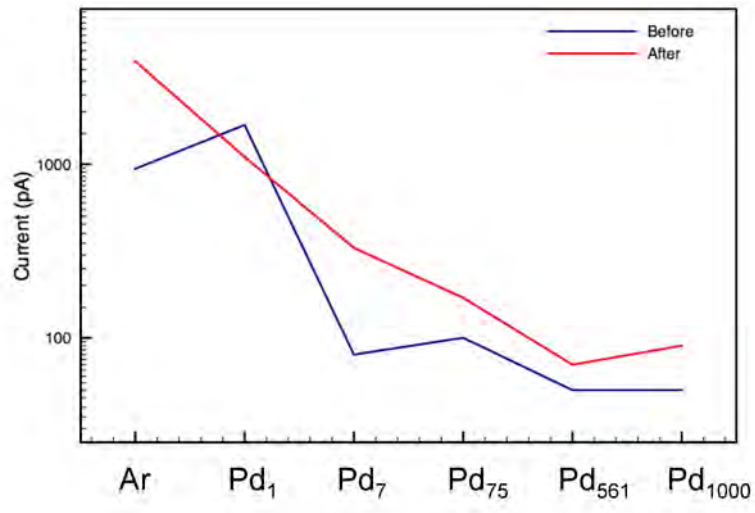

Figure 3.6: Comparison of typical beam currents for different cluster sizes before and after LTOF-MS slit change and the nozzle-skimmer alignment.

3.3 Tape Drive

The tape drive was used and commissioned for the first time during this project, despite being designed and built prior to this work (designed jointly by previous colleague and

Gary Walsh, who also built it). The tape drive consists of a tape drive base, which holds all necessary components and the flange and slides assembly, which is fitted to the deposition chamber and that the base slides on, see Figure 3.7. The drive is sealed with a cup attached to the system and is manoeuvred with an external electronic control box wired to it. The graphite tape which was used when developing the tape drive was a test sample from a chinese supplier. The roll had a width of 5.0 mm and a thickness of 0.3 mm and was wound up between two spools (source spool and take-up spool). The source spool was freely connected (low friction) as the tape was strapped over two casters, a sensor, the capstan head, a second sensor, a third caster and finally wound up in the take-up spool. The tape was biased, through a pressing wheel holding it against the capstan head, and was therefore isolated from the tape drive and chamber. The spool and capstan head holders, casters as well as tape drive base slide supports were made from teflon for electric isolation. Two DC-motors were used to roll the tape, one motor connected to the take-up spool winding up the tape, and one motor connected to the capstan head in order to create the necessary friction to make the tape roll without problems. The two sensors warned whenever the tape moved up and out of the grooves of the casters and capstan head, which happened somewhat frequently and caused the tape to either loose tension and stop rolling, or gain tension and break.

The thin and delicate tape was very sensitive to tension and broke easily while running the drive. This caused a lot of down-time when depositing samples. Each break or stall caused a delay (~1 h) as one had to vent the chamber, mend the tape and pump down again before continuing the deposition. This regularly happened more than three times during a deposition. A far more dangerous aspect is the fact that the tape was biased with a high voltage that could short circuit, which happened on a couple of occasions, causing damage to instruments etc. A thicker (0.5 mm) and wider (5.3 mm) tape, from an american supplier (Minseal) was thought to eradicate all problems. The increased width did rectify the problem with the tape moving up and out of grooves, but the increased

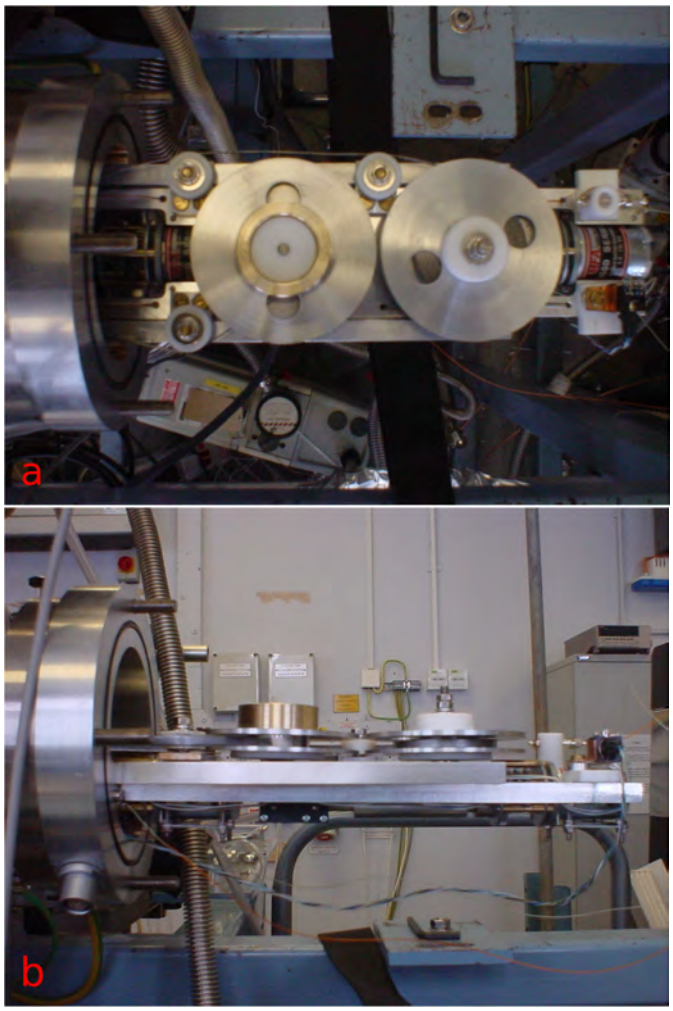

Figure 3.7: (a) Top view of the tape drive, before any changes, when attached to the back flange of the deposition chamber. (b) Side view of the tape drive, before any modifications.

thickness caused other problems. The sharp turns of the thick tape in the drive caused it to crease and subsequently break. Moreover, the rolled tape of the freely connected source spool acted as a spring, due to its stiffness, it wound up and touched the cup chamber wall with every movement instead of rolling over the casters.

In order to avoid creasing of the tape, the spring action of the source spool and the tape touching the chamber, a teflon track substituted the two casters. Two sturdy weights were put on both spools to increase stability and give a more cadenced motion of the tape. Everything in close proximity to the tape and spools were isolated and changed to teflon, such as the caster bases, see Figure 3.8.

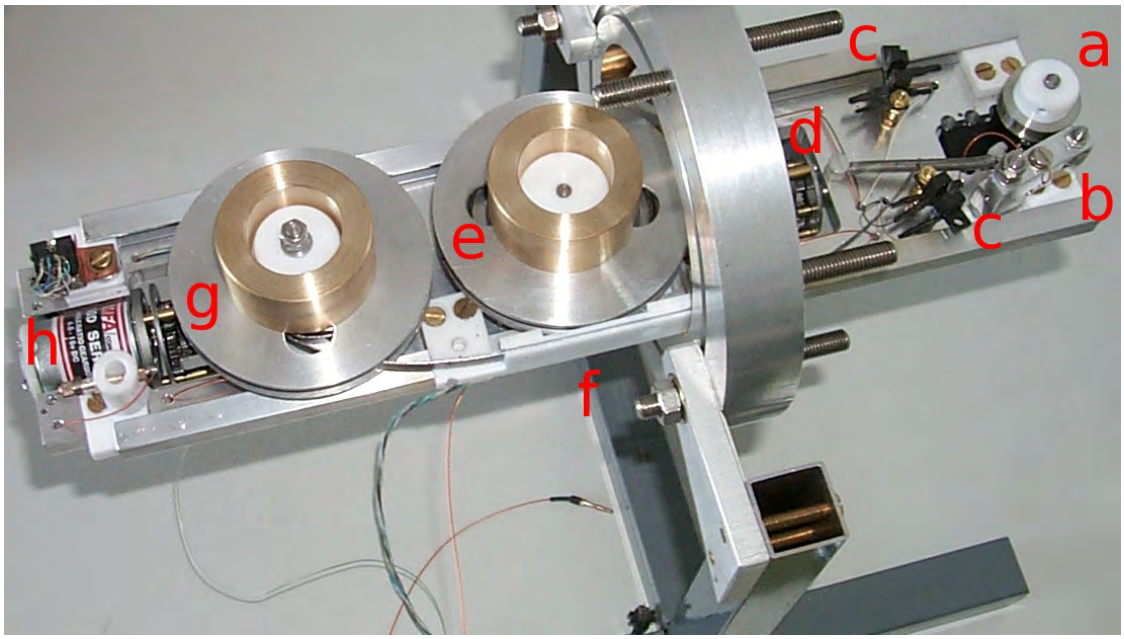

Figure 3.8: Top-side view of the tape drive, after modifications, when attached to its stand. (a) Capstan head; (b) pressing wheel; (c) sensors; (d) DC-motor rotating capstan head; (e) take-up spool with sturdy weight on top; (f) teflon track substituting two casters; (g) source spool with sturdy weight on top; (h) DC-motor rotating take-up spool.

The start of each tape sample was marked before pumping down the deposition chamber and depositing clusters. After deposition, the system was vented and the produced tape sample taken out. This procedure was repeated for all tape samples.

3.3.1 Computer Control

The tape drive was initially controlled manually through an electronic control box controlling the speed of the two DC motors running the tape drive capstan head and take-up spool. Optimised motion is achieved by having a slightly higher speed setting of the take-up spool motor than the capstan head motor, see Figure 3.9. The USB control board MotorBee (PC-Control Limited) is used to interface the DC motors.

Both the manual control and the computer control uses pulse-width modulation to control the DC motor speed, which is essential to reduce the heat dissipation. The heat has nowhere to go in vacuum and causes wear of motor brushes, thus decreasing the lifetime

Figure 3.9: Front view of modified control box, including switch to change between manual and computer control. Sequence programming in computer software allows for basic control of repetitive motion. Advanced programming exists for more elaborate control. Manual box control makes it possible to quickly and easily control the tape motion by turning the capstan head and take-up spool buttons.

of motors. The purpose-built application MotorWay is used to easily control the motor speeds (255 steps) and easily programme sequences controlling motor motion. More advanced programming is also available.

3.4 Liquid Nitrogen Cooling

A full dewar of liquid nitrogen contains 25 litres and was sufficient to run the cluster source continuously for approximately four hours. The cooling procedure was later refined in order to allow for a longer continuous deposition time. The deposition time was extended by a further two hours resulting in a total time of six hours. It was possible to go one step further in extending the continuous deposition time, by sophisticatedly and gradually reducing the pressure of the nitrogen gas that pushes the liquid nitrogen into the double-walled inner chamber of the cluster source. By gradually reducing the pressure of the nitrogen gas from 0.85 bar to 0.1–0.2 bar, whenever liquid nitrogen would flow out from the outlet of the double-walled inner chamber, it was possible to extend the continu-

ous deposition time by a further two hours resulting in a total of eight hours, which is the record so far.

The stretch to eight hours cooling is sufficient for most purposes, but would still require a refill of liquid nitrogen when depositing high area samples like graphite tapes, which would require up to 9 h (12 h in total with preparation etc.) or even more. The source was therefore equipped with a new dewar, with a capacity of up to 50 l of liquid nitrogen, which easily surpasses the previous dewar's eight hour maximum running time. The cooling does not even have to be sophisticatedly pressure regulated in order to cool for a long (~12 h excluding preparation time) deposition session. However, when the cooling is optimised through finely regulating the pressure during the cooling down process one can achieve 16-18 h cooling. This duration is more than enough for most given applications performed in one go under regular user supervision.

3.5 Applications of Cluster Deposition

The most important initial cluster deposition work performed with the cluster source, was increasing the palladium cluster density on high-area graphite tape substrates, which acted as catalysts for the hydrogenation of nitrobenzene. Part of that work involved investigating whether the shape of the palladium clusters changes the catalytic activity and if the shape could be controlled by the cluster deposition energy. That effort was the precursor to the work of Habibpour *et al.*, who continued depositing size-selected Pd clusters on high-area graphite tape, which were then diced into powders for heterogeneous catalysis under realistic reaction conditions [154]. Various successful projects have benefitted from the cluster source advancements [155–158], of which three will be presented here.

3.5.1 Calibration of HAADF-STEM with Size-Selected Clusters

Palladium cluster deposition on carbon coated TEM grids was used to obtain chemical composition within HAADF-STEM [159]. Different sizes (147, 309, 923) of (Pd & Au) clusters were soft landed, to maintain their structure, onto samples for HAADF-STEM imaging, see Figure 3.10 (a, left; b, left & right). A near linear relationship between intensity and cluster size exist for Pd and Au for sizes up to at least 923 atoms, which can be used to investigate the contrast (depending on element) of STEM imaging (HAADF-STEM performed by Zhi Wei Wang). This linear relationship is depicted in Figure 3.10 (a, right) for size-selected Pd clusters.

The HAADF intensity is dependent on the atomic number Z with exponent α and by comparing Pd_{923} and Au_{923} a relationship could be found between the inner acceptance angle of the detector (HAADF) and α, see Figure 3.10 (b, bottom ; c). This can be used to get chemical composition of the areas imaged, in one go, if one knows the global chemical composition of the sample, i.e. without going through any additional steps of spectroscopic characterisation.

The overall improvements to the cluster source benefitted the experiments in allowing reliable runs and availability of the source. Moreover, faster depositions could be made improving the overall turnover time for analysis and repeat/further experiments. Additionally, the bias on the aperture mask and sample holder was decoupled, lowering the voltage applied to the sample in order to achieve better soft landing.

3.5.2 Sintering of Size-Selected Clusters under Realistic Catalytic Reaction Conditions

Palladium cluster deposition was performed on HOPG substrates for catalysis experiments with collaborators (Sungsik Lee performed the catalysis and Feng Yin part of the

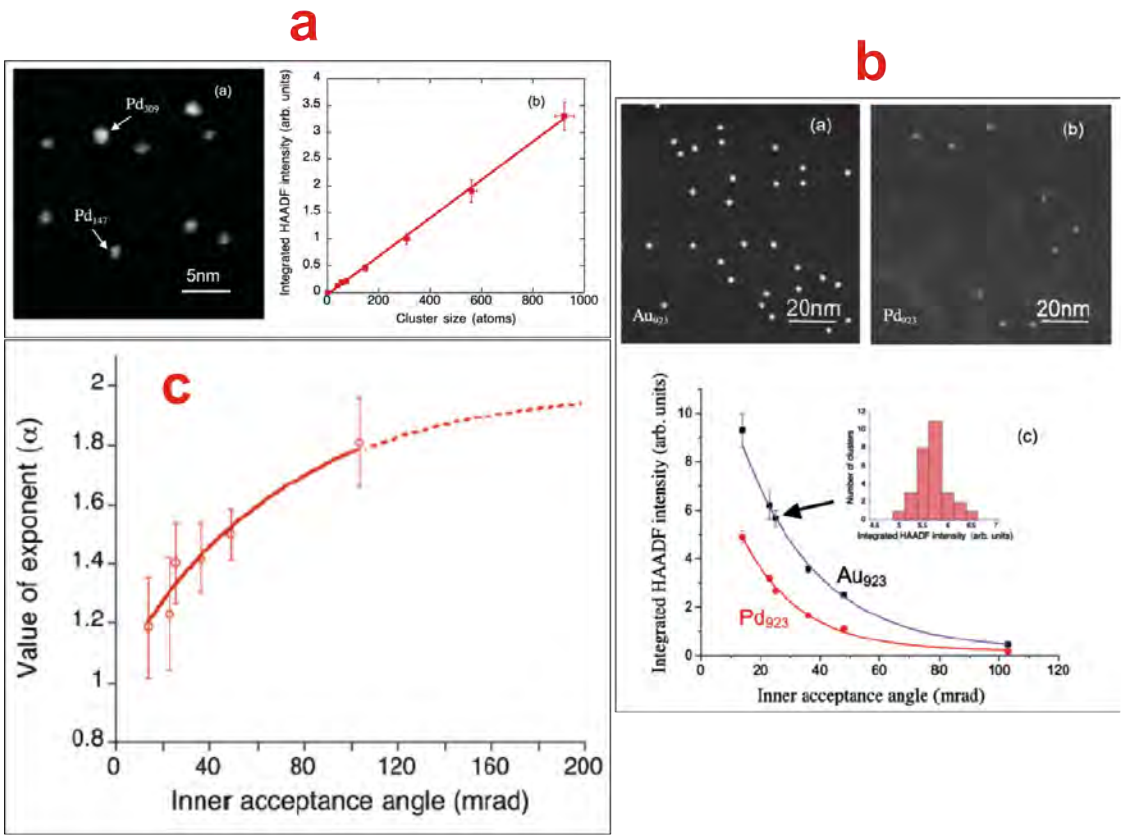

Figure 3.10: (a): (left) Typical HAADF-STEM image of co-deposited Pd_{147} and Pd_{309} clusters. (right) HAADF intensity integrated over vs cluster size. ; (b): HAADF-STEM images, recorded with same experimental conditions, of (left) Au_{923} and (right) Pd_{923} depicted with the same brightness/contrast settings. (bottom) The integrated HAADF intensity vs inner acceptance angle (detector) for Au_{923} and Pd_{923} clusters. ; (c): By assuming that HAADF intensity is proportional to Z^{α}, one can derive (from the previous figure) the value of the exponent α vs the inner acceptance angle (adapted from [159]).

STM) [160]. Both Pd_{55} and Pd_{309} clusters on HOPG substrates were used in realistic catalytic reaction conditions in order to see how well they fare (in comparison to industrial catalysts). The samples were deposited with an average coverage of ~35 000 clusters/μm^2 at an energy of 2 keV (for Pd_{55} and 3 keV for Pd_{309}) resulting in a higher coverage at the centre of the sample compared to the edges, see Figure 3.11 (a).

Using the samples as catalysts in the reaction, whereby methane is oxidised (see Figure 3.11, b), showed that the high coverage multilayer cluster deposited centres were quite prone to sintering while the mono-dispersed cluster deposited edges did not sinter

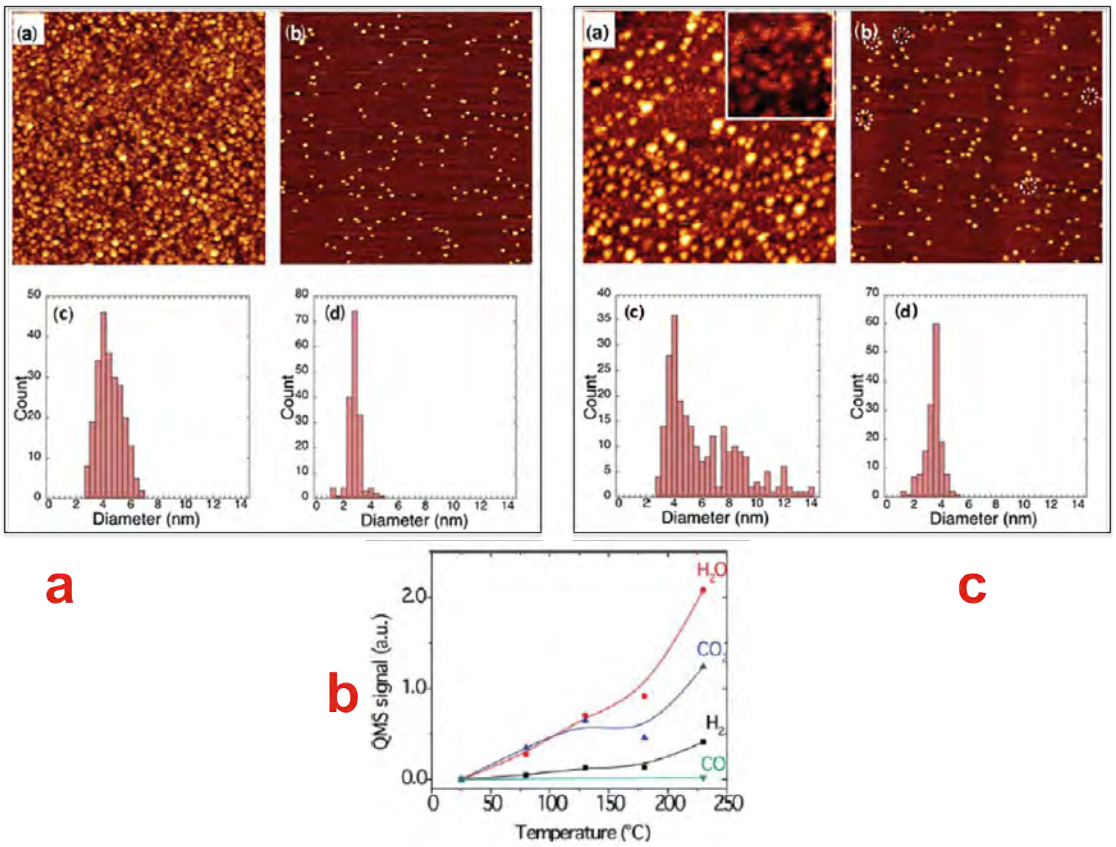

Figure 3.11: (a): Constant current STM images of (as-deposited) Pd_{55} clusters (top left) in high coverage area and (top right) low coverage area (0.2 nA, 0.8 V, 200 × 200 nm^2). Corresponding diameter distributions of as-deposited clusters (bottom left) in high coverage area and (bottom right) low coverage area. ; (b): Evolution of the oxidation products of methane over the Pd_{55} catalysts as a function of temperature. The temperature was increased in steps with a ramp of 5 min and dwell time of 15 min for each step (25, 80, 130, 180 and 230 °C) before ending at 30 °C. ; (c): Constant current STM images of Pd_{55} clusters after reaction (top left) in high coverage area and (top right) low coverage area (0.2 nA, 0.8 V, 200 × 200 nm^2). (top left) the inset (30 × 30 nm^2) depicts pinned clusters between the coalesced particles and (top right) the dashed circles mark pinholes arising after the release of pinned clusters. Corresponding diameter distributions of clusters after reaction (bottom left) in high coverage area and (bottom right) low coverage area (adapted from [160]).

so much, see Figure 3.11 (c). The pinned mono-dispersed clusters did not sinter at any great degree, but when they did, they left their pinning sites, which were subsequently occupied with oxygen and resembled dark holes in the STM images. The degree of sintering is related to the impact energy in respect to the pinning energy of the pinned palladium clusters.

Just as in the previous example, the experiments could be run reliably and the time limiting factor became the shipping time and the catalysis experiments by our collaborators. The availability of the source came down very much to the overall improvements, which allowed for quick deposition times. This was particularly helpful with these samples as the centre had a much higher coverage than the edge.

3.5.3 Size-Selected Clusters as Mass Standards to Obtain Size and Shape of Unknown Particles

Industrial Pd catalysts' (see Figure 3.12, a) shape and size can be determined through the use of STEM and mass standards made out of size-selected clusters [161] (HAADF-STEM performed by David Pearmain and Zhi Wei Wang). Samples with Pd cluster sizes ranging from 454 to 4500 atoms were deposited with Pd_{887} clusters (all at 0.5 keV), as an internal reference for calibration purposes in the HAADF-STEM image analysis, see Figure 3.12 (b). By using the information obtained from the clusters with known sizes and comparing it with the information obtained from the unknown industrial catalysts, their 3D morphology could be evaluated.

The first step was to map out the calibration curve for Pd using the size-selected clusters using their HAADF intensity integrated over clusters as a function of their number (N) of Pd atoms, see Figure 3.13 (a). Comparing the integrated intensities of the industrial Pd catalysts to the calibration curve made by the size-selected clusters, gave a range of sizes between 30 and 1700 atoms, see Figure 3.13 (a). The second step involved relating the diameter of the 2D projection of the industrial catalysts as a function of their number of atoms ($N^{1/3}$). Also comparing the size-selected clusters with the spherical- and hemispherical cluster approximations, revealed that the industrial catalysts had hemispherical shapes while the size-selected clusters had spherical shapes, see Figure 3.13 (b).

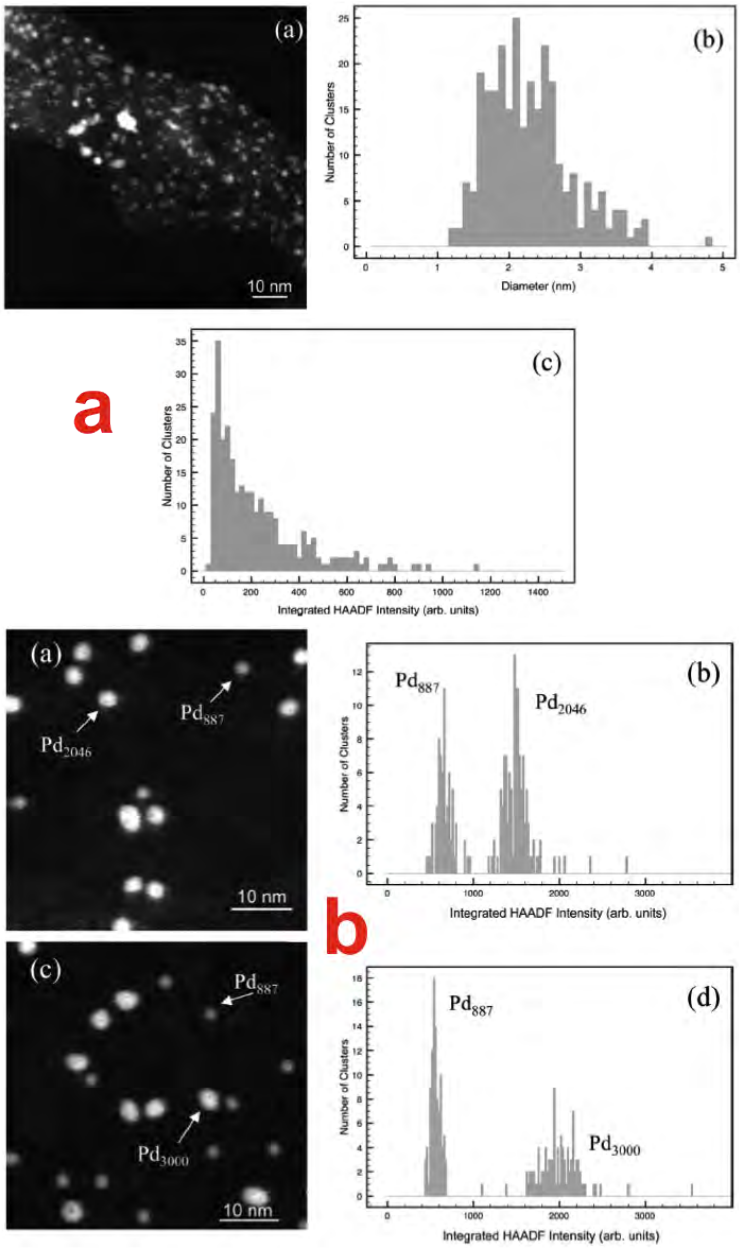

Figure 3.12: (a): (left) HAADF-STEM image of industrial Pd nanocatalysts on carbon blacks and histograms of their (right) diameters and (bottom) HAADF intensity. ; (b): (top left) HAADF-STEM image of mixed sample co-deposited with size-selected Pd_{887} and Pd_{2046} clusters and (top right) histogram of integrated cluster intensity. (bottom left) HAADF-STEM image of mixed sample co-deposited with size-selected Pd_{887} and Pd_{3000} clusters and (bottom right) histogram of integrated cluster intensity. All Pd cluster sizes are calibrated with Pd_{887}. (adapted from [161]).

These experiments benefitted the most from the availability and reliable runs provided by the overall improvements of the source. As many samples had to be deposited it was

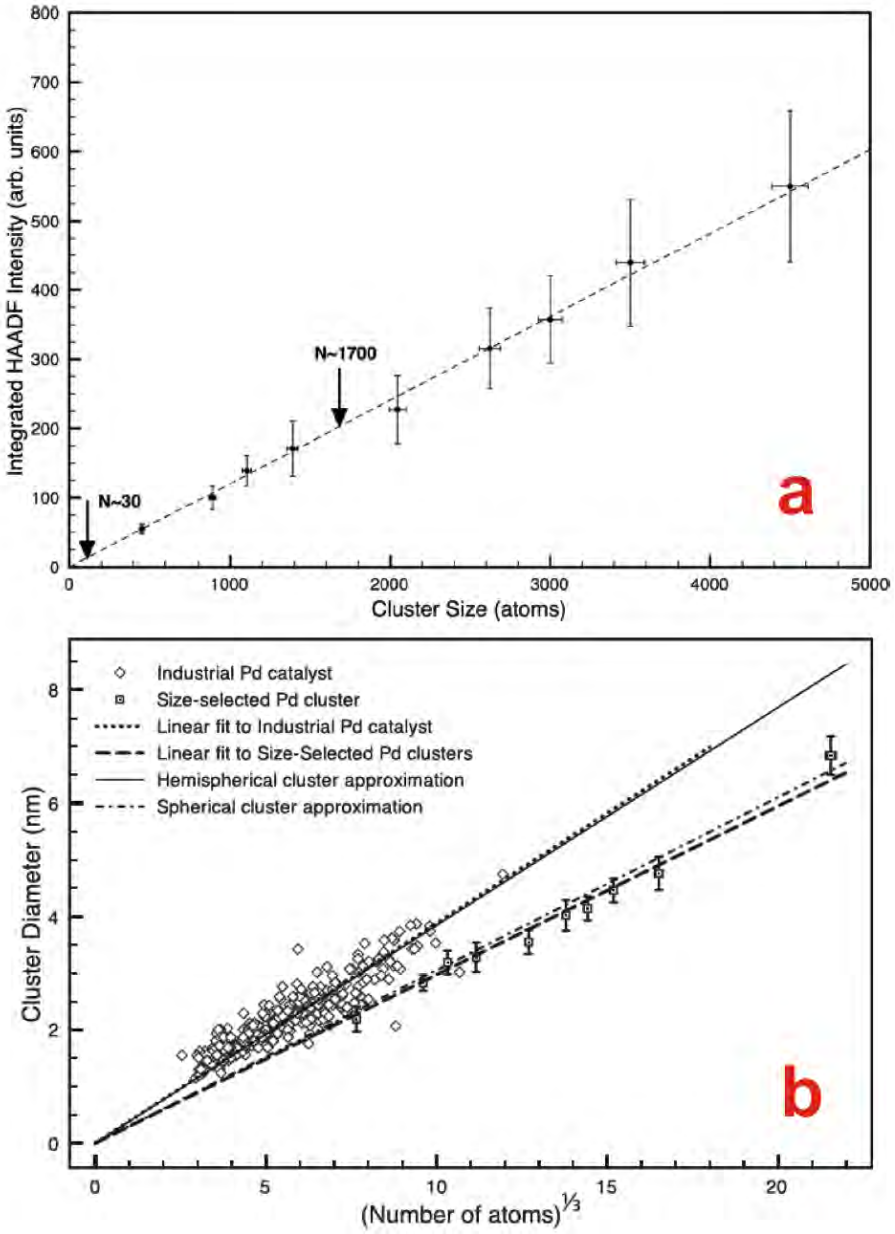

Figure 3.13: (a): The HAADF intensity integrated over clusters vs cluster size (N). Two arrows indicate the corresponding range of the integrated intensities of industrial Pd catalysts along the the line of best fit (30-1700 atoms). ; (b): The size (number of atoms, N) and diameter compared between industrial Pd catalysts (hollow diamonds) and size-selected Pd clusters (dotted squares). The dash-dotted and solid lines correspond to the spherical and hemispherical cluster approximations, respectively. Linear fits to the industrial Pd catalyst and size-selected cluster data are represented by the dotted and dashed lines, respectively (adapted from [161]).

important that the source was working when desired and that samples were made quickly for analysis and feedback for subsequent experiments. Also here, soft landing was of

crucial importance in order to ensure the clusters maintained there spherical shape.

3.6 Summary

The NPRL cluster source had already seen its better days when the work presented in this thesis started. The first tasks related to commissioning of the tape drive and improving the cluster flux began with a, more than ten year old, work horse of a cluster source. The new tape drive, at the time, was thoroughly tested and all issues were successfully ironed out. When depositing the high-area carbon tape samples with enough clusters, higher flux was achieved partly by changing the lateral time of flight mass selector (LTOF-MS) apertures.

The change of LTOF-MS apertures and acquisition of mass spectra shed light on the behaviour of the size-selection filter. The mass resolution $R = m/\Delta m$ is not, as treated previously, the lateral displacement over the exit aperture size ($R = x/\Delta x$). This is only true when the beam is focused at the virtual aperture, otherwise the beam will have a size corresponding to the virtual aperture size. The convolution of the real exit aperture and virtual aperture gives an effective aperture with a certain size ($a_{eff}^2 = b_{rea}^2 + c_{vir}^2$). Hence, the mass resolution is the lateral displacement over the effective aperture size.

The change of the entrance and exit mass filter slits together with the alignment of the nozzle with respect to the first skimmer increased the cluster beam current almost two-fold for relevant cluster sizes (Pd_{55} and Pd_{309}). This in turn decreased the deposition time with ~28 % (from 12.5 h to 9 h) for ~1 m Pd_{55} on graphite tape samples. Also the use of a computer-controlled tape drive (programmed), enabled the deposition of several graphite tape samples for catalysis in real conditions.

Size-selected clusters have successfully been used to internally calibrate the difference in integrated HAADF intensity over size-selected clusters due to changes in the working conditions of the STEM from day to day, which is very crucial in the overall STEM

image intensity analysis. Moreover, it was possible to obtain the morphology and size of industrial catalysts using clusters with known sizes as mass standards and the HAADF-STEM as a quantitative electron probe. The industrial Pd catalyst particles were found to be hemispherical in shape, in contrast with the spherically shaped size-selected Pd clusters. The two step process in finding both the size and shape of the unknown particles, involved mapping the image intensity of the size-selected clusters with their size and compare the image intensity of the unknown particles to the calibration curve to obtain the size. Thereafter, the diameter of the unknown particles' 2D projections were plotted against their, now known, sizes and compared to both the size-selected clusters and the two different models.

HOPG substrates deposited with Pd_{55} and Pd_{309} at an energy of 2 and 3 keV, respectively, with an average coverage of ~35 000 clusters/μm^2 catalysed the oxidation of methane. The clusters in the highly dense and multi-layered centre of the samples showed sintering during the realistic catalytic reaction conditions while the clusters in the edges of the deposition area of the samples were more stable. Pinning sites being left by pinned unstable mono dispersed clusters on the edges are occupied with oxygen, which shows as dark holes in STM images. The relation between the impact energy to the pinning energy of the pinned Pd clusters affect the degree of sintering.

With (147, 309, 923) size-selected (Pd & Au) clusters softly landed onto carbon coated TEM grids, a linear relationship between intensity and cluster size was found through HAADF-STEM imaging. This can be used in contrast investigations of STEM imaging. HAADF intensity depends on the atomic number, Z, with exponent α, which could be related to the inner acceptance angle of the (HAADF) detector by comparing Pd_{923} and Au_{923}. This (Z-contrast) imaging will give the chemical composition of imaged areas, without any additional spectroscopic characterisation, if the global chemical composition of the sample is known.

The future outlook for the cluster source is bright as it is such a versatile tool. The main idea that should be pursued regarding the NPRL cluster source is to replace the magnetron head with a remotely generated plasma source called HiTUS from Plasma Quest Limited. It will rid the system from instabilities and generates a high intensity plasma for efficient and economic sputtering of targets, which get completely and uniformly consumed. A complete computer control of the source would make it even more stable, easier to operate and reuse process parameters for reproducible results.

CHAPTER

FOUR

IN-FLIGHT COATING OF SIZE-SELECTED CLUSTERS

The pursuit of a new technique to coat clusters will be presented in this chapter. The novelty of the technique is that the coating process of the clusters is done while they are "in-flight", which will be explained first. The changes to the cluster source, necessary to enable the technique, are presented thereafter. The experiments performed and the results obtained are covered at the end.

As previously mentioned, making binary clusters by physical methods can give a more precise size control as well as cleaner clusters than chemical methods. Binary clusters can be made from an already mixed source (e.g. alloys), at the deposition site (by annealing) or by in-flight coating. In-flight coating is, just like it sounds, a way to coat elemental clusters/nanoparticles with another elemental material while "in-flight", i.e. in the gas phase, before further study or final deposition onto a support. Despite thorough research, no utilisation of in-flight coating or any similar kind of technique could be found for the generation of binary clusters. However, e.g. Seto et al. report on an interesting way to produce CoPt/SiO_2 core-shell nanoparticles [162]. A multi-component disk target containing

silicon dioxide, platinum and cobalt was laser ablated, i.e. vaporized by a high-energy laser beam into a helium background pressure (1000 Pa) to form mixed nanoparticles. While in the gas-phase the mixed nanoparticles were transported and annealed (1273 K) in an aerosol post annealing chamber. The mixed nanoparticles restructured during the annealing process so that the SiO_2 separated to the surface to form a shell structure around a core of CoPt. TEM study revealed the alloy CoPt cores with diameters between 1-18 nm were covered with SiO_2 shells with thicknesses of 1-2 nm.

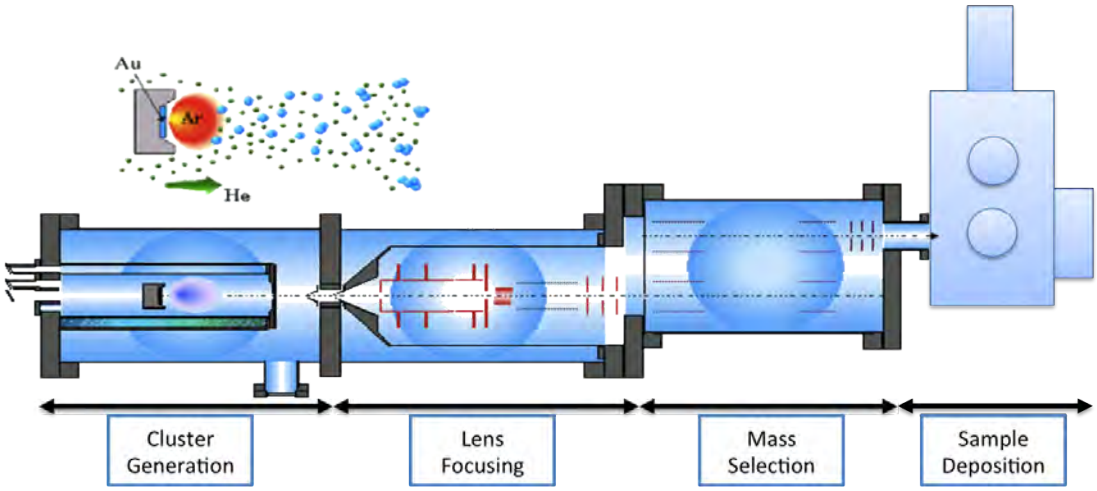

Figure 4.1: Diagram showing the position of the different chambers of the cluster source.

Even though this last example produces core-shell clusters while "in-flight" it is not in the same logical way described earlier. Therefore, to the best of the author's knowledge no one has previously pursued such or similar production methods. Different techniques for in-flight coating can be pursued, e.g., co-deposition through thermal evaporation or thermal evaporation with sputtering or similar methods. The technique opted for allowed for the utilisation of the cluster source with all of the benefits that came along with it, such as high flux and good size control. That meant that all the changes and additions, in order to enable in-flight coating functionality, had to be done after the mass selection chamber in the cluster beam source system (Figure 4.1).

The approach to in-flight coating was to evaporate materials (metals) onto thin layers of

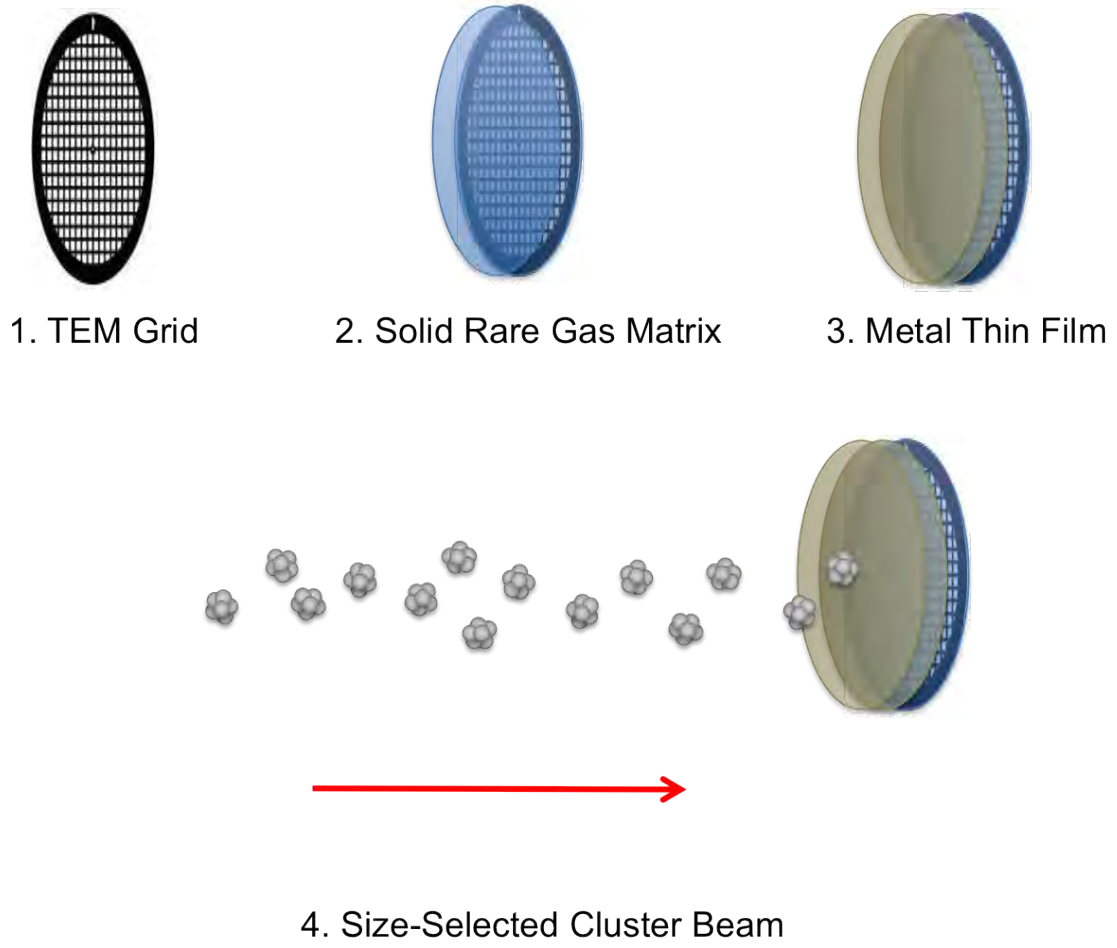

Figure 4.2: Diagram showing the in-flight coating process. (1) A TEM grid is cooled with liquid helium (~19 K) so that (2) rare gas (Ar) atoms condense on it and form a solid matrix. (3) Metal (Au) is evaporated onto the solid rare gas (Ar) matrix and forms a thin film, which is then (4) exposed to the size-selected (Pd) cluster beam.

rare gas films condensed on TEM grids and penetrate it with the cluster beam. The size-selected clusters would pick up material from the loaded TEM grid and then deposit onto TEM grid samples behind, see Figures 4.2 and 4.3. The thickness of the deposited metal films would affect the final thickness of the binary clusters and act as a parameter of control. The carbon coated TEM grids were then characterised by HAADF-STEM and the built-in electron energy loss spectrometer (EELS). Results from each sample batch characterisation session were fed back in to the in-flight coating process in order to optimise all the relevant parameters and approach the desired results.

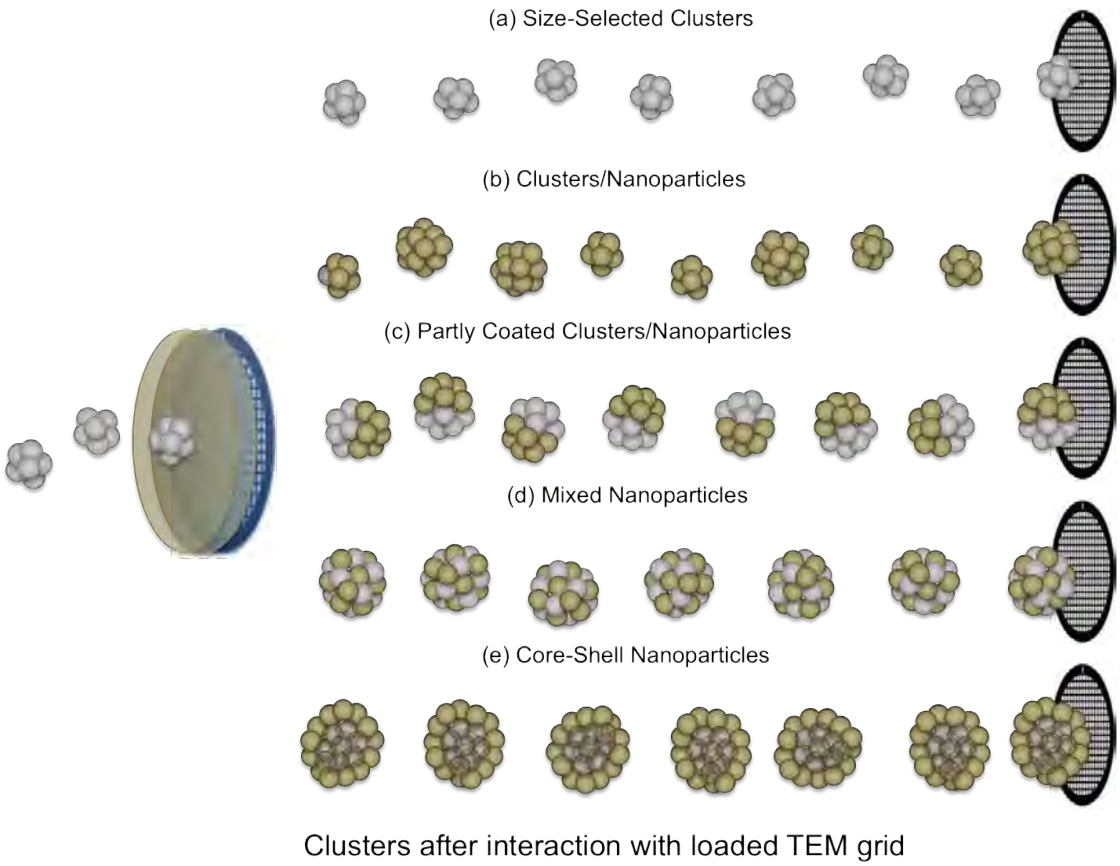

Figure 4.3: Diagram showing the potential results after the in-flight coating process. In the in-flight coating process, clusters interact with the metal loaded matrix and can either (a) penetrate without being coated, (b) transfer their energy and knock off (Au) metal nanoparticles, (c) become partly coated, (d) mix with (Au) metal or (e) form core-shell nanoparticles.

For the in-flight coating process, several significant changes had to be made to the system (Figure 4.1). In order to have a versatile system we opted to cool our setup with liquid helium in order to reach low enough temperatures to condense small(er) (rare) gases nitrogen and neon. The heavier (rare) gases have a much higher condensation temperature and liquid nitrogen is sufficient to condense them. A liquid helium cryostat was fitted to the cluster source deposition chamber and cooled via a siphoning transfer arm and self rigged pumping system from a liquid helium dewar. The tape drive was used as sample holder for the TEM grids and was situated behind the cryostat, which held the metal coated TEM grid to be penetrated by the cluster beam. At right angle to the cluster beam axis, an evaporator was mounted for metal evaporation as shown in Figure 4.4.

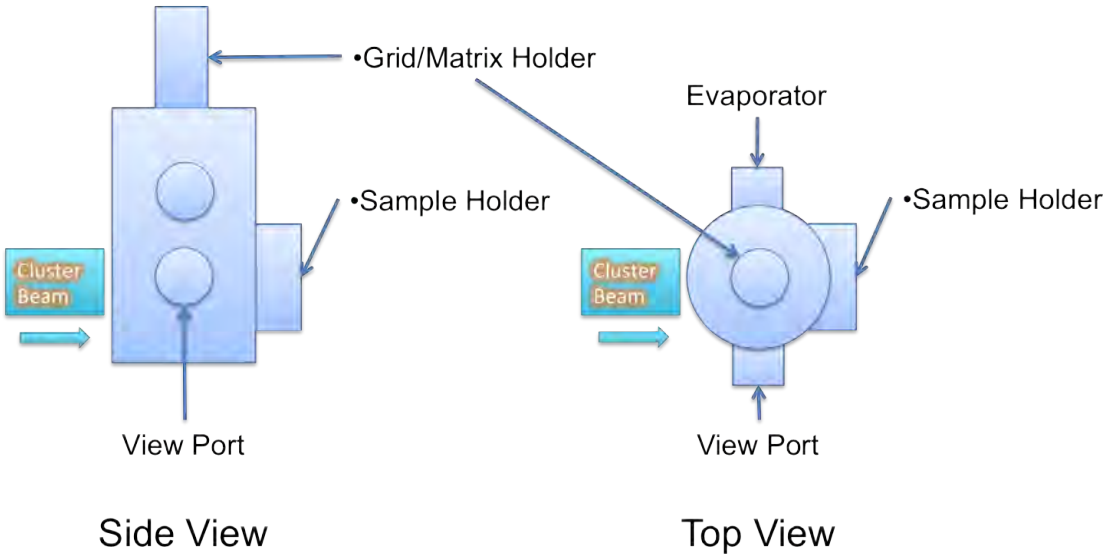

Figure 4.4: Diagram showing the position of the additional parts for the setup of the in-flight coating at the deposition chamber of the cluster source.

4.1 Setup

The in-flight coating setup consists of additional parts assembled to the cluster beam source, more precisely the deposition chamber, in order to allow for the in-flight coating functionality. First thing that strikes you when looking at the deposition chamber from the start of the cluster source (flight direction of the cluster beam) is the liquid helium siphoning transfer arm connected to the cryostat attached to the XYZ-translator arm. The side viewport has not been changed and gives crucial inspection possibilities when running the system pre-, during and post in-flight coating experiments, see Figure 4.4. At the back port of the deposition chamber, the tape drive has been assembled with some minor adjustments in order to act as a sample holder with in-situ multi-sample deposition capability.

At the other side of the deposition chamber, opposite of the view port, a bespoke metal evaporator has been attached and is also where the rare gas cylinder is connected to the chamber via a two valve system, for a semi controlled input of the gas. The extended support plate on the same side, which is connected to the frame of the system, was holding

the electronic equipment used to monitor the cryostat temperature and the metal evaporator current source. At the back of the system, on the frame below the tape drive cup, a flow meter control panel for the liquid helium flow was mounted. An additional helium gas cylinder was fitted to the frame and used to pressurise the liquid helium dewar, placed next to the system, in order to get the flow going quicker to the cryostat and hence cool it quicker. A diaphragm pump was placed next to the system to turbo boost the flow further and decrease the time for the cryostat to reach its lowest possible temperature (with that setup), considerably.

4.1.1 Maintenance & Optimisation

Before commencing with the assembly of the new pieces for the in-flight coating, the cluster source itself was thoroughly maintained and optimised. Everything from the magnetron gun to the deposition chamber was serviced in order to have the system in the best condition prior to the in-flight coating experiments. Most of the roughing (rotary) pumps were serviced and their oil change was due just before the experiments. All the roughing lines (metal hoses) connecting the rotary pumps to the turbo-molecular pumps and the system were cleaned. The magnetron gun was disassembled, serviced and cleaned as well as the inner condensation chamber and the outer generation chamber was also thoroughly cleaned. As everything was reassembled, the realignment of all crucial bits was done with great care in order to get the best possible optimisation of the cluster beam current. In the process, the nozzle/iris fixture was upgraded to aid in the tedious, but crucial realignment and fixing of the nozzle after cleaning sessions and other disassembles, see Figure 4.5.

First and second skimmers leading to the ion-optics chamber, in the direction of the cluster beam, have been cleaned and the connections inspected and redone. The ion-optics chamber was also given quite some attention, all the elements of the ion-optics were inspected, serviced and realigned. The chamber itself was cleaned as well as extra-exposed

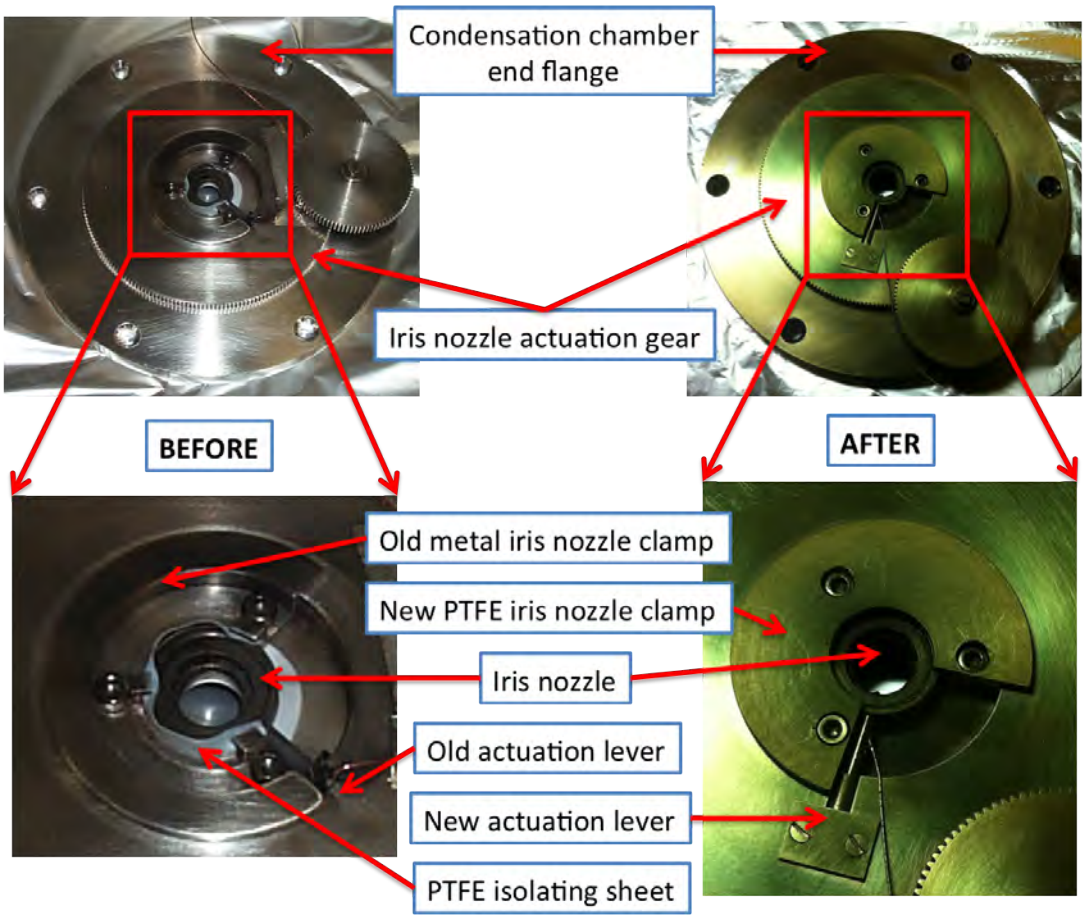

Figure 4.5: The new PTFE nozzle fixture is helpful when realigning the iris after cleaning and keeping it fixed in place together with the actuation gear surrounding it, which enables it to open and close via its lever.

parts within the chamber and certain connections were also rewired. The TOF chamber was checked some while before and deemed to be in quite good shape and only an outside inspection as well as a test was carried out to reassure it was still performing at its best prior to the in-flight coating experiments. Most attention was given to the deposition chamber, as it would host all new parts necessary for the in-flight coating. All parts were removed, in order to assemble the new parts, additionally the chamber itself was cleaned thoroughly and baked, see Figure 4.6.

The pressure gauges were also inspected and some were refurbished and others replaced. All the controllers were checked and the RF power supply to the magnetron was func-

Figure 4.6: The deposition chamber covered with heat tapes and aluminium foil during baking.

tioning intermittently and was therefore replaced from time to time with the reinstated DC power supply. After all initial background work, started with the in-flight coating parts.

4.1.2 Cooling

Liquid nitrogen cooling is used routinely when running the cluster source in order to get the sputtered atoms to condense and form clusters. To get more flexibility with the in-flight coating system we opted to use liquid helium for our cryostat, therefore more specific equipment was necessary for handling this coolant.

The basis of the cooling system is of course the source from where the coolant flows and if not from a tap, usually a dewar is used. The dewar used was a standard liquid helium compatible dewar with specific fittings for the refurbished transfer arm and pressure gauge, see Figure 4.7. The liquid helium is then transferred to the cryostat through a transfer arm, which has a sleeve-tip design in order to shield the liquid helium flowing in the inner tip channel from thermal radiation.

As can be seen in Figure 4.8, the end of the transfer arm that goes into the dewar, has been fitted with a brass end with a slot hole in the side, in order to protect the inner tip channel

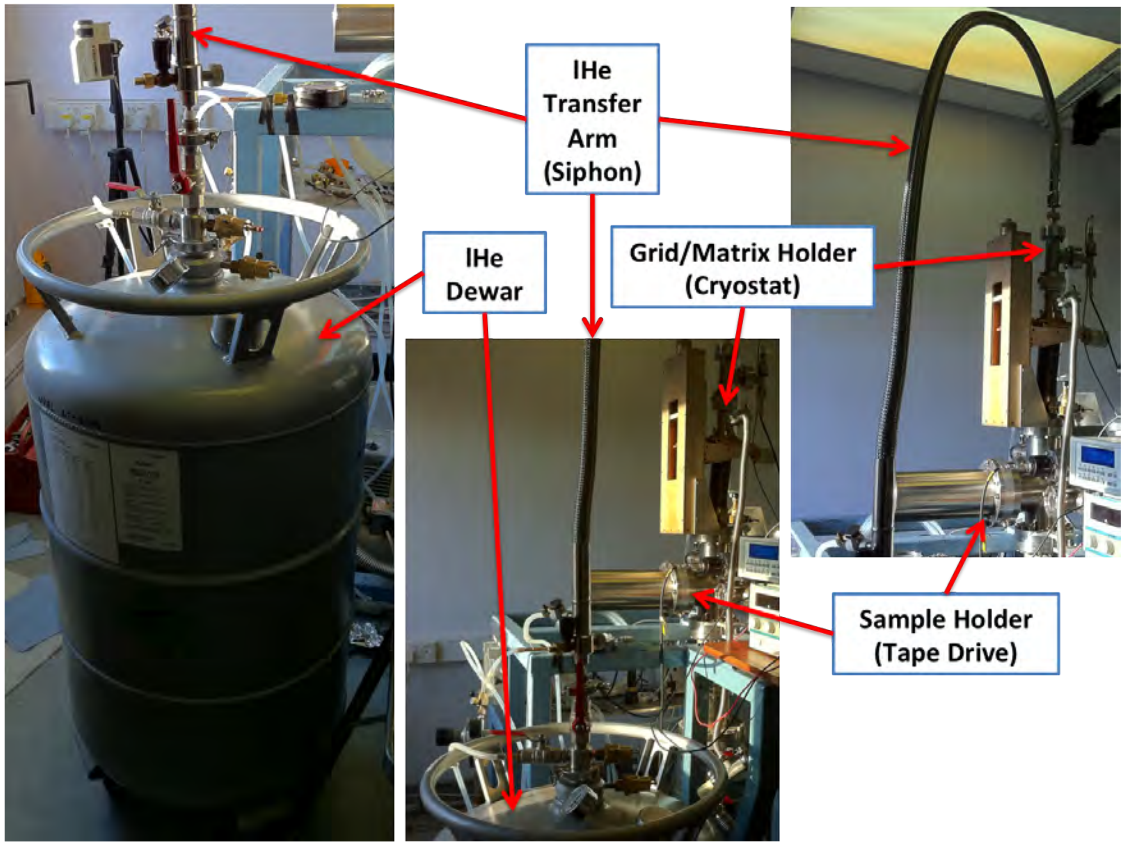

Figure 4.7: The liquid helium dewar and transfer arm used in the in-flight coating experiments.

when hitting the bottom of the dewar or when moving the transfer arm about. Similarly, the other end of the transfer arm, which goes into the cryostat (see Figure 4.10), is fitted with a protective copper pipe. The copper pipe extends the arm so that it reaches the end of the cryostat, as well as making sure that the inner tip channel does not get damaged. The end of the copper pipe has groves in order to allow for the free flow of liquid helium between the inner tip channel and the outer concentric sleeve (radiation shield). Specific fittings were made to fasten the transfer arm to both dewar and cryostat as one can see in Figure 4.8.

As mentioned earlier, a helium gas cylinder was connected to the dewar in order to pressurise it and get the liquid helium flowing and thus decrease the cooling time. The flow of the liquid helium in the system is monitored via flow meters, one for the tip channel

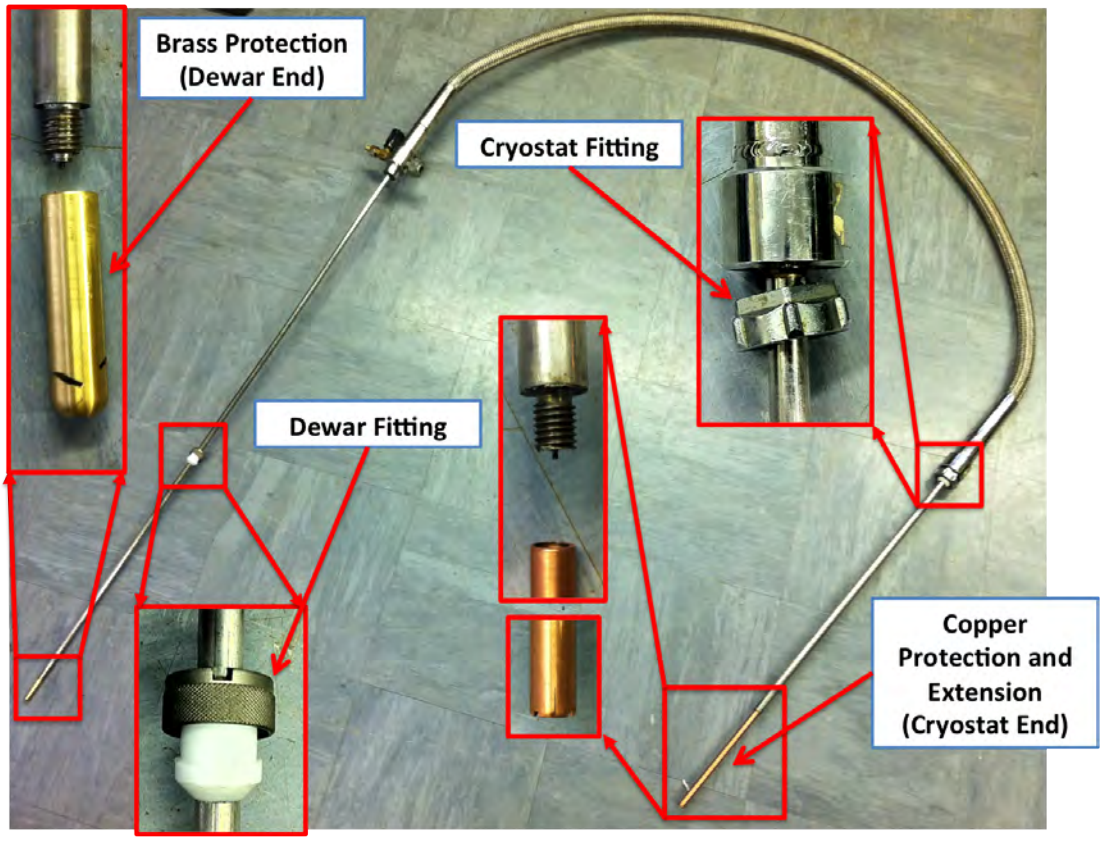

Figure 4.8: The refurbished transfer arm used in the in-flight coating experiments.

flow and the other for the concentric sleeve flow, see Figure 4.9. When pressurising the dewar with helium gas from the cylinder at around ~0.5 bar, the cooling process started very slowly with the liquid helium flowing through the transfer arm, first filling the concentric sleeve (initially any liquid helium in the inner tip channel boils of as it is to warm and the concentric sleeve is not filled to shield from thermal radiation) and thereafter the inner tip channel. This can be seen as the float of the concentric sleeve flow metre starts to oscillate frenetically and rise after ~10 min, as the liquid helium slowly flows through the concentric sleeve, initially getting boiled off until the temperature is low enough for it to flow through as a liquid. After a couple of minutes, the float of the flow metre, indicating the flow of the inner tip channel, starts to oscillate frenetically and rise, as the liquid helium starts to flow inside the tube. After yet another ~10 min the whole process starts again, but backwards. Now, the inner tip channel flow metre float starts to oscillate

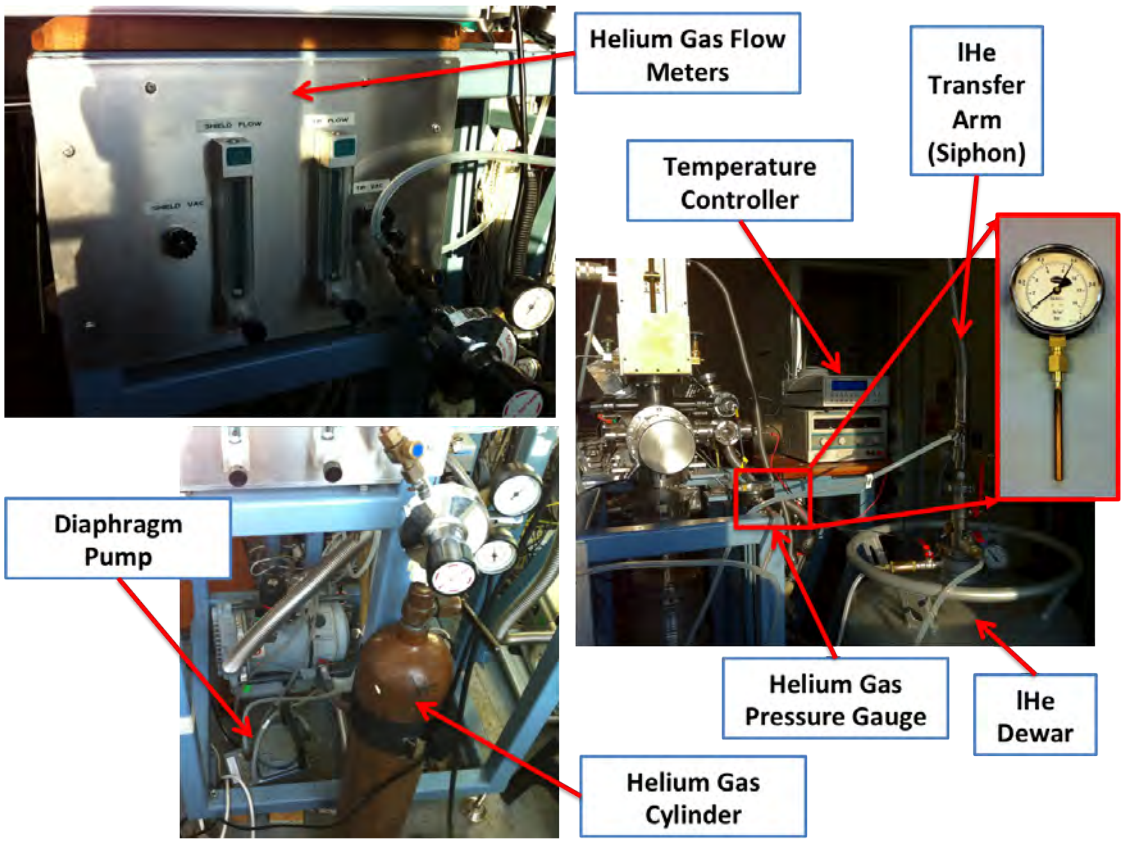

Figure 4.9: The flow metre board, helium gas cylinder and diaphragm pump used in the cooling process of the in-flight coating experiments.

and sink, followed by the outer concentric sleeve flow metre float. After another ~10 min the cycle starts again and for each cycle the temperature of the TEM-grid holder, at the end of the cryostat, decreases a bit. The cycle goes on (let it run for more than 2 hours) until a plateau is reached in regards to the temperature, however this is still far away from the desired target temperature. The flow of the liquid helium is too slow in the system to be able to achieve lower temperatures, as the dewar pressure is too low and the ambient temperature is too high. Increasing the dewar pressure, by supplying helium gas from the cylinder into the dewar, is one solution, but the dewar used has a safety valve, which vents when the pressure exceeds 0.5 bar.

The only solution to this problem is to lower the pressure at the other end, which was achieved with a diaphragm pump (see Figure 4.9) in order to get the liquid helium to

quickly flow through the system and obtain the target temperature of the cryostat. In routine operation, the desired target temperature of the TEM-grid holder is reached after ~20–30 min with the aid of the diaphragm pump. All boiled off liquid helium is directed to the general gas exhaust for safety reasons as the system is not closed. Of course, it is not possible to reach the ideal temperature of liquid helium as there are losses in the overall process, but for our purposes of solidifying (rare) gases as light as neon and nitrogen, the achieved low temperatures are more than enough. The temperature is obtained with a thermal sensor in the TEM-grid holder attached to the cryostat, and fed through special wires into a low-temperature electronic reader.

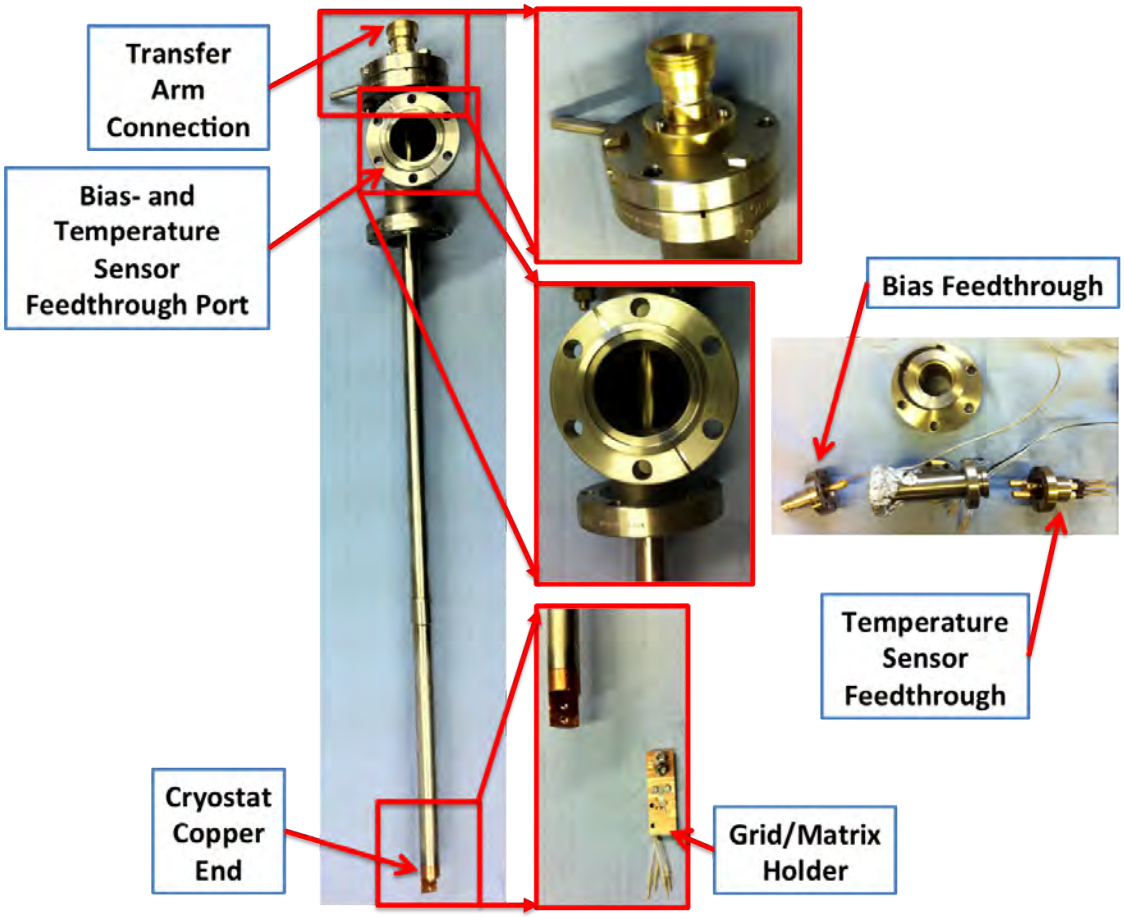

Figure 4.10: The refurbished cryostat used in the in-flight coating experiments.

4.1.3 TEM-grid & Sample Holder

The TEM-grid holder is a small block of copper with a circular hole through it, see Figure 4.11. A blank Cu TEM-grid is positioned over the hole and gently clamped into place. The fixtures to fasten the block to the cryostat as well as the connection point of the bias wire is located at one of the ends. A sapphire piece, sandwiched between the grid/matrix copper block and the cryostat (at the connection point), isolates them both electrically while coupling them thermally. The thermal sensor is a (small cylindrically shaped) Rh-Fe thermometer, which is fitted inside a hole, reaching the vicinity of the TEM-grid and glued in position. There are four Kapton covered manganin wires (thermally insulating and electrically conducting) connected to the rhodium-iron thermal sensor in one end and connected to a Lakeshore low-temperature electronic reader in the other. Another wire is connected to the TEM-grid holder copper block in one end and a voltage power source in the other. The wires are gently wrapped around the cryostat inside the deposition chamber, in order to allow for free movement and rotation of the assembly, and connected to a feedthrough for further connection.

The sample holder of the in-flight coating experiments is placed after the TEM-grid holder and in order to deposit as many samples as possible, while the system is in vacuum, a multi-sample holder is necessary. The deposition chamber of the cluster source normally uses a multi-sample holder for sample deposition, which is located at the same position of the cryostat and TEM-grid holder for the in-flight coating experiments. The tape drive sample holder (Figure 4.12) has been attached at the back flange of the deposition chamber for previous experiments and used to deposit clusters on long graphite tape samples. The position of the tape drive is ideal in relation to the cryostat and TEM-grid holder with regards to the in-flight coating experiments, so the tape drive was modified to handle several samples while the system is in vacuum. The modified tape drive was loaded with up to ~5–6 samples to be deposited sequentially, after each other, under vacuum, during

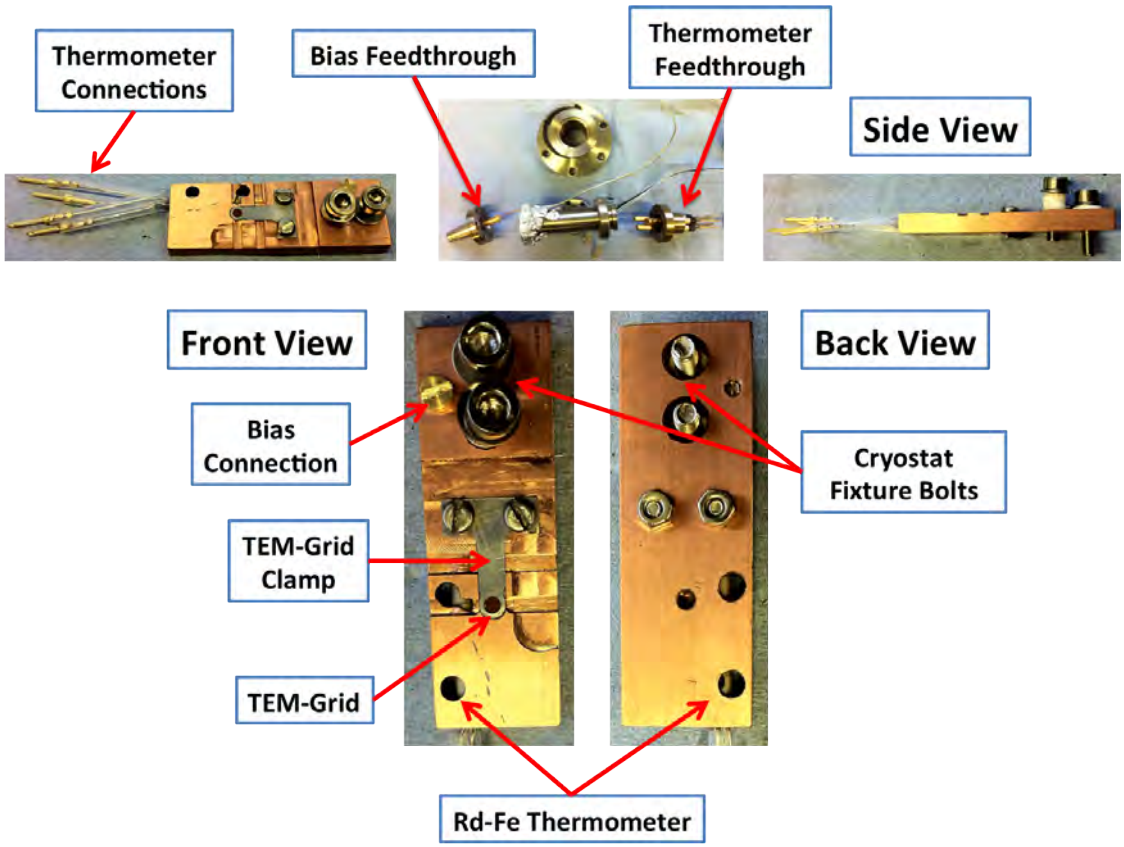

Figure 4.11: The TEM-grid holder used in the in-flight coating experiments.

in-flight coating experiments. The samples are carbon coated copper TEM-grids which are placed within (sandwiched between) two small metal rectangles (10×5 mm) with circular aperture at the centre. One of the metal rectangles have a grove where the TEM grid can be placed without moving around and the other metal plate is placed on top so that the TEM grid does not fall out when e.g. the whole assembly is rotated and/or placed on the side. The metal plates are fixed to each other with small strips of conducting "silver" metal tape on the short sides and fastened to the tape drive.

The tape used in the tape drive had to be strong, reliable and conducting, which somewhat ruled out the graphite tape used for earlier experiments. Instead, conducting "silver" metal tape was cut into a long (~100 cm) strip having a width of 1 cm, which was then folded so that the adhesive side stuck to itself and the metal side faced outwards, resulting in a new width of the tape of 5 mm. This bespoke "tape" fit perfectly to the tape drive and had

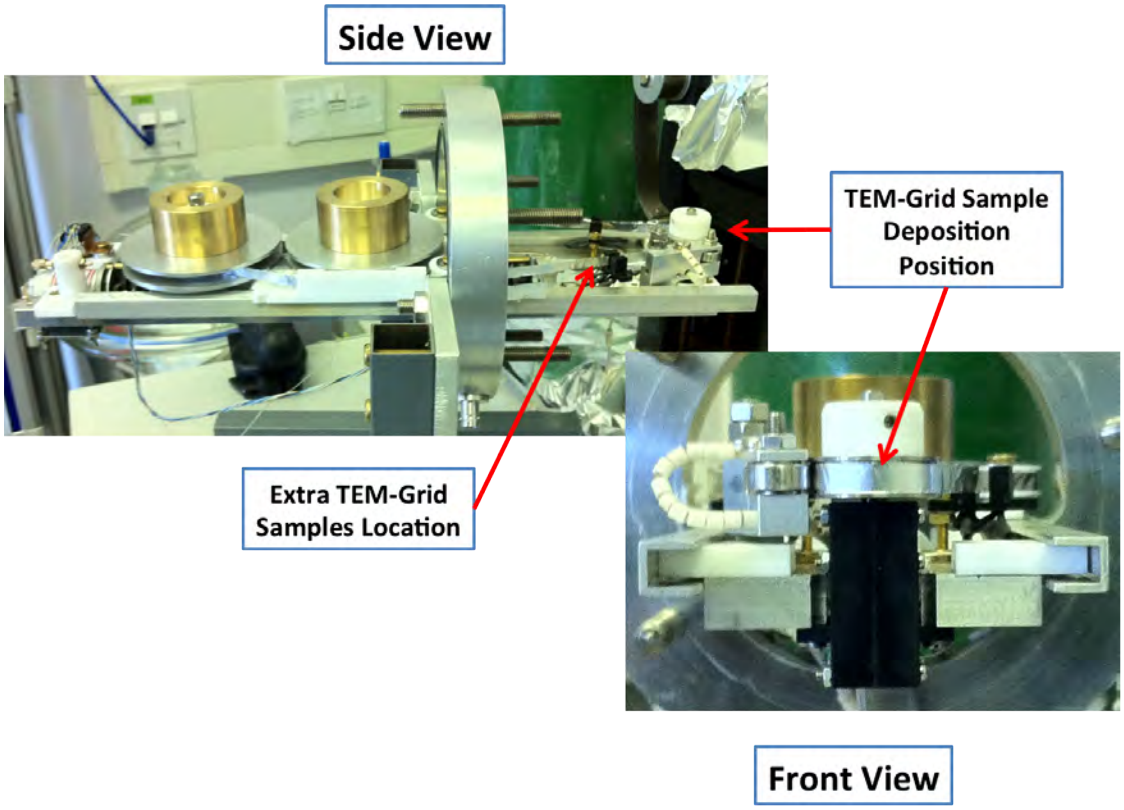

Figure 4.12: The sample holder used in the in-flight coating experiments.

all the sought after properties for the in-flight coating experiments. The TEM grid metal rectangle sample assembly was fastened to the tape by conducting double sided carbon tape, ensuring the TEM grid was biased through the connection on the tape drive. For our purposes, we fitted ~5–6 samples each run of the experiment, but more samples can be loaded onto the sturdy conducting tape if required. As the tape drive can only move in one direction, the samples are loaded after each other. One sample was placed just before the actual deposition area at the centre, in order to test the beam current before the actual experiment. The subsequent samples were closely packed behind while allowing enough room to test the beam current before each actual deposition.

4.1.4 Evaporation

Our metal thin film deposition is made through a bespoke thermal evaporator using a filament heater, see Figure 4.13. The filaments are from small light bulbs where the glass has been cut out and the filaments fitted to a two copper rod evaporator feedthrough. The setup is then covered by a bespoke cylindrical metal housing with an orifice at the front for directed evaporation and an orifice at the side, at the position of the filament, in order to measure the filament temperature with a pyrometer when evaporating metals. The feedthrough is connected to a 4-way (cross) piece, where the opposite side connects to the cluster source deposition chamber. The side next to the filament orifice, of the cross piece, is fitted with a viewport, while the other side is blanked, but could be used for gauging the pressure or improve the vacuum by additional pumping. The viewport is covered with two semicircular glass pieces for protection and ease of cleaning away the deposited metal thin film, which would prevent the accurate temperature reading of the evaporator with the pyrometer.

Gold, palladium and copper rods/wires were pressed into delicate thin tapes, which were gently rolled onto evaporator filaments for deposition. When resistively heating the filaments, the rolled thin metal tapes, on the filaments, melt and wet the filaments, concentrating inside the middle of them. Most filaments break after one deposition run, making it necessary to change filament and roll another thin metal tape onto them. In some cases the filament can break instantaneously or last for several deposition runs, i.e. if enough metal remains to be deposited. The filament evaporator was connected to a DC-regulated power supply (Velleman PS3010), which was run as a current source when using it in constant current (C.C.) mode. A current as high as 10 A can be generated with this power supply, which is more than required, when using the evaporator. E.g. when evaporating gold, the current was increased until the temperature, read with the pyrometer, reached ~900 °C and the Au thin tape, rolled onto the filament, melted and wetted it, residing at

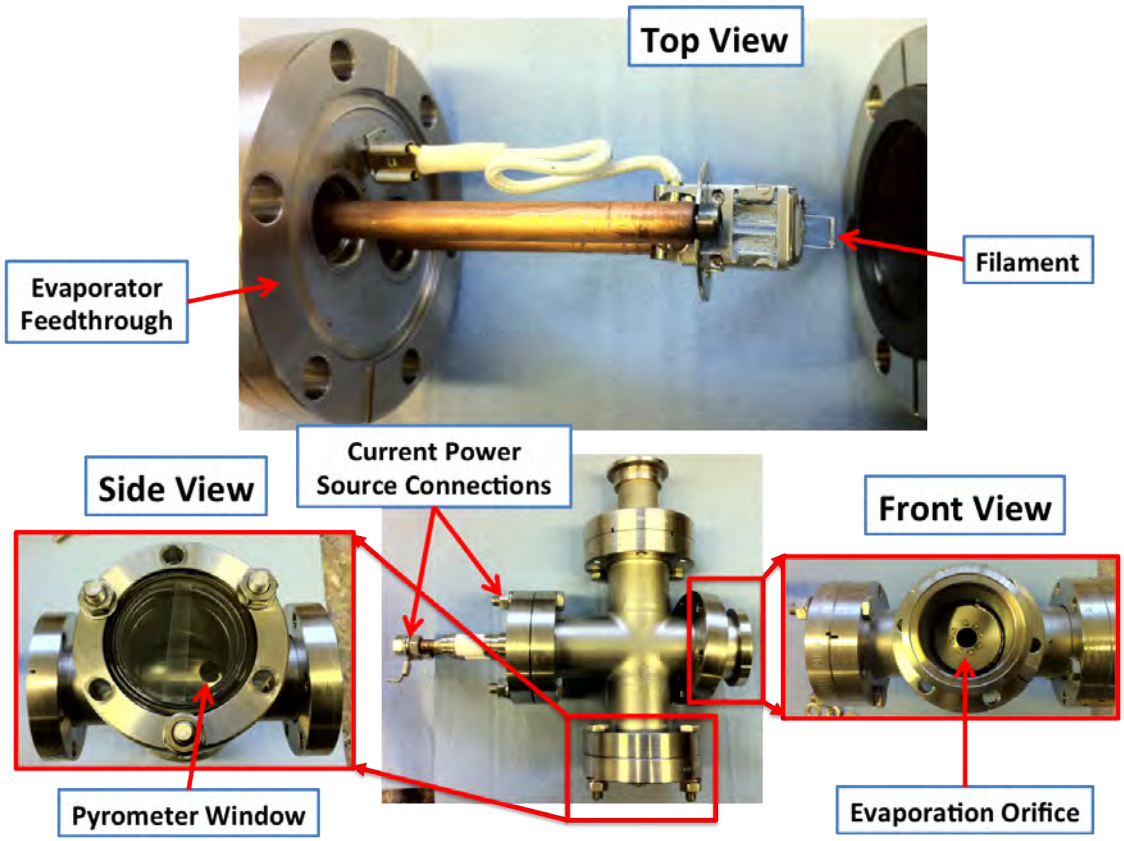

Figure 4.13: The evaporator used in the in-flight coating experiments.

the centre of it. Start of the deposition time is taken at this point, while slowly increasing the current, avoiding the filament to break, until the temperature reaches ~1500 °C, which takes roughly 1 min. The deposition is continued for another minute at the evaporation temperature, totalling the deposition time to ~2 minutes. Rotating the TEM grid/matrix holder (cryostat) 90° acts like a shutter during start and stop of evaporation.

4.2 Experiments

The in-flight coating experiments were done in a trial and error fashion (proof-of-principle demonstration) with a number of samples at each run/batch to quickly investigate and adjust experiments in order to map out the different parameters related to the desired end results. However, the first runs with the in-flight coating enabled system, was to test that

the system worked as expected. The first test was to ensure that the argon beam (current) can be registered by the tape drive without the TEM grid matrix holder in the line-of-sight and the whole system at room temperature. The second step was to introduce the TEM grid matrix holder in the line-of-sight of the argon beam and, momentarily, register the dip in the current measured at the tape drive sample position as, initially, the matrix holder blocked the beam while moving towards its final position. The argon beam current was also measured at the TEM grid matrix holder, in order to ensure the tuning of the beam without interfering with the sample deposition at the tape drive sample position.

The same trials were done by cooling the cluster source with liquid nitrogen and testing the cluster beam of small copper clusters. These trials were also redone while the TEM grid matrix holder was cooled down with liquid helium. The evaporator was also tested by depositing a thin film of Au on a TEM grid sample at the back of the TEM grid matrix holder at room temperature and also after cooling the cryostat with liquid helium. The TEM grid matrix holder connected to the cryostat was translated and rotated (xyz-translator at the deposition chamber) in order to ensure proper operation at both room temperature and when system cooled to operation temperature. Finally, trials with argon gas introduction into the deposition chamber were performed both before and after cooling of the cryostat and TEM grid matrix holder followed with Au evaporation and at last cluster beam penetration before and after Au thin film deposition onto the thin Ar film on the cold TEM grid.

In the experiments performed, the Au thin film thickness, the cluster sizes and their deposition energies were varied, while the Ar gas matrix thickness was kept roughly the same.

4.2.1 Evaporation Calibration

A Foil of Au corresponding to a weight of 13.7 mg was used to evaporate a thin film of Au onto a TEM grid masked sample of glass attached to the TEM grid sample holder. The Au evaporation was performed in similar conditions as in experiments, i.e. the same position (distance from evaporator), the same temperature (liquid helium cooling), the same timeframe (evaporation time of seconds), etc., with an evaporation time of 2 seconds. The glass sample was then analysed, by measuring the thickness of the deposited thin Au film. This was done by using a profiler to make scans of masked and unmasked areas of the Au thin film to measure the thickness of the deposited Au.

Different areas of the deposited Au thin film were chosen at random for the thickness measurements with the profiler. The profiler was run a couple of times (i.e. 2-5 times) at each position in order to get a more accurate value of the thickness in that particular position. The average of the heights obtained is 5.35 nm and if assuming a linear growth of the thickness of the thin film as the metal is evaporated with time, it is possible to deduce the thickness of other Au thin films depending on the evaporation time (with all other variables kept the same). The standard error in the mean value 5.35 nm of the profiler measurements is 0.39 nm (according to equation 4.4 [27]), which bounds the real value of the Au thin film thickness between 4.96–5.74 nm.

$$\bar{x} = \frac{\sum_{i=1}^{i=n} x_i}{n}, \tag{4.1}$$

$$d_i = x_i - \bar{x}, \tag{4.2}$$

$$s = \sqrt{\frac{\sum_{i=1}^{i=n} d_i^2}{n-1}} = \sqrt{\frac{\sum_{i=1}^{i=n} (x_i - \bar{x})^2}{n-1}}, \tag{4.3}$$

$$u = \frac{s}{\sqrt{n}} = \sqrt{\frac{\sum_{i=1}^{i=n} (x_i - \bar{x})^2}{n(n-1)}}, \tag{4.4}$$

Some of the assumptions made for the validity of the linear nature between film thickness and deposition time are that the evaporation is uniform, the sample temperature constant and the filament degradation is negligible over short times. Additionally, evaporation conditions were quite reproducible in the different experiments. Taking the errors into account, an interval of possible values of the Au thin film thicknesses is obtained for different times of evaporation (e.g. for value 5.35±0.39 nm after 2 s evaporation time, interval values are between 4.96–5.74 nm).

4.2.2 In-Flight Coating with Small Sized Clusters

For the actual experiments Pd (Z = 46) was used instead of Cu (Z = 29), mainly due to improved cluster source versatility and tuning ability for larger cluster sizes as well as enhanced intensity making clusters more defined, but still lower than Au (Z = 79) for easy identification in HAADF-STEM. Clusters of 55 atoms were mainly produced as smaller sizes would be more difficult to detect with HAADF-STEM and much more so with EELS. However, for consistency, a sample with Pd_4 was deposited as well.

Initially, the cluster source was operated to tune and optimise the Pd_4 and Pd_{55} beam currents on the matrix holder and then on the tape drive, with and without the matrix holder at the line-of-sight. Directly afterwards the cryostat was cooled with liquid helium so that the TEM grid matrix holder, attached to the cryostat, reached ~19 K (within ~10-20 min). When the operating temperature of the TEM grid matrix holder was reached, Ar gas was introduced to the deposition chamber (exposure of ~200 L) for the formation of thin solid Ar matrix on the TEM grid (covering the holes as much as possible). 200 L (Langmuir) of argon equals roughly 200 monolayers of argon on top of the grid resulting

in a thickness of ~40 nm. Assuming coverage on both sides of the grid and growing in towards the square holes (27 μm), the thickness would be around 80 nm around the edges and gradually thinner reaching in towards the centre of the TEM grid square holes. At best, the holes would be completely covered and at worst ~40-80 nm from the edges to the centres would be covered (~1 %), assuming the film would grow at least evenly thick going from one side of the grid and around the edge to the other side. Corners would cover more as two edges would support each other in growing the film. There is a tradeoff between increasing the thickness of the Ar film, thus ensuring higher coverage of the grid holes, and making sure that the clusters would be able to penetrate it. The first sample consists of Pd_{55} clusters deposited through the thin solid Ar matrix and onto a carbon coated TEM grid sample at an energy of 1.5 keV (1.5 kV bias on thin film/solid matrix/grid and sample) with a current of 2 pA for 20 min.

Before the deposition of the rest of the samples in the batch, another argon exposure of ~230 L was added before evaporating Au by slowly increasing the current of the filament onto which the thin Au wire was wrapped around until the temperature reached ~900 °C. At this temperature, the thin Au wire shrank and melted, whereby the evaporation time commenced and ended after 5 s. After the thin film deposition, another deposition where Pd_{55} clusters were allowed to penetrate through the thin film on the Ar solid matrix on the TEM grid and deposited onto a carbon coated TEM grid. The clusters were deposited for 15 min with a current of 2 pA at an energy of 1 keV. The next sample in this batch was Pd_4 clusters with a beam current of 20 pA impacted on the film setup and deposited onto a carbon coated TEM grid with an energy of 1 keV for 5 min. The final sample in the batch was Pd_{55} clusters impacted on the film setup and deposited with an energy of 1.5 keV. The deposition lasted for 15 min with a 2 pA beam current. As an indirect evidence of the interaction of the cluster beam with the thin film on the solid matrix on the TEM grid, the resulting particle/cluster beam was measured directly after the last sample deposited on the tape drive without the matrix holder in the line-of-sight. The Pd_{55} cluster (particle)

beam at an energy of 1.5 keV was measured to be 2 pA at the tape drive after interacting with the thin film and solid matrix and 0 pA when the matrix holder (Cu block) blocked the beam current from reaching the tape drive. The beam current was measured to be 20 pA at the tape drive after translating the matrix holder away from the line-of-sight of the cluster beam. This clear indication of a 90 % decrease of the cluster beam current with and without the coating assembly is indirectly a proof of the interaction of the clusters and tentatively a proof of their material pickup/coating or knock-off of particles as well.

4.2.3 In-Flight Coating with Medium Sized Clusters

The second in-flight coating experiments were done with medium sized palladium clusters. Clusters having sizes of 147, 309 and 561 Pd atoms were impacted on the thin film setup in batch number two. In the same manner as the first batch was made, firstly, the liquid helium cooling was initiated in order to cool the TEM grid holder so that the Ar gas (<~400 L) would solidify, when introduced to the deposition chamber, building up a thin film (<~80 nm), acting as a support for evaporated Au to form a thin film when deposited. Au was evaporated for 3 s, i.e. 2 s less than the evaporation for the first batch, which was done over 5 s. This was to decrease the thin film thickness, which preliminary results from the first batch suggested was too thick and might thus have decreased the number of clusters penetrating it.

The first sample made in the second batch was Pd_{147} clusters impacted on the thin film setup and deposited on a carbon coated TEM grid at an energy of 1 keV. The cluster beam current for Pd_{147} was 10 pA and the sample was deposited for 5 min. The cluster beam current for Pd_{309}, which was the second sample, was 9 pA and was deposited for 6 min at an energy of 1 keV. Pd_{561} at an energy of 1 keV was the third and last sample in the batch, with a cluster beam current of 11 pA the deposition time was 5 min, under which the palladium clusters impacted the thin film and subsequent particles landed on a carbon

coated TEM grid.

4.2.4 In-Flight Coating with Large Sized Clusters

The third and last in-flight coating experiment included five samples in the batch containing palladium clusters of large size. The sizes focused on were, clusters of 923 and 2000 Pd atoms, with two samples of each size deposited with different energy and an extra uncoated sample of Pd_{923} was also deposited for comparison. Feedback from previous batch suggested that an even thinner film would be more ideal in covering the palladium clusters in-flight and allowing them to penetrate more easily. Only 1 s evaporation time of Au was made after cooling the TEM grid holder with liquid helium and introducing Ar gas (<~400 L). That is a reduction of 2 s compared to previous batch.

Pd_{923} clusters, with a beam current of ~10 pA, were deposited for 30 min at an energy of 0.5 keV on the first carbon coated TEM grid sample after being coated in-flight, when penetrating the TEM grid matrix. The second carbon coated TEM grid sample, in the third and last batch of the in-flight coating experiments, was deposited with coated Pd_{923} at an energy of 1.5 keV for 37.5 min with a cluster beam current of ~8 pA. One should note that the beam current of 8 pA was measured when the deposition energy was set to 0.5 keV and increased to 20 pA when the energy was raised to 1.5 keV. Clusters of palladium with 2000 atoms were covered in-flight and deposited at an energy of 1.5 keV on the third carbon coated TEM grid sample. The clusters were deposited for 30 min at a cluster beam current of ~5 pA. The fourth and last carbon coated TEM grid sample, of the batch, was deposited with in-flight coated Pd_{2000} clusters having a beam current of 4 pA for 30 min and at an energy of 0.5 keV. An additional (reference) sample of Pd_{923} clusters with a beam current of 70 pA was deposited at an energy of 0.5 keV for 15 min.

4.3 HAADF-STEM Imaging and Analysis

Through HAADF-STEM a thorough study was made possible by imaging of the in-flight coated clusters in order to analyse and verify the results of the experiments in comparison to the hypothesis.

All HAADF-STEM images (and EELS) of the in-flight coating samples were taken with the JEOL 2100F microscope (courtesy of Dr. Zhi Wei Wang, with the author sitting in from time to time) and subsequently analysed with ImageJ, a free image analysis software suite. Clusters in the HAADF-STEM images were mapped so that a circular selection overlapped most of the flat cluster projections' circumference. By obtaining the area of a cluster's circular projection the diameter can be deduced from the equation of a circle's area $A = \pi r^2$, where A is the area and r the radius, of which two makes up the diameter d of a circle. Microsoft Excel was used to calculate the cluster diameters from the areas and further data representation into histograms and fitting Gaussians was performed with SciDAVis, an open source data analysis and visualisation software suite.

The bin sizes of histograms were chosen to best reflect the data, i.e. the number of clusters analysed and the underlying pattern of histograms. Too large bin sizes will not resolve the pattern of the data and too small bin sizes will mince it. By gradually varying the bin size from large to small, a certain pattern is uncovered for each histogram. The bin size that maintains the uncovered pattern and uses a reasonable number of clusters to form the said histogram is chosen in each instance.

Initially, blank TEM grids were imaged with the HAADF-STEM in order to verify their cleanliness, before use as samples for deposition. Although, certain low intensity features (possibly carbon based compounds, hydrocarbons) were observed, they don't show visible lattice information at large magnification as well as having irregular shapes, it is easy to differentiate between them and deposited clusters.

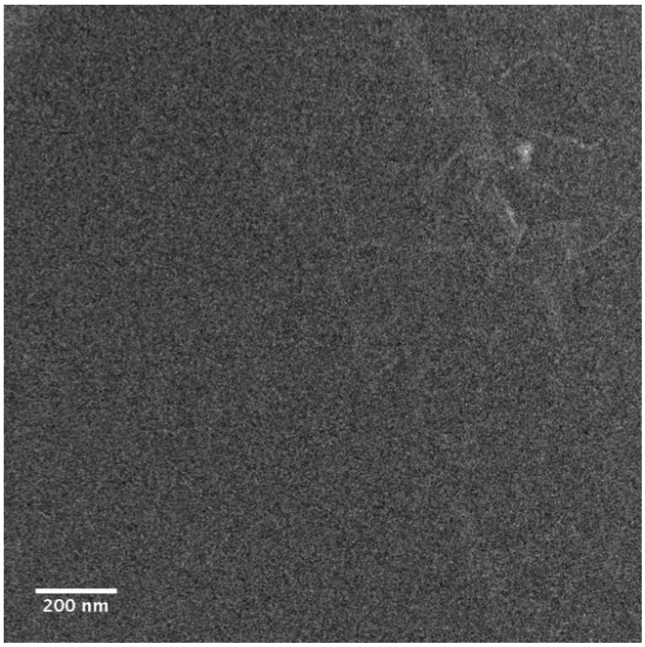

Figure 4.14: HAADF-STEM image of blank carbon coated TEM grid. Overly clean with weak intensity irregularly shaped features, possibly hydrocarbons (200 nm bar).

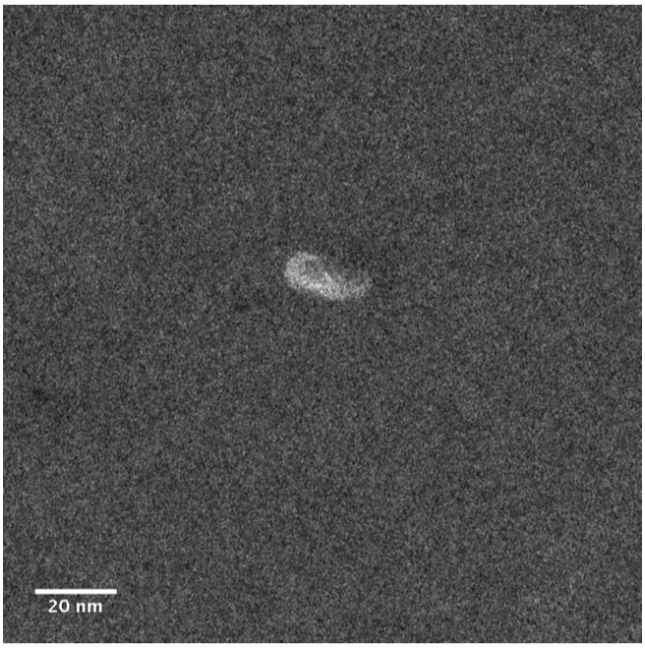

Figure 4.15: HAADF-STEM image close-up of hydrocarbon particle (see arrow) on otherwise clean carbon coated TEM grid (20 nm bar).

The HAADF-STEM images of the Pd_{55} clusters penetrating through the solid Ar matrix show typical sized clusters, as can be seen from images of samples with Pd_{55} clusters

deposited onto carbon coated TEM grids without passing through a solid Ar matrix. The size deduced from the images is ∼1 nm for particles observed, which is close to the spherical cluster approximation of 1.16 nm suggesting that the clusters have maintained their shape after the solid Ar matrix impact and deposition.

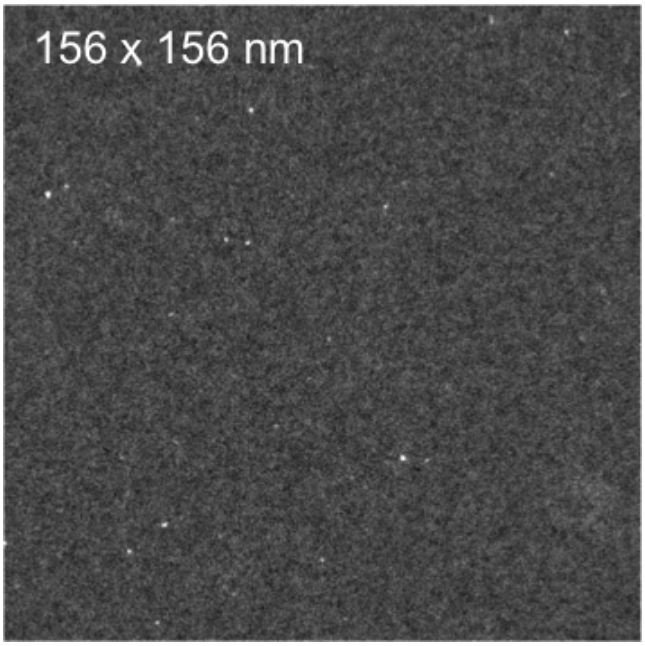

Figure 4.16: HAADF-STEM image of carbon coated TEM grid sample deposited with Pd_{55} clusters at an energy of 0.5 keV through a solid Ar matrix (156 nm × 156 nm).

Figures 4.16 and 4.17 show typical images of the 3 mm diameter carbon coated TEM grid sample covered with Pd_{55} clusters. The cluster density was found to be rather homogeneous throughout the TEM grid samples as images (156 nm x 156 nm) were taken from the centre, ∼1 mm to the right and left of the centre as well as ∼1 mm above and below the centre.

The cluster diameter is, as can be seen from the histogram in Figure 4.18, very close to the spherical approximation diameter of Pd_{55}. The data is taken from ∼400-500 clusters found on the TEM grid sample where the mean of the cluster diameters is 1.32 nm with the standard deviation being 0.4 nm. A gaussian fit of the dataset using function 4.5,

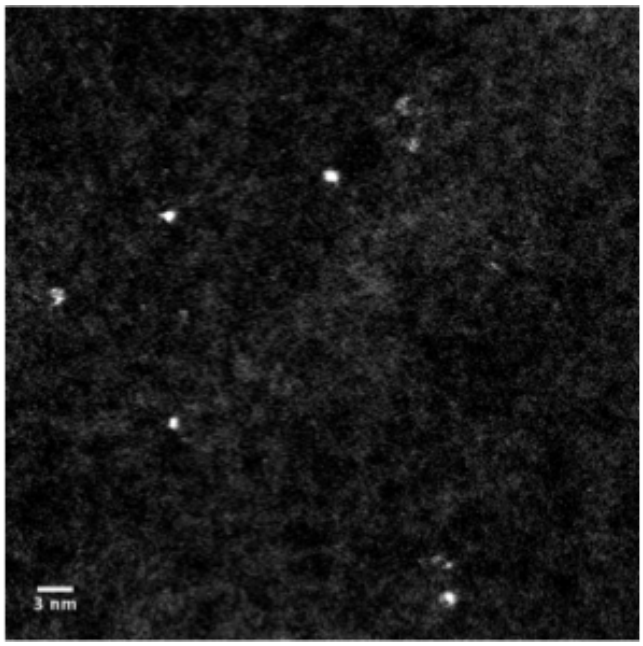

Figure 4.17: HAADF-STEM image of carbon coated TEM grid sample deposited with Pd_{55} clusters at an energy of 0.5 keV through a solid Ar matrix (3 nm bar, 52 nm × 52 nm).

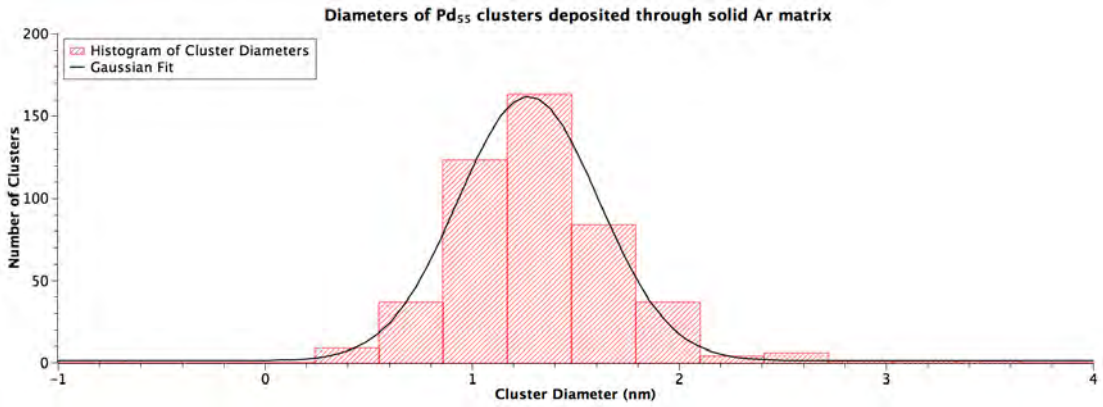

Figure 4.18: Diameters of individual clusters of Pd_{55} deposited through a solid Ar matrix at an energy of 0.5 keV on a carbon coated TEM grid sample. The histogram bin size has been chosen to best reflect the data.

$$y_0 + \frac{A\sqrt{\frac{2}{\pi}}}{w} e^{-2\left(\frac{(x-x_c)}{w}\right)^2}, \tag{4.5}$$

with y_0 being the offset (should be close to 0), A representing the amplitude, w the width and the centre denoted with x_c was utilised, see black Gaussian graph in Figure 4.18. A scaled Levenberg-Marquardt algorithm was employed (implemented in SciDAVis open

source software suite) to fit the Gaussian function 4.5 for $-1 \leq x \leq 4.89$ with a tolerance of 0.0001. After 7 iterations, the value of 1.19 ± 1.16 for fitting parameter y_0, the value 137.10 ± 3.89 for the amplitude A, 0.68 ± 0.02 for w and the value of 1.12 ± 0.01 for the fitting parameter x_c were obtained. The x_c value is in nm as it is the fit for the dataset comprising of cluster diameters in nm. The value of 1.12±0.01 nm for the cluster diameter matches very well with the value for the diameter obtained from the spherical cluster approximation of Pd_{55}. Shifting the centre of the Gaussian function to 1.27 ± 0.01 nm gives a perfect fit to the histogram, which is between the diameter value of the SCA of Pd_{55} (1.16 nm) and the mean of the cluster diameters (1.32 ± 0.4 nm).

The first sample, turned out to be a trial sample, as the carbon coated TEM grid placed on the tape drive was not shielded off properly with a mask during the Au evaporation stage, it got homogeneously covered with a high density of Au cluster particles. Therefore the subsequent in-flight coating experiment result became subdued due to the overwhelmingly larger amount of Au cluster particles compared to the resulting particles due to the thin film impacted Pd_{55} clusters, see Figures 4.20 and 4.21. During the evaporation stage, one of the carbon coated TEM grid samples, which were attached on the tape drive (one after another in a row), faced the cluster beam and the one after faced the Au evaporation beam at ∼45° while the subsequent ones were safely shielded away from the Au evaporation beam by teflon masks attached to the tape drive.

The evaporation time of the Au lasted for 5 s, expected to give rise to a thin film on top of the solid Ar matrix film produced on the TEM grid that is held on the copper matrix holder at the end of the cryostat. The cryostat, with the copper matrix holder at its end, was then rotated 90° towards the cluster beam, with the freshly evaporated thin film facing the impacting palladium clusters. The tape (drive), on which the TEM grid samples were attached, was subsequently advanced forwards. This, in order to let, what was thought to be, a new blank carbon coated TEM grid sample, but was instead a sample densely

covered with Au particles, face the resulting particles due to the thin film impacted Pd clusters.

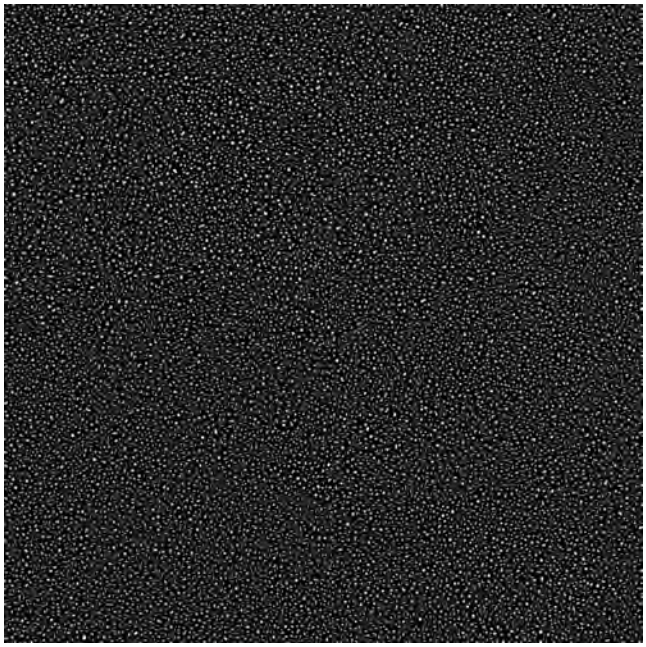

Figure 4.19: HAADF-STEM image of amorphous carbon coated TEM grid sample covered with Au clusters from the Au evaporation process as the sample was not shielded from the evaporation field of view. Very faint ripples of the background carbon is visible at this large field-of-view, which also reveals the huge density and coverage of the Au particles that actually stretches throughout the whole sample (782 nm × 782 nm).

As can be seen in Figures 4.19 and 4.20, the 5 s Au evaporation time gave rise to a dense coverage of Au particles on the unshielded TEM grid sample. The dense Au particle coverage is very uniform throughout the sample, where most Au particles have diameters of ~2-6 nm and some have detectable symmetries (fivefold, icosahedral), see Figure 4.21. Smaller particles are also visible (<2 nm), however, using the onboard electron energy loss spectrometer (EELS), no palladium could be detected in order to confirm coating of Pd_{55} clusters in-flight. The very high density of Au particles play a huge role in preventing detection of palladium with EELS as well as the possibility of the ~1 nm Pd_{55} clusters being covered with a very thick layer of material in-flight (>1 nm).

Figures 4.20 and 4.21 clearly depict the different sizes of Au particles and not distinguishable resulting particles due to the thin film impacted by Pd_{55} clusters. Figure 4.22,

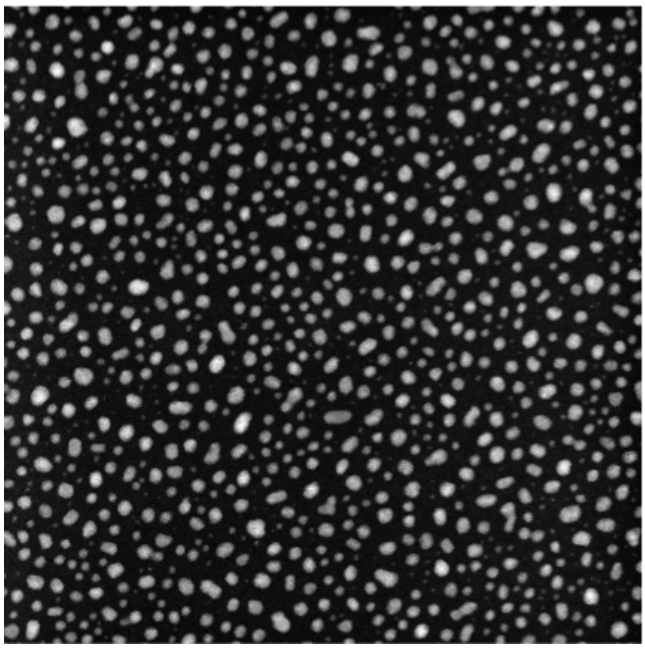

Figure 4.20: Zoomed in HAADF-STEM image of carbon coated TEM grid where the resulting particles due to the impact of the thin film and Pd_{55} clusters, which were deposited with an energy of 1 keV are hardly visible among the Au particles that covers the TEM grid densely (156 nm × 156 nm).

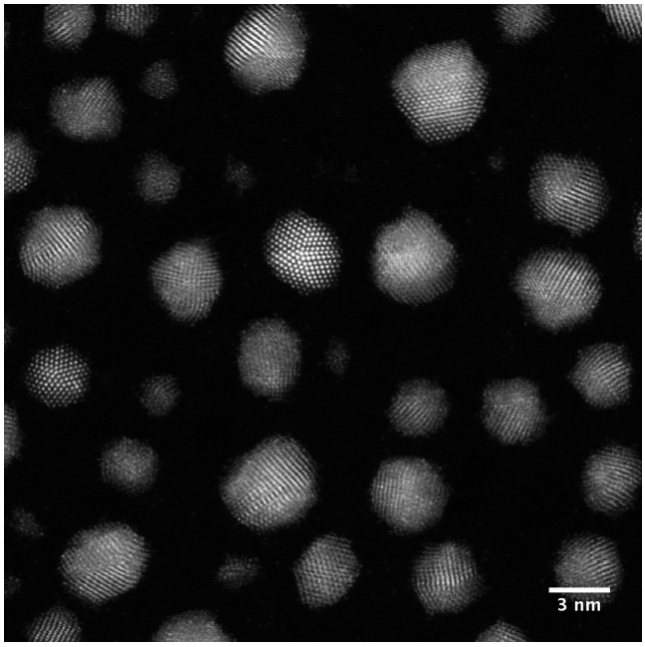

Figure 4.21: A higher magnification HAADF-STEM image of carbon coated TEM grid which is densely covered with larger Au particles from the evaporation process as well as few smaller clusters that might be coated Pd or Au particles due to the impact of the thin film and Pd_{55} clusters (3 nm bar).

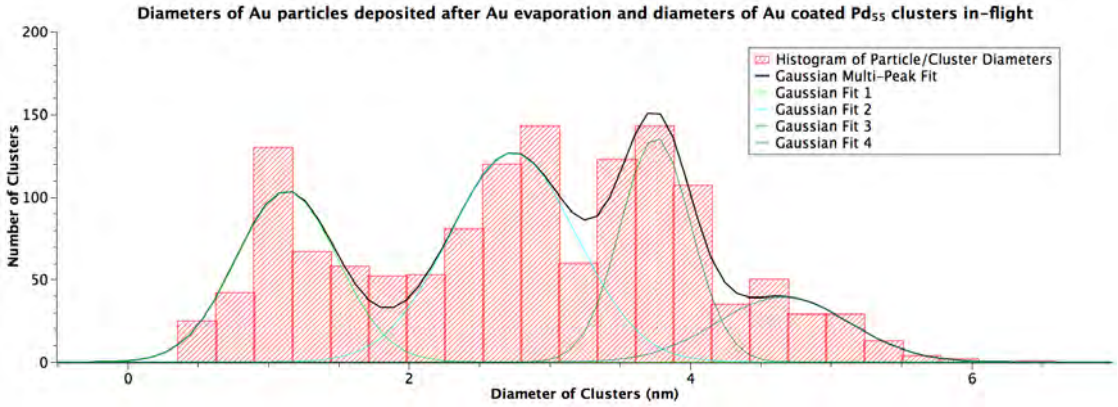

Figure 4.22: Diameters of individual Au particles and resulting particles due to the thin film impacted by Pd_{55} clusters deposited at an energy of 1 keV on a carbon coated TEM grid sample. The histogram bin size has been chosen to best reflect the data.

however, gives further insight to the diameters of the particles and the typical sizes encountered. The histogram clearly shows four peaks, around which the majority of the particles'/clusters' diameters are concentrated. Performing the same Gaussian fit as before, but for each peak, results in a multi-peak fit, which is a superposition of the individual Gaussian peak fits. The first peak has its centre at 1.13 ± 0.05 nm and a width of 0.72 ± 0.11 nm, which would be quite consistent with the diameter of non-coated Pd_{55} clusters, but as EELS has not verified any Pd clusters, these particles have to consist of Au. The second Gaussian fit has its centre at 2.74 ± 0.07 nm and a width of 0.90 ± 0.17 nm, which is roughly 1.5x larger than the first diameter. In-flight coated Pd_{55} clusters could very well have similar diameters, but one can only speculate as no evidence is present from e.g. EELS. Gaussian fit three has the narrowest width (0.51 ± 0.12 nm) and is centred at 3.76 ± 0.06 nm, where it is also quite possible for the coated Pd_{55} clusters to be masked by the Au particles. The centre of the final Gaussian fit is 4.66 ± 0.32 nm and the width is 0.94 ± 0.61 nm, which is the broadest. The concentration of certain diameter sizes of the Au particles after Au evaporation and deposition on the amorphous carbon coated TEM grid sample is linked to the specific parameters and conditions during the evaporation process and subsequent Pd cluster deposition. Further similar experiments are necessary in order to discuss the specific particle diameter sizes arisen, which is beyond

the scope of this work, as this action and result was not intended to begin with.

It is possible to estimate the thin film thickness at ∼45° from Figure Figure 4.21. There are roughly 30 particles in the 30×30 nm^2 (=900 nm^2) image, i.e. 1 particle per 30 nm^2. An average particle (with radius 2 nm) has volume $\frac{4\pi 2^3}{3} \approx 30$ nm^3 and would yield a film thickness of roughly 30 nm^3/30 nm^2 = 1 nm. Using the cosine law of emission ([91]) and taking our evaporator to be a surface source, the film thickness on the TEM grid would roughly be 4 nm when the thickness is ∼1 nm at an angle 45° from the evaporator.

The first successful in-flight coating experiment sample was the carbon coated TEM grid sample positioned just after the Au particle covered TEM grid on the tape. Pd_{55} clusters interacted with the 5 s Au evaporated thin film at the matrix holder (end of the cryostat) as they impacted it when being deposited on the carbon coated TEM grid on the tape drive at an energy of 1.5 keV. The difference between this sample and the first sample in the session is the deposition energy value and the presence of the thin film on the solid matrix in latter sample while the difference compared to the second sample is only the difference of 0.5 keV in deposition energy.

The HAADF-STEM images depict particles having sizes ranging from ∼5–30 nm (even one as large as 70 nm), giving indirect indication of coating of Pd_{55} clusters in flight, see Figures 4.23–4.28. The morphology and shape of the particles seem to be platelet-like with irregular structures as if the fast Pd clusters have taken them away from the matrix, as is, when penetrating through. Observing more closely around these clusters, one can clearly find smaller separated clusters and atoms scattered all around, see Figure 4.25. According to the Gaussian fit of the histogram (Figure 4.26), the size of these particles is 0.20±0.03 nm, which is consistent with the size of a single atom. Figure 4.27 shows that EELS analysis, however, do not pick up the Pd signal from the potentially in-flight coated clusters (maybe only transfer energy and knock off particle), suggesting that the Pd_{55} cluster size is too small and/or that the thickness of the coating is too large. Pd has a

very small inelastic scattering cross section (smaller than Cu), and previous investigation shows that even for just Pd_{55} clusters on the carbon coated TEM grid sample, the core-loss threshold are still almost unseen. Moreover, the signal becomes much weaker when covered by layers of other materials. According to previous experience of CuAu clusters, the cluster size suitable for EELS analysis should not be smaller than several hundreds of atoms.

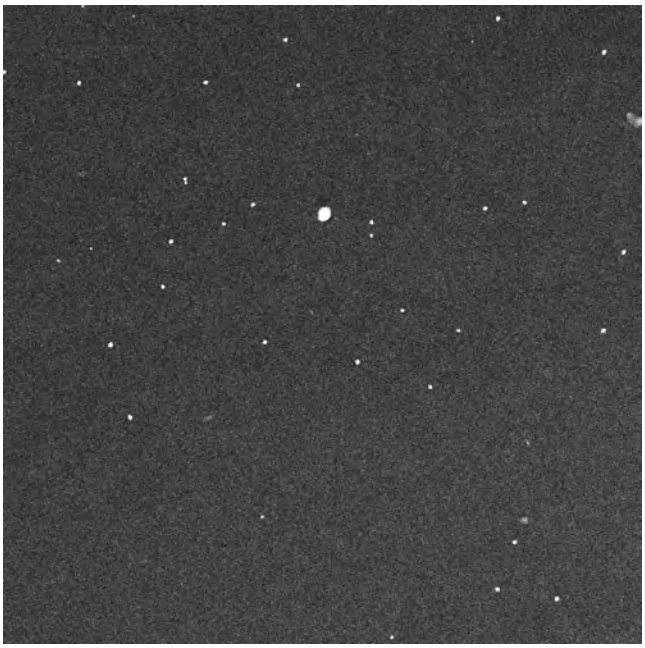

Figure 4.23: HAADF-STEM image of carbon coated TEM grid sample deposited with resulting particles from impact of Pd_{55} clusters with the thin film setup at an energy of 1.5 keV (3130 nm × 3130 nm).

What is interesting with this sample is that such large resulting cluster sizes (sometimes even ≥30 nm) are observed within images (see Figure 4.28), despite the relatively small size of the initial Pd clusters (Pd_{55} ∼1 nm), making it desirable to investigate the smallest size of starting particle necessary to achieve a result of a much larger particle. The side-discovery aside, the logical thing to do for further investigation is to increase the size of the palladium clusters and also reduce the thickness of the thin film in order to explicitly verify the in-flight coating by detecting the EELS signal of the Pd clusters.

Pd_4 clusters were impacted on thin film setup and deposited onto TEM grid samples in the

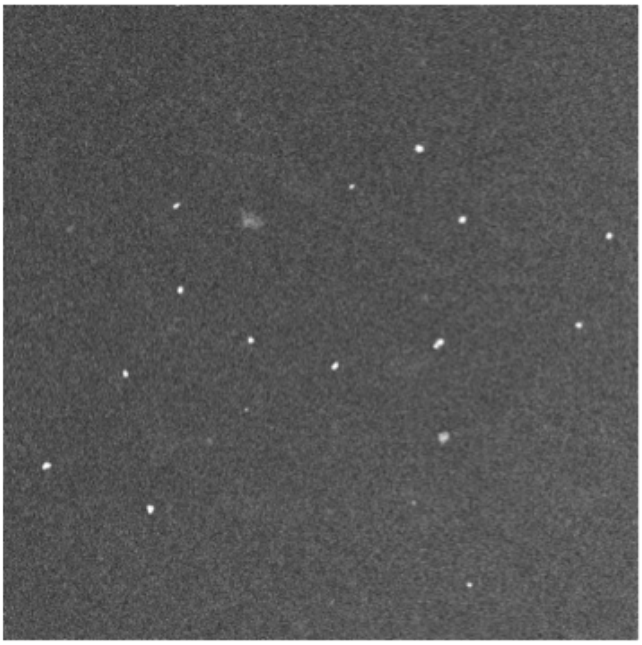

Figure 4.24: Zoomed in HAADF-STEM image of carbon coated TEM grid sample deposited with resulting particles from impact of Pd_{55} clusters with the thin film at an energy of 1.5 keV (1560 nm × 1560 nm).

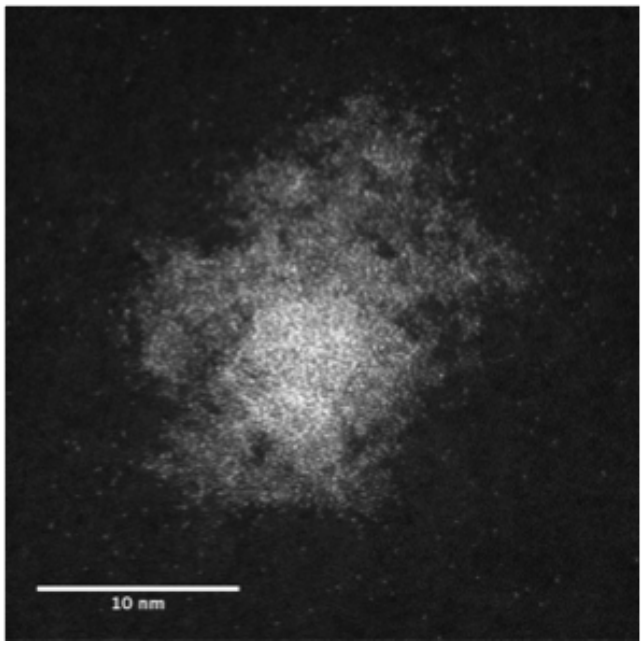

Figure 4.25: Zoomed in HAADF-STEM image of ~20 nm resulting particle from impact of Pd_{55} clusters with the thin film setup and deposited at an energy of 1.5 keV on carbon coated TEM grid sample (10 nm bar). Notice the small clusters and atoms separated and scattered around the resulting particle.

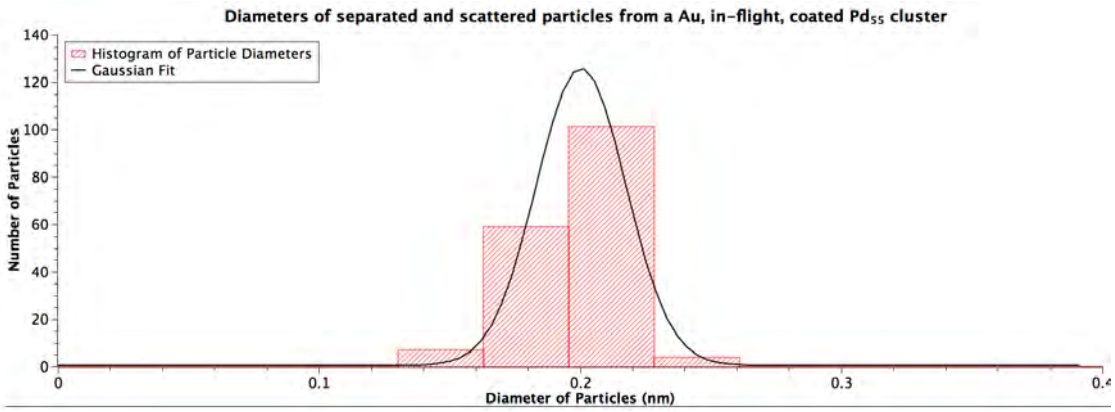

Figure 4.26: Diameters of individual small clusters/atoms separated and scattered from ~20 nm resulting particle from impact of Pd_{55} clusters with the thin film setup. The histogram bin size has been chosen to best reflect the data.

same batch, but the smaller size of the clusters compared with the size of the Pd_{55} clusters seems to have had a profound impact on the result. What is clearly noticeable from the HAADF-STEM images is the much lower particle density of the resulting particles from impact of Pd_4 clusters with thin film compared to the Pd_{55} clusters. Throughout the 3 mm diameter carbon coated TEM grid sample, very few clusters could be observed, see Figure 4.29. Occasionally, however, some large particles of the size of several nm in diameter can be found, as marked by the arrow in Figure 4.30. These clusters often look damaged (structure-wise) in high resolution HAADF-STEM images, see Figure 4.31. Evidently, the clusters are not stable under the electron beam and single atoms are observed to be diffusing on the support due to electron beam scanning.

It is interesting that it is possible to get an output of larger resulting particles from impact of Pd clusters with thin film for input of clusters with sizes as small as 4 atoms. The result of Pd_{55} clusters (diameter of ~1 nm) impacting the thin film setup, saw sizes of ~20 nm (even up to 30 nm), which is a magnification of up to 30× in diameter size. The size of Pd_4 clusters is 0.44 nm according to the spherical cluster approximation, which compared to ~20 nm, the size of imaged resulting particles from impact with thin film setup, results in a magnification of nearly 45×. As Pd_4 is the smallest clusters used in the in-flight coating

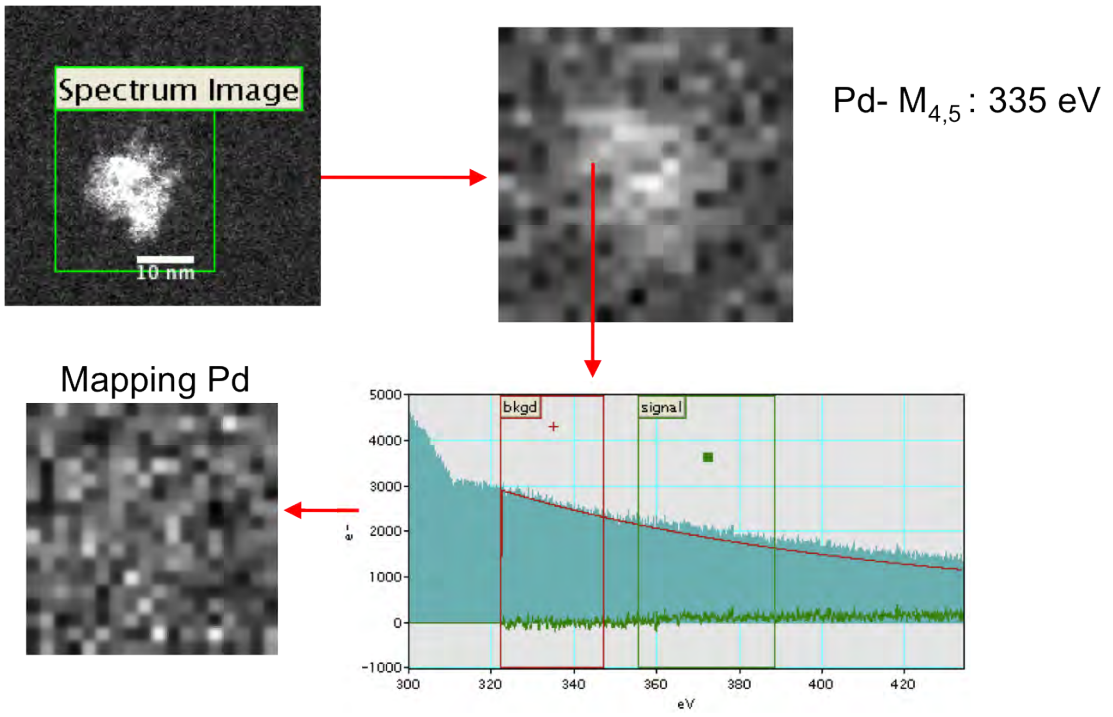

Figure 4.27: EELS spectrum and spectrum imaging of ~20 nm resulting particles from impact of Pd_{55} clusters through the thin film setup and deposited at an energy of 1.5 keV on carbon coated TEM grid sample. A spectrum image is taken from the HAADF-STEM image (top left) as indicated by the green square and adjacent label. The spectrum image is a combination of the HAADF-STEM image and EELS spectra at different points in the image. These different points, which are larger than the original HAADF-STEM image pixel sizes are seen making up the top right image. The red arrow indicates the point in the image where the EELS spectrum (at the bottom right) is taken. The EELS spectrum does not show the principal energy edge $M_{4,5}$ for Pd at 335 eV, which is being mapped for in the spectrum image. In the same way, EELS spectra are taken at the other points to register the Pd signal, with the results then being put together to form the spectrum image at the bottom left.

experiments one does not know what the size limit is for the initial particles in order to produce larger coated clusters. It might be possible to use only one metal atom/ion (Pd) or even single atoms/ions of other elements, e.g. rare gas atoms/ions (Ar) or even smaller particles.

The size of the initial particles, alone, is of course not the whole picture in this matter. The first thing already mentioned is the deposition energy of which the effect has not been dealt with as of yet. The Pd_{55} clusters were deposited with an energy of 1.5 keV, which translates into ~30 eV/atom, compared to the Pd_4 clusters with a deposition energy of

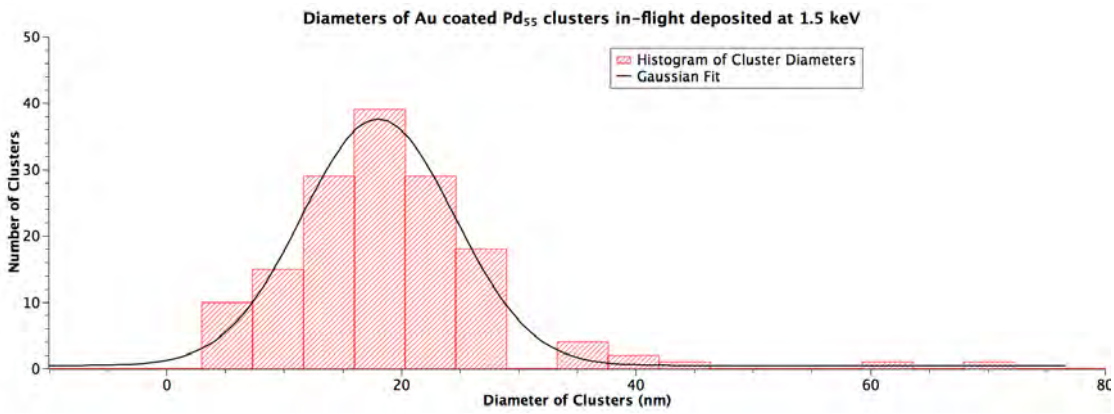

Figure 4.28: Diameters of individual resulting particles from impact of Pd_{55} clusters through the thin film setup and deposited at an energy of 1.5 keV on a carbon coated TEM grid sample. The histogram bin size has been chosen to best reflect the data.

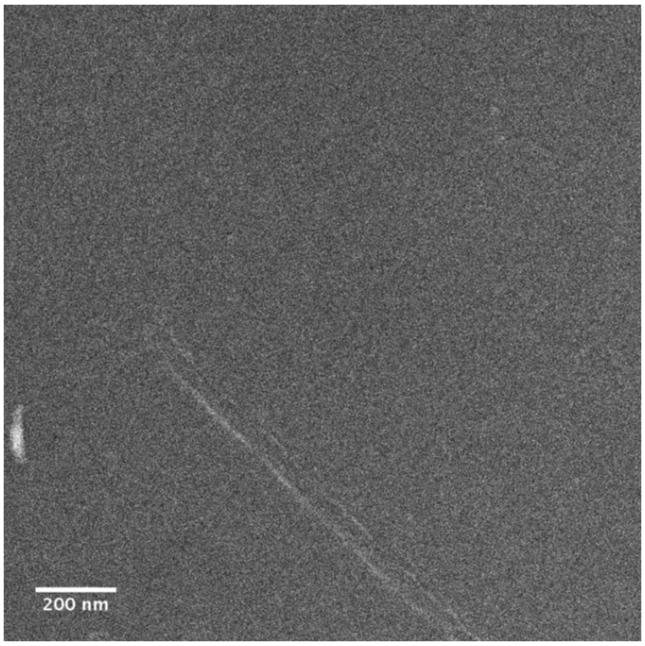

Figure 4.29: HAADF-STEM image of carbon coated TEM grid sample deposited with resulting particles from impact of Pd_4 clusters with thin film setup at an energy of 1 keV, however, no particles can be seen (200 nm bar).

1 keV (~250 eV/atom). The energy per atom is almost 10× larger for the Pd_4 clusters suggesting that the majority of the clusters just penetrate through the thin film and solid matrix without being coated or picking up anything as the cross-section of the clusters is much smaller than the Pd_{55} clusters. The cluster beam current for the Pd_{55} clusters was 2 pA with a deposition time of 15 min, resulting in a coverage of 1800 pA·s. Trying to

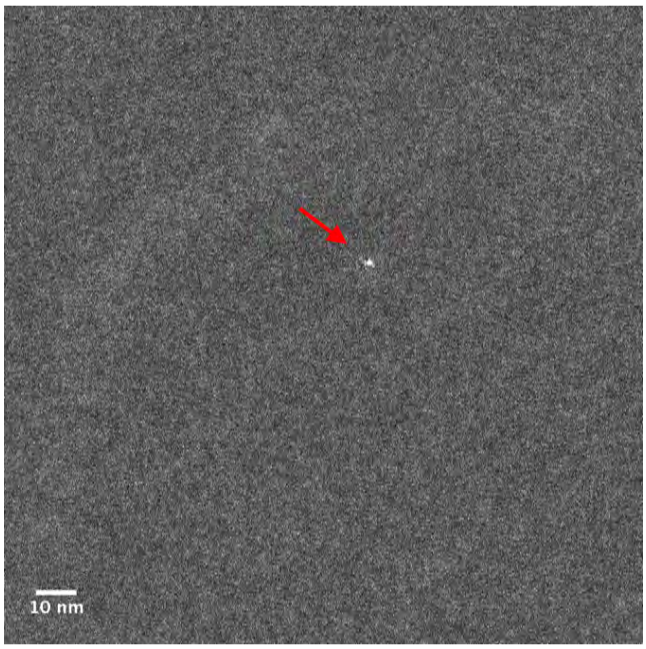

Figure 4.30: HAADF-STEM image of carbon coated TEM grid sample deposited with resulting particles from impact of Pd_4 clusters with thin film setup at an energy of 1 keV (10 nm bar).

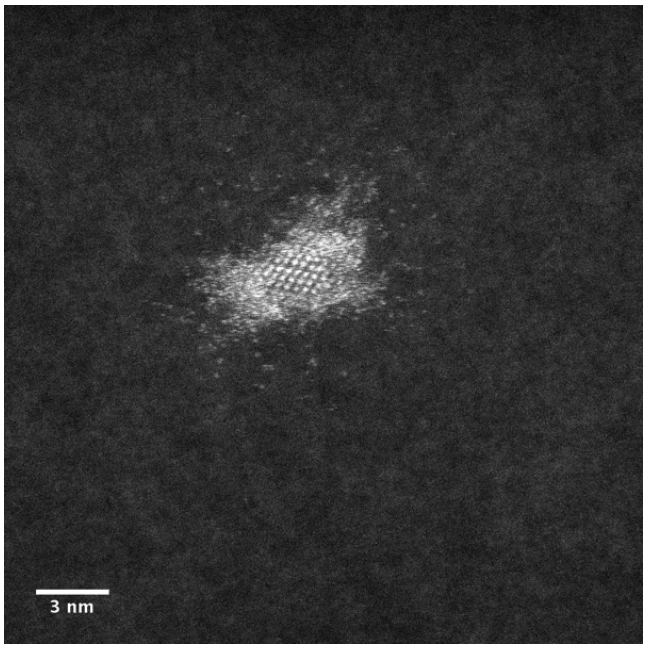

Figure 4.31: HAADF-STEM image of carbon coated TEM grid sample deposited with ~6 nm size particle resulting from impact of Pd_4 clusters with the thin film setup at an energy of 1 keV (3 nm bar).

maintain the same coverage of 1800 pA·s, the Pd_4 clusters with a beam current of 20 pA should have been deposited for 1.5 min, but was deposited for 5 min. This larger coverage of 6000 pA·s for the smaller clusters was thought necessary as earlier trials, before these in-flight coating experiments, did not reveal deposited small clusters. An even larger coverage might have been necessary for the smaller clusters, i.e. a longer deposition time, in order to observe more of the large and irregularly shaped in-flight coated Pd_4 clusters on the carbon coated TEM grid sample. However, a coverage of 1800 pA·s is more than enough in order to observe deposited clusters, despite the beam current being as low as 2 pA. So, when an even larger coverage of 6000 pA·s does not come near the actual coverage of deposited clusters, one must turn to the cross-section of the impinging clusters and their deposition energy to understand the reason behind this big difference. The smaller cross-section and higher deposition energy per atom of the Pd_4 clusters seem to make them act like spear-heads when they penetrate the thin film and solid matrix. The larger cross-section of the Pd_{55} clusters and lower deposition energy per atom compared to Pd_4 clusters, make them better suited for in-flight coating as they seem to pick up or knock off more material, which is evident from the higher density of deposited in-flight coated clusters that can be observed in the sample. The issue could also be caused by mass, making the larger clusters have an advantage in being coated and picking up or knocking off matter as their mass is larger than the mass of the smaller clusters.

Taking lessons from the first batch of samples and utilising the preliminary results from their observation and analysis, a second batch of samples was made in the in-flight coating experiment. Taking on board the issues of not finding the Pd signal from EELS analysis (spectrum imaging and EELS spectrum), larger cluster sizes and a thinner film was used. The Au evaporation time lasted for 3 s, which would be equivalent to a thin film thickness of ~8.03 nm according to the calibration method mentioned earlier. The palladium cluster sizes used for the samples deposited in this batch were 147, 309 and 561 atoms.

One of the samples in the second batch was Pd_{561} clusters impacted on the thin film setup and deposited at 1 keV on a carbon coated TEM grid sample. The density of deposited particles is quite uniform across the 3 mm diameter TEM grid sample as can be observed from HAADF-STEM images, see Figure 4.32 for typical coverage. The resulting particles have similar size as the resulting particles from impact of Pd_{55} clusters with thin film, in the first batch, with diameters ranging between 10–20 nm, see Figure 4.35 for histogram of cluster diameters. The structures of the resulting particles are, similarly, irregular in shape (see Figure 4.33) and some have the same platelet-like structure as the resulting particles from impact of Pd_4 clusters through thin film, in batch I. From the images, one can deduce that the size of the impinging Pd_{561} clusters (2.31 nm in diameter) does not seem to have changed the size of the deposited resulting particles in comparison with the results of the Pd_{55} cluster sample of the first batch.

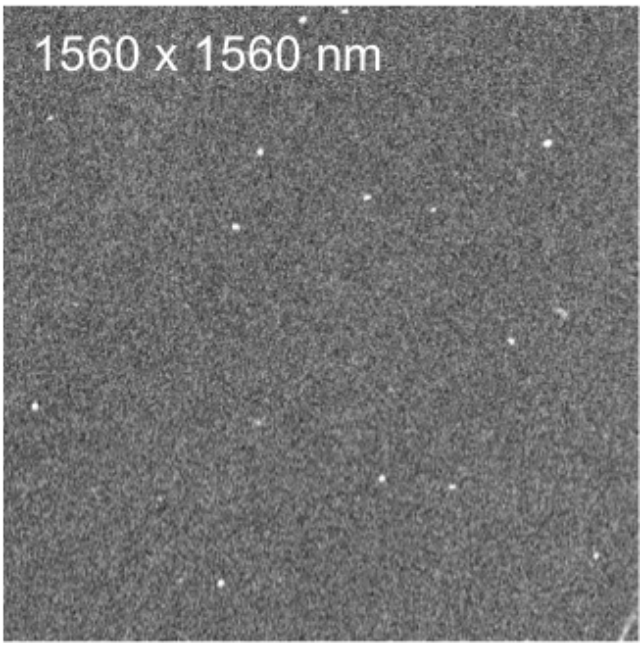

Figure 4.32: HAADF-STEM image of carbon coated TEM grid sample deposited with resulting particles from impact of Pd_{561} clusters with thin film setup at an energy of 1 keV (1560 nm × 1560 nm).

The diameter of Pd_{561} clusters is more than double the diameter of Pd_{55} (1.06 nm), which should have warranted a visible change. Also, the thinner film (~8.03 nm vs ~13.38 nm)

was expected to lead to a change in deposited resulting particle size. As the resulting clusters are not in any way resemblant to core-shell structures, their size is not a tradeoff between the increase of the Pd_{561} cluster size and the decrease of the thin film thickness, thus yielding the same final resulting size as for the Pd_{55} cluster sample. Rather, it seems, both Pd_{561} and Pd_{55} clusters pick up or knock off similarly sized pieces of the thin film as they interact with it during the deposition process and that their size does add little to the overall final size. However, some pieces land relatively flat and some entangle to make more 3D-like amorphous structures, but most look quite fragile and are unstable under the electron beam.

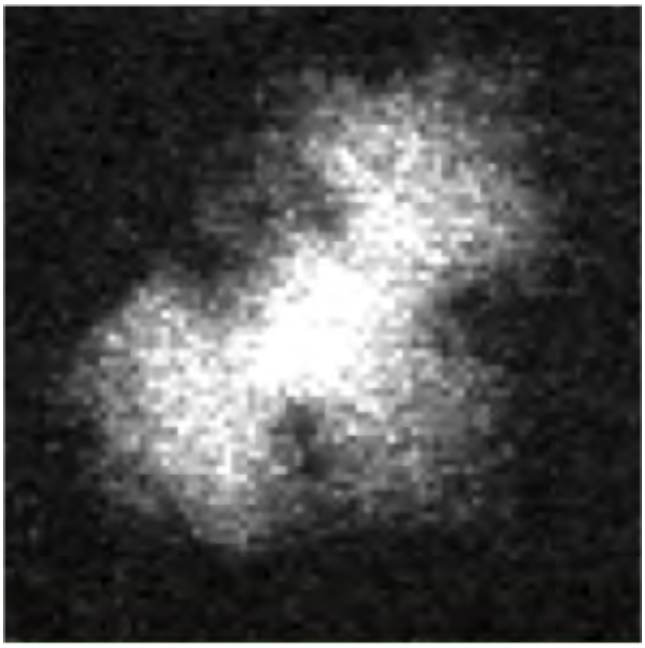

Figure 4.33: HAADF-STEM image of a resulting particle from impact of Pd_{561} cluster with thin film and deposited at an energy of 1 keV on a carbon coated TEM grid sample (3 nm scale bar).

Unfortunately, the larger size of the Pd_{561} clusters, compared to the Pd_{55} clusters, had no effect in registering the Pd signal with EELS analysis either. This fact adds to the explanation above, regarding the role of the Pd clusters and the thin film on the final resulting particle shape, structure and size. The usage of both EELS spectrum and spectrum imaging, as can be seen in Figure 4.34 for cluster A and B, did not detect any Pd. For Pd_{561}

clusters deposited directly on carbon coated TEM grid samples, the core-loss peak (~335–400 eV) indicating Pd in the EELS spectrum, was identified in other previous work. This fact further corroborates the explanation given above, regarding the results of the impact of Pd clusters with the thin film. The lack of Pd signal from the Pd_{561} clusters, as well as the similar size of resulting particles from impact of palladium clusters with thin film setup (for both Pd_{561} and Pd_{55}) and possibly the lack of core-shell clusters could be due to the deformation of the Pd_{561} clusters (even more plausible for the Pd_{55} clusters).

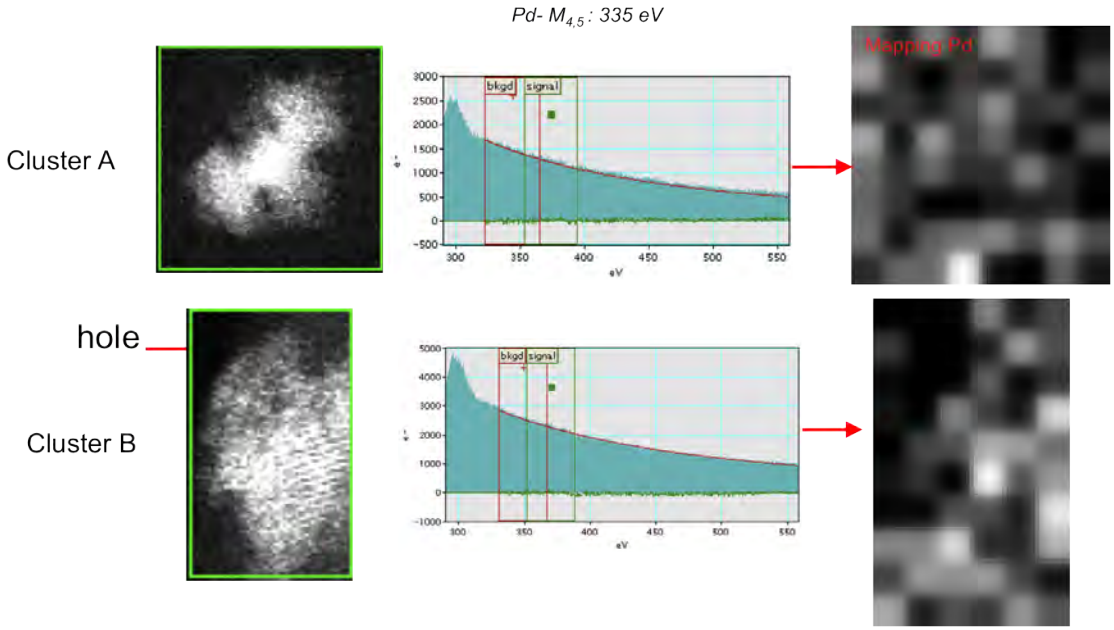

Figure 4.34: EELS spectrum and spectrum imaging of two ~20 nm size resulting particles from impact of Pd_{561} clusters with thin film and deposited at an energy of 1 keV on carbon coated TEM grid sample.

As the Pd_{561} clusters penetrate the thin film and solid matrix and get deposited with an energy of 1 keV, which is 1.78 eV/atom, they deform and get flatter. The deposition energy for Pd_{55} clusters were 27.27 eV/atom, which is much higher and would certainly make the smaller clusters deform much more. The electron probe size is ~1 Å, so roughly 1 atomic column detected for each pixel. Furthermore, the size of the thin film in both cases is too thick, masking any Pd from detection in the EELS analysis of resulting particles from impact of Pd clusters through thin film. Evidently, what is necessary is larger sized

palladium clusters in order to get lower deposition energy per atom and thus avoid deformation and maintaining the clusters' spherical shape as well as further decreasing the thickness of the thin film.

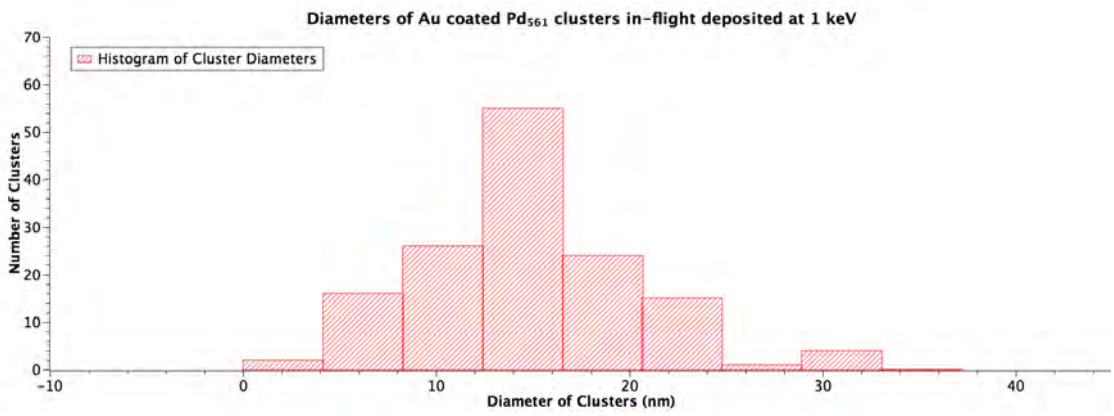

Figure 4.35: Diameters of individual resulting particles from impact of Pd_{561} clusters through thin film setup, deposited at an energy of 1 keV on a carbon coated TEM grid sample. The histogram bin size has been chosen to best reflect the data.

Samples that should contain resulting particles from impact of Pd_{147} and Pd_{309} clusters through thin film, in the same second batch, did not reveal any particles when investigated with HAADF-STEM. Both TEM grid samples were searched thoroughly for deposited clusters/particles at different areas, but none could be found, see Figures 4.36 and 4.37 for typical features of areas of samples with missing clusters. No real explanation could be found for the absence of these clusters as both samples were dealt with in the same way as previous samples. Successful samples were achieved with smaller sizes such as Pd_4 (partly) and Pd_{55} as well as larger sizes such as Pd_{561}. Similar deposition energies were used for all samples (1 keV and 1.5 keV) and both sizes are just in between two extreme ends of successfully deposited samples. The Pd_{561} sample was the last sample deposited in the batch with the same thin film thickness and all three samples had similar beam currents of ~10 pA and were deposited for ~5 min, which should have yielded the same density of resulting particles.

With the new insights gained from the two first batches, a third batch of samples was pre-

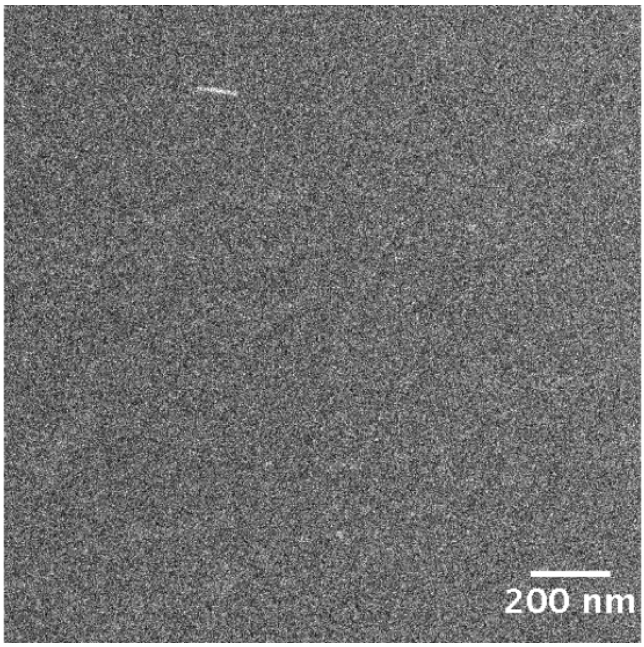

Figure 4.36: HAADF-STEM image of a carbon coated TEM grid sample with missing resulting particles from impact of Pd_{147} clusters through the thin film setup with a deposition energy of 1 keV (200 nm scale bar).

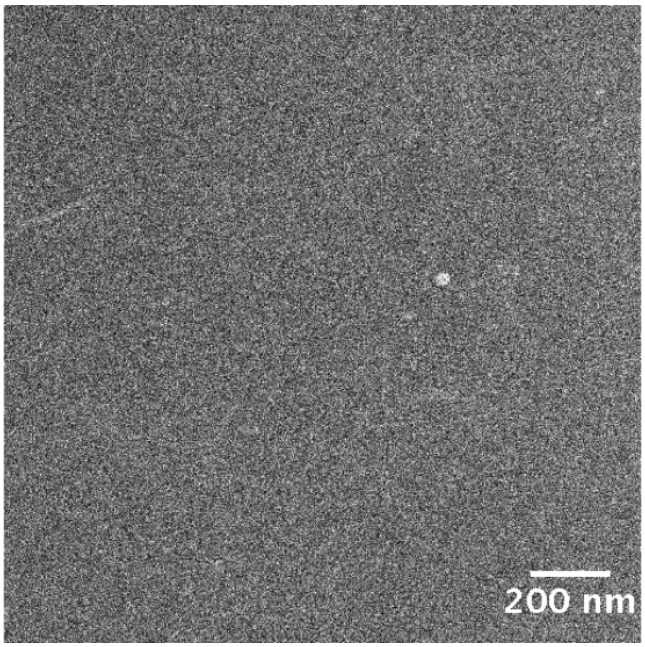

Figure 4.37: HAADF-STEM image of a carbon coated TEM grid sample with missing resulting particles from impact of Pd_{309} clusters through the thin film setup with a deposition energy of 1 keV (200 nm scale bar).

pared, making sure that this time, the samples would give explicit evidence of the success of the overall in-flight coating experiments with the methods and techniques pursued. The three areas where changes were made, from lessons which were learnt in production of previous samples, were the sizes of the clusters, the thickness of the thin film and the cluster density. With larger Pd clusters and a thinner film on the solid matrix, one would expect a higher probability of detecting the Pd signals of in-flight coated clusters with EELS analysis. Using similar impact energies as previous samples (0.5–1.5 keV, which has proven successful), with larger Pd clusters, would result in a lower deposition energy per atom and thus reduce their deformation as they impact the thin film and get coated in-flight and subsequently deposited onto the samples. The coverage of all previous samples were in the range of scarce to adequate and increasing the deposition time in order to increase the density would only make things easier when confirming the results without having to worry to much about diffusion and coalescence of the clusters.

The first sample prepared in the third and last batch was Pd_{923} clusters, which were coated by a ~2.68 nm thin film (Au evaporation time of 1 s) in flight and deposited at an energy of 0.5 keV. The beam current was ~10 pA and the deposition time lasted for 30 min giving a theoretical coverage of 18000 pA·s and typical coverage can be seen in Figure 4.41. The cluster density throughout the TEM grid sample is more or less the same as the HAADF-STEM image shown. The diameter of clusters in this sample was around 4 nm, with the mean being 3.83±0.57 nm, see Figure 4.39. The Gaussian fit of the histogram data has its centre at 4.09 nm and the width is 0.59 nm, which is quite consistent with the value of the mean. The theoretical diameter of Pd_{923} is 3.0 nm for spherical approx. (3.7 nm for hemispherical), which therefore, again, indicates a successful coating of the Pd clusters.

Strong contamination of the sample did, however, prevent an atomic-resolution investigation and EELS analysis of the clusters in order to explicitly confirm the success of the in-flight coating. Usually, light contamination through normal handling of samples in air

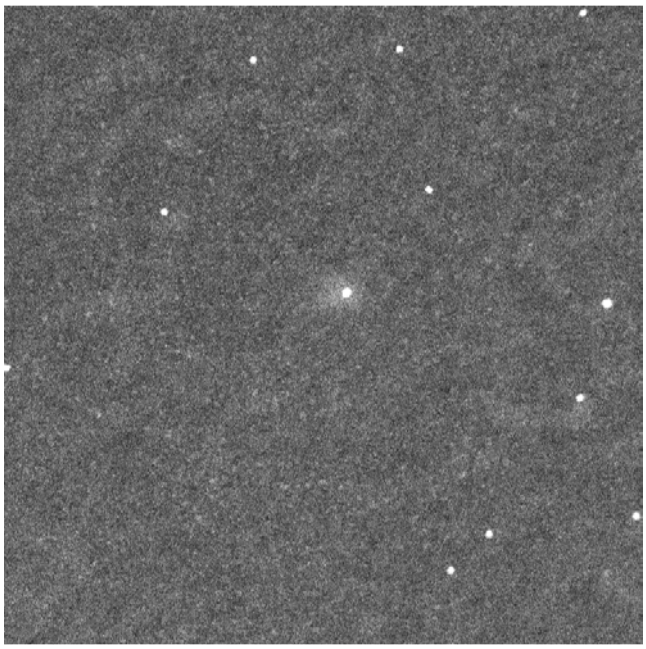

Figure 4.38: HAADF-STEM image of carbon coated TEM grid sample deposited with coated Pd_{923} clusters in flight at an energy of 0.5 keV (320 nm × 320 nm).

during preparation is suppressed in the microscope through the use of the microscope itself to "shower" the sample with the electron beam. This method would at least give a few minutes suppression in order to analyse the sample, but this sample was treated twice and then left in the TEM column for 2 hours in order to get rid of the contamination. Despite the efforts, imaging was only possible the first couple of seconds after commencement of the beam. The contamination absorbed on the TEM grids in this instance is thus stronger (has higher density) than usual.

The second carbon coated TEM grid sample also contained coated Pd_{923} clusters in-flight, but now deposited at an energy of 1.5 keV. The beam current reached at best ~8 pA, after tuning and optimisation at 0.5 keV deposition energy, which would give a theoretical coverage of 18000 pA·s with 37.5 min deposition time. After deposition it was found that the actual beam current rose to 20 pA, at the deposition energy of 1.5 keV, which would yield a coverage of 45000 pA·s (i.e. 2.5× larger than expected) if it maintained that beam current throughout the deposition. As can be observed in Figures 4.40 and 4.41

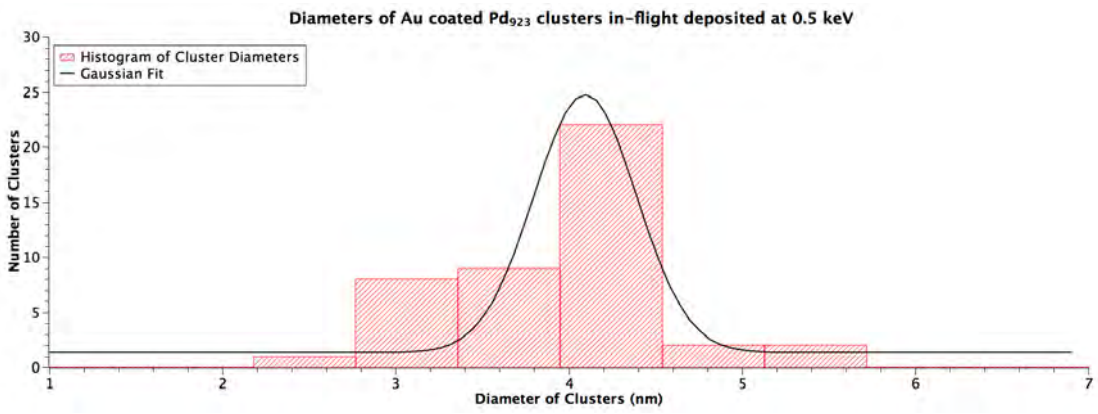

Figure 4.39: Diameters of individual clusters of coated Pd_{923} clusters, in flight, and deposited at an energy of 0.5 keV on a carbon coated TEM grid sample. The histogram bin size has been chosen to best reflect the data.

the coverage is good and seem to be similar to the coverage of the previous sample (with the main difference being the deposition energy). The increased beam current registered does not guarantee that all clusters are deposited on the TEM grid sample, as the metal rectangles holding the samples as well as the tape drive silver tape are all metallic and could all potentially register the clusters as they impact on these biased parts.

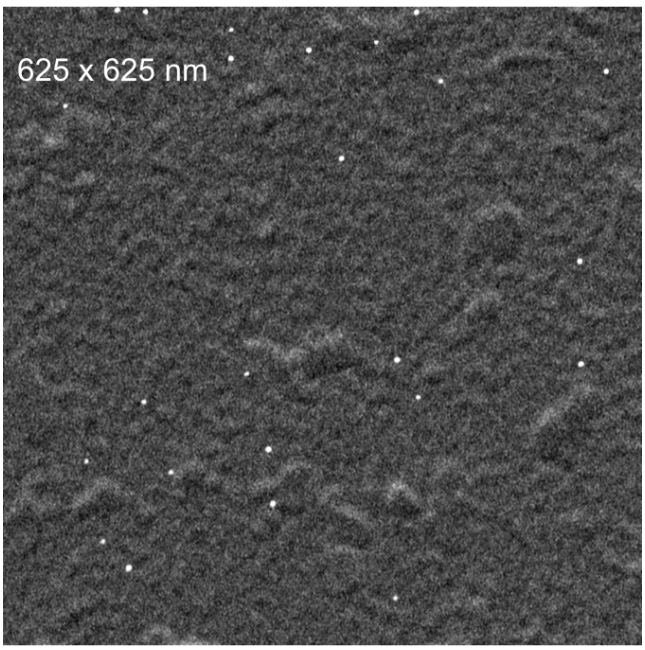

Figure 4.40: HAADF-STEM image of carbon coated TEM grid sample deposited with coated Pd_{923} clusters in flight at an energy of 1.5 keV (625 nm × 625 nm).

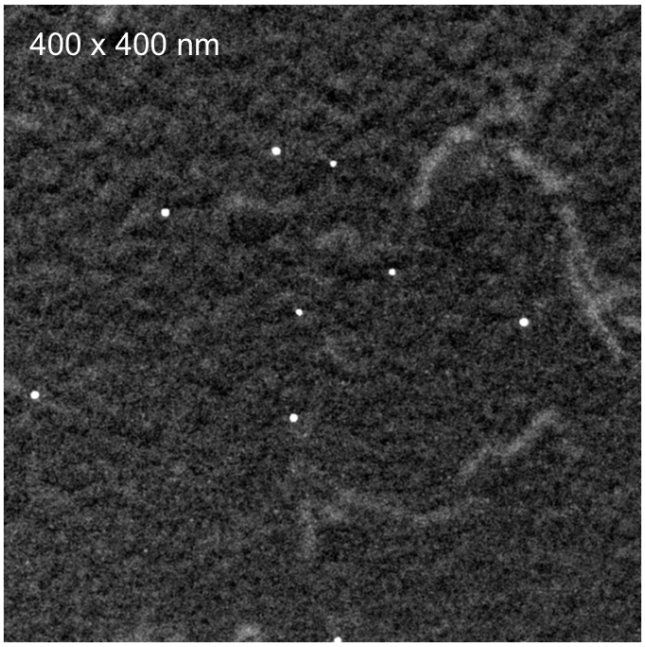

Figure 4.41: HAADF-STEM image of carbon coated TEM grid sample deposited with coated Pd_{923} clusters in flight at an energy of 1.5 keV (400 nm × 400 nm).

Most cluster sizes are much larger than the theoretical diameter sizes of Pd_{923} (3.0 nm for spherical approx. and 3.7 nm for hemispherical), see Figure 4.42. The majority of clusters have diameters above 4 nm, with many around 5 nm, and some clusters have diameters similar to the theoretical diameters, which indicates that they might not be coated. As can be seen from the histogram, few clusters have much larger diameters (6–11 nm), which could be attributed to a variable thickness of the thin film (or patchy film) covering the solid matrix. The Gaussian fit of the histogram in Figure 4.42 has its centre at 5.03 nm and the width is 1.31 nm.

Looking at some individual clusters in the atomic-scale investigation, reveals the difference in size between clusters and also the ordered lattice structure of some of them, e.g. the FCC polyhedron on the top-left in Figure 4.43. As was evident in the graph in Figure 4.42, the range of sizes mainly goes between ∼3–6 nm, which is clearly observed in Figure 4.43, the top- and bottom-centre clusters have ∼3 nm diameters and the bottom-left cluster has a diameter of ∼6 nm.

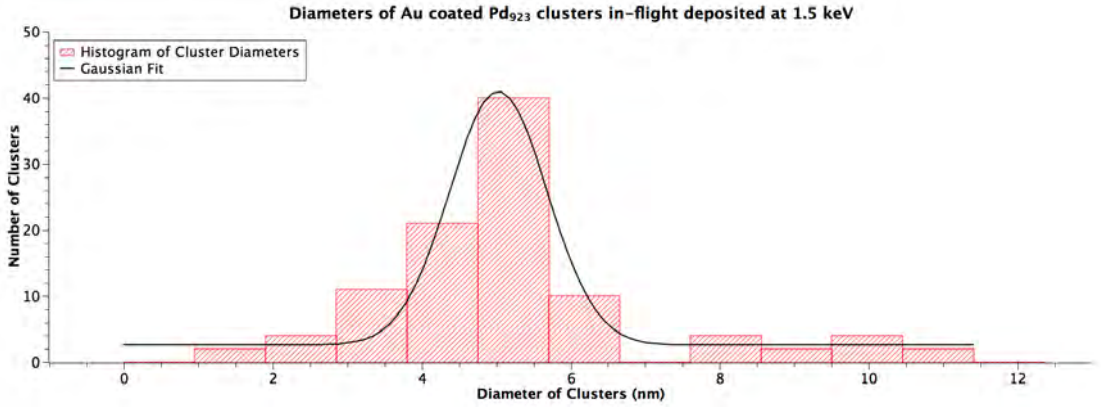

Figure 4.42: Diameters of individual in-flight coated Pd_{923} clusters, deposited at an energy of 1.5 keV on a carbon coated TEM grid sample. The histogram bin size has been chosen to best reflect the data.

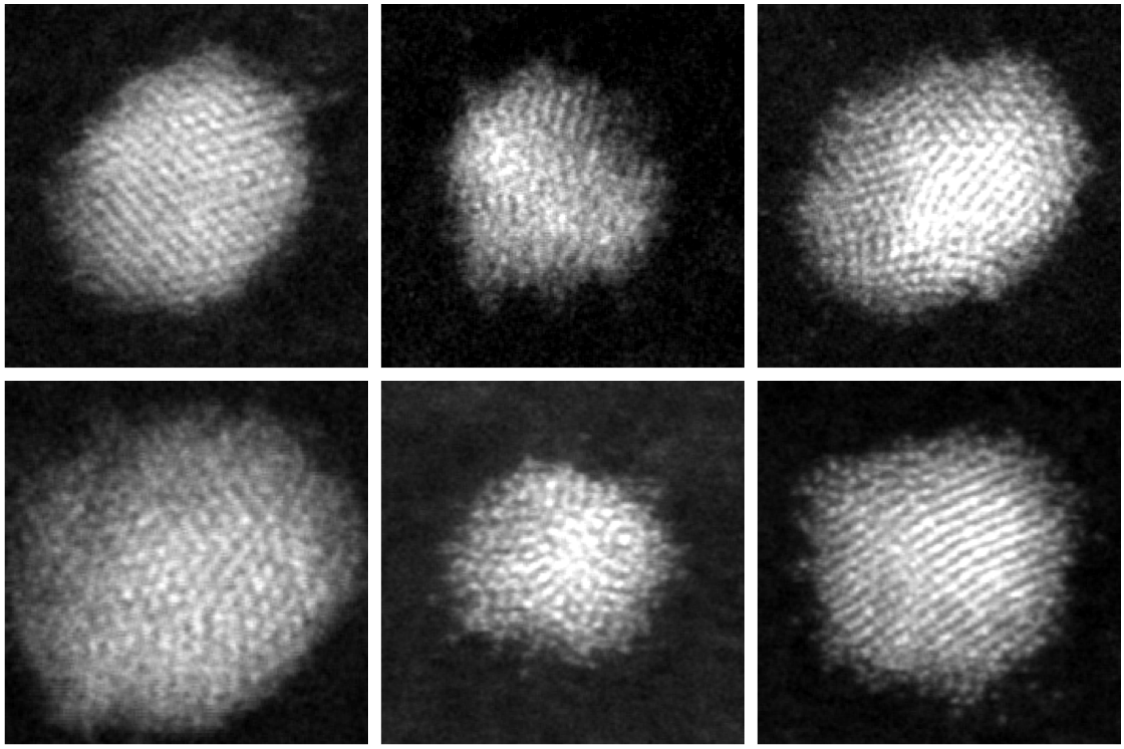

Figure 4.43: HAADF-STEM image gallery consisting of 6 coated Pd_{923} clusters in flight and deposited at an energy of 1.5 keV on the same carbon coated TEM grid sample, but at different positions (6 nm × 6 nm).

EELS analysis, explicitly confirms the presence of Pd of the in-flight coated Pd_{923} clusters. As can be seen in Figure 4.44, by taking a line profile and obtaining the EELS spectrum at points A and B, the strong core-loss edge is clearly evident indicating that the ~4 nm

cluster investigated is dominated by the Pd element.

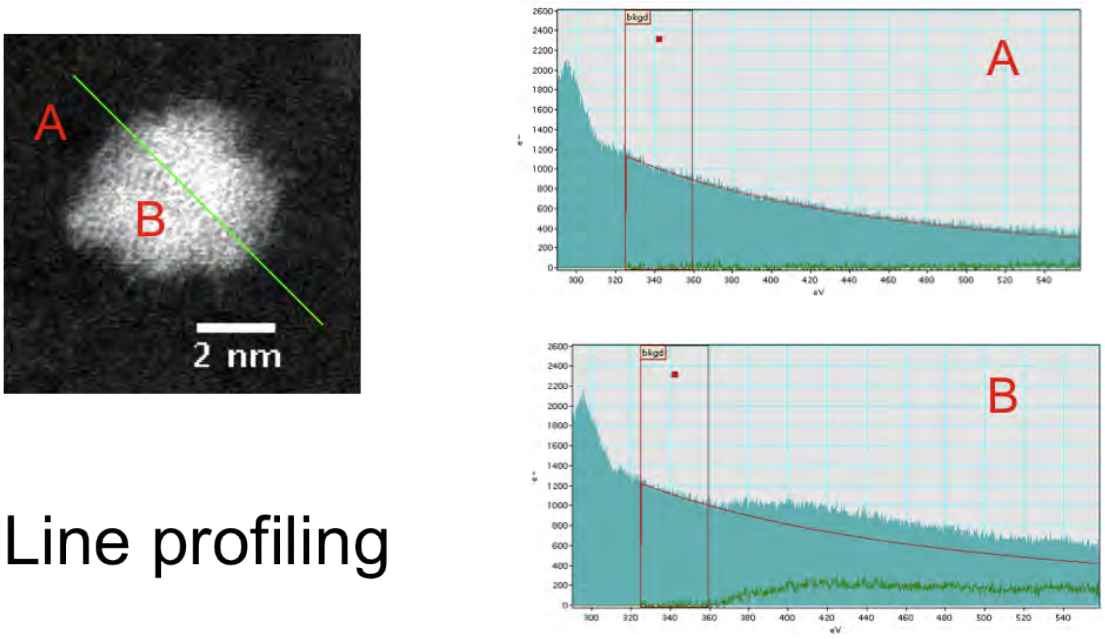

Figure 4.44: EELS spectrum of a ~4 nm size in-flight coated Pd_{923} cluster deposited at an energy of 1.5 keV on carbon coated TEM grid sample. The spectrum at points A and B at the line profile indicates the absence and presence of the element Pd respectively.

Furthermore, by using spectrum imaging to map the Pd in a cluster to compare it with its HAADF image, corroborates the evidence of the EELS spectrum indicating Pd element dominated clusters, see Figure 4.45.

For comparison Pd_{923} clusters were deposited on a carbon coated TEM grid sample at an energy of 0.5 keV without being coated in flight. The beam current reached 70 pA and the deposition lasted for 15 min, yielding a coverage of 63000 pA·s. This much higher theoretical coverage is also quite evident from the HAADF-STEM images, which show much higher actual coverages of clusters (see Figures 4.46 and 4.47) than previous samples. The actual coverage is comparable to the actual coverage observed for the sample deposited with Pd_{55} clusters through the Ar matrix. As was found for the in-flight coated Pd_{55} cluster sample with a deposition energy of 1.5 keV, the beam current increased from 2 pA to 20 pA when translating the matrix holder from the beam's line-of-sight. This clearly shows that the thin film blocks the Pd clusters more than the solid matrix. How-

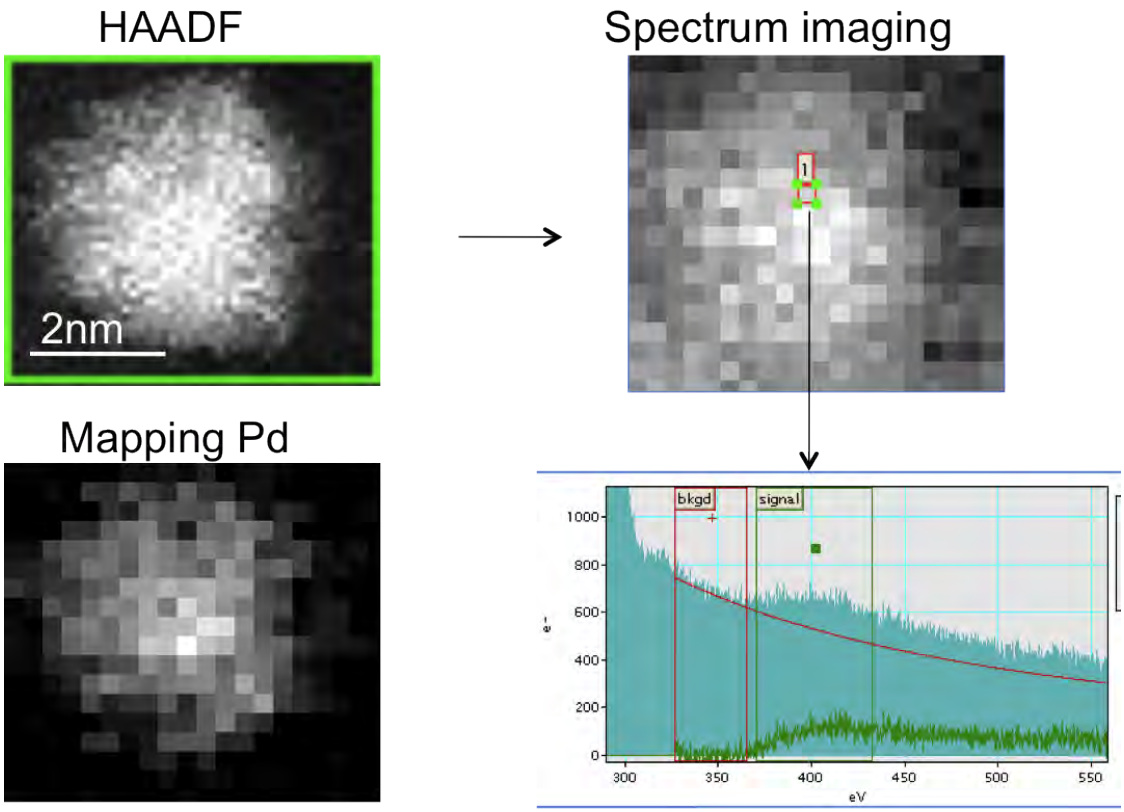

Figure 4.45: Spectrum imaging of a ~4 nm size in-flight coated Pd_{923} cluster deposited at an energy of 1.5 keV on carbon coated TEM grid sample.

ever, it is also known that the actual coverage can be quite different from the theoretical coverage. More so if the experiment lacks a purposeful mask to ensure that all clusters counted (through beam current) are actually deposited onto the area desired. This seems to be the case with the Pd_{923} cluster comparison sample, as no mask (aperture) was used, one can expect that the clusters would deposit on any piece of the tape drive (and/or TEM grid metal rectangle sample holder) that is biased. It might well be, that the largest actual coverage possible with the setup used, is the coverage obtained for the Pd_{923} cluster comparison sample and the sample with Pd_{55} clusters deposited through the Ar matrix. Any increases to the parameters controlling the coverage would probably just increase the coverage on or cover other non-expected, or even non-desired areas (instead of increasing the coverage of the desired area).

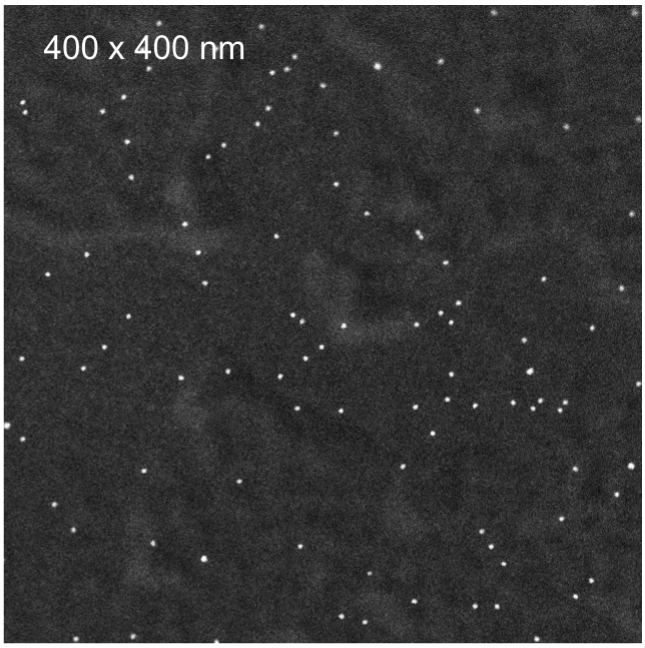

Figure 4.46: HAADF-STEM image of carbon coated TEM grid sample deposited with Pd_{923} clusters at an energy of 0.5 keV (400 nm × 400 nm).

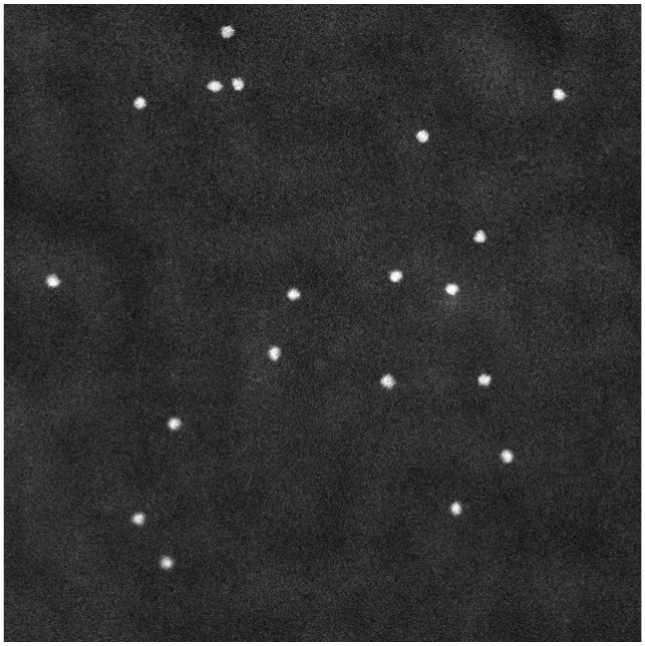

Figure 4.47: HAADF-STEM image of carbon coated TEM grid sample deposited with Pd_{923} clusters at an energy of 0.5 keV (160 nm × 160 nm).

Studying the diameters of the deposited Pd_{923} clusters, shows they consistently correspond to the size of the theoretically calculated diameter for Pd_{923} according to the spherical

approximation, see Figure 4.48. The Pd_{923} clusters had a mean diameter of 3.00±0.26 nm, which is in agreement with the theoretical value 3.0 nm (SCA). In addition, the centre and the width of the Gaussian fit of the histogram, in Figure 4.48 is 3.03 nm and 0.17 nm, respectively. The theoretical diameter of a hemispherical Pd_{923} cluster is 3.7 nm, a very small number of deposited clusters had a diameter as big or larger than this, see Figure 4.48.

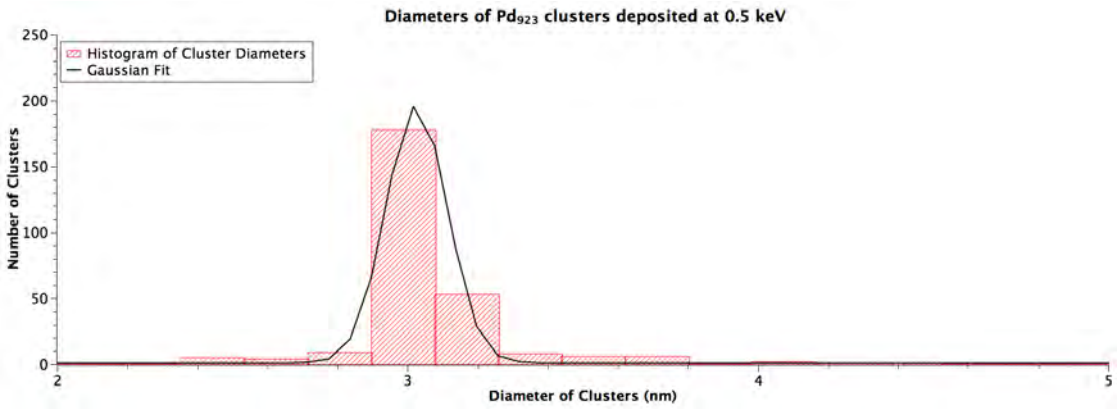

Figure 4.48: Diameters of individual clusters of Pd_{923} clusters deposited at an energy of 0.5 keV on a carbon coated TEM grid sample. The histogram bin size has been chosen to best reflect the data.

By looking at the clusters at the atomic-scale, one can confirm that most of them have low-symmetry structures (see Figure 4.49) similar to previous results from earlier samples. As can be seen in Figure 4.50, icosahedral structures can be observed, see the 2-fold icosahedron pointed out by the red arrow.

EELS analysis clearly shows the presence of Pd in the cluster. The EELS spectrum, taken at the two points A and B of the line profile across a Pd_{923} cluster, shows the absence of Pd at A indicating the carbon coated TEM grid sample background and the presence of Pd at B indicating the centre of the cluster shown by the Pd core-loss signal, see Figure 4.51.

The final Pd cluster size studied in the in-flight coating experiments was 2000 atoms. Two carbon coated TEM grid samples were prepared with Pd_{2000} clusters coated in flight, one

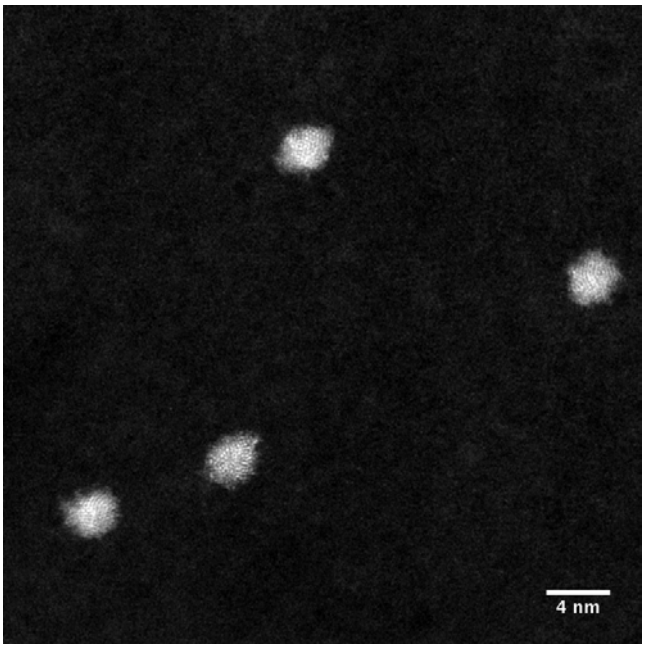

Figure 4.49: HAADF-STEM image of carbon coated TEM grid sample deposited with Pd_{923} clusters at an energy of 0.5 keV (4 nm scale bar).

deposited at an energy of 0.5 keV and the other at 1.5 keV. On the 1.5 keV sample, the beam current reached ~5 pA, yielding a theoretical coverage of ~9000 pA·s with a deposition time of ~30 min. The actual cluster density is very low, as can be observed in Figure 4.52, which depicts the typical coverage throughout the TEM grid. As indicated by the red arrow, only one in-flight coated Pd_{2000} cluster can be found in the image, which covers an area of 320 nm × 320 nm, while at the same time, two, much larger, contaminants can be found (see arrows in Figure 4.52).

The coverage is the lowest detected from all samples, where clusters have been observed. The theoretical coverage is approximately half the calculated coverage of the in-flight coated Pd_{923} cluster samples (0.5 and 1.5 keV deposition energy), which of course should render an expectation of lower actual cluster density for the Pd_{2000} cluster sample. Furthermore, at 0.75 eV/atom (1.5 keV deposition energy, Pd_{2000}) the deposition energy per atom is slightly higher, but comparable to 0.54 eV/atom (0.5 keV deposition energy, Pd_{923}) and more than half the value 1.63 eV/atom (1.5 keV deposition energy, Pd_{923}), which could

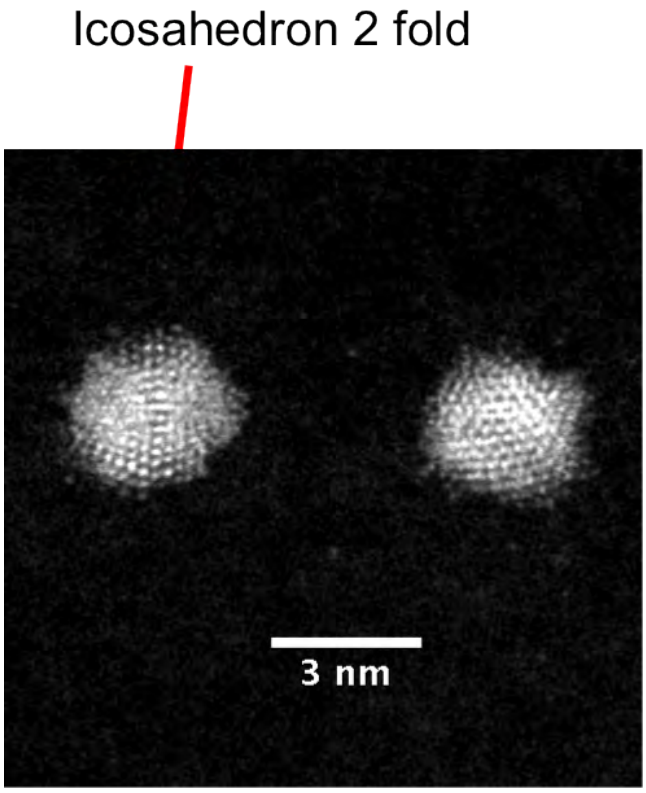

Figure 4.50: HAADF-STEM image of carbon coated TEM grid sample deposited with Pd_{923} clusters at an energy of 0.5 keV (3 nm scale bar).

explain the matter. Lower deposition energy per atom for larger clusters would render it more difficult to penetrate the thin film and solid matrix during the in-flight coating process. For both Pd_{923} in-flight coated cluster samples the actual coverage is comparable, with the 0.5 keV deposition energy sample having a slightly higher cluster density. This is also despite finding out that the beam current of the 1.5 keV deposition energy sample having a higher beam current, partly or fully, throughout its deposition time yielding it a higher theoretical coverage than the 18000 pA·s for the 0.5 keV deposition energy sample (between 18000–45000 pA·s). Therefore, the much lower calculated cluster density together with the lower deposition energy per atom (in relation to mass/cross section), explains somewhat the quite low actual coverage of in-flight coated Pd_{2000} cluster TEM grid sample.

Figure 4.53 shows the histogram of different observed cluster diameters, where most clus-

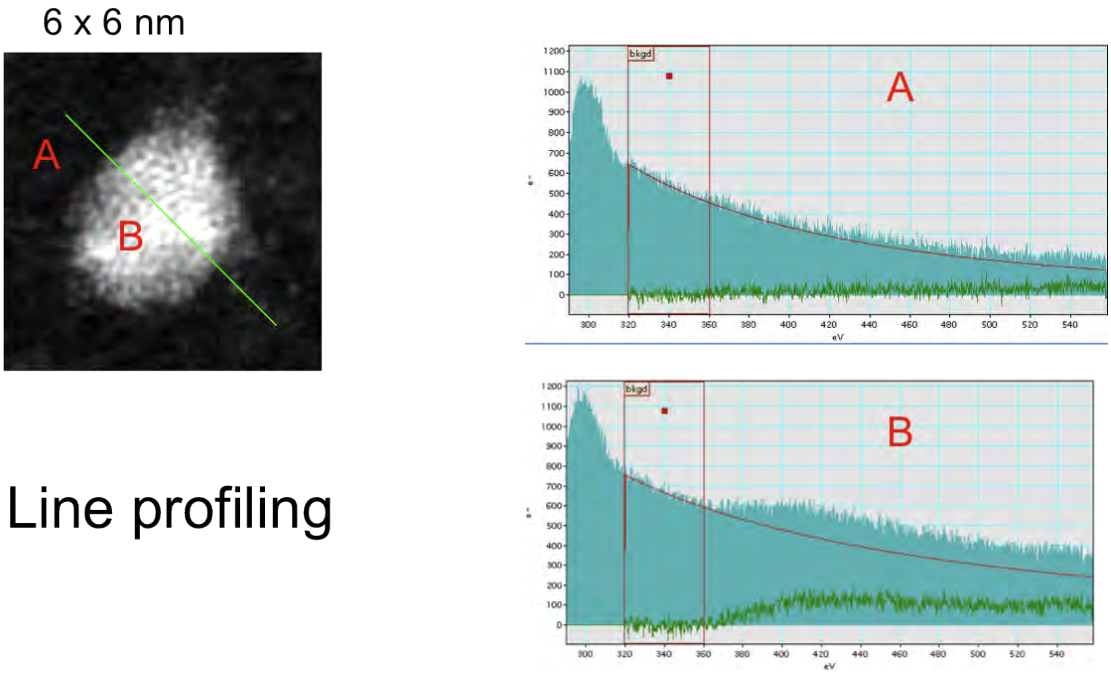

Figure 4.51: EELS spectrum of a ~3–4 nm size Pd_{923} cluster deposited at an energy of 0.5 keV on carbon coated TEM grid sample.

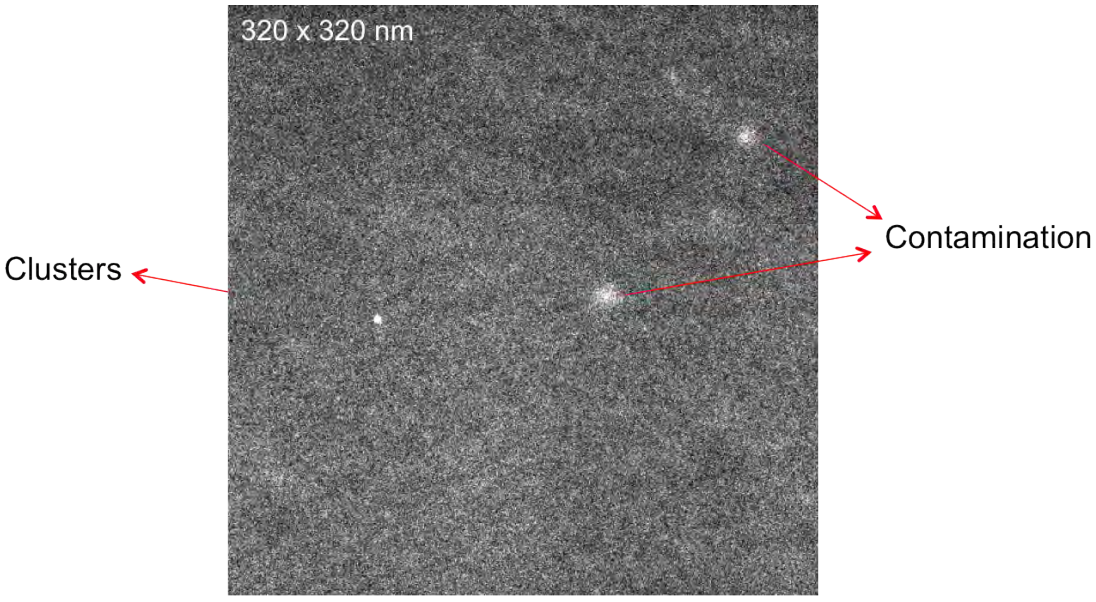

Figure 4.52: HAADF-STEM image of carbon coated TEM grid sample deposited with coated Pd_{2000} clusters in flight at an energy of 1.5 keV (320 nm × 320 nm).

ter sizes are found to be around 5 nm. The theoretical diameter for Pd_{2000} is 3.8 nm according to the spherical approximation and 4.8 nm according to the hemispherical approximation. As the measured diameters are larger for the majority of the clusters than

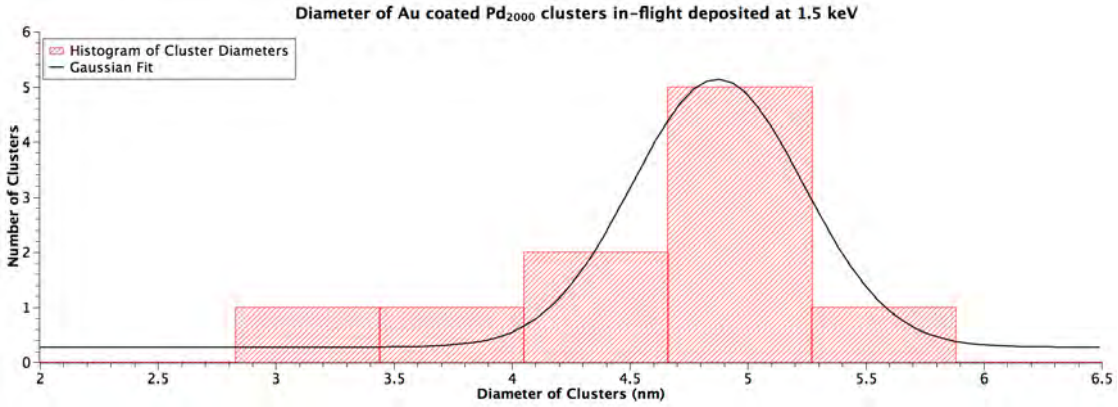

Figure 4.53: Diameters of individual clusters of coated Pd_{2000} clusters in flight and deposited at an energy of 1.5 keV on a carbon coated TEM grid sample. The histogram bin size has been chosen to best reflect the data.

both those values and any deformation of the clusters is ruled out, the success of the in-flight coating is once again clearly evident. The deformation of both Pd_{923} clusters and coated Pd_{923} clusters in flight has been contested against above with the actual diameters of Pd clusters more or less matching the theoretical diameter according to the spherical approximation. As no deformation was found for Pd_{923} clusters with a deposition energy per atom of 0.54 eV/atom (0.5 keV deposition energy), similarly, no deformation should be expected from Pd_{2000} clusters with a slightly higher, but still comparable deposition energy per atom (0.75 eV/atom, 1.5 keV deposition energy). As all clusters have larger diameters than the spherical approximation diameter for Pd_{2000} they have all been successfully coated in flight, with the slight differences in the size of their final diameters being both variations in the Pd cluster sizes and the thin film coverage.

EELS analysis also indicates the presence of palladium in the clusters. Figure 4.54 shows EELS spectra of both a coated Pd_{2000} cluster in flight and the carbon coated TEM grid sample background, verifying the Pd core-loss signal detected on the cluster. The corroborating evidence build up a strong case in favour of the success of the in-flight coating method and technique.

Pd_{2000} clusters deposited at an energy of 0.5 keV (deposition energy per atom of 0.25 eV/atom)

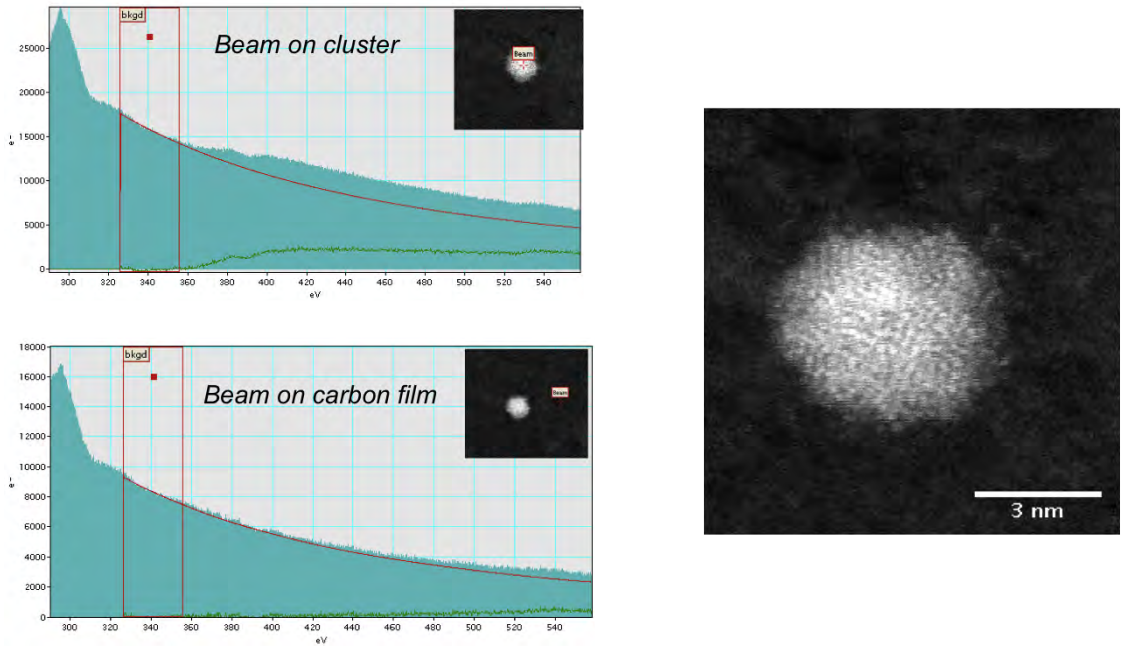

Figure 4.54: EELS spectrum of a ~5–6 nm size in-flight coated Pd_{2000} cluster deposited at an energy of 1.5 keV on carbon coated TEM grid sample. The spectrum at the carbon background and at the cluster centre indicates the absence and presence of the element Pd respectively.

and coated in flight would have quite a resemblance to the Pd_{2000} cluster sample deposited at 1.5 keV, and including the previous deposition-energy argument, even more so as the deposition energy (per atom) is three times lower. The actual cluster coverage is as expected quite similar to the actual coverage of the in-flight coated Pd_{2000} cluster sample at 1.5 keV deposition energy, see Figure 4.55. The cluster density observed in the HAADF-STEM image is the typical coverage across the whole sample, but sometimes areas with higher density are observed, as in Figure 4.56. The theoretical coverage of the sample is 7200 pA·s as the deposition time was ~30 min and the palladium cluster beam current roughly 4 pA, which is lower, but comparable to 9000 pA·s, the calculated coverage of in-flight coated Pd_{2000} at 1.5 keV deposition energy. The density in Figure 4.56 certainly is a rare case and actually the exception rather than the norm.

The diameters of the coated Pd_{2000} clusters in flight lie around 5 nm (see Figure 4.57), which is slightly higher than the hemispherical approximation value of Pd_{2000} 4.8 nm

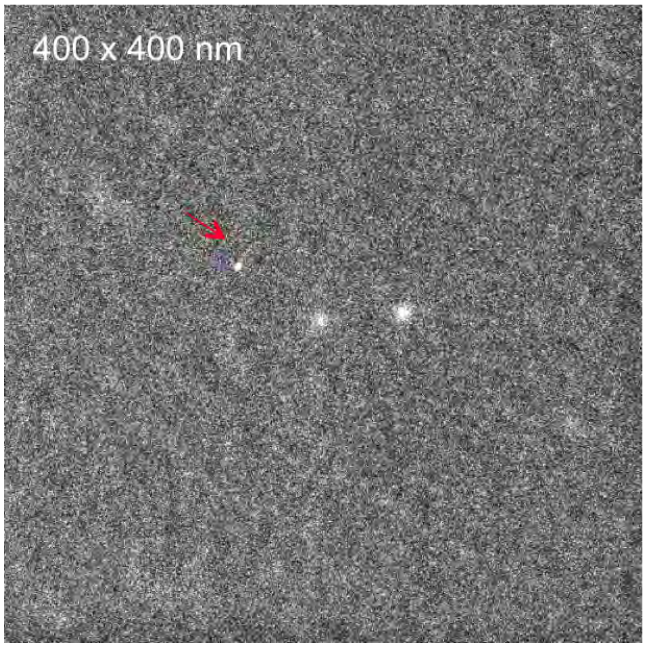

Figure 4.55: HAADF-STEM image of carbon coated TEM grid sample deposited with coated Pd_{2000} clusters in flight at an energy of 0.5 keV (400 nm × 400 nm).

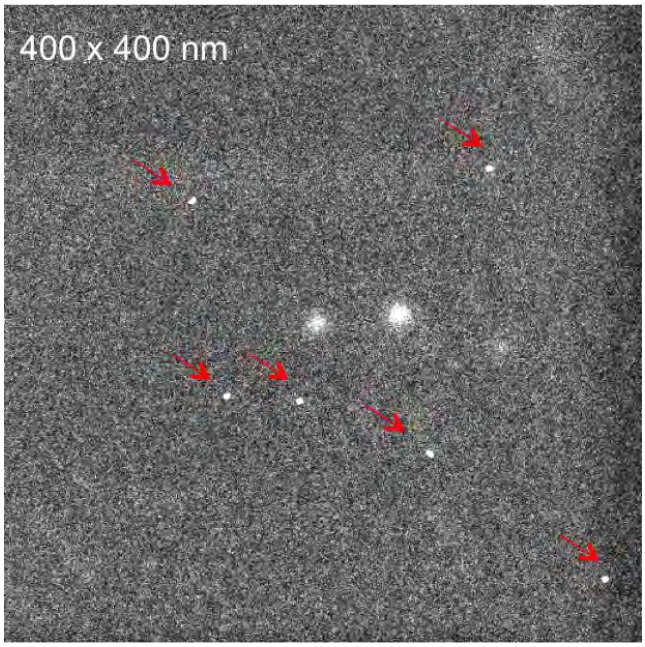

Figure 4.56: HAADF-STEM image of carbon coated TEM grid sample deposited with coated Pd_{2000} clusters in flight at an energy of 0.5 keV (400 nm × 400 nm).

and much higher than 3.8 nm which is the value of the spherical approximation for same cluster. The previous argument and evidence of non-deformation due to low deposition

energy per atom holds even more for this sample, as it has the lowest deposition energy per atom of all the samples deposited in this batch. The much larger cluster diameters measured, therefore, give clear evidence of the Pd_{2000} clusters (with diameters of 3.8 nm) being coated in flight (by penetrating ~2.68 nm thin film), giving them a final diameter of around 5 nm.

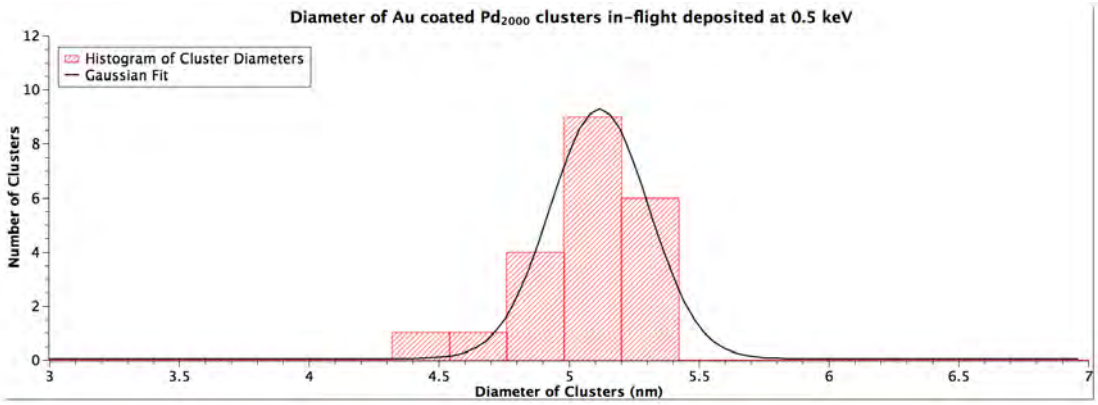

Figure 4.57: Diameters of individual clusters of coated Pd_{2000} clusters in flight and deposited at an energy of 0.5 keV on a carbon coated TEM grid sample. The histogram bin size has been chosen to best reflect the data.

By atomic-scale investigation of the clusters one can clearly observe their low-symmetry structure, see Figure 4.58. Finding symmetric structures among the in-flight coated clusters was not expected nor anticipated due to the complexity of the method. In that light, the first results obtained, that showed platelet-like structures with irregular shapes, were not too surprising. Verifying the presence of the Pd clusters (somewhere) inside the resulting particles would have made the whole effort worthwhile and labelled it a success. The lack of Pd could potentially be due to the Pd clusters being blocked and only transfer their energy at impact with the thin film, which knocks off particles for deposition.

The deposition of Pd_{55} clusters through the Ar matrix covered TEM grid (without the Au metal film), verified that the deposited particles have sizes consistent with Pd_{55} clusters. Thus, resulting particles have no (significant) inclusion of Ar from the solid matrix nor Cu from the TEM grid. Deposition of a Au metal film was verified through visual inspection

during testing, profiler measurements, AFM imaging and HAADF-STEM imaging. The resulting particles with their much larger sizes and differing shapes in comparison to the impacting Pd_{55} clusters, onto the metal/matrix covered TEM grid, are therefore attributed to the differing factor, which is the presence of the evaporated metal film. In addition, EELS analysis together with HAADF-STEM imaging implicitly verified that the resulting particles are (at least) made up of a material other than Pd, which (with a very high likelihood) is Au. Furthermore, the much larger sizes and differing shapes of the resulting particles compared to both Pd_4 and Pd_{561} clusters, impacting onto the metal/matrix covered TEM grid, also corroborate the role of the evaporated metal film in the formation of the resulting particles. Again, EELS analysis together with HAADF-STEM imaging implicitly verified that the resulting particles are (at least) made up of a material other than Pd, which (with a very high likelihood) is Au. Moreover, the deposition of Pd_{923} clusters verified that the deposited particles have sizes consistent with Pd_{923} clusters. The resulting particles with their much larger sizes and broader size distribution compared to the impacting Pd_{923} clusters, onto the metal/matrix covered TEM grid, further support the role of the evaporated metal film in the formation of the resulting particles. Now, however, EELS analysis also explicitly confirms the presence of Pd. This is also the case for Pd_{2000} clusters, which allows for the conclusion that the Au metal is coating the original impacting Pd clusters.

EELS analysis was focused on finding one species (the original cluster i.e. Pd) of the resulting binary particles as the other (i.e. Au) can be deducted from verifying the size increase of the particles compared to the original clusters. They can also be verified by observing the resulting particles in HAADF-STEM images and find areas with relative intensity difference if the materials are segregated. Au (79) with a higher atomic number than Pd (46) would have a higher relative intensity and a clear contrast would distinguish the two materials, in a particle, when clearly segregated.

Not being able to verify the presence of Pd through neither HAADF-STEM (e.g. if core-shell structure) nor EELS analysis, pushed the pursuit of more favourable parameters of the in-flight coating experiments until it was possible to explicitly verify the presence of palladium within the final structure. The clear bonus here, of course, is that instead of having irregularly shaped platelet-like structures of in-flight coated Pd clusters, the end results have at least low-symmetry structures. Some in-flight coated clusters even show ordered lattice structures, such as FCC polyhedra, which is quite different from the results of the first two batches of samples. The evidence of a clear-cut core-shell structure would have been the dream result. For now, however, that can neither be ruled out nor verified explicitly.

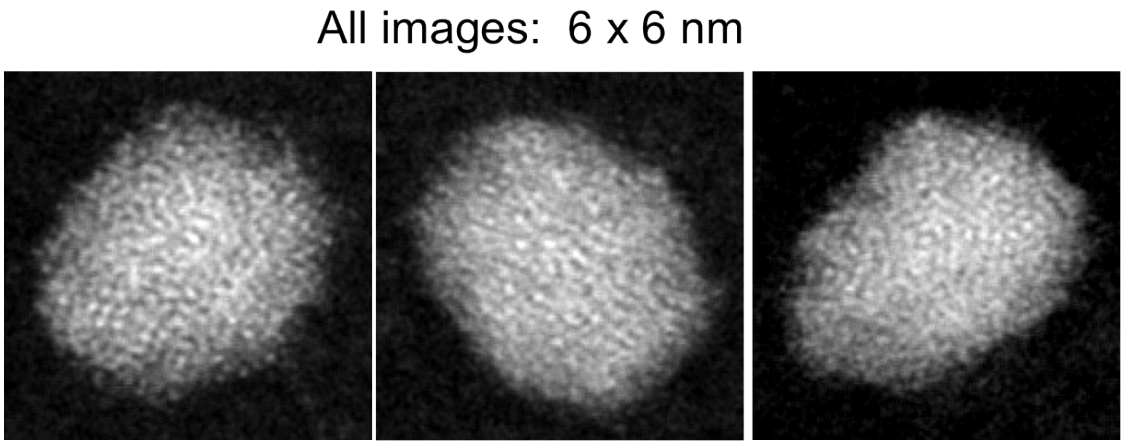

Figure 4.58: HAADF-STEM image gallery consisting of 3 coated Pd_{2000} clusters in flight and deposited at an energy of 0.5 keV on the same carbon coated TEM grid sample, but at different positions (6 nm × 6 nm).

Ending this chapter with the novel use of in-flight coating of clusters, which could be used to enhance catalysis, yet a novel use of clusters to fabricate better catalysts is embarked upon in the coming chapter.

4.4 Summary

The cluster source was refurbished and the deposition chamber was upgraded with a liquid helium cryostat with all compatible parts (dewar, transfer arm, thermometer, etc.) in order to cool argon gas into a solid matrix onto a TEM grid on a holder at the end of the cryostat. A bespoke evaporator was also fitted so that a thin metal (Au) film could be evaporated onto the solid argon matrix, which was successfully impinged by Pd clusters as particles were deposited on carbon coated TEM grids on the multi-sample holder (converted tape drive).

For smaller Pd clusters (Pd_4 & Pd_{55}) impacting the thin film on solid argon matrix, e.g. Pd_{55} (~1 nm in gas phase SCA) at 1.5 keV, irregularly shaped particles were deposited with 5-40 nm sizes. Much fewer of these similar particles were deposited by the, even smaller, Pd_4 clusters impacting the thin film at 1 keV. Pd_{561} clusters impacting on a thinner film at 1 keV have, more or less, similar end result as for the Pd_{55}. These results show the feasibility of the in-flight coating technique as Pd clusters are clearly able to deposit particles, but as no Pd signal can be found in the EELS analysis of these samples and because of the actual shapes of the deposited particles, one can not talk about a coating process of the impacting Pd clusters. The Pd clusters could be blocked at impact with the thin film and only transfer their energy, which knocks off particles for deposition. Moreover, the multifold increase in size of the resulting particles compared to the initial clusters (30-40× for Pd_{55} and ~45× for Pd_4) suggest an interesting feature that could be developed and adapted for different uses.

For larger Pd clusters (Pd_{923} & Pd_{2000}) impinging on even thinner film (~2.68 nm), with even lower deposition energies per atom (0.5- and 1.5 keV), the deposited particles are spherical in shape and show relatively larger sizes than the initial impacting Pd clusters. For Pd_{923} clusters having a theoretical (SCA) diameter of ~3 nm and actual diameter the same (deposition energy of 0.5 keV) and resulting in-flight coated particles having

diameters around and above 4 nm for deposition energies of 0.5- and 1.5 keV, respectively, it is evident that the initial impacting clusters have increased in mass by either partial or complete atomic layer(s) coating from the thin film. Moreover, the detection of a Pd signal from the coated Pd clusters through EELS corroborates this clear fact, instead of assuming that the larger deposited clusters are Au nano particles evaporated onto the solid argon matrix and knocked off by the impacting Pd clusters. Similarly, Pd_{2000} clusters with theoretical diameters of 3.8 nm show deposited in-flight coated particles having diameters around 5 nm for both deposition energy of 0.5 keV and 1.5 keV, which together with the detection of a Pd signal from the in-flight coated clusters by EELS analysis, once again proves the success of the in-flight coating technique used.

There are many things that can be thought of for future continuation of ongoing projects. However, following, investigating and developing serendipitous discoveries should always take precedence. It is in the front of these waves that new exciting breakthroughs are made and in which current knowledge are expanded upon.

The in-flight coating experiments were truly uplifting in the above sense and can easily be improved in order to better evaluate many of the factors that were speculative in the process due to the proof-of-principle nature of the experiments forced by the rapid project prototyping undertaken. All of that can be improved upon and is, to be fair, worth a mention for future proposals. However, the focus should be on something new, based on discoveries made during the in-flight coating experiments.

The badly shielded off carbon coated TEM grid sample being Au evaporated and exhibiting a high coverage of Au nano particles sparks a new idea together with the Pd_4 clusters knocking off huge chunks of the thin film, supported on the solid argon matrix, when being impacted. A new way of generating clusters (a new cluster source) is envisaged using similar techniques utilised in the in-flight coating experiments. The evaporation of metals (materials) when confined can be highly efficient and economical compared to current

and other methods of generating clusters. Developing new ways of measuring/controlling the solid argon matrix thickness and the metal thin film(s), would allow for a way to control the size of resulting clusters deposited on samples on the other end when small particles impact the 'sandwich' surface. These small particles could be single ions and maybe, in certain cases, even alpha particles (helium nucleus), protons/neutrons (nucleons), beta particles (electrons) or photons. It would be possible to run it continuously or pulsed, have single element clusters or multi-element clusters (high material versatility) while keeping a much smaller footprint and using much less resources than current systems. The possibility of high throughput and mass resolution would make it well suited for catalyst production as has been pursued at points during the work.

It is encouraging that people in the NPRL group have picked up the mentioned insights from the in-flight coating experiments and built a new novel kind of (compact) cluster source, which utilises an ion gun to create a beam of clusters when hitting a co-deposited metal/rare-gas matrix covered TEM grid.

CHAPTER

FIVE

FORMATION OF MOS_2 NANO PILLAR STRUCTURES

MoS_2 is of huge interest (see Section 1.4.1 in Chapter 1) as it can be used as a photocatalyst in the hydrogen evolution of water, using solar energy. Dealing with this semiconductor material at the nanoscale is key to enhancing its catalytic properties. This could for example be achieved by structuring the surface through etching, applying clusters (and other types of etch masks) as tools when forming these nanostructures.

In this chapter, the fabrication, characterisation and testing of MoS_2 nanopillar structures will be covered. The first section will cover randomly positioned pillars with accurate size control. In the second section a novel multi-step method of nano-lithography is used to create a regular nanopillar array structure. A simplified method is covered, in the third section, to produce regular well-shaped pillars with close-packed latex polymer nano spheres and size reducing processing steps. The electrochemistry measurements of these samples are also presented in comparison to references.

MoS_2 was processed similarly to other known and ubiquitous semiconductors such as silicon for example. As mentioned in Chapter 2, Section 2.2 on page 74, the fabrication

of the structures was performed in a plasma etcher from Oxford Instruments in cleanroom conditions. The formation of different pillar structures was controlled by varying etching parameters such as the process gases, their flows and the plasma powers. The parameter space leading to specific geometries after etching is quite confined, which gives similar repeat results.

5.1 Non-Ordered MoS_2 Nano Pillar Structures

The first approach to pillar structures is by using metal clusters (Pd and Au) as etch masks to selectively etch exposed MoS_2. Fabrication-wise, this technique uses the least number of steps in the structure formation, however the price is paid by the complex process of cluster formation, manipulation and deposition. The cluster part of this work will not be covered in great detail here, as it has already been dealt with in all previous chapters, see Chapter 1, 2 and 3. However, brief information about the deposited clusters on the substrates will be given for the obvious benefit.

Sample	Name	R3	R4
	Batch	1	"
	Substrate	MoS_2	"
Pre-deposition	Deposit	Ar_1^+	-
	Impact Energy (keV)	0.5	-
	Beam Current (pA)	200	-
	Deposition Time (s)	23	-
	Coverage (pA·s)	4600	-
Deposition	Deposit	Pd_{10000}	"
	Impact Energy (keV)	0.5	"
	Beam Current (pA)	20	"
	Deposition Time (s)	115	"
	Coverage (pA·s)	2300	"

Table 5.1: Batch One contains two samples, with the only difference being that one sample (R3) is bombarded with argon ions prior to deposition in order to create defects for metal clusters to bind to. The beam current was deposited on a circular area having 4 mm diameter.

There were several batches of size-selected metal clusters on MoS_2 samples. Figures 5.1a

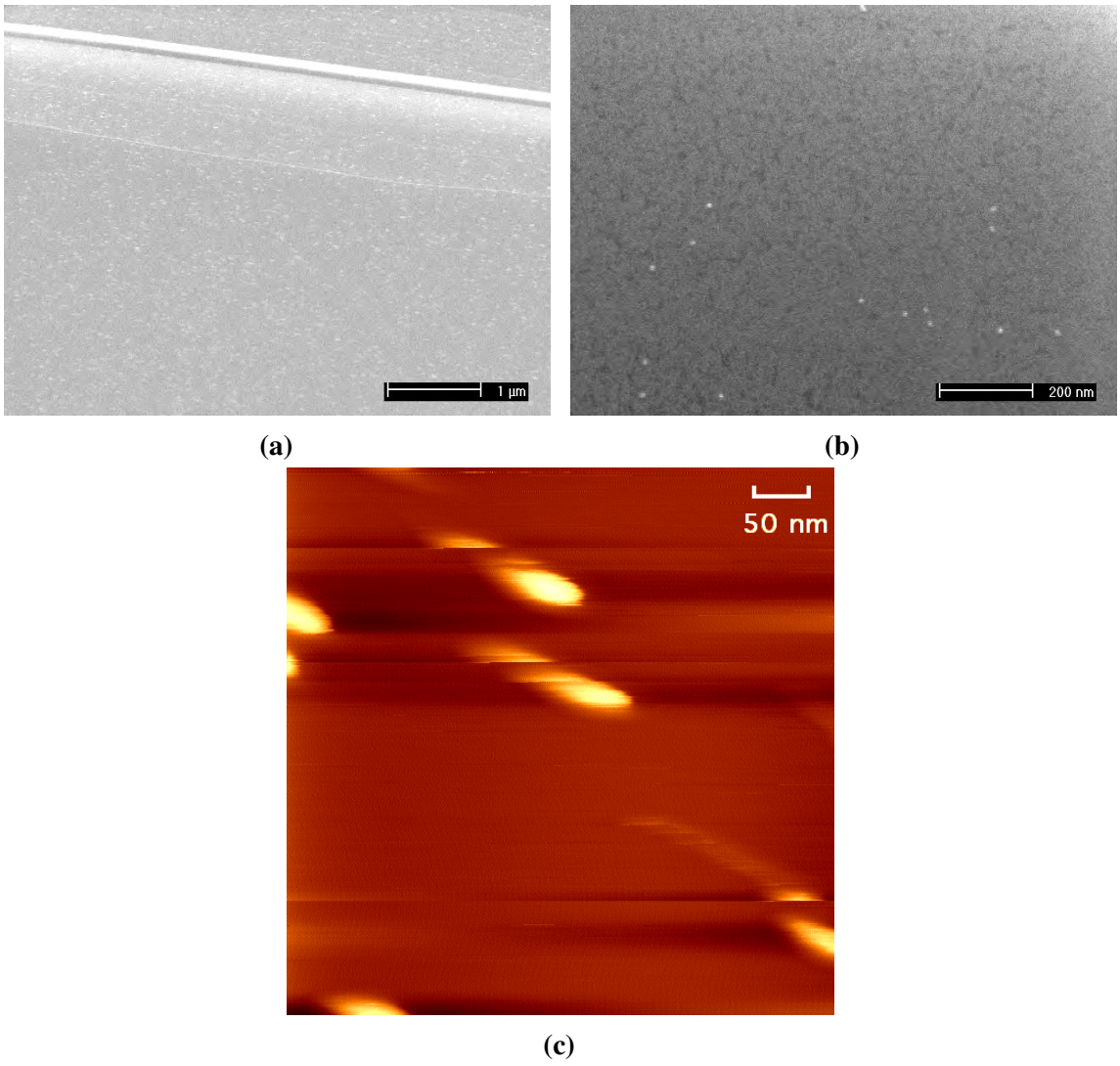

Figure 5.1: SEM image (40000× magnification) of Pd_{10000} clusters deposited on MoS_2 with a coverage of ~2300 pA·s and at an energy of 0.5 keV. The substrate was pre-deposited with Ar_1^+ with a coverage of ~4600 pA·s at an energy of 0.5 keV in order to create defects to immobilise the palladium clusters. (a) The clusters are visible as bright short streaks (caused by slight drift during the acquisition of the image), on the natural MoS_2 crystal substrate and can be found throughout the sample, on different terrace layers (45°, 1 μm scale bar). (b) SEM image of zoomed in area (200000× magnification) depicting a couple of Pd_{10000} clusters deposited on MoS_2 (45°, 200 nm scale bar). The theoretical gas phase diameter, according to the spherical approximation, is ~6 nm for Pd_{10000} and the instrument used can typically resolve ~5-10 nm. (c) AFM image of Pd_{10000} clusters deposited on MoS_2 with a coverage of ~2300 pA·s and at an energy of 0.5 keV. This sample has not been pre-deposited with argon ions to create defect sites in order to pin the clusters and thus the clusters are moved by the tip (downwards and to the right) during image scanning (50 nm scale bar).

and 5.1b depict SEM images from the first sample (R3), from the first batch, and Figure 5.1c an AFM image of the second sample (R4), see Table 5.1 for sample information. The clusters in Figure 5.1a are visible as bright short streaks (caused by slight drift during the acquisition of the SEM image) on the natural MoS_2 crystal substrate and can be found throughout the sample. A couple of Pd_{10000} clusters (~6 nm diameters) deposited onto MoS_2 are seen with greater magnification in Figure 5.1b. The second sample has not been pre-deposited with argon ions to create defect sites, in order to pin the clusters, and thus the clusters are moved by the tip (downwards and to the right) during AFM image scanning, see Figure 5.1c.

Sample	Name	R3
	Deposit	Ar_1^+/Pd_{10000}
	Substrate	MoS_2
Strike Step	Time (s)	5
	APC Pressure (mTorr)	15
	Temperature (°C)	20
	He Pressure (Torr)	10
	O_2 (sccm)	-
	SF_6 (sccm)	1
	C_4F_8	50
	RF Power (W)	50
	ICP Power (W)	300
Main Step	Time (s)	30
	APC Pressure (mTorr)	15
	Temperature (°C)	20
	He Pressure (Torr)	10
	O_2 (sccm)	-
	SF_6 (sccm)	30
	C_4F_8	20
	RF Power (W)	20
	ICP Power (W)	100

Table 5.2: Batch one containing two samples, where one of the samples was etched. The etching process was similar to the second test sample and all relevant parameters of the process are shown in the table.

As can be seen from the AFM images (Figures 5.2a to 5.2c) of the etched sample, the etching parameters in Table 5.2 give rise to nano pillars with conically shaped bases (~20 nm

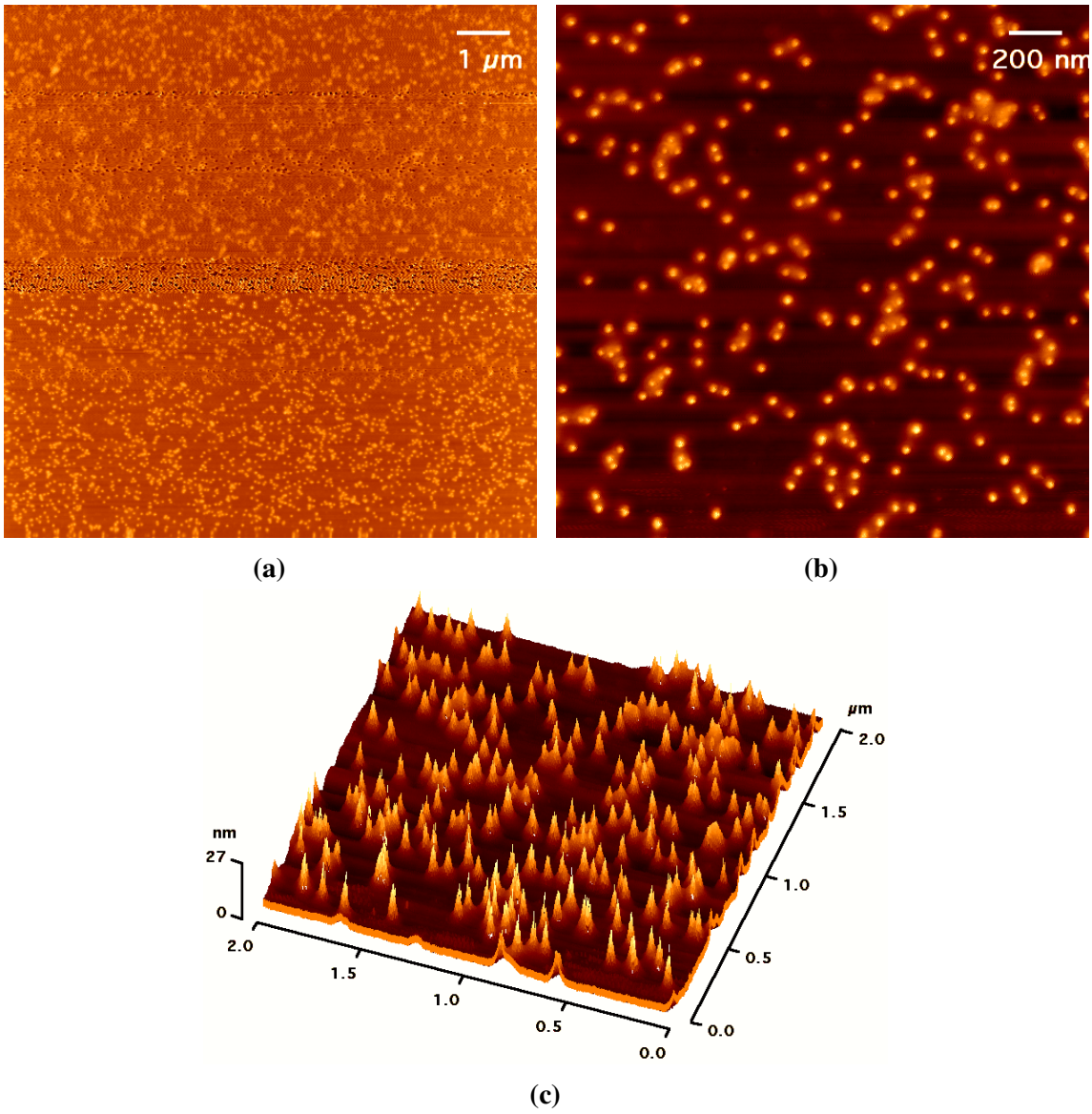

Figure 5.2: AFM image of the above-mentioned sample of Pd_{10000} clusters deposited on MoS_2, after mixed etching with parameters in Table 5.2, depicting nano pillars of MoS_2. (a) The MoS_2 nano pillars are visible as round circles (~30 nm diameters) from the top view, with lighter areas being higher parts. Note that the AFM tip picks something up half-way through the scanning, which distorts the image, but recovers somewhat near the end of the scanning (1 μm scale bar). (b) AFM image of zoomed in area (200 nm scale bar). (c) 3D AFM image with NPs visible as conically shaped pillars (~30 nm heights & ~30 nm diameters). Note that the shapes of the nano pillars visible in the SEM images is not visible in this AFM image due to the inherit nature of scanning probe microscopes' (such as the atomic force microscope) difficulty to resolve certain lateral features close to high features due to the usage of a tip (2×2 μm×27 nm).

heights & ~30 nm diameters) and cylindrically shaped tips (~10 nm heights & ~5 nm diameters).

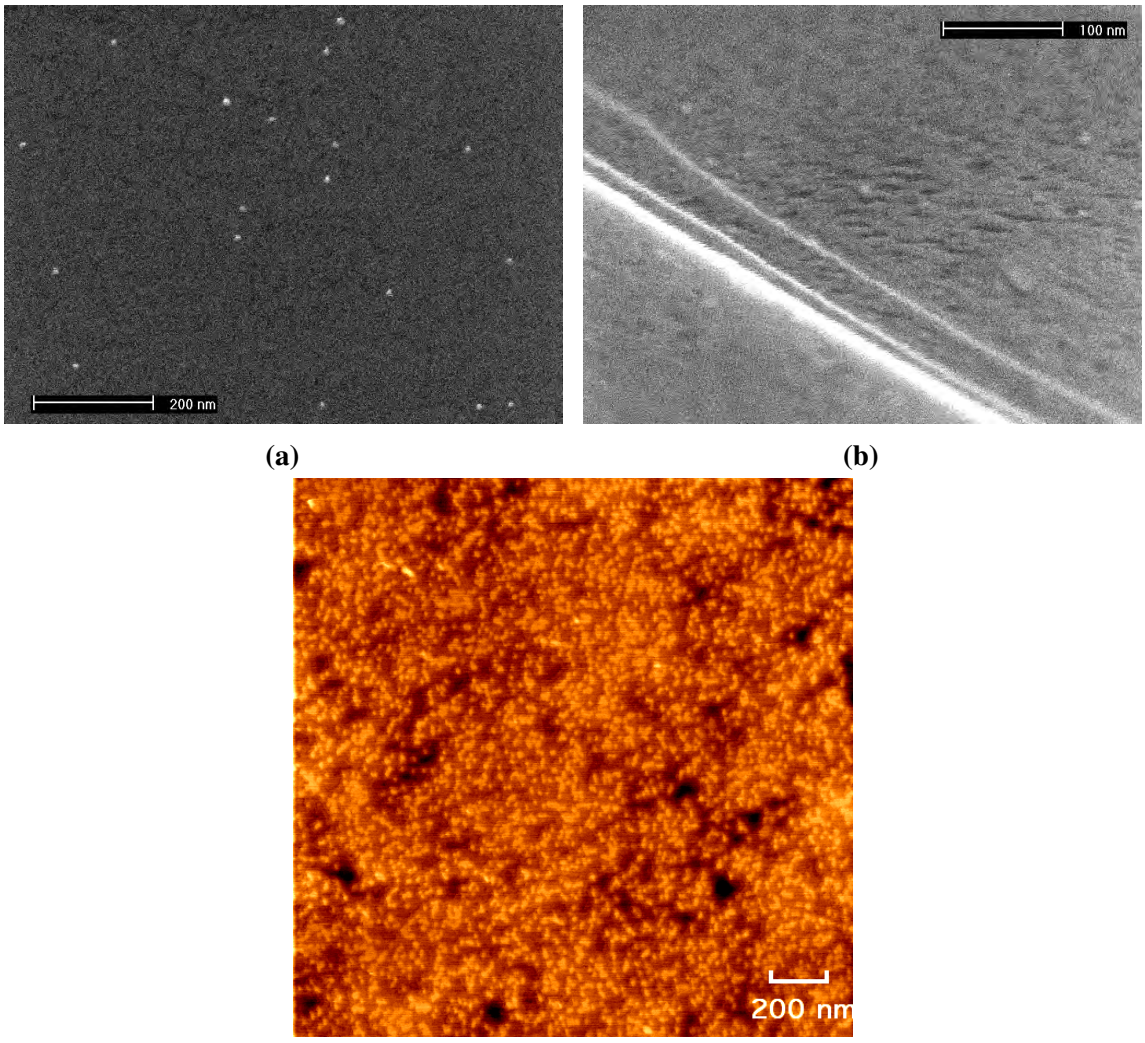

(a) **(b)**

(c)

Figure 5.3: SEM images of Pd_{10000} clusters deposited on MoS_2 with a coverage of ~2300 pA·s and at an energy of 0.5 keV. The substrate was pre-deposited with Ar_1^+ with a coverage of ~4600 pA·s at an energy of 0.5 keV in order to create defects for the palladium clusters to attach to and be pinned. The clusters are visible as bright circles, on the natural MoS_2 crystal substrate and can be found throughout the sample, on different terrace layers. The theoretical gas phase diameter, according to the spherical approximation, is ~6 nm for Pd_{10000} and the instrument used can typically resolve ~5-10 nm. (a) 250000× magnification at 45° with 200 nm scale bar and (b) 500000× magnification at 85° with 100 nm scale bar. (c) AFM image with 200 nm scale bar depicting the high coverage centre, with the very small bright yellow/orange dots representing the clusters.

	Name	R1	R2	R3	R4	R5	R6	L6	L5	L4	L3	L2	L1
Sample	Batch	2	"	"	"	"	"	"	"	"	"	"	"
	Substrate	MoS_2	"	"	"	"	"	"	"	"	"	"	"
Pre-deposition	Deposit	Ar_1^+	"	"	"	"	"	"	"	"	"	"	"
	Impact Energy (keV)	0.5	"	"	"	"	"	"	"	"	"	"	"
	Beam Current (pA)	200	180	"	190	"	"	185	190	180	185	"	180
	Deposition Time (s)	23	26	"	24	"	"	25	24	26	25	"	26
	Coverage (pA·s)	4600	4680	"	4560	"	"	4625	4560	4680	4625	"	4680
Deposition	Deposit	Pd_{10000}	"	"	"	"	"	"	"	"	"	"	"
	Impact Energy (keV)	0.5	"	"	"	"	"	"	"	"	"	"	"
	Beam Current (pA)	15	"	"	"	"	"	"	"	"	"	"	"
	Deposition Time (s)	153	"	"	"	"	"	"	"	"	"	"	"
	Coverage (pA·s)	2295	"	"	"	"	"	"	"	"	"	"	"

Table 5.3: Twelve samples were deposited in the second batch. The relevant parameters are listed in the table.

In Batch number two, 12 similar samples were deposited (see Table 5.3 for sample information). Figure 5.3 show two SEM images (a & b) and an AFM image (c) depicting the ~6 nm diameter clusters as bright circles (white in the first two and yellow/orange in the last).

Using the samples in Batch 2, different etching parameters were investigated by starting with the etching parameters for the first sample (R3), in the first batch.

	Name	R3 Batch 1	L3 Batch 2
Sample	Deposit	Ar_1^+/Pd_{10000}	"
	Substrate	MoS_2	"
Strike Step	Time (s)	5	"
	APC Pressure (mTorr)	15	"
	Temperature (°C)	20	"
	He Pressure (Torr)	10	"
	O_2 (sccm)	-	-
	SF_6 (sccm)	1	"
	C_4F_8	50	"
	RF Power (W)	50	"
	ICP Power (W)	300	"
Main Step	Time (s)	30	25
	APC Pressure (mTorr)	15	”
	Temperature (°C)	20	”
	He Pressure (Torr)	10	”
	O_2 (sccm)	-	-
	SF_6 (sccm)	30	”
	C_4F_8	20	”
	RF Power (W)	20	”
	ICP Power (W)	100	”

Table 5.4: One of the samples (L3) in the second batch was etched with similar parameters as the first sample (R3), in the first batch, except for the main step etch time, which was reduced with 5 s. All the samples' relevant etching parameters are listed in the table.

Nano pillars with conically shaped bases (~20 nm heights & ~30 nm diameters) and cylindrically shaped tips (~10 nm heights & ~5 nm diameters) are formed after etching of sample R3 from the first batch (etching parameters in Table 5.4), as can be seen from the SEM images (Figures 5.4a and 5.4b).

The pillar structures cover the etched sample (see L3 in Table 5.4 for parameters), see

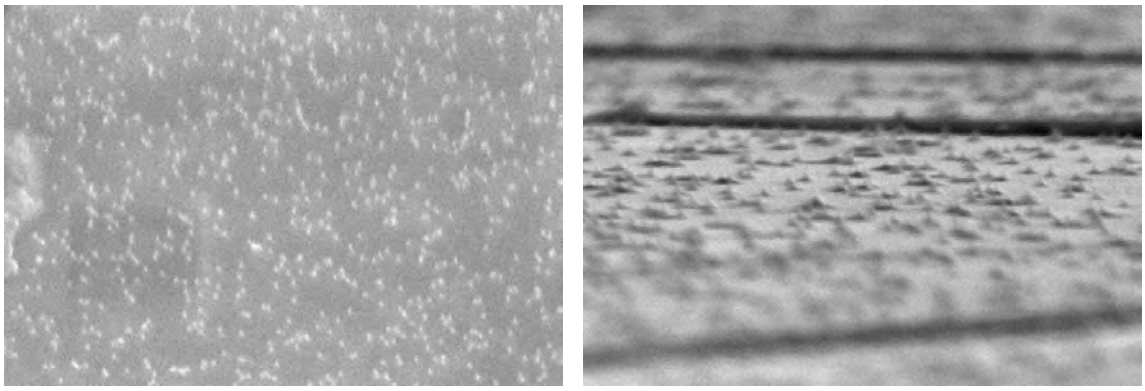

(a) **(b)**

Figure 5.4: SEM image of sample R3 after mixed etching with parameters in Table 5.4, depicting nano pillars of MoS_2. (a) The MoS_2 nano pillars, found throughout the sample, are visible as bright vertically oriented rectangles/triangles, on the natural MoS_2 crystal substrate, at a viewing angle of 45° (with respect to the surface normal). (b) Nano pillars, on different terraces (see foreground and background out of focus), are visible as conically shaped bases (~20 nm heights & ~30 nm diameters) and cylindrically shaped tips (~10 nm heights & ~5 nm diameters), on the natural MoS_2 crystal substrate, at a viewing angle of 85°

SEM images in Figures 5.5a–5.5d. The structures can be seen suspended in air after they have been etched from below and seem to have fused together, see Figures 5.5c and 5.5d. The only parameter that is different between the etching of samples R3 and L3 in Table 5.4 is the etching time of the main step. The pillars in sample R3 with the longer etch time (30 s) is more defined, while the pillar structures in sample L3 with the lower etch time (25 s) is less defined and also fused together.

Another set of samples were etched with the same different parameters, but also with the etching time of the main step varied.

Figures 5.6a to 5.6c depicts the SEM images of sample R1 etched (see Table 5.5 for parameters). 15 s etch time seem only to have resulted in roughening of the surface.

The SEM images of sample R4, etched according to the parameters in Table 5.5, can be seen in Figures 5.7a to 5.7c. A slightly higher roughening of the surface can be noticed compared to sample R1 as well as the oil contamination, in sample R4.

Nothing was found on samples L4 and R5, after etching, either, which shows that the

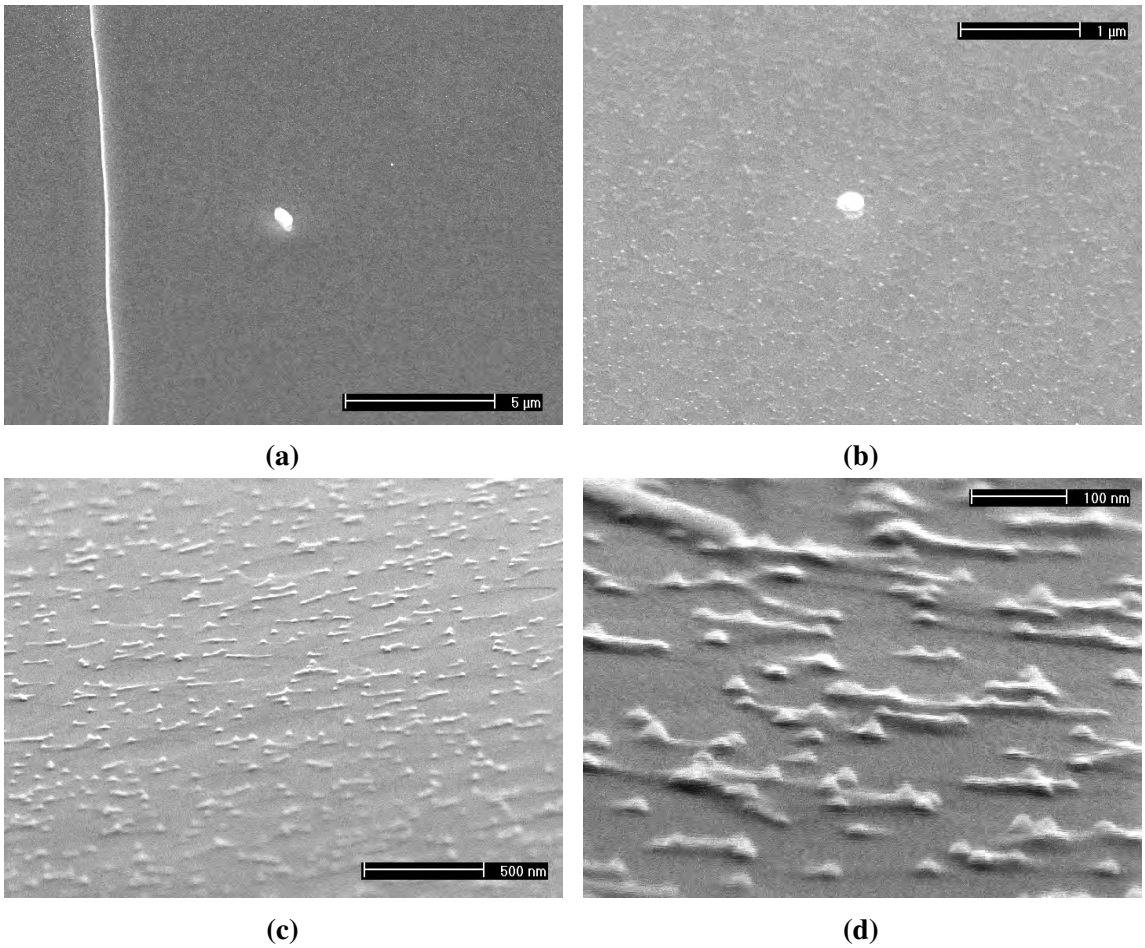

Figure 5.5: SEM images of sample L3 etched (see Table 5.4 for parameters). (a) (12500× magnification) Large area depicting terraces and large contaminant feature as well as a high coverage of (etched out) remnant pillar structures (more visible at top part of image) (45°, 500 nm scale bar). (b) (50000× magnification) Zoomed in area (45°, 1 μm scale bar). (c) (100000× magnification) Another zoomed in area with similar features (85°, 500 nm scale bar). (d) (400000× magnification) Further zoomed in area (85°, 100 nm scale bar).

overall differences in the other parameter values (Temperature and etch gas flows) have played a larger role in forming MoS_2 nano pillars.

SEM images of sample L1, as seen in Figures 5.8a and 5.8b, after etching with the parameters in Table 5.6 show pillar structures.

The SEM images of sample R6 etched (see Table 5.6 for parameters) can be seen in Figures 5.9a to 5.9c. The larger pillar at the centre in Figure 5.9c indicates that the etching time of 30 s is still too long and the metal cluster etch masks get etched away. The

	Name	R1	L4	R4	R5
Sample	Deposit	Ar_1^+/Pd_{10000}	"	"	"
	Substrate	MoS_2	"	"	"
Strike Step	Time (s)	5	"	"	"
	APC Pressure (mTorr)	15	"	"	"
	Temperature (°C)	10	"	"	"
	He Pressure (Torr)	10	"	"	"
	O_2 (sccm)	-	-	-	-
	SF_6 (sccm)	1	"	"	"
	C_4F_8	50	"	"	"
	RF Power (W)	50	"	"	"
	ICP Power (W)	200	"	"	"
Main Step	Time (s)	15	30	45	60
	APC Pressure (mTorr)	15	"	"	"
	Temperature (°C)	10	"	”	”
	He Pressure (Torr)	10	"	”	”
	O_2 (sccm)	-	-	-	-
	SF_6 (sccm)	20	"	”	”
	C_4F_8	30	"	”	”
	RF Power (W)	20	"	”	”
	ICP Power (W)	100	"	”	”

Table 5.5: Four samples from Batch Two etched with varied etching time in the main step. All the samples' relevant etching parameters are listed in the table.

etch mask of the large pillar could be aggregation of metal clusters or any other kind of impurity masking off the underlying MoS_2 during the etching process.

The SEM images in Figures 5.10a and 5.10b show sample R2 after etching (see Table 5.6 for parameters). No pillar structures are visible, only a roughening of the surface indicates that the flat atomic layered surface has been etched.

The increase of the ICP power in the main step from 100 W to 150 W, in this set of samples compared to the two previous sets (when looking at the variation of the etching time parameter), have increased the overall density of ions. This is evident as a much lower flow of the etching gas, sulphurhexafluoride (SF_6), is necessary to etch pillar structures (see SEM images for sample L1 in Figures 5.8a and 5.8b). When increasing the SF_6 gas flow (and decreasing the C_4F_8 gas flow) in the etching process, as for samples R6 and R2,

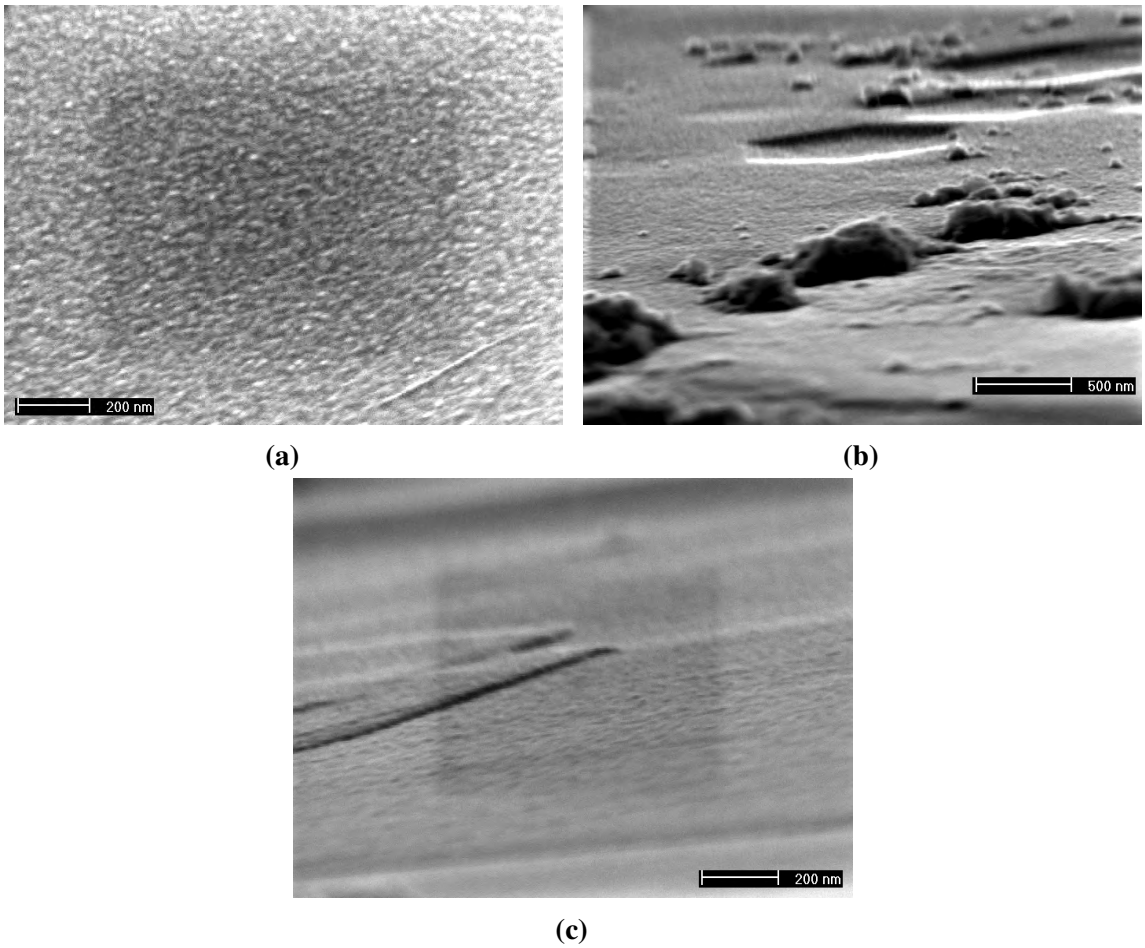

Figure 5.6: SEM images of sample R1 etched (see Table **??** for parameters). (a) (150000× magnification) Only a roughening of the surface is visible (55°, 200 nm scale bar). (b) (80000× magnification) Deliberate choice of area with contaminants to show that no pillar structures can be found throughout the sample (85°, 500 nm scale bar). (c) (160000× magnification) The area shows the roughening of the sample on different terraces (85°, 200 nm scale bar).

the much denser plasma etches away the pillar structures for the given etching time. Thus fewer, less dense, shorter or no pillar structures will be visible, see Figures 5.9a to 5.9c, 5.10a and 5.10b for corresponding SEM images of samples R6 and R2 etched.

As mentioned previously, nothing was found on sample L4 after etching, which can be compared to the pillar structures seen on sample R6 SEM images in Figures 5.9a to 5.9c. From Table 5.7, it is evident that the higher ICP power value, of 150 W, when etching sample R6, has helped to form the pillar structures through the increase of the overall ion

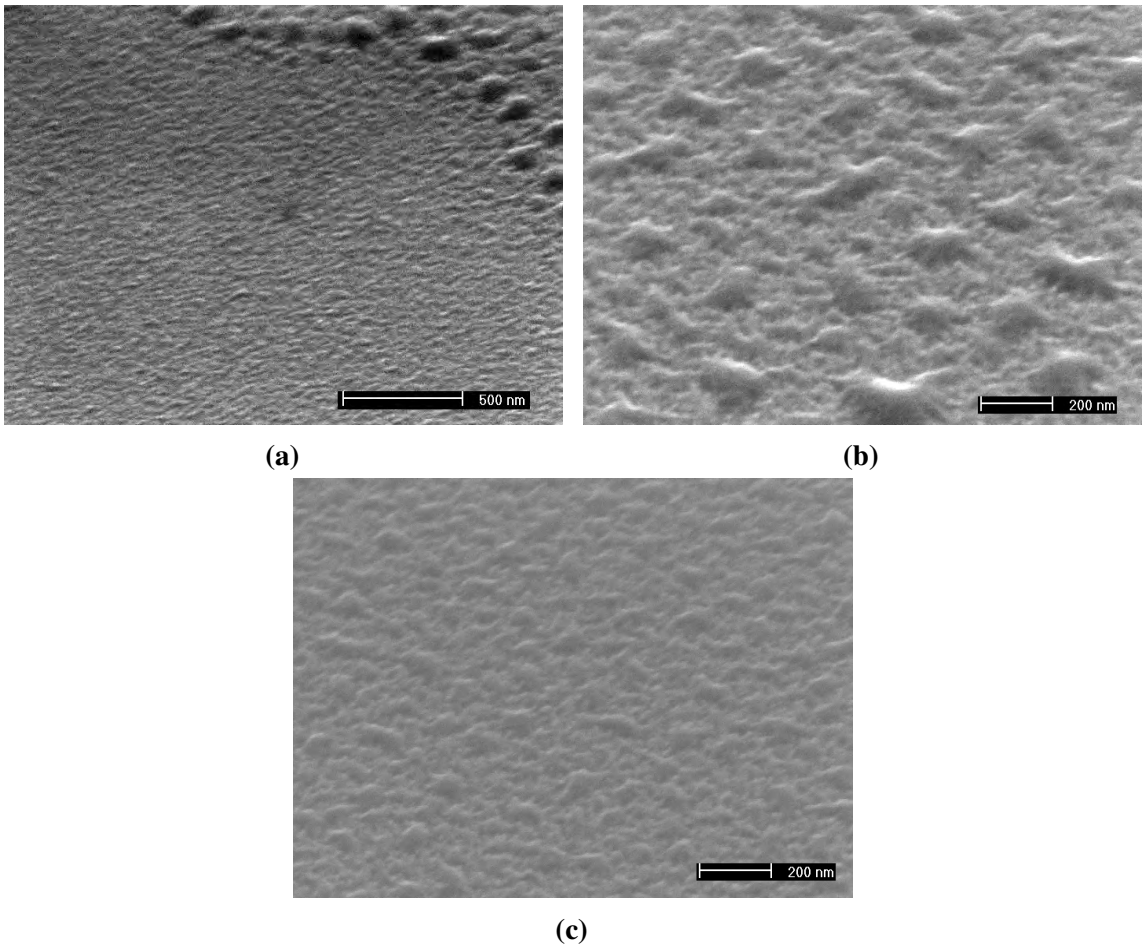

Figure 5.7: SEM images of sample R4 etched (see Table 5.5 for parameters). (a) (100000× magnification) No pillar features can be found throughout the sample, it is however evident from the surface roughening that the sample has been etched (45°, 500 nm scale bar). Moreover, oil, used for the sample base to get good thermal seal to the etcher base electrode plate, contaminated the sample surface during handling when SEM imaging. The oil contamination can be clearly seen on the top-right corner of the image. (b) & (c) (150000× magnification) Two zoomed in areas showing the roughening of the surface and smaller droplets of oil not wetting the surface (45°, 200 nm scale bar).

density. A longer etching time would not have left any pillar structures behind, and only a rough surface would have resulted. For the same etching time, however, a lower ion density (ICP power value of 100 W) do not result in any pillar structures as shown by sample L4.

All pillar structures with the palladium cluster etch masks were etched out when parameters for sample L6, in Table 5.7, were used. What can be seen in Figures 5.11a–5.11c

	Name	L1	R6	R2
Sample	Deposit	Ar_1^+/Pd_{10000}	”	”
	Substrate	MoS_2	”	”
Strike Step	Time (s)	5	”	”
	APC Pressure (mTorr)	15	”	”
	Temperature (°C)	10	”	”
	He Pressure (Torr)	10	”	”
	O_2 (sccm)	-	-	-
	SF_6 (sccm)	1	”	”
	C_4F_8	50	”	”
	RF Power (W)	50	”	”
	ICP Power (W)	200	”	”
Main Step	Time (s)	30	”	”
	APC Pressure (mTorr)	15	”	”
	Temperature (°C)	10	”	”
	He Pressure (Torr)	10	”	”
	O_2 (sccm)	-	-	-
	SF_6 (sccm)	15	20	25
	C_4F_8	35	30	25
	RF Power (W)	20	”	”
	ICP Power (W)	150	”	”

Table 5.6: Three of the samples (L1, R6 & R2) from the second batch were etched with the same parameters except for the mix etch gas flows, which were varied. All the samples' relevant etching parameters are listed in the table.

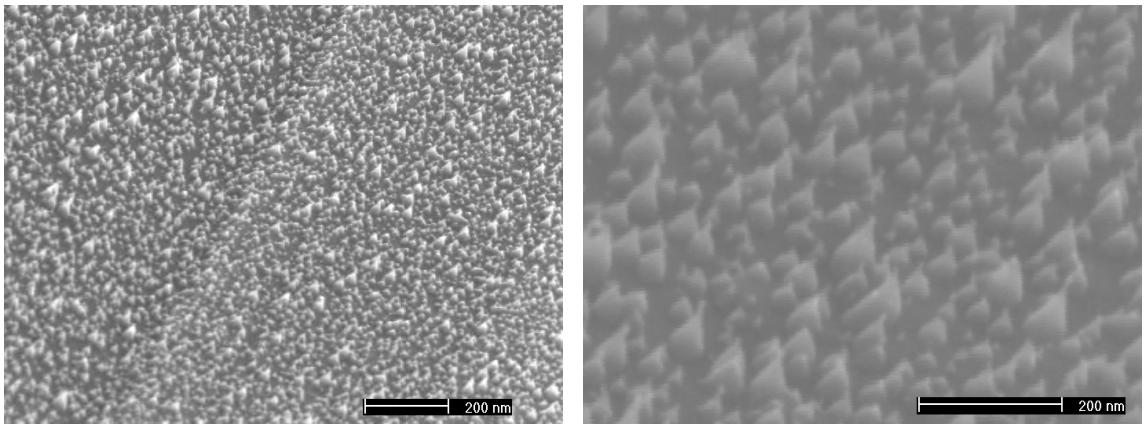

(a) **(b)**

Figure 5.8: SEM images of sample L1 etched (see Table 5.6 for parameters). (a) (175000× magnification) & (b) (300000× magnification) Pillar structures are visible where palladium cluster etch masks were deposited (45°, 200 nm scale bar).

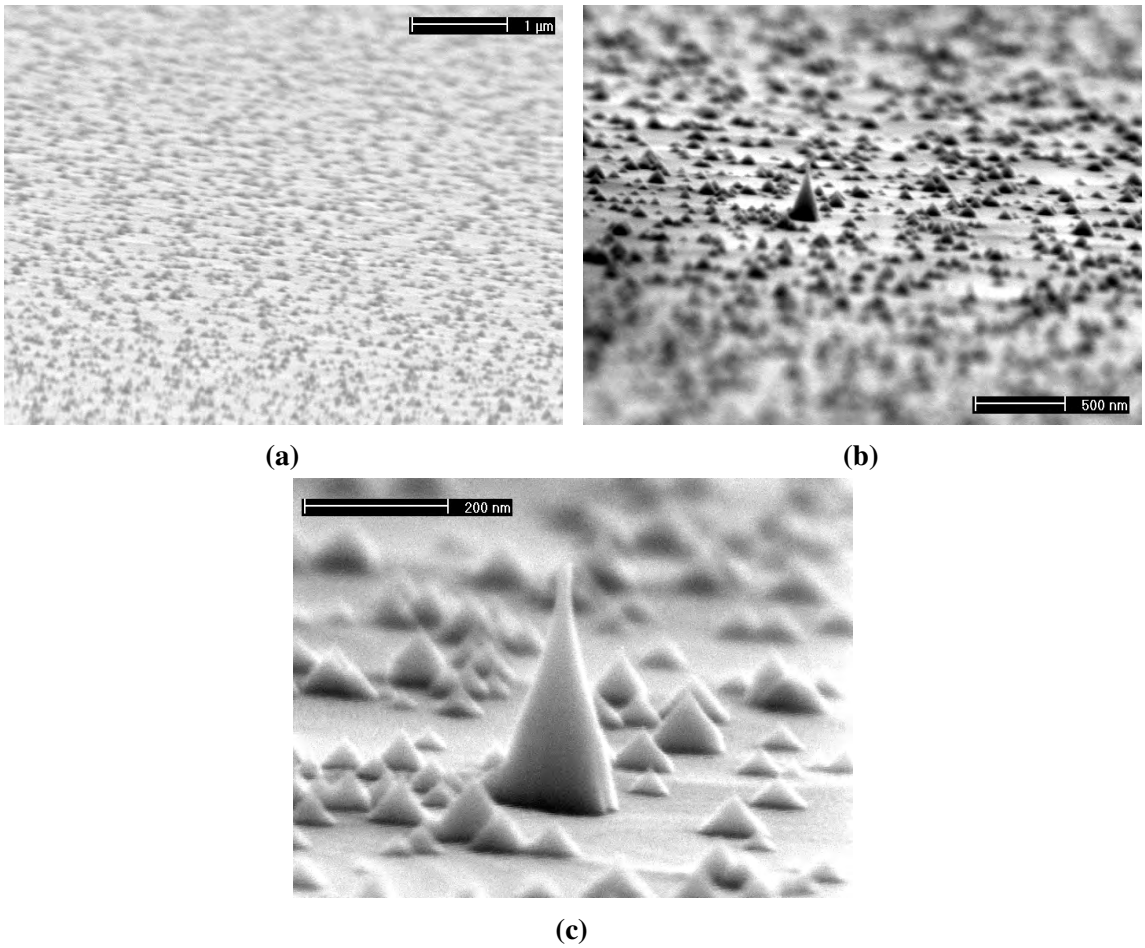

Figure 5.9: SEM images of sample R6 etched (see Table 5.6 for parameters). (a) (40000× magnification) Pillar (conical) features can be found in the image, which covers a large area of the sample (85°, 1 μm scale bar). (b) (75000× magnification) Zoomed in area at 85° with 500 nm scale bar. (c) (300000× magnification) A further zoomed in area of the sample showing cone-shaped pillars. What is evident from the larger pillar at the centre, is that the etching time is still too long. (85°, 200 nm scale bar).

are a few localised pillar structures with either contaminant etch masks or aggregates of palladium clusters. Moreover, ordered patterns of concentric rings have also been etched onto the surface and can be seen in Figures 5.11b and 5.11c.

The ICP power value of 150 W is clearly too high with the other given etching parameters for sample L6. In comparison, for the same given other etching parameters (see Table 5.7), sample R3 (from the first batch) with its lower ICP power (100 W), clearly shows MoS_2 nano pillar structures (see Figure 5.12).

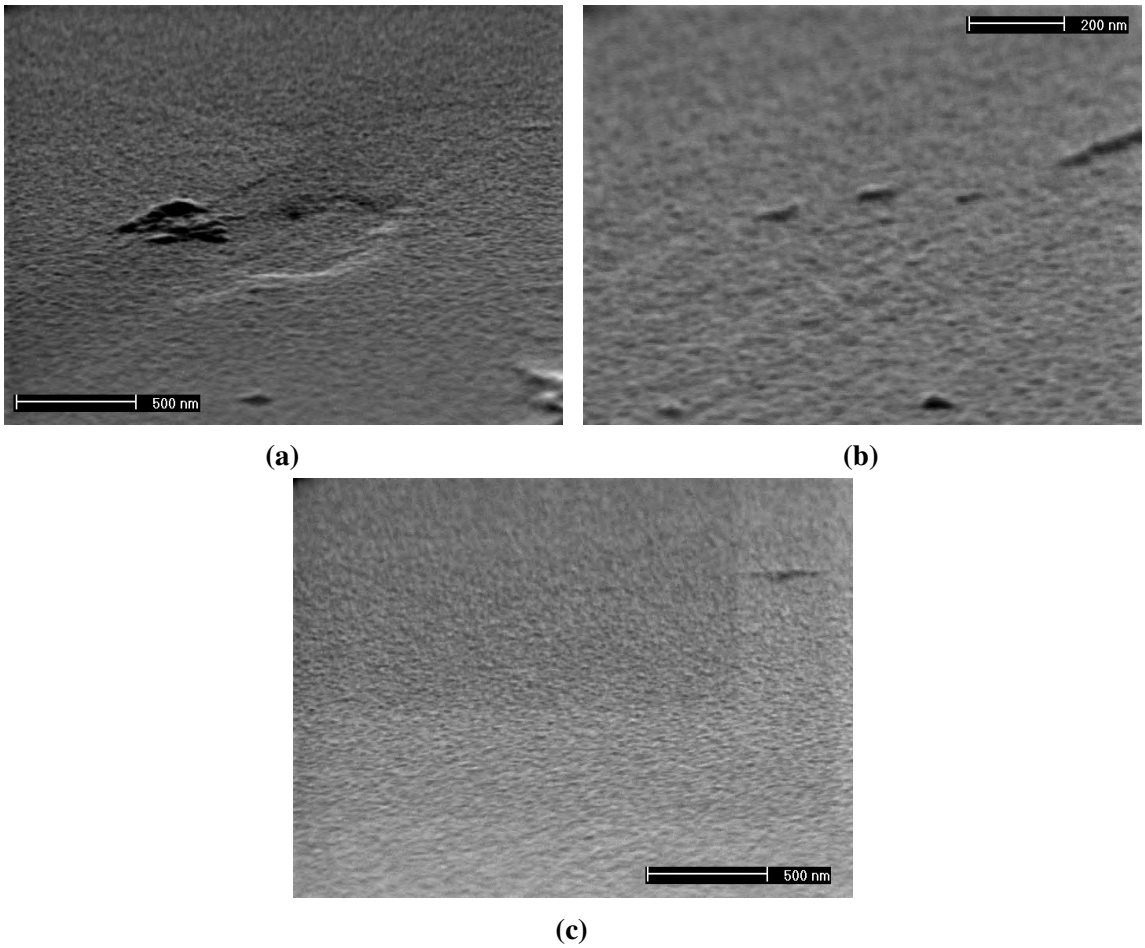

(a) **(b)**

(c)

Figure 5.10: SEM images of sample R2 etched (see Table 5.6 for parameters). (a) (100000× magnification) Deliberate choice of area with contaminants to show that no pillar structures can be found throughout the sample, only a roughening of the surface is visible (85°, 500 nm scale bar). (b) (200000× magnification) Zoomed in area of the etched sample showing the roughening of the surface (85°, 200 nm scale bar). (c) (100000× magnification) A larger area showing the uniform roughening of the surface after etching (85°, 500 nm scale bar).

The surface looks like the waves on the sea, the waves being the (etched out) remnants of pillar structures, as can be seen in Figures 5.13a to 5.13d, after etching of sample L2 (see Table 5.8 for parameters).

The RF power controls the impact energy of the etching ions and thus a higher value (like 25 W for L2 compared to 20 W for R3, see Table 5.8) will result in a more etched surface (i.e. flatter/rough surface and no nano pillar structures). This is clearly evident from the images of R3 in Figure 5.12 compared to images of L2 in Figure 5.13.

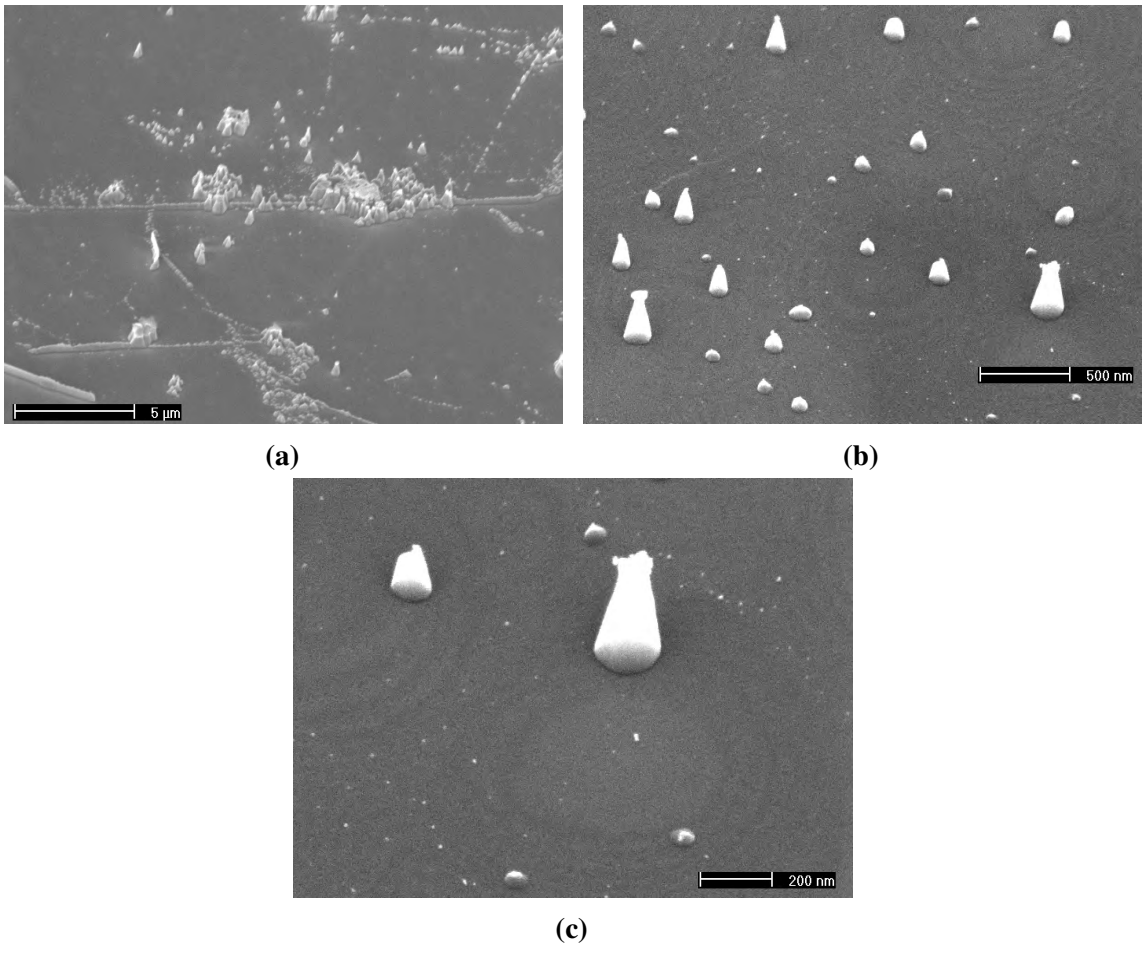

(a) **(b)**

(c)

Figure 5.11: SEM images of sample L6 etched (see Table 5.7 for parameters). (a) (10000× magnification) No pillar structures were found except for contaminant etch masks or aggregates of palladium clusters. (45°, 5 μm scale bar). (b) (75000× magnification) Zoomed in area (45°, 500 nm scale bar). (c) (150000× magnification) Further zoomed in area (45°, 200 nm scale bar).

Sample	Name	L4	R6	R3 Batch 1	L6 Batch 2
	Deposit	Ar_I^+/Pd_{10000}	”	Ar_I^+/Pd_{10000}	”
	Substrate	MoS_2	”	MoS_2	”
Strike Step	Time (s)	5	”	5	”
	APC Pressure (mTorr)	15	”	15	”
	Temperature (°C)	10	”	20	”
	He Pressure (Torr)	10	”	10	”
	O_2 (sccm)	-	-	-	-
	SF_6 (sccm)	1	”	1	”
	C_4F_8	50	”	50	”
	RF Power (W)	50	”	50	”
	ICP Power (W)	200	”	300	”
Main Step	Time (s)	30	”	30	”
	APC Pressure (mTorr)	15	”	15	”
	Temperature (°C)	10	”	20	”
	He Pressure (Torr)	10	”	10	”
	O_2 (sccm)	-	-	-	-
	SF_6 (sccm)	20	”	30	”
	C_4F_8	30	”	20	”
	RF Power (W)	20	”	20	”
	ICP Power (W)	100	150	100	150

Table 5.7: Samples L4 & R6 were etched with only the ICP power values differing and so was sample R3 from batch 1 & L6 from batch 2. All the samples' relevant etching parameters are listed in the table.

Figures 5.14a to 5.14c depict SEM images of sample R3 (Batch 2) after etching (Table 5.9), showing (etched out) remnant pillar structures.

Lower APC pressure insures better etching conditions, given the other parameters in Table 5.9, when forming MoS_2 nano pillar structures. This can be seen in the images of sample R3 (Batch 1) in Figure 5.12, which is quite different from the images of sample R3 (Batch 2) in Figure 5.14.

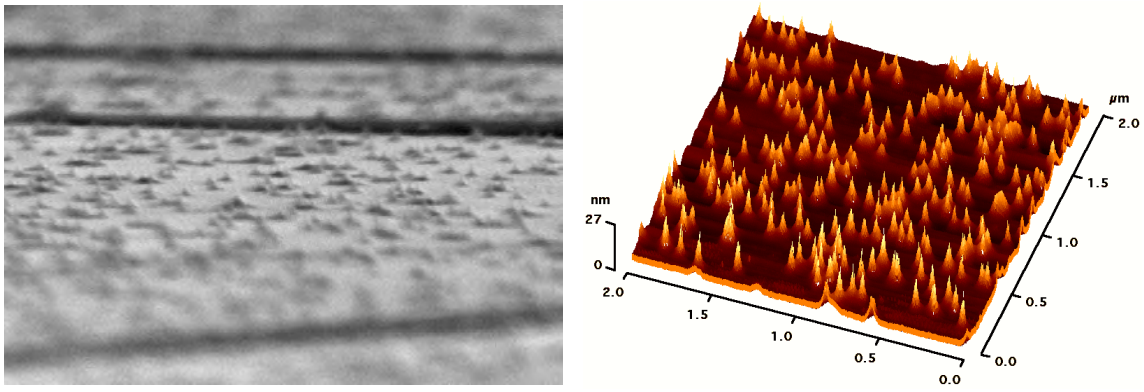

(a) **(b)**

Figure 5.12: SEM and AFM images of sample R3 (Batch One) after mixed etching with parameters in Table 5.7, depicting nano pillars of MoS_2. (a) Nano pillars, on different terraces (see foreground and background out of focus), are visible as conically shaped bases (~20 nm heights & ~30 nm diameters) and cylindrically shaped tips (~10 nm heights & ~5 nm diameters), on the natural MoS_2 crystal substrate, at a viewing angle of 85°. (b) 3D AFM image with NPs visible as conically shaped pillars (~30 nm heights & ~30 nm diameters). Note that the shapes of the nano pillars visible in the SEM images is not visible in this AFM image due to the inherit nature of scanning probe microscopes' (such as the atomic force microscope) difficulty to resolve certain lateral features close to high features due to the usage of a tip (2×2 μm×27 nm).

The overall conclusion, from varying key etching parameters, is that a very narrow part of parameter space (probably different for different given parameters) yields well defined MoS_2 nano pillar structures. The etching time was the first parameter investigated. For two different sets of, other given, etching parameters, one can see that even a small change of 5 s can give a drastically different end result (compare Figure 5.4 and Figure 5.5 for etched samples R3 and L3, respectively). The values of the other given etching parameters such as the gas flows, the ICP & RF power, the APC pressure and temperature were ideal for the etching time range observed. The particular pocket of values in parameter space as given in Table 5.4 give rise to nano pillars. In contrast, the lower gas flow of SF_6 (20 sccm compared to 30 sccm), higher gas flow of C_4F_8 (30 sccm compared to 20 sccm) and lower sample temperature (10°C compared to 20°C) when etching R1, L4, R4 and R5 with different etching times (in overlapping range with times for R3 and L3) do not result in nano pillars. A comparison of the etching parameters in Tables 5.4 and 5.5 as well as

	Name	R3 Batch 1	L2 Batch 2
Sample	Deposit	Ar_1^+/Pd_{10000}	”
	Substrate	MoS_2	”
Strike Step	Time (s)	5	”
	APC Pressure (mTorr)	15	”
	Temperature (°C)	20	”
	He Pressure (Torr)	10	”
	O_2 (sccm)	-	-
	SF_6 (sccm)	1	”
	C_4F_8	50	”
	RF Power (W)	50	”
	ICP Power (W)	300	”
Main Step	Time (s)	30	”
	APC Pressure (mTorr)	15	”
	Temperature (°C)	20	”
	He Pressure (Torr)	10	”
	O_2 (sccm)	-	-
	SF_6 (sccm)	30	”
	C_4F_8	20	”
	RF Power (W)	20	25
	ICP Power (W)	100	”

Table 5.8: Sample R3 from Batch 1 and sample L2 from Batch 2 have the same etching parameters except for the RF power, which is varied. All the samples' relevant etching parameters are listed in the table.

Figures 5.6 and 5.7 do confirm this. When investigating the gas flows, the etch time was kept at 30 s and the ICP power was increased from 100 W to 150 W, which made it ideal with a lower SF_6 flow and higher C_4F_8 flow (see Table 5.6) in the formation of nano pillars (see Figures 5.8 to 5.10). The variation of the ICP power was done to also see the effect of the gas flows and the temperature, see Table 5.7. When the sample temperature was lower (10°C), the SF_6 flow lower (20 sccm) and C_4F_8 (30 sccm) flow higher, the increase in ICP power from 100 W to 150 W was more favourable in forming nano pillars (R6) as can be observed in Figure 5.9 (nothing observed on L4). However, when the values of the same etching parameters were changed (10°C to 20°C, 20 sccm to 30 sccm SF_6 and 30 sccm to 20 sccm C_4F_8), the increase in ICP power from 100 W to 150 W was less favourable in forming nano pillars (compare Figure 5.12 for R3 and Figure 5.11 for L6). The case was

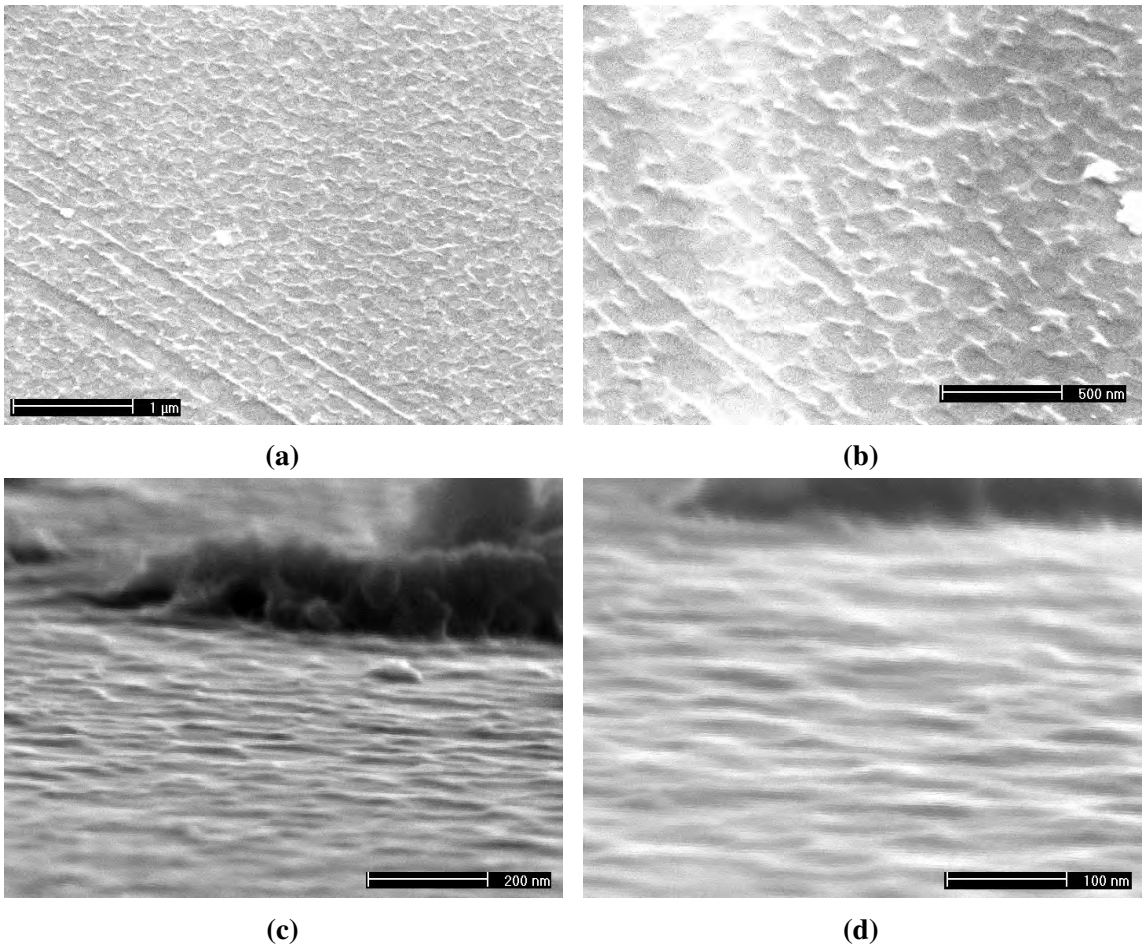

Figure 5.13: SEM images of etched sample L2 (see Table 5.8 for parameters). (a) (50000× magnification) The (etched out) remnant pillar structures visible on the surface resemble the waves of the ocean (45°, 1 μm scale bar). (b) (100000× magnification) Zoomed in area of the sample (45°, 500 nm scale bar). (c) (250000× magnification) Deliberate choice of area with contaminants in the background in order to better view the (etched out) remnant pillar structures visible on the surface (85°, 200 nm scale bar). (d) (500000× magnification) Zoomed in area (85°, 100 nm scale bar).

similar if either the RF power (Table 5.8) or the APC pressure (Table 5.9) was increased (compare Figure 5.12 for R3 Batch 1 with Figure 5.13 for L2 and Figure 5.14 for R3 Batch 2). This further shows that a very narrow set of values (maybe different pockets) yields well defined MoS_2 nano pillar structures in the etching parameter space.

The third and final batch of cluster deposited samples consisted of 12 substrates of MoS_2, see Table 5.10 for all relevant values (see Figures 5.15a to 5.15c for SEM images of the deposited clusters).

	Name	R3 Batch 1	R3 Batch 2
Sample	Deposit	Ar_1^+/Pd_{10000}	"
	Substrate	MoS_2	"
Strike Step	Time (s)	5	"
	APC Pressure (mTorr)	15	"
	Temperature (°C)	20	"
	He Pressure (Torr)	10	"
	O_2 (sccm)	-	-
	SF_6 (sccm)	1	"
	C_4F_8	50	"
	RF Power (W)	50	"
	ICP Power (W)	300	"
Main Step	Time (s)	30	”
	APC Pressure (mTorr)	15	20
	Temperature (°C)	20	”
	He Pressure (Torr)	10	”
	O_2 (sccm)	-	-
	SF_6 (sccm)	30	”
	C_4F_8	20	”
	RF Power (W)	20	”
	ICP Power (W)	100	”

Table 5.9: Sample R3 from Batch 1 and sample R3 from Batch 2 have the same etching parameters except for the APC pressure, which is varied. All the samples' relevant etching parameters are listed in the table.

The etching of the samples was performed together with other differently fabricated samples (ordered MoS_2 nano pillar structures by latex polymer nano spheres), so similar etching parameters were chosen for comparison. The twelve samples were divided into groups of three (i.e. four groups). All the samples were etched with the same parameters, except for the etching time of the main mix etch step.

Figures 5.16a and 5.16b show the SEM images of the first sample (L6 in Group one) etched with the parameters in Table 5.11.

SEM images of ninth sample (L2 in Group three), etched according to parameters in Table 5.11, can be seen in Figures 5.17a and 5.17b. 7 s etch time has not etched away all the gold cluster etch masks, which still can be visible on the top of some of the pillar structures.

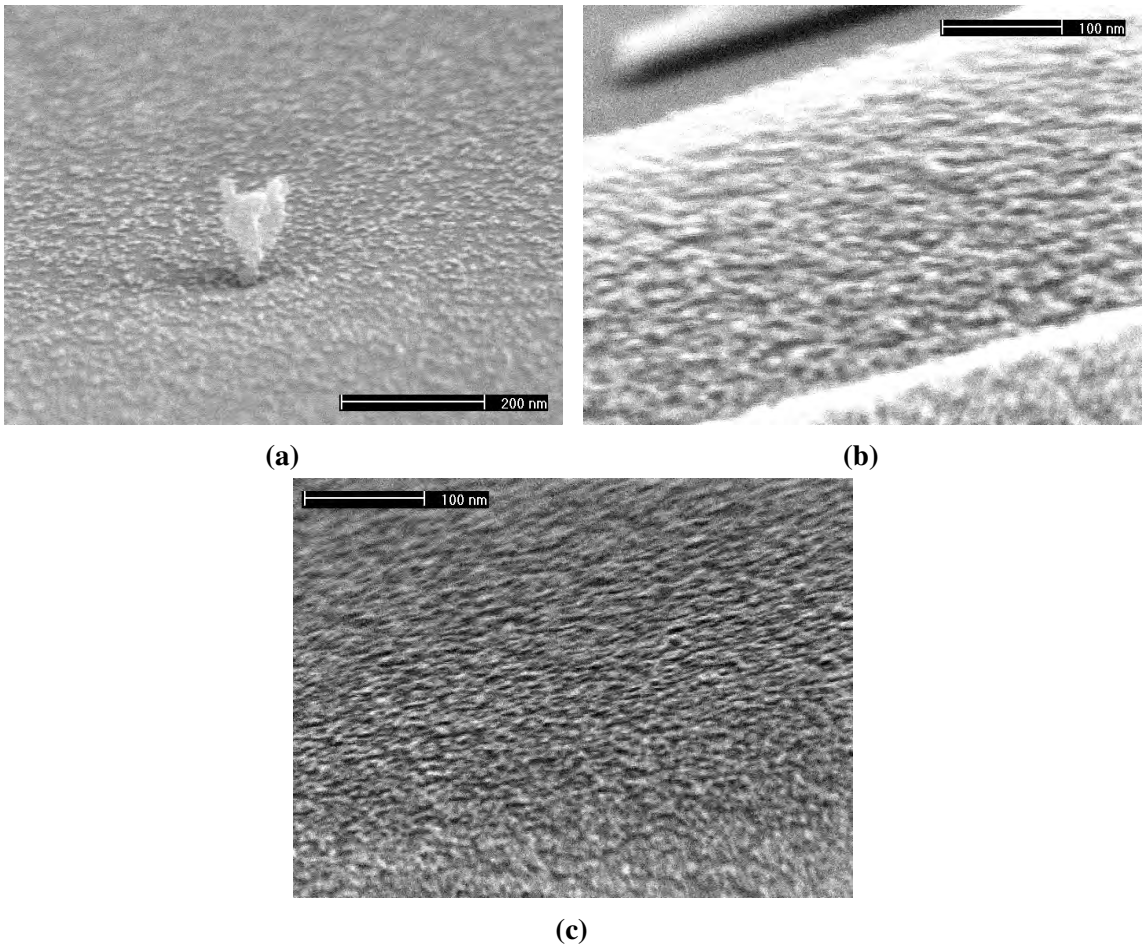

Figure 5.14: SEM images of etched sample R3 (see Table 5.9 for parameters). (a) (300000× magnification) Deliberate choice of area with (angel-like) contaminant to show that (etched out) remnant pillar structures can be found throughout the sample (85°, 200 nm scale bar). (b) (500000× magnification) Zoomed in area showing (etched out) remnant pillar structures can be found on different terraces (85°, 100 nm scale bar). (c) (500000× magnification) Depicted area fully covered with (etched out) remnant pillar structures (85°, 100 nm scale bar).

Figures 5.18a to 5.18d, 5.19a and 5.19b show SEM images of sample twelve (R1 in Group four) etched according to parameters in Table 5.11. 5 s etch time has not etched away all the gold cluster etch masks, which still can be visible on the top of some of the pillar structures. The pillar structures in the images have the shape of cones with diameters of ~30 nm and heights of ~30 nm. Some of the tips are cylindrically shaped with diameters of ~5 nm and heights of ~5-10 nm and, at least partially, consist of the remaining gold cluster etch masks.

	Name	R1	R2	R3	R4	R5	R6	L6	L5	L4	L3	L2	L1
Sample	Batch	3	”	”	”	”	”	”	”	”	”	”	”
	Substrate	MoS_2	”	”	”	”	”	”	”	”	”	”	”
Pre-deposition	Deposit	Ar_1^+	”	”	”	”	”	”	”	”	”	”	”
	Impact Energy (keV)	0.5	”	”	”	”	”	”	”	”	”	”	”
	Beam Current (pA)	350	”	”	”	”	”	”	”	”	”	”	250
	Deposition Time (s)	13	”	”	”	15	18	13	”	”	18	13	24
	Coverage (pA·s)	4550	”	”	”	4950	5940	4550	”	”	5940	4550	6000
Deposition	Deposit	Au_{10000}	”	”	”	”	”	”	”	”	”	”	”
	Impact Energy (keV)	0.5	”	”	”	”	”	”	”	”	”	”	”
	Beam Current (pA)	6	”	”	”	”	”	4	”	”	”	”	”
	Deposition Time (s)	360	”	”	”	”	”	540	”	”	”	”	”
	Coverage (pA·s)	2160	”	”	”	”	”	”	”	”	”	”	”

Table 5.10: Twelve samples were deposited in the third batch. The relevant parameters are listed in the table.

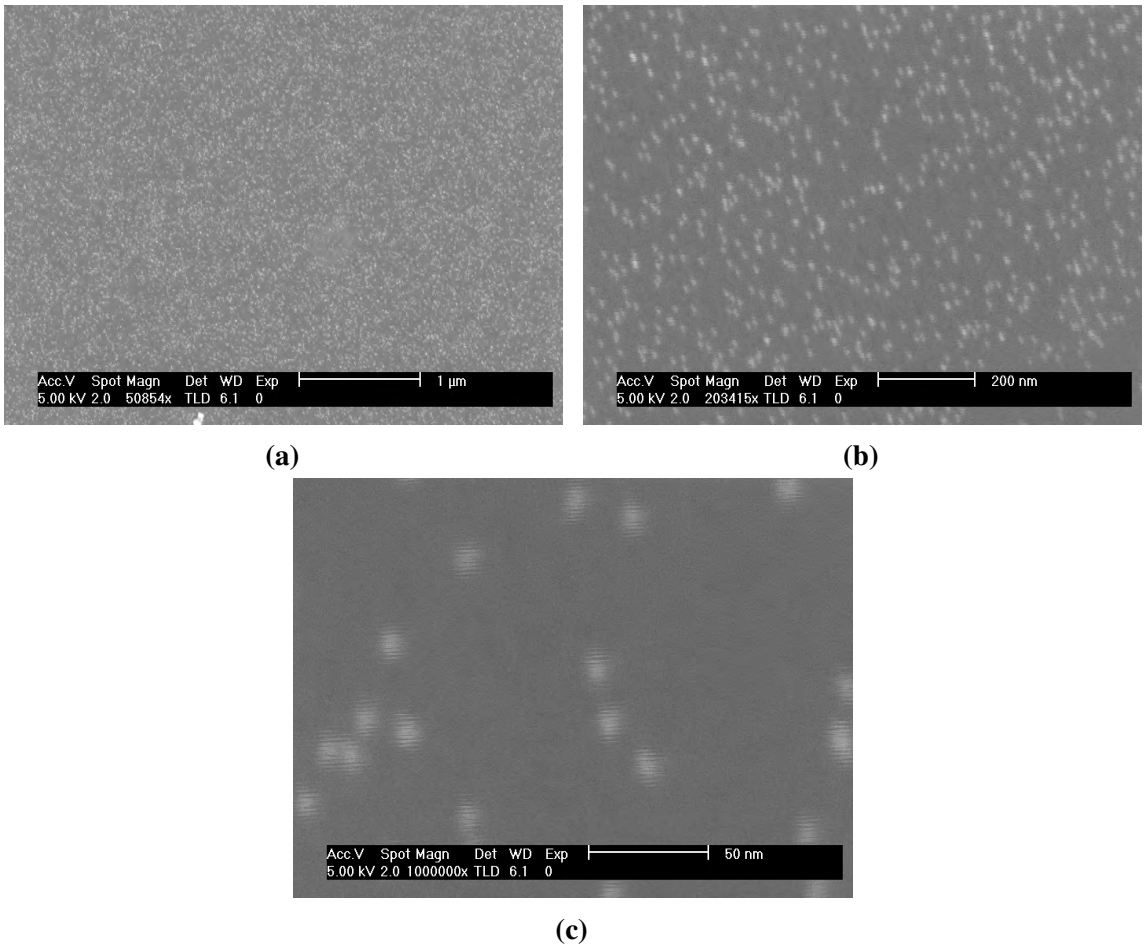

Figure 5.15: SEM images of Au_{10000} clusters deposited on MoS_2 with a coverage of ~2300 pA·s and at an energy of 0.5 keV. The substrate was pre-deposited with Ar_1^+ with a coverage of ~4600 pA·s at an energy of 0.5 keV in order to create defects for the gold clusters to attach to and be pinned. (a) The clusters are visible as bright circles on the natural MoS_2 crystal substrate and can be found throughout the sample (1 μm scale bar). (b) Zoomed in area of sample (200 nm scale bar) and (c) further zoomed in area (50 nm scale bar). The clusters are visible as bright cut elongated circles (caused by slight drift during the acquisition of the image) on the natural MoS_2 crystal substrate and can be found throughout the sample.

What was experienced when etching Pd cluster samples (Batch 1 & 2), with varied parameter values, was used when etching Au cluster samples in order to ensure that a narrow set of values forming nano pillars would be achieved. Assuming almost the same etch rate for Pd and Au cluster etch masks (especially at these small dimensions) and using a much higher ICP & RF power (see Table 5.11) than before together with a comparable temperature (20°C) and a lower SF_6 flow and a higher C_4F_8 flow, the necessity of a much lower

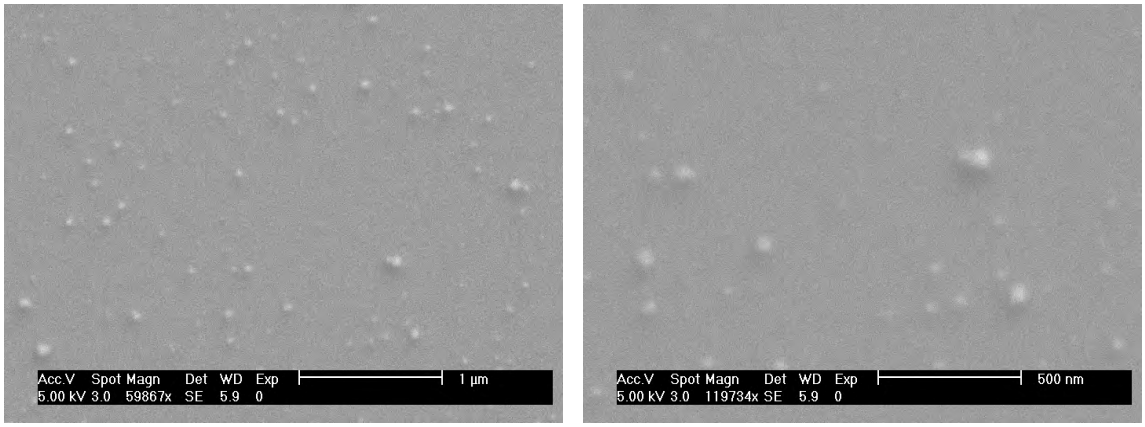

(a) **(b)**

Figure 5.16: SEM images of the first sample (L6 in Group one) etched in Batch 3 (see Table 5.11 for parameters). (a) The area (1 μm scale bar) and (b) the zoomed in area (500 nm scale bar) depict pillar structures as seen from above, with the remaining gold cluster etch masks on top after 1 s etch time. The pillar structure summits are visible as bright circles on the natural MoS_2 crystal substrate and can be found throughout the sample.

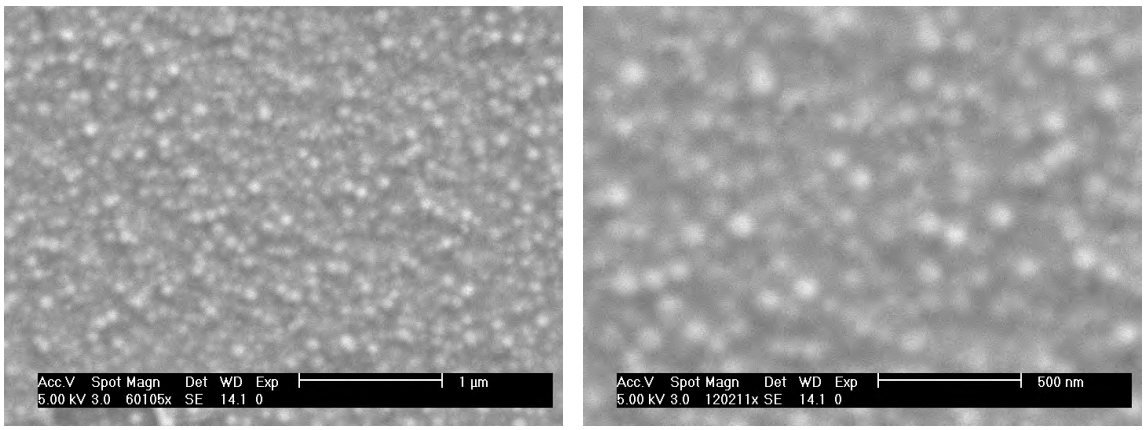

(a) **(b)**

Figure 5.17: SEM images of the ninth sample (L2 in Group three) etched in Batch 3 (see Table 5.11 for parameters). (a) The area (1 μm scale bar) and (b) the zoomed in area (500 nm scale bar) depict pillar structures as seen from above, with some, very possibly, having the remaining gold cluster etch masks on top after 7 s etch time. The pillar structure summits are visible as bright circles on the natural MoS_2 crystal substrate and can be found throughout the sample.

Sample	Name	L6	R4	L1	R5	L3	R2	R6	L5	L2	L4	R3	R1
	Deposit	Ar_1^+/Au_{1000}	"	"	"	"	"	"	"	"	"	"	"
	Substrate	MoS_2	"	"	"	"	"	"	"	"	"	"	"
Strike Step	Time (s)	5	"	"	"	"	"	"	"	"	"	"	"
	APC Pressure (mTorr)	15	"	"	"	"	"	"	"	"	"	"	"
	Temperature (°C)	20	"	"	"	"	"	"	"	"	"	"	"
	He Pressure (Torr)	10	"	"	"	"	"	"	"	"	"	"	"
	O_2 (sccm)	-	-	-	-	-	-	-	-	-	-	-	-
	SF_6 (sccm)	1	"	"	"	"	"	"	"	"	"	"	"
	C_4F_8	50	"	"	"	"	"	"	"	"	"	"	"
	RF Power (W)	50	"	"	"	"	"	"	"	"	"	"	"
	ICP Power (W)	300	"	"	"	"	"	"	"	"	"	"	"
Main Step	Time (s)	1	1	1	3	3	3	7	7	7	5	5	5
	APC Pressure (mTorr)	15	"	"	"	"	"	"	"	"	"	"	"
	Temperature (°C)	20	"	"	"	"	"	"	"	"	"	"	"
	He Pressure (Torr)	10	"	"	"	"	"	"	"	"	"	"	"
	O_2 (sccm)	-	-	-	-	-	-	-	-	-	-	-	-
	SF_6 (sccm)	25	"	"	"	"	"	"	"	"	"	"	"
	C_4F_8	30	"	"	"	"	"	"	"	"	"	"	"
	RF Power (W)	25	"	"	"	"	"	"	"	"	"	"	"
	ICP Power (W)	220	"	"	"	"	"	"	"	"	"	"	"

Table 5.11: Batch number three contains 12 samples that were etched. All the samples' relevant etching parameters are listed in the table.

etch time was identified. Indeed, the set of values making up a narrow pocket in etching parameter space, which forms well defined MoS_2 nano pillar structures, was achieved.

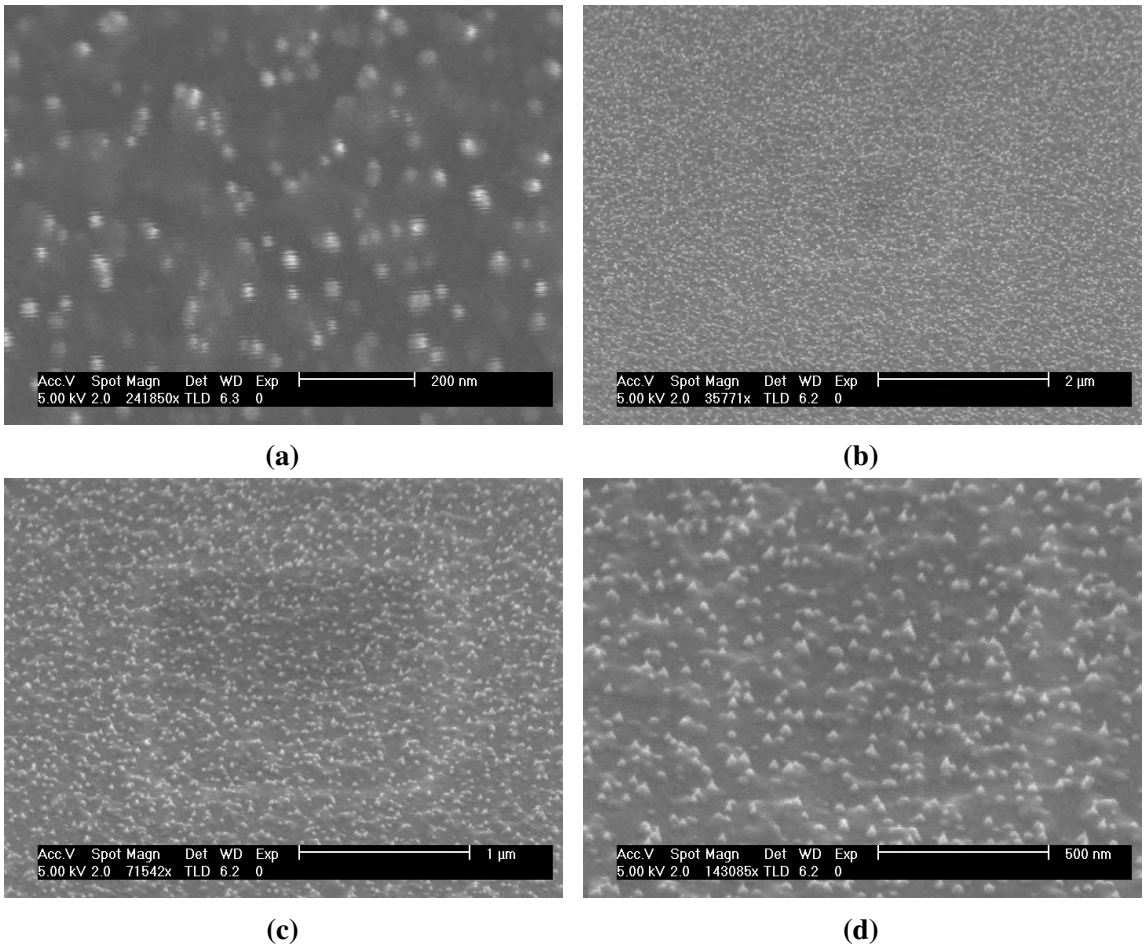

Figure 5.18: SEM images of the twelfth sample (R1 in Group four) etched in Batch 3 (see Table 5.11 for parameters). (a) The area depicts pillar structures as seen from above, with some having the remaining gold cluster etch masks on top after 5 s etch time. The pillar structure summits are visible as bright cut elongated circles (caused by slight drift during the acquisition of the image) on the natural MoS_2 crystal substrate and can be found throughout the sample (200 nm scale bar). (b) The image shows a large area with a good coverage of pillar structures (45°, 2 μm scale bar). (c) Zoomed in area of (b) (45°, 1 μm scale bar) and (d) further zoomed in area (45°, 500 nm scale bar).

Moreover, even the minute variations in etch time changes the end results as can be seen in the images.

With size-selected metal cluster etch masks, only a certain order of pillar sizes (typically ~1-10 nm tip diameters possible) could be achieved and their locations are random. In the coming sections two other, very similar, approaches are sought to try to expand these two constraints.

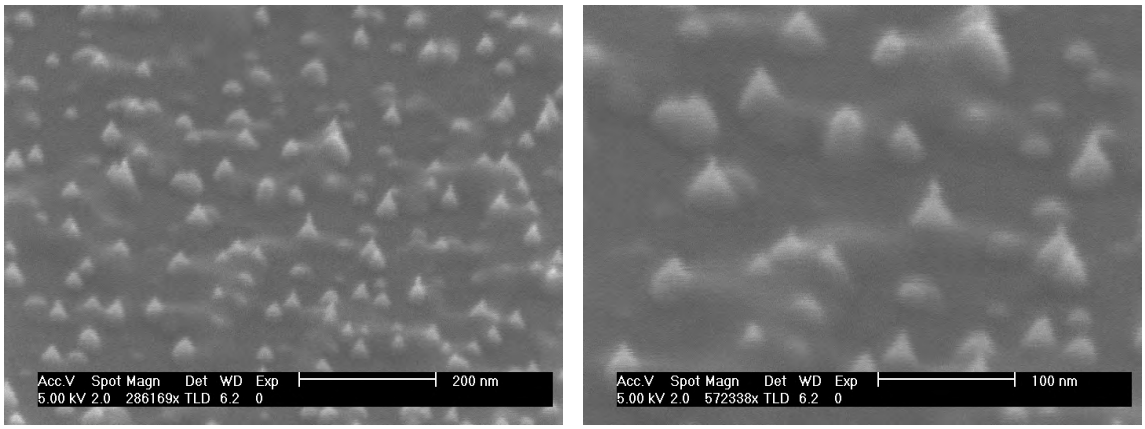

(a) **(b)**

Figure 5.19: (a) The image, which is a further zoomed in area of 5.18d, clearly shows the remaining gold cluster etch masks on top of some of the pillar structures after 5 s etch time (45°, 200 nm scale bar). (b) The pillar structures in the image have the shape of cones with diameters of ~30 nm and heights of ~30 nm. Some of the tips are cylindrically shaped with diameters of ~5 nm and heights of ~5-10 nm, which consist of the remaining gold cluster etch masks (45°, 100 nm scale bar).

5.2 Ordered MoS_2 Nano Corrugated Structures

The fabrication of the ordered nano corrugated structures (pillar samples) from MoS_2, using latex nano spheres as masks for metal island etch masks, was the most complex pillar formation process. The fabrication process involved 4 steps; (1) nano sphere deposition on substrate, (2) metal evaporation on nano sphere masked substrate, (3) removal of excess metal and nano sphere mask from substrate and (4) etching substrate covered with ordered metal island masks.

5.2.1 Nano Sphere Deposition

Different approaches and methods were tested, for the best results, when using nano sphere lithography, as was mentioned in Chapter 2, Section 2.2.5 on page 77. Additionally to the immersion coating method, described in the aforementioned section, drop (drip) coating techniques as well as spin coating recipes were utilised, as guided by the

literature.

Drop Coating

The simplest deposition method should have been drop coating as it is explained in the literature. However, drawing from experimental experience, this rather straight-forward technique proved more difficult than expected. The first nano spheres used, were ~82 nm polystyrene polymers suspended in water (15 ml vials), supplied from Duke Scientific.

The first drop coating (drip coating used interchangeably in the literature) trials were done with pure de-ionised (DI) water (Purite Neptune, 18.2 MΩ) drops on silicon samples. The first method tried was accelerated evaporation, where the silicon samples were placed in a sealed box and the pressure decreased with a roughing pump. As the pressure decreased in the box, the evaporation process was accelerated and would roughly not take longer than 2 min before the dropped water on the silicon samples would completely disappear. The process is much faster than leaving the water of the drop coated samples to evaporate at the normal pressure in the clean room, which would take up to an hour depending on the volume. The problem with the accelerated evaporation process is the turbulent and uncontrollable nature of the rapid evaporation. Air bubbles build up just to "jump" out of the dropped water, which starts to crystallise and freeze. The accelerated evaporation box is equipped with a valve that could be used to alter the rate of the evaporation, but the tuning was still to crude for a desired process to occur. So instead of dwelling any longer with this method a normal evaporation process was sought when drop coating nano spheres in solution, anticipating their self-assembly into hexagonal close-packed layer as the solvent evaporated.

The first batch of drop coated samples consisted of three silicon samples coated with 10 μl, 5 μl and 2 μl (nano sphere suspended solution with traces of surfactants, i.e. as is with a concentration of 10^{12} NS/ml = 10^9 NS/μl), respectively. The samples were coated

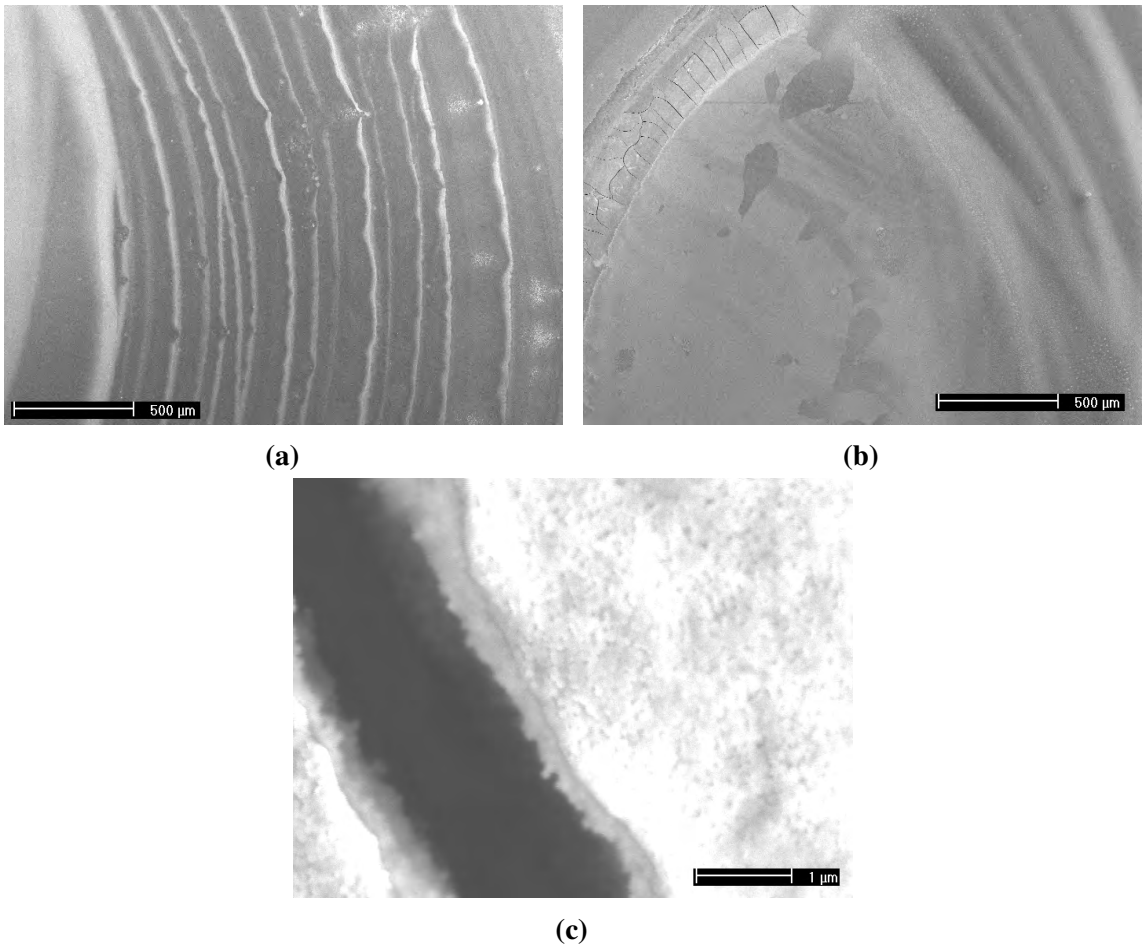

(a) **(b)**

(c)

Figure 5.20: (a) & (b) (100× magnification) SEM images (500 μm scale bar) and (c) (40000× magnification) SEM image (1 μm scale bar) of silicon sample drop coated with 2 μl of latex polymer nano sphere suspension after the evaporation of the solvent (water + traces of surfactants). Instead of the expected self-assembly of the nano spheres into hexagonally close-packed mono to multilayers, aggregates of them are found scattered chaotically throughout the sample and are sometimes even seen to have coalesced.

at the same time and the solvent was left to evaporate at a tilt angle of ~4.7 °.

None of the samples showed any signs of mono or bilayers of hexagonally close-packed latex polymer nano spheres, instead several layers of aggregated nano spheres were found and could be distinguished most easily for the lowest concentration (2 μl), see Figures 5.20a to 5.20c. The drying patterns are typical of particles in a drop after solvent evaporation, and is covered extensively in the literature [163–167].

For the second batch, consisting of two samples, a new diluted nano sphere solution mix

was prepared. The 1 wt% nano sphere suspension (with traces of surfactants) was diluted with DI water (ratio 1:4, i.e. 4 parts water and 1 part polymer suspension). The two silicon substrates were both drop coated with 5 μl of the newly diluted mix (10^8 NS/μl).

AFM imaging one of the samples mostly showed aggregation of the nano spheres just as before, see Figures 5.21a and 5.21b. However, when looking near the edges of where the diluted suspension was dropped, individual nano spheres as well as multilayers of hexagonally close-packed nano sphere islands could be found, see Figure 5.21c.

The third batch saw both of its samples drop coated with one new nano sphere dilution each. Two new nano sphere suspensions were mixed for drop coating purposes. One was diluted with DI water at ratio 1:10 (20 μl nano spheres with 200 μl DI water totalling 220 μl diluted nano sphere suspension, high 10^7 NS/μl) and the other at ratio 1:20 (10 μl nano spheres with 200 μl DI water totalling 210 μl diluted nano sphere suspension, low 10^7 NS/μl). Each sample was drop coated with 30 μl of one of the two new diluted nano sphere suspensions and left together in a glass base-lid petri dish assembly. The solvent was left to evaporate with the two samples at a 5 $^\circ$ incline and with a covering glass lid to shield from turbulent air flow. The evaporation process took much longer than in previous samples and after a couple of hours there was no clear sign of the solvent evaporating, thus it was left to continue for a couple of days.

Figures 5.22a and 5.22b depict AFM images of the silicon sample drop coated with (1:20) nano sphere suspension after the evaporation of the solvent. It is clear that the nano spheres have aggregated and formed multilayers instead of a hexagonally close-packed monolayer. Single nano spheres can be seen on top of this aggregated multilayer in Figure 5.22b. The layers of nano spheres are not close-packed in a hexagonal pattern, but rather form islands and patches with differently sized openings, which allows for the observation of lower layers. Darker colours indicate lower layers of nano spheres and the brighter the colour the higher the layer of nano spheres is indicated. Furthermore, due to

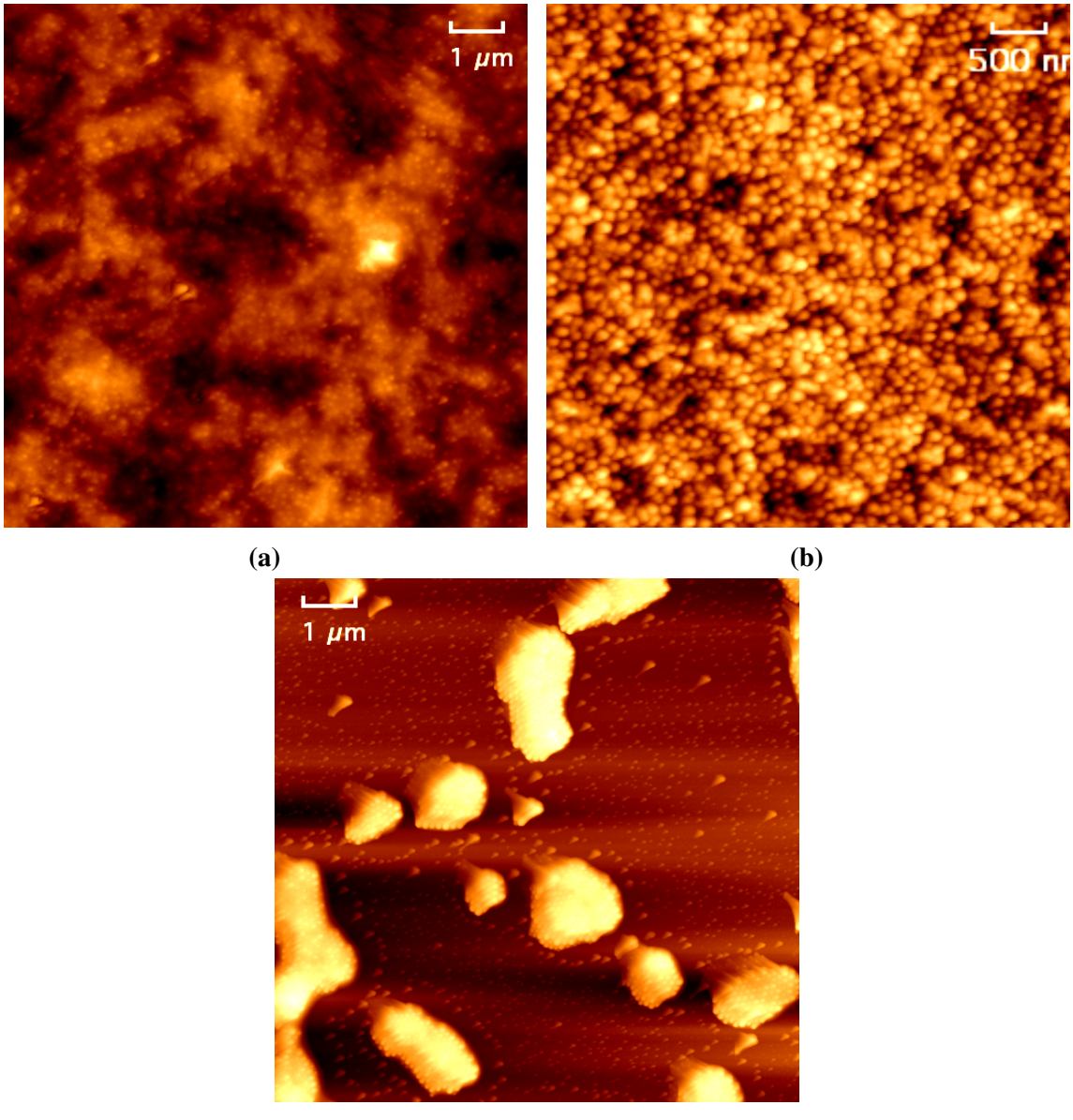

Figure 5.21: (a), (c) (1 μm scale bar) & (b) (500 nm scale bar) AFM images of silicon sample drop coated with 5 μl of diluted nano sphere suspension (4 parts DI water and 1 part polymer suspension) after the evaporation of the solvent (water + traces of surfactants). Instead of the expected self-assembly of the nano spheres into hexagonally close-packed mono to multilayers, aggregates of them are found scattered chaotically throughout the sample and are sometimes even seen to have coalesced.

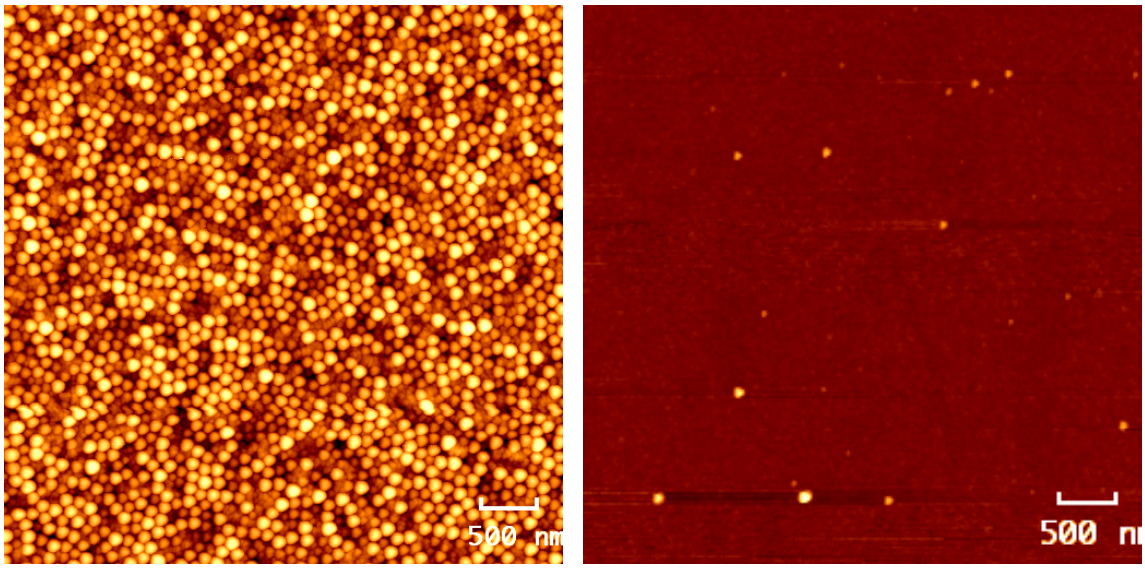

(a) **(b)**

Figure 5.22: AFM images (500 nm scale bar) of silicon sample drop coated with 30 μl of diluted nano sphere suspension (20 parts DI water and 1 part polymer suspension) after the evaporation of the solvent (water + traces of surfactants). (a) Instead of the expected self-assembly of the nano spheres into hexagonally ordered close-packed mono to multilayers, a multilayered aggregate of nano spheres is found within the drop coated area. (b) On top of the multilayered aggregates of nano spheres, single nano spheres can be found.

intrinsic limitations of AFM (e.g. among them, tip convolution), nano spheres in lower layers (i.e. with darker colours) appear smaller as the tip can not reach the nano sphere from one edge to the other, when scanning, but rather start to register some distance in from the edge as a function of the depth to the sphere and the shape of the tip.

In batch four, in addition to a silicon substrate, a graphite (HOPG) substrate was drop coated with 5 μl of a new nano sphere concentration. One part of the original nano sphere suspension was diluted with 50 parts of DI water and 50 parts ethanol to reduce the concentration and enhance the wetting/spreading of the drop. The silicon sample was drop coated with 10 μl with the same nano sphere solution (10^6 NS/μl).

AFM images of the more diluted nano sphere suspension drop coated onto a Si sample can be seen in Figures 5.23a to 5.23c. Patches of low density aggregated mono and multilayer nano spheres can be found throughout the drop coated region on the Si sample.

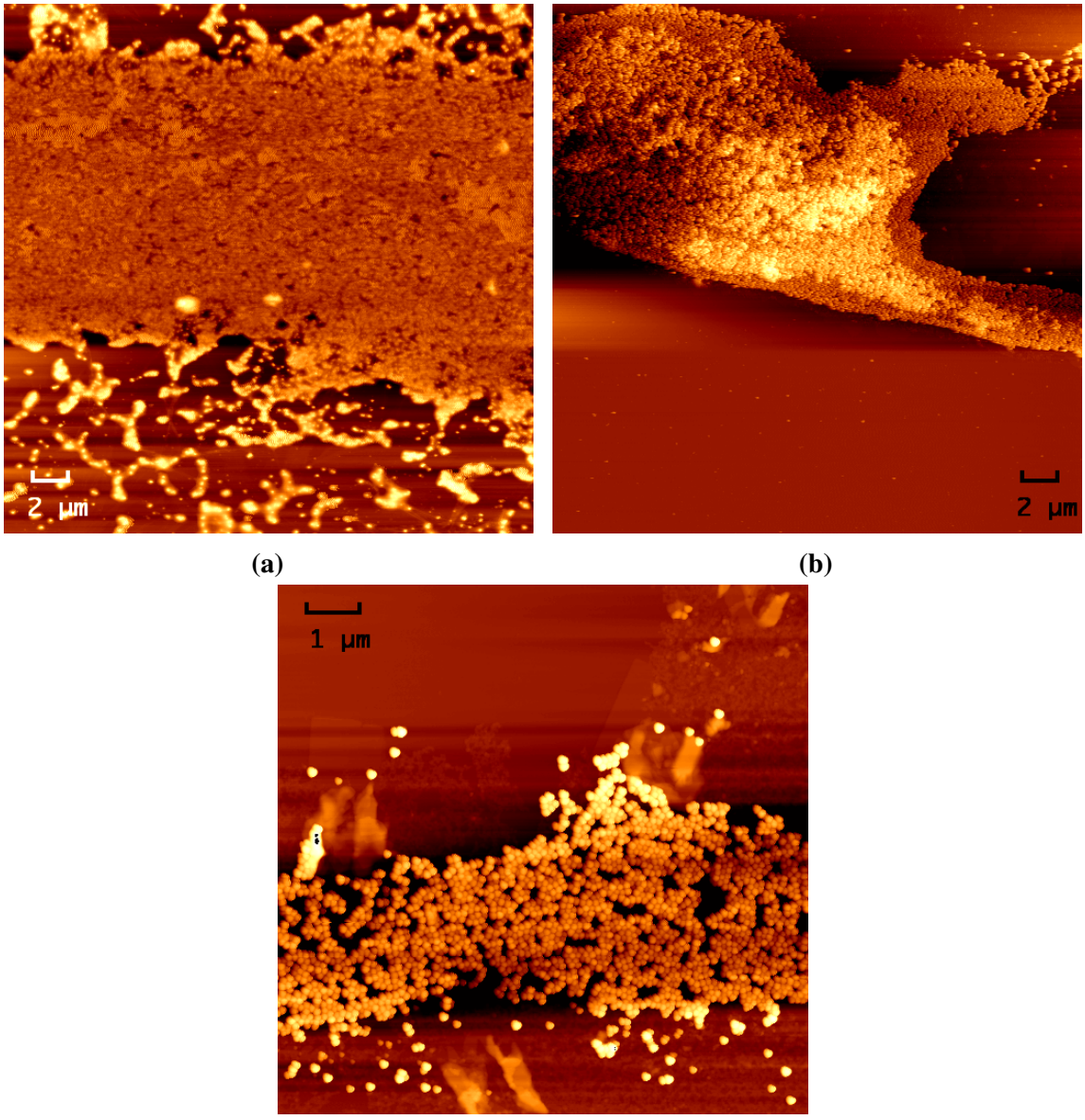

(a) **(b)**

(c)

Figure 5.23: AFM images of silicon sample drop coated with 10 μl of diluted nano sphere suspension (50 parts DI water, 50 parts ethanol and 1 part polymer suspension) after the evaporation of the solvent (water + ethanol + traces of surfactants). (a) Typical coverage, as can be seen from the visible patch, do not even form a hexagonal close-packed monolayer at the densest region (2 μm scale bar). (b) Some nano sphere patches, as the one visible in this image, have several aggregated and loosely packed layers of nano spheres on top of each other (2 μm scale bar). (c) Zoomed in image showing the low density packing of the nano spheres of one of the several patches found throughout the drop coated area on the sample (1 μm scale bar).

Efforts to reduce the nano sphere concentration in drop coating, from the as-is supplied concentration (10^9 NS/μl diluted to 10^8 NS/μl, 10^7 NS/μl and 10^6 NS/μl), did not yield any high-area coverage of a hexagonally close-packed nano sphere monolayer on sample surfaces. Using ethanol, to spread the drop better over substrate surfaces, helped a little, but high-area coverage of the patches was not observed nor were the spheres close-packed. All in all, very little success was achieved with drop coating, so another technique was tried instead.

Spin Coating

When drop coating (with all its different variants) proved to be inconsistent with results outlined in the literature, spin coating was pursued instead. The spinning would ensure that much less solvent would remain on the drop coated samples as well as making sure that the hexagonal close-packed spheres would not stack on top of each other and create multilayers instead of the sought after single layer.

The first sample tried out was drop coated with 5 μl of original nano sphere suspension prior to spin coating (10^9 NS/μl). The spin coating parameters were adopted from similar operation when coating samples with resists. The first stage had the sample revolving for 5 s at 100 rpm (revolutions per minute) after a 5 s acceleration step. Afterwards, the sample rotation accelerated (for 10 s) towards 1000 rpm, which was maintained for another 5 s, in stage two of the process. The third and final stage saw the sample reach its top rotation speed of 8000 rpm (also the machines highest value), after 10 s of acceleration, which it kept for 100 s before decelerating for 15 s to a complete halt.

Sample two was drop coated with 5 μl of a diluted nano sphere suspension (1 part original nano sphere suspension to 50 parts DI water and 50 parts ethanol, 1:50:50) prior to spin coating (10^6 NS/μl). The same spin coating parameters were employed as in the first sample, except for the final rotation speed, which was decreased from 8000 rpm to

1000 rpm.

The third spin coating sample was drop coated with 5 μl of the same nano sphere solution as the second sample (10^6 NS/μl). The main spin coating parameters changed was the maximum rotation speed, which was reduced from 1000 rpm to 500 rpm and the rotation time, which was increased from 5 s to 240 s. The time span of the first rotation speed, in the recipe, of 100 rpm, was increased from 5 s to 20 s. The time to reach a halt from the top rotation speed of 500 rpm was decreased from 15 s to 5 s of the second sample.

Sample number four was drop coated with 5 μl of a 1:1 ratio nano sphere and ethanol solution (10^8 NS/μl). The same spin coating parameters were used as for sample one. Two drops of 1 μl from a solution of nano spheres, DI water and ethanol, mixed at a ratio of 2:1:1, was deposited on the fifth sample (10^8 NS/μl). The spin coating recipe for the sample was, however, changed so that the top rotation speed was set to 100 rpm and the corresponding time was set to 300 s. The exact same spin coating recipe was also used for the sixth sample, which was coated with 1 μl from diluted nano sphere suspension (1 part original nano sphere suspension and 20 parts DI water, 10^7 NS/μl).

Varying the concentrations, the amount of ethanol as well as the spin parameters did not produce any monolayers of polymer nano spheres, closely packed in a hexagonal pattern, covering a large area of the substrate surface. Unfortunately, all results from the spin coating trials only repeated the undesired outcomes achieved with the previous drop coating method.

Immersion Coating

The last method to be used was immersion coating, which was found to be much more useful than the two tried and failed methods above. The first tests and trials of the immersion coating technique helped to perfect the method, which was then used to successfully coat all subsequent samples.

One Si sample was submerged and raised so that the nano spheres (close-packed monolayer at the air-water surface interface) coated its surface when it was gently raised. A second Si sample was turned upside-down and coated by the nano spheres, at the water surface, by gently lowering the sample and touching the water surface. A MoS_2 substrate was used in the same way as the previous Si support to be coated with a monolayer of close-packed nano spheres.

A new nano sphere solution was mixed for the immersion coating trials (10^8 NS/μl). Latex polymer nano spheres of 220 nm diameters suspended in water (with traces of surfactants in the mixture) and making up 10 wt% were diluted with an equal part of ethanol (1:1 ratio). The nano sphere solution was transferred to the surface of water filling the glass basin with a 2×2 cm^2 Si square substrate acting as a vehicle, and together making up some of the crucial parts of the immersion coating system. Four samples in total were prepared in the immersion coating of hexagonally close-packed monolayers of nano spheres onto their surfaces.

The newly prepared solution was used for immersion coating of nano spheres on a natural MoS_2 crystal substrate attached to a Si substrate with carbon tape.

Most of the nano sphere solution goes into the water, when trying to transfer it from the surface of a Si substrate to the air-water surface interface, creating a fog of nano spheres that need to settle before commencing the deposition (through siphoning of the water to lower the hexagonally close-packed latex polymer nano sphere monolayer floating atop the water surface). The volume of the NS solution has therefore been reduced from 20 μl to 10-15 μl.

These refinements of the method were used in all samples made in the remaining work. The results visible in figures of coming sections are the strength of this method.

5.2.2 Metal Deposition on Substrates Masked with Nano Spheres

In the pursuit of ordered MoS_2 nano corrugated structures, metal was deposited on nano sphere masked samples. The experiments pursued and the sputter coated samples are covered here.

Four slightly different samples were palladium sputter coated. Two of these samples were Si substrates sputter deposited with MoS_2 and subsequently immersion coated with nano spheres. One sample was a Si substrate drop coated with nano spheres and the fourth sample, a Si substrate supporting a MoS_2 substrate, which was also drop coated with nano spheres. The samples were sputter coated with Pd for 4 min at 50 W (~113 V_b) at a pressure of 2.0×10^{-2} mbar.

Pd is sputter coated onto a natural MoS_2 crystal substrate (supported on Si with carbon tape) masked with a monolayer of close-packed latex polymer nano spheres. The Pd sputtering process takes place at a pressure of 2×10^{-2} mbar for 4 min with a plasma at 50 W (114 V_b).

A further four samples of nano sphere immersion coated MoS_2 natural crystals, supported by Si, are deposited with Pd. The metal is sputter coated onto the samples in a pressure of 2×10^{-2} mbar with a power of 123 W (forward power, 40 W reflected power) and a bias voltage of 114 V_b during the deposition time of 4 min.

Ag was sputter deposited on two silicon substrates to get the process parameters relationship with the metal film thickness. Both samples were deposited in a pressure of 2.4×10^{-2} mbar and with a plasma at 100 W, but the first sample was deposited for 4 min and the second sample for 1 min. The average thickness of the first sample is 64 nm, while the average thickness of the second sample is 17 nm.

Another batch, with four samples, was sputter coated with Ag for a duration of 4 min at 100 W (115 V_b) and in a pressure of 2.4×10^{-2} mbar.

These samples coated with metal on top of the nano sphere masks covering the samples were cleaned in order to reveal the metal masks formed in the interstices of the close-packed nano sphere masks.

5.2.3 Cleaning off Nano Spheres Deposited with Metal

The cleaning of the previously metal sputter coated samples is explained here.

The sputter coated palladium on top of the nano spheres is initially cleaved away with scotch tape, so more of the nano spheres are exposed when cleaned with chloroform in ultrasonic bath for 4 min.

Yet another advantage of the cleaning procedure was observed when a Pd sputter coated sample of natural MoS_2 crystal substrate attached to a Si support with carbon tape and masked with a monolayer of close-packed latex polymer nano spheres was processed. The sample was initially cleaned with acetone in an ultrasonic bath for 10 min, after which the carbon tape is loosened from the Si support and the MoS_2 samples can easily be picked up or flushed off the carbon adhesive. The samples underwent another sonication bath with chloroform for 10 min to get rid of the latex polymer nano spheres.

The batch with four samples sputter deposited with Pd was initially cleaned with acetone for 15 min in ultrasonic bath, in order to remove the metal layer deposited on top of the hexagonally close-packed latex polymer monolayer. A clear change was visible, as the solution in the beaker was foggy and the sample surface was devoid of the palladium metal layer. The samples were then cleaned with chloroform for 15 min in an ultrasonic bath, but as no clear indication was visible of the removal of the nano sphere layer by the colour change of the reflected light, the samples were cleaned again for another 15 min.

Four similar samples, as the previous NS/MoS_2/Si samples, but sputter deposited with Ag, were firstly cleaned with acetone in ultrasonic bath. A clear change was visible, as

the colour of the reflected light from the sputter deposited areas on the samples, which was light red before the cleaning step, turned dark purple. The samples were then cleaned with chloroform in ultrasonic bath for 15 min, after which the reflected light turned from dark purple to normal colour of the samples.

After the cleaning, all samples were ready for the etching process.

5.2.4 Etching of Substrates Covered with Metal Island Masks

For the first sample (Table 5.12 first column), during the whole etching process (strike step + main mixed etch step) the sample base electrode plate temperature, the chamber pressure and helium pressure were all kept constant at 20 °C, 15 mTorr and 10 Torr, respectively. During the 5 s strike step the process gas flows were kept at 1 sccm (SF_6) and 50 sccm (C_4F_8), while the plasma RF power was 50 W and the ICP 300 W. The values are, however, changed in the 30 s main mixed etch step, where the plasma powers are kept at 20 W (RF) and 100 W (ICP) and the process gases are kept at 30 sccm (SF_6) and 20 sccm (C_4F_8).

The exact same etching recipe, but with a main mix etch step time increased from 30 s to 40 s, was used for a natural MoS_2 crystal deposited with ordered Pd etch mask islands (Table 5.12 second column).

Another three similar samples were etched with the same recipe (see first three columns in Table 5.13 for parameters), but where the main mix etch step time was 25 s (B1), 30 s (D1) and 35 s (C1), respectively.

The etching recipe was used on further three similar samples, but with ordered Ag etch mask islands instead of palladium. The main mixed etch step time for the three samples was set to 25 s (A2), 30 s (B2) and 35 s (C2), respectively (see last three columns in Table 5.13). However, the plasma was extinguished prematurely for both the 30 s (B2) and 35 s

Sample	Name	1	2
	Deposit	Pd/NS	”
	Substrate	MoS_2	”
Strike Step	Time (s)	5	”
	APC Pressure (mTorr)	15	”
	Temperature (°C)	20	”
	He Pressure (Torr)	10	”
	O_2 (sccm)	-	-
	SF_6 (sccm)	1	”
	C_4F_8	50	”
	RF Power (W)	50	”
	ICP Power (W)	300	”
Main Step	Time (s)	30	40
	APC Pressure (mTorr)	15	”
	Temperature (°C)	20	”
	He Pressure (Torr)	10	”
	O_2 (sccm)	-	-
	SF_6 (sccm)	30	”
	C_4F_8	20	”
	RF Power (W)	20	”
	ICP Power (W)	100	”

Table 5.12: First and second sample (batch) etched with ordered metal island masks, with all the relevant etching parameters listed in the table.

(C2) samples, at 12 s (B2) and 27 s (C2) remaining, rendering the actual etch time for the two samples 18 s (B2) and 8 s (C2), respectively.

The Si squares used to support the masked MoS_2 samples during metal sputter deposition, were etched to obtain etch rates of the etching process. Two samples were sputter deposited with Pd and two with Ag and all with a thickness of ~60 nm. All samples were initially cleaned with chloroform in ultrasonic bath for 15 min, to make sure no nano spheres were present, before etching. The same etching recipe (as for previous similar samples) was utilised, but the main mixed etch step time and ICP powers were set to 60 s and 150 W for one partially Pd and Ag covered Si sample set and to 40 s and 200 W for the other set (see Table 5.14). The plasma went on and off several times during the etch process of the partially Ag covered Si sample of 150 W (ICP) and 60 s, making it unreliable in the analysis.

	Name	B1	C1	D1	A2	C2	D2
Sample	Deposit	Pd/NS	”	”	Ag/NS	”	”
	Substrate	MoS_2	”	”	”	”	”
Strike Step	Time (s)	5	”	”	”	”	”
	APC Pressure (mTorr)	15	”	”	”	”	”
	Temperature (°C)	20	”	”	”	”	”
	He Pressure (Torr)	10	”	”	”	”	”
	O_2 (sccm)	-	-	-	-	-	-
	SF_6 (sccm)	1	”	”	”	”	”
	C_4F_8	50	”	”	”	”	”
	RF Power (W)	50	”	”	”	”	”
	ICP Power (W)	300	”	”	”	”	”
Main Step	Time (s)	25	30	35	25	18	8
	APC Pressure (mTorr)	15	”	”	”	”	”
	Temperature (°C)	20	”	”	”	”	”
	He Pressure (Torr)	10	”	”	”	”	”
	O_2 (sccm)	-	-	-	-	-	-
	SF_6 (sccm)	30	”	”	”	”	”
	C_4F_8	20	”	”	”	”	”
	RF Power (W)	20	”	”	”	”	”
	ICP Power (W)	100	”	”	”	”	”

Table 5.13: Third and fourth batch containing samples covered with ordered Pd and Ag etch mask islands, respectively. All the relevant etching parameters can be found in the table.

Unfortunately, the efforts to make ordered MoS_2 nano corrugated samples repeatedly, were not so successful. However, the best attempt at this feat can be seen in Figure 5.24. The egg cardboard box resemblance is quite striking even when the features are in nano scale. The height difference between the bottom and top is ~19 nm at the highest point and roughly 15 nm on average.

The other attempts did not have as nicely defined patterns due to several problems. Those issues were, in particular, caused by the sputter deposition process not being able to produce uniform ordered metal island etch masks and failure to completely clean off the nano sphere masks afterwards. Despite the difficult reproducibility of these structures, all gained experience and techniques perfected during these experiments were utilised in the fabrication of ordered MoS_2 nano pillars, which will be covered in the coming sections.

	Name	A1	B2	C1	A2
Sample	Deposit	Pd	Ag	Pd	Ag
	Substrate	Si	”	”	”
Strike Step	Time (s)	5	”	”	”
	APC Pressure (mTorr)	15	”	”	”
	Temperature (°C)	20	”	”	”
	He Pressure (Torr)	10	”	”	”
	O_2 (sccm)	-	-	-	-
	SF_6 (sccm)	1	”	”	”
	C_4F_8	50	”	”	”
	RF Power (W)	50	”	”	”
	ICP Power (W)	300	”	”	”
Main Step	Time (s)	60	60	40	40
	APC Pressure (mTorr)	15	”	”	”
	Temperature (°C)	20	”	”	”
	He Pressure (Torr)	10	”	”	”
	O_2 (sccm)	-	-	-	-
	SF_6 (sccm)	30	”	”	”
	C_4F_8	20	”	”	”
	RF Power (W)	20	”	”	”
	ICP Power (W)	150	150	200	200

Table 5.14: Four Si samples making up batch number five, were etched with Pd and Ag masks. The relevant etching parameters of the four samples are all listed in the table.

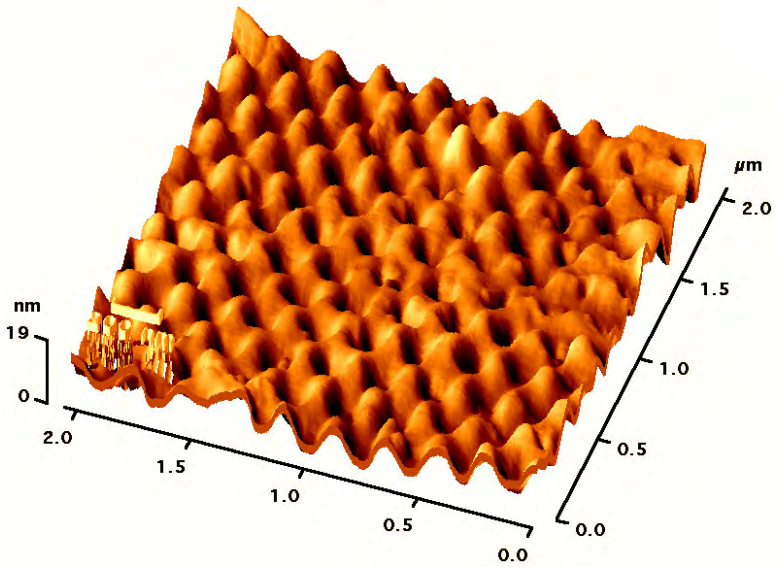

Figure 5.24: 3D AFM image of ordered MoS_2 nano corrugated structures resembling an egg cardboard box. The lowest part is where a nano sphere mask would have been situated and the highest part is where, in this case, Pd metal island masks were residing (2 μm×2 μm×19 nm).

5.2.5 Sputter Deposition of Molybdenum Disulfide

Long-range flat substrates of molybdenum disulfide were sought through deposition, using Si as a reliably uniform support. Two Si substrates were plasma sputter deposited with MoS_2 in the sputter coater using a MoS_2 target. MoS_2 was deposited for 10 min at 100 W (202 V_b) at a pressure of 2.8×10^{-2} mbar. Both samples are more hydrophilic than the Si (native oxide layer), that was masked off during the sputtering. One of the samples was scratched and measured to show an average thickness of ~119 nm, while the other sample was prepared for annealing.

The annealing process started at room temperature, ~24 °C, and reached the annealing temperature, 550 °C, after 8 min and actually overshot to 560 °C before stabilising at the set value. The annealing was performed at ambient air pressure, with the gas inlet enabled lid of the furnace closed, for 30 min. However, the sample was left in the furnace for a further 40 min, with the gas inlet lid open, to allow it to cool down and reach 400 °C.

In the second attempt of MoS_2 sputter deposition, three Si substrates were used to support the sputtered material from the MoS_2 target. The sputter deposition process lasted for 20 min at 100 W (202 V_b) and at a pressure of 2.9×10^{-2} mbar.

One of the sputter coated samples had a thickness gradient, which manifests itself by a colour gradient of the ambient light reflected onto the Mo_xS_y surface, where one side has a green hue and the other side a purple hue. The thickness of this sample is 315 nm on the green side and 303 nm on the purple side.

The first, scratched and measured, non-annealed sample was placed in the furnace, which was filled with flowing nitrogen gas at a rate of ~160 sccm before commencing ramping up towards the annealing temperature of 550 °C. The temperature was ramped up from ~27 °C and reached the annealing temperature (550 °C) after 8 min (8 min 19 s) and overshot to 562 °C. The temperature was maintained for 30 min before closing the furnace,

while leaving the sample inside and the flow of nitrogen running. After 3 h the temperature had decreased to 170 °C, so the nitrogen flow was stopped, but the sample left inside the furnace with the lid closed until reaching room temperature.

The initial sputtering and annealing of samples did not lead to long-range flat crystal MoS_2 substrates, but rather to grainy quasi-crystal films. As it became evident that this approach is more complex and time consuming than first thought, it was quickly abandoned and the natural crystals of MoS_2 were used as substrates instead.

5.3 Ordered MoS_2 Nano Pillar Structures

Hexagonally ordered nano pillar structures are fabricated by using the latex polymer nano spheres as etch masks, in the pillar formation step. The fabrication steps are almost similar as for the previous method in Section 5.2 on page 209. However, instead of steps (2) metal evaporation and (3) removal of excess metal and the nano sphere mask, another etch step is introduced. Hence, after step (1) nano sphere deposition on substrate, step (2) is where nano sphere masks are shrunk through O_2 plasma etching, before the final step (3) etching substrate covered with ordered masks.

5.3.1 Immersion Coating vs Adhesion Coating

All samples were initially immersion coated with a hexagonally close-packed latex polymer nano sphere monolayer. The nano sphere solution used was similar to what was finally used in Section 5.2.1 on page 217, i.e. 10 wt% of 220 nm nano spheres suspended in water (with traces of surfactants) mixed with ethanol at a 1:1 ratio. Small volumes were then transferred to the water surface of a glass basin through a silicon substrate acting as a vehicle.

Three Si samples were immersion coated with nano spheres for the first trials of the O_2 plasma etching to shrink the nano spherical latex polymer masks.

Five more samples, making up a second test batch, were immersion coated with the same nano sphere concentration solution, which was sonicated 15 min before use in order to get a good spread. 20 μl of the solution was dropped on the Si transfer substrate, which was gently immersed at a high angle into the water basin, transferring the nano spheres on top of the air-water surface interface, where they built up a hexagonally close-packed monolayer. The samples to be coated were pre-immersed in the water basin on their sample holder stands and ready to be deposited with nano spheres after their transfer to the water surface of the basin, by lowering the water surface through siphoning. Three of the samples were electrodeposited MoS_2 on Au film on quartz substrates on Si supports (attached with carbon tape). Two of the samples only have fragmented coverage of MoS_2, while the third sample has slightly more and better coverage of the semiconductor on the Au film. The three samples proved to be hydrophobic, which made the immersion coating much more difficult, only one successful coating and one partly. The other two samples in the batch were natural MoS_2 crystal on Si supports and were successfully coated with nano spheres.

A third test batch was prepared, consisting of four natural MoS_2 crystal samples, in a similar way as Batch 2, except for one of the samples. A new deposition method, adhesion coating, was tried out as a solution to the issue with the hydrophobic samples pushing away the water and the nano sphere monolayer, floating on top of the water surface, with it. This happens when the water surface is lowered, by siphoning, and very closely approaches the substrates during the immersion coating process. The unique and novel method utilises the problem and makes it part of the solution. Instead of immersing the substrates inside the water in the glass basin, prior to the nano sphere monolayer transfer on the water surface, they were kept dry and outside the water basin altogether. After the

transfer of the nano sphere monolayer the hydrophobic MoS_2, attached (with carbon tape) on hydrophilic Si support, was turned upside-down and gently lowered towards the water surface. The nano sphere monolayer is locked and sandwiched between the hydrophobic MoS_2 surface on top and the water below, which moves up around the edges of the MoS_2 and wets the surrounding hydrophilic Si surface. The sample was then gently raised and held until all water was evaporated, with the nano sphere monolayer remaining on the MoS_2 surface. This could be clearly seen by inspection as a coloured hue was visible on top of the MoS_2 surface corresponding to the presence of close-packed nano spheres.

To ensure less vibrations ruining the close-packing of the nano spheres, another sample was adhesion coated, but now attached to a firm stand with a coarse vertical translation mechanism. Despite the deposition being more stable, the water surface on which the nano sphere monolayer resided, moved a lot due to uncontrollable air flow.

5.3.2 O_2 Plasma Etching

After the deposition of nano spheres on top of the sample surfaces they were shrunk in size through oxygen plasma etching. The etching process proved to be useful for yet another thing, which would make the overall fabrication process more efficient. The immersion coating proved to be useful still despite the huge potential of the adhesion coating method. Instead of trying to improve the new adhesion coating technique of samples with nano spheres, which cut down some of the overall processing time, a way to make samples hydrophilic was sought to continue using the immersion coating method. The first sample tried was a natural MoS_2 crystal, which at initial test with water turned out to be hydrophobic. Oxygen plasma etching was employed to make sample surfaces hydrophilic.

The parameters of O_2 plasma etching is also divided up between a strike step and a main step. The helium backing pressure in the etching chamber was kept at 10 Torr, while the

temperature of the sample back electrode plate was constant at 20 °C. The flow of the process gas O_2 was 100 sccm, while the plasma power was set to 100 W (RF) throughout the process. The only parameter that was changed was the APC pressure, which changed from 40 mTorr during the 7 s strike step to 20 mTorr, in the 30 s main O_2 plasma etch step. As the sample (C5) was still hydrophobic another etching, also set to 30 s, was employed. With no change observed, the sample underwent a third etching, now with the etch time set to 90 s (see Table 5.15).

Sample	Name	C5	C5	C5
	Deposit	-	”	”
	Substrate	MoS_2	”	”
Strike Step	Time (s)	7	”	”
	APC Pressure (mTorr)	40	”	”
	Temperature (°C)	20	”	”
	He Pressure (Torr)	10	”	”
	O_2 (sccm)	100	”	”
	SF_6 (sccm)	-	”	”
	C_4F_8	-	”	”
	RF Power (W)	100	”	”
	ICP Power (W)	-	”	”
Main Step	Time (s)	30	30	90
	APC Pressure (mTorr)	20	”	”
	Temperature (°C)	20	”	”
	He Pressure (Torr)	10	”	”
	O_2 (sccm)	100	”	”
	SF_6 (sccm)	-	”	”
	C_4F_8	-	”	”
	RF Power (W)	100	”	”
	ICP Power (W)	-	”	”

Table 5.15: Sample being oxygen plasma etched in order to make it hydrophilic for better immersion coating with nano spheres. The relevant etching parameters for the samples are all listed in the table.

The now hydrophilic sample (C5) was prepared for nano sphere deposition (immersion coating), but was not covered successfully on the first attempt. After chloroform and piranha cleaning, the (hydrophilic) sample was yet again immersion coated, now with successfully deposited nano spheres.

Figure 5.25 show an AFM image of how latex polymer nano spheres, with a diameter of ~200 nm, form a hexagonally close-packed monolayer on MoS_2 substrate. This self assembly of the nano sphere etch masks is clearly an advantage when forming ordered nano pillar structures. Furthermore, through oxygen plasma etching, the size of the nano spheres can be reduced in order to control the diameter of the nano pillars to be etched.

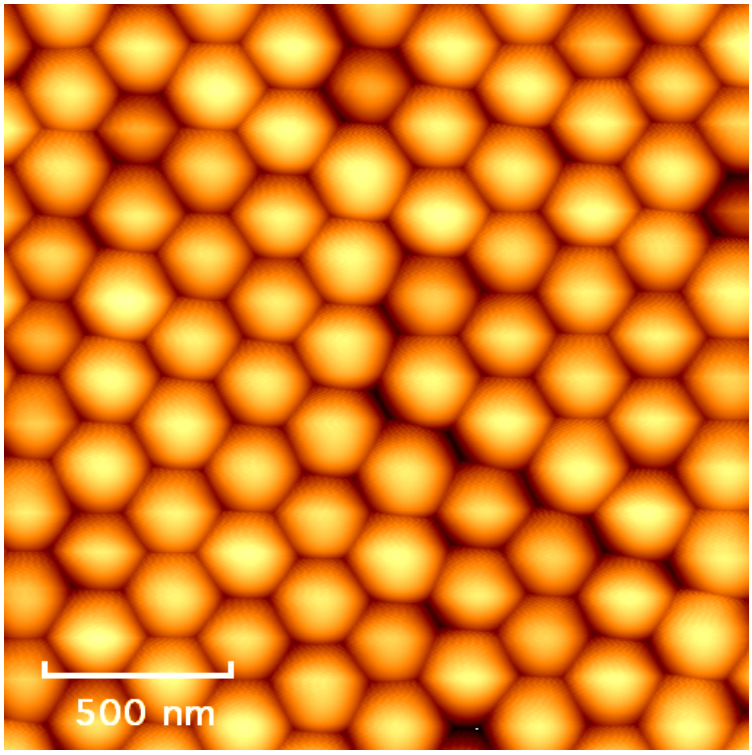

Figure 5.25: AFM image of MoS_2 sample immersion coated with NS after the evaporation of the solvent (water + ethanol + traces of surfactants). As can be seen, a hexagonal close-packed monolayer has been formed by the ~200 nm diameter latex polymer nano spheres (500 nm scale bar).

After oxygen plasma etching, the hexagonally close-packed nano spheres shrink in size as can be seen in Figure 5.26. The SEM image depicts hexagonally ordered nano spheres reduced to almost a quarter of their original diameters of around 200 nm, after an etch time of 60 s. The surface of the spheres look uneven due to remnants of the etched off latex polymer, which is quite little considering the original size and would not, anyhow, limit the function of the nano spheres as etch masks.

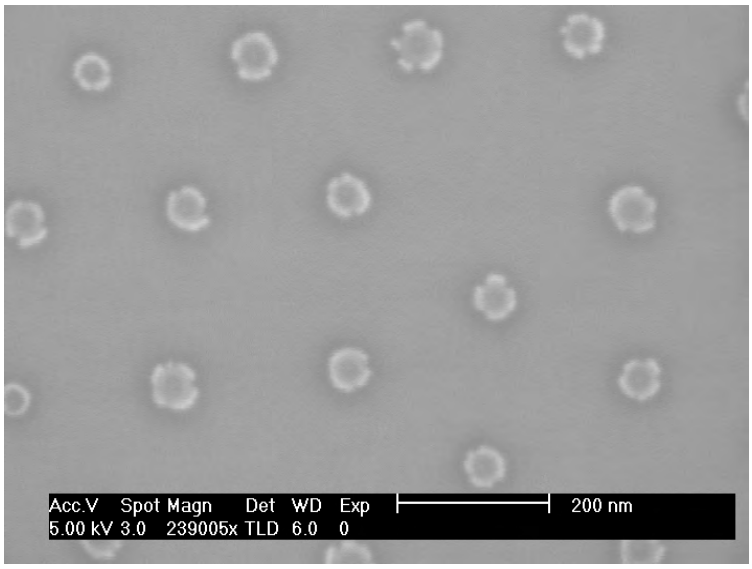

Figure 5.26: SEM image of sample showing the decreased sizes of the hexagonally ordered nano spheres, which were close-packed before oxygen plasma etching. Their sizes have decreased to almost a quarter of their original diameter of 200 nm after 60 s etch time. Remnants of the etched off latex polymer can be seen on the surface of the nano spheres, making them look uneven (200 nm scale bar).

Taking the average reduced diameter of the latex polymer nano spheres as a function of the oxygen plasma etch time gives a linear relationship as depicted in Figure 5.27. The equation of the linear fit is $f(x) = -2.37x + 214.89$ and predicts the total disappearance of the nano spheres after an oxygen plasma etch time of 90 s.

With the above in mind, the choice to etch the nano spheres, of the final ordered nano pillar structure samples, therefore fell on the times 35 s and 55 s, to also get the spread in sizes. According to the fit, an etch time of 35 s would result in nano spheres with diameters roughly being 130 nm and for a 55 s etch time the diameter would be reduced to ~85 nm.

Before immersion coating of samples with nano spheres, they were cleaned (first with Piranha) and their surfaces were checked to be hydrophilic. The majority of surfaces of MoS_2 samples, found to be hydrophobic, were oxygen etched according to the same parameters as in the trials, see third column in Table 5.15. When found hydrophilic through visual inspection with water, the samples were deposited with nano spheres through im-

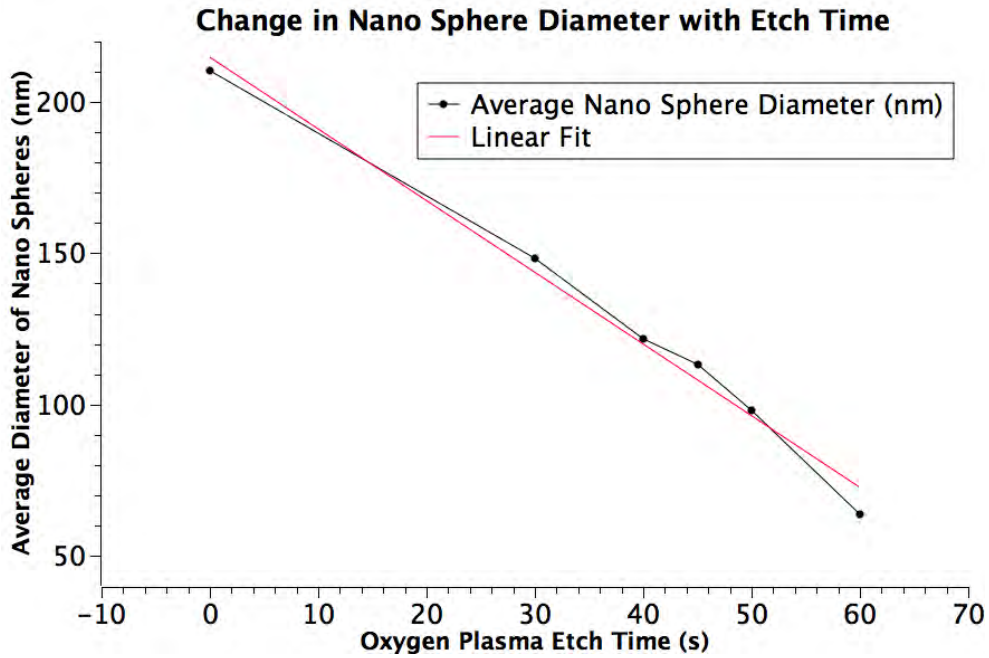

Figure 5.27: The graph depicts the change in diameter size of the latex polymer nano spheres with the oxygen plasma etch time. Each data point ('black' dot) is the average diameter of nano spheres after a certain time in oxygen plasma etching. The data points ('black' dots) are connected with a 'black' line to show their interrelations and the 'red' straight line is the linear fit of the data points.

mersion coating and prepared for another round of oxygen etching in order to reduce their size.

Four sample groups (three samples in each group) with their respective reference sample groups (etched with the same parameters, but without nano sphere etch masks) were oxygen plasma etched with same parameters except for the etch time. Two groups, A10 & B10 (with respective reference groups, A11 & B11), were oxygen plasma etched for 55 s and the other two groups', C10 & D10 (with respective reference groups, C11 & D11), etch time was 35 s, see Table 5.16.

The natural MoS_2 crystal samples (B4 & B5), adhesion coated with nano spheres, were also O_2 plasma etched with similar parameters as previously but for 50 s to shrink the size of the nano sphere masks, see first two columns in Table 5.17.

After the reduction in size of the NS etch masks, the samples were ready for mix etching

	Name	A10	A11	B10	B11	C10	C11	D10	D11
Sample	Deposit	NS	-	NS	-	NS	-	NS	-
	Substrate	MoS_2	”	”	”	”	”	”	”
Strike Step	Time (s)	7	”	”	”	”	”	”	”
	APC Pressure (mTorr)	40	”	”	”	”	”	”	”
	Temperature (°C)	20	”	”	”	”	”	”	”
	He Pressure (Torr)	10	”	”	”	”	”	”	”
	O_2 (sccm)	100	”	”	”	”	”	”	”
	SF_6 (sccm)	-	”	”	”	”	”	”	”
	C_4F_8	-	”	”	”	”	”	”	”
	RF Power (W)	100	”	”	”	”	”	”	”
	ICP Power (W)	-	”	”	”	”	”	”	”
Main Step	Time (s)	55	”	”	”	35	”	”	”
	APC Pressure (mTorr)	20	”	”	”	”	”	”	”
	Temperature (°C)	20	”	”	”	”	”	”	”
	He Pressure (Torr)	10	”	”	”	”	”	”	”
	O_2 (sccm)	100	”	”	”	”	”	”	”
	SF_6 (sccm)	-	”	”	”	”	”	”	”
	C_4F_8	-	”	”	”	”	”	”	”
	RF Power (W)	100	”	”	”	”	”	”	”
	ICP Power (W)	-	”	”	”	”	”	”	”

Table 5.16: Four sample groups and their references (i.e. eight sample groups) of which four groups of samples were oxygen plasma etched in order to decrease the size of the nano sphere etch masks. The relevant etching parameters for the samples are all listed in the table.

in order to form MoS_2 nano pillars.

	Name	B4	B5	B4	B5
Sample	Deposit	NS	”	”	”
	Substrate	MoS_2	”	”	”
Strike Step	Time (s)	7	”	6	”
	APC Pressure (mTorr)	40	”	15	”
	Temperature (°C)	20	”	”	”
	He Pressure (Torr)	10	”	”	”
	O_2 (sccm)	100	”	-	”
	SF_6 (sccm)	-	”	1	”
	C_4F_8	-	”	50	”
	RF Power (W)	100	”	50	”
	ICP Power (W)	-	”	300	”
Main Step	Time (s)	50	”	30	25
	APC Pressure (mTorr)	20	”	15	”
	Temperature (°C)	20	”	”	”
	He Pressure (Torr)	10	”	”	”
	O_2 (sccm)	100	”	-	”
	SF_6 (sccm)	-	”	25	”
	C_4F_8	-	”	20	”
	RF Power (W)	100	”	25	”
	ICP Power (W)	-	”	220	”

Table 5.17: Two MoS_2 samples, adhesion coated with nano spheres, were first oxygen plasma etched and then mixed etched in order to decrease the size of the nano sphere masks and form ordered nano pillars. The relevant etching parameters for the samples are all listed in the table.

5.3.3 Etching of Substrates Covered with Shrunk Nano Sphere Masks

The mix etching process of the NS adhesion coated MoS_2 samples (B4 & B5) lasted for 36 s, in total, for one of them and 31 s for the other (6 s strike step + 30/25 s main mix etch step). In this whole duration, the sample back electrode plate temperature, the helium backing pressure and the APC pressure was kept at 20 °C, 10 Torr and 15 mTorr, respectively. The process gas flow rate increased for SF_6 from 1 sccm to 25 sccm, between strike step and main mixed etch step, while it decreased for C_4F_8 from 50 sccm to 20 sccm. Moreover, the ICP power was decreased from 300 W to 220 W, while the RF power was decreased from 50 W to 25 W between the two etching steps of the overall process.

Where the new adhesion coating method does away with one step (oxygen etching to

make the surface hydrophilic) of the overall fabrication process and speeds up the actual NS coating step, compared to the immersion coating technique, it does not produce as ordered end results as the latter procedure. The usage of a crude stand to lower the surface of MoS_2 substrates to coat NS, lying on the surface of water in a glass basin on top of a desk top (not free from noise and vibrations), resulted in quasi-ordered MoS_2 nano pillars as can be seen in Figures 5.28a to 5.28c.

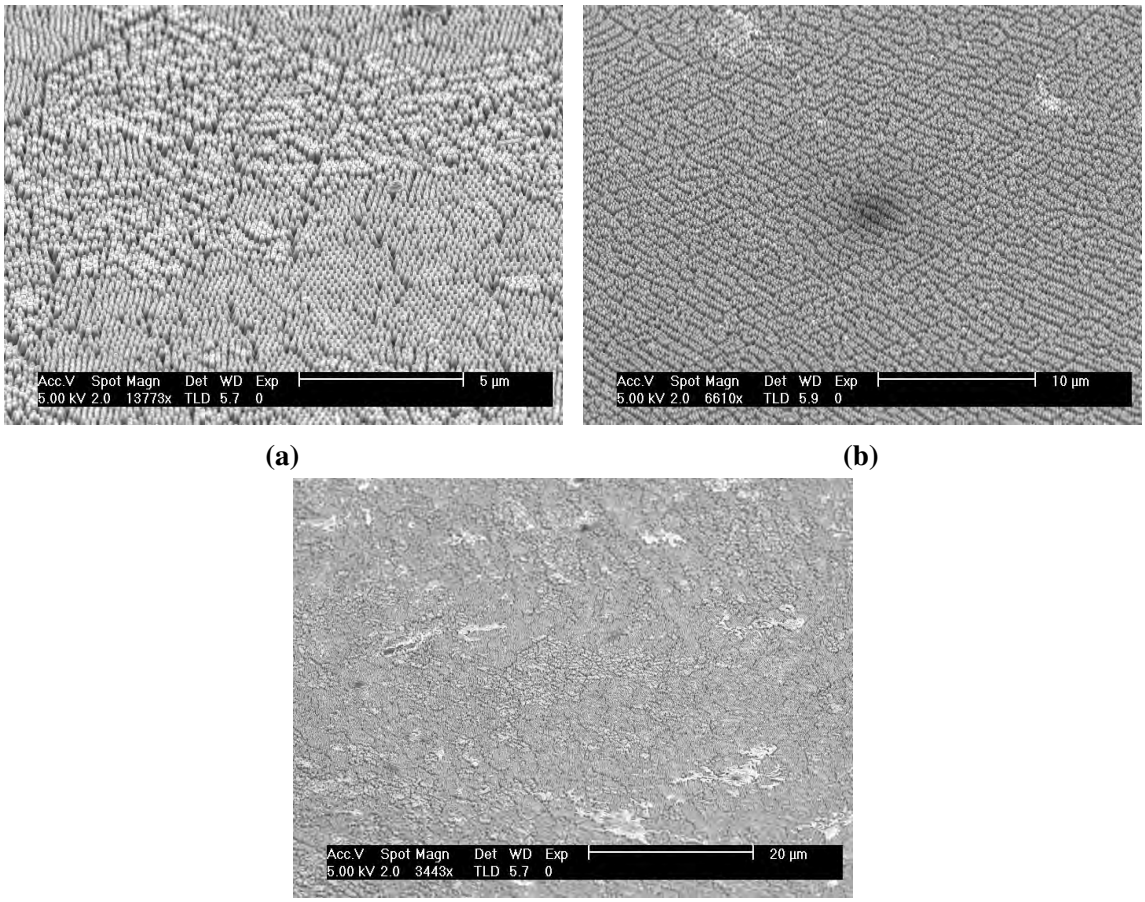

(a) **(b)**

(c)

Figure 5.28: SEM images of sample (B5) adhesion coated with nano sphere etch masks after oxygen and mix etching (see last two columns in Table 5.17 for parameters). (a) Large areas with ordered nano pillars can be seen as well as large areas of nano pillars with positions slightly perturbed from the hexagonal pattern of their originally close-packed NS etch masks (45 °, 5 μm scale bar). (b) Zoomed out area with positions of small nano pillar patches being quite perturbed (45 °, 10 μm scale bar). (c) Further zoomed out area showing different patches of nano pillars being ordered to different degrees (45 °, 20 μm scale bar). The average tip diameter of the MoS_2 nano pillars is ~100 nm and the average height is ~590 nm.

This side-discovery of a method could easily outperform the immersion coating process if more time was spent refining the mechanics of the sample translation and reducing the vibrations and noise experienced by the water basin. However, this was not possible in the scope of this work as no time was available to investigate and develop the technique further. Instead, MoS_2 samples immersion coated with NS were used in further work.

Samples from the first and third groups (A10 & C10), together with samples from their respective reference groups (A11 & C11), were mix etched with similar parameters as previously for a duration of 30 s. Samples from the other two groups (B10 & D10) and their reference groups (B11 & D11) were etched similarly but for 10 s. All samples from the four groups were SEM imaged afterwards.

The selectivity of the mix etching process is higher for MoS_2 than for the nano spheres, ensuring the formation of (high aspect ratio) ordered MoS_2 nano pillars, see Figures 5.29a to 5.29d. The etching process reduced the size of the latex polymer nano sphere etch masks further, thus decreasing the diameter of the nano pillars more (compare nano sphere sizes before and after the mix etching process). Consequently, more of the underlying MoS_2 was also gradually exposed, during the mix etching, thus decreasing the nano pillar edge slope and increasing the height further.

For comparison the average tip diameters of the ordered MoS_2 nano pillars of the differently etched sample groups have been included in a graph, see Figure 5.30. Each vertical bar (with the distinct colour labels 'black' A10, 'red' B10, 'green' C10 and 'blue' D10) represents a sample group (i.e. A10, B10, C10 or D10) and the position of the bars indicate the oxygen and mix plasma etch time of the corresponding group. The average tip diameter of the ordered nano pillars are represented by the heights of the bars.

It is evident that the oxygen plasma etch time has the biggest effect on the nano pillar tip diameter as can be seen by comparing the diameters of the two groups (C10 & D10) oxygen etched for 35 s and the two groups (A10 & B10) oxygen etched for 55 s. The

	Name	A10	A11	B10	B11	C10	C11	D10	D11
Sample	Deposit	NS	-	NS	-	NS	-	NS	-
	Substrate	MoS_2	”	”	”	”	”	”	”
Strike Step	Time (s)	6	”	”	”	”	”	”	”
	APC Pressure (mTorr)	15	”	”	”	”	”	”	”
	Temperature (°C)	20	”	”	”	”	”	”	”
	He Pressure (Torr)	10	”	”	”	”	”	”	”
	O_2 (sccm)	-	”	”	”	”	”	”	”
	SF_6 (sccm)	1	”	”	”	”	”	”	”
	C_4F_8	50	”	”	”	”	”	”	”
	RF Power (W)	50	”	”	”	”	”	”	”
	ICP Power (W)	300	”	”	”	”	”	”	”
Main Step	Time (s)	30	”	10	”	30	”	10	”
	APC Pressure (mTorr)	15	”	”	”	”	”	”	”
	Temperature (°C)	20	”	”	”	”	”	”	”
	He Pressure (Torr)	10	”	”	”	”	”	”	”
	O_2 (sccm)	-	”	”	”	”	”	”	”
	SF_6 (sccm)	25	”	”	”	”	”	”	”
	C_4F_8	20	”	”	”	”	”	”	”
	RF Power (W)	25	”	”	”	”	”	”	”
	ICP Power (W)	220	”	”	”	”	”	”	”

Table 5.18: Samples from four groups and their respective reference groups were mix etched to form ordered nano pillars using (shrunk) latex polymer nano spheres as etch masks. The relevant etching parameters for the samples are all listed in the table.

two later groups (with the longer oxygen plasma etch time) have the two smallest average nano pillar tip diameters with group A10 having the smallest. Moreover, the mix etch time is the second factor affecting the average nano pillar tip diameter, which explains why group A10 (longer mix etch time, 30 s) has a smaller average nano pillar tip diameter than group B10 (shorter mix etch time, 10 s) despite both being oxygen plasma etched for

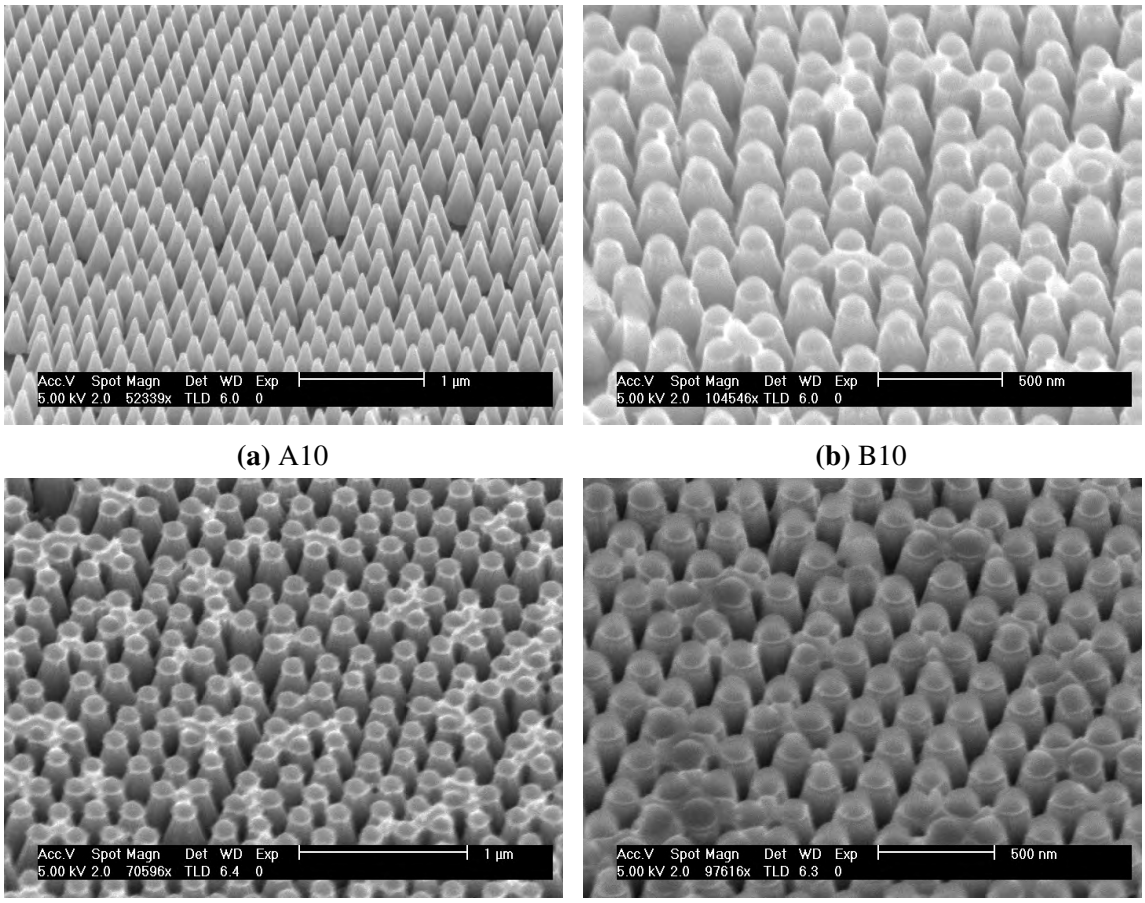

(a) A10 **(b)** B10

(c) C10 **(d)** D10

Figure 5.29: SEM images of samples from group A10, B10, C10 and D10 after oxygen and mix etching (see Table 5.18 for parameters). (a) The average tip diameter of the MoS_2 nano pillars is ~60 nm and the average height is ~820 nm (45°, 1 μm scale bar). (b) The average tip diameter of the MoS_2 nano pillars is ~120 nm and the average height is ~280 nm (45°, 500 nm scale bar). (c) The average tip diameter of the MoS_2 nano pillars is ~130 nm and the average height is ~530 nm (45°, 1 μm scale bar). (d) The average tip diameter of the MoS_2 nano pillars is ~150 nm and the average height is ~290 nm (45°, 500 nm scale bar).

55 s. In the same way, even though, the former two groups had a 35 s oxygen etch time, group D10 (shorter mix etch time, 10 s) has a larger average nano pillar tip diameter than group C10 (longer mix etch time, 30 s).

The group with the tallest pillars is A10 (Figure 5.31), which has both the longest oxygen etch time (55 s) and longest mix etch time (30 s). Group C10 has the second tallest nano pillars, with an average MoS_2 nano pillar height of ~530 nm, and shares the same mix etch time of 30 s with group A10, but has a lower oxygen etch time (35 s compared to

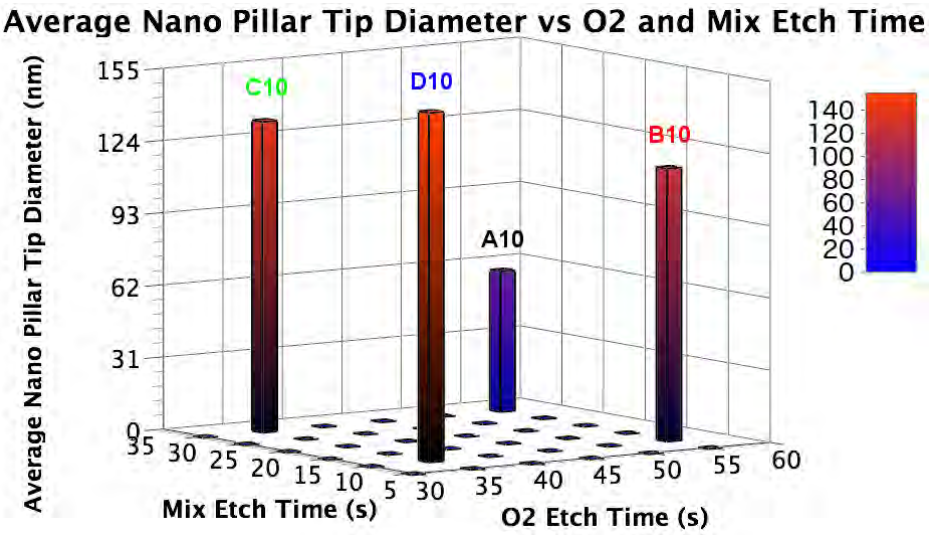

Figure 5.30: The average nano pillar tip diameters obtained with different latex polymer nano sphere etch mask sizes (using different etch times) are represented in the graph. Each vertical bar represents a data point, i.e., the average tip diameter of nano pillars post oxygen and mix plasma processes by various etch times.

55 s). With the same difference in oxygen etch time as previous two groups, groups B10 and D10 have similar heights of their nano pillars at around 280 nm and share the same low 10 s mix etch time.

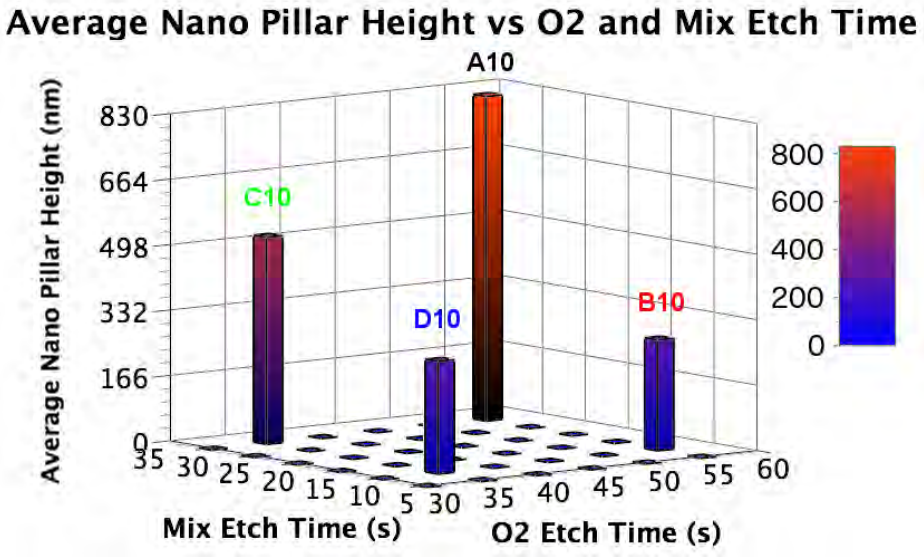

Figure 5.31: The average nano pillar heights obtained with different latex polymer nano sphere etch mask sizes and mix etch times are represented in the graph as bars. Each bar corresponds to one of the four sample groups (A10, B10, C10 and D10) oxygen and mix etched with different etch times forming MoS_2 nano pillars with different average heights.

This chapter has, so far, demonstrated the formation of MoS_2 nano pillars of different orders of size by utilising various fabrication techniques. Through initial trial and error it became possible to discover the (a) parameter space allowing for the fabrication of nano pillars from MoS_2 for the first time. Not only has this additional form of MoS_2 added to its repertoire of shapes and structures, but it is also thought to enhance its properties. Among the properties of particular interest, to us, in this study, is the catalytic properties of this intriguing semiconductor in its newfound shape. The coming sections are, therefore, dedicated to covering the experimental investigation of the catalytic properties of the fabricated MoS_2 nano pillar samples.

5.4 Electrochemistry of MoS_2 Nano Pillar Catalysts

The electrochemistry experiments were performed at the Technical University of Denmark (DTU), Denmark, with collaborators in Center for Individual Nanoparticle Functionality (CINF). Different nano structured MoS_2 samples, as described in the previous sections in this chapter, were used as catalysts to test their chemical reaction enhancing properties in the hydrogen evolution reaction (HER).

These tests (HER activity measurements, cyclic voltammetry) were conducted in order to get an initial indication of the (relative) performance of the samples made in order to get feedback for future improvements. The coming sections will go through the specific work related to the electrochemical measurements, such as the electrode construction and the results obtained.

5.4.1 Electrochemistry of MoS_2 Catalysts

The first sample tested was a natural MoS_2 crystal with ordered nano pillars. In the first trial(s), the catalyst sample (the backside) was directly attached to copper tape and teflon

tape was used to mask off everything except for the active area being tested. The surface layer, which is where the base of the pillars reside, was connected to the copper tape with liquid silver adhesive. A small hole (a couple of mm in diameter) was made on the teflon tape, with scalpel, to expose the area investigated. Issues arose early on with the first design, such as difficulties to control position of samples/electrodes, teflon tape not masking off the intended catalyst area properly and silver adhesive leaking out and being exposed in the catalytic area. From SEM it was evident that the latex polymer nano sphere masks remained on the samples after etching, so therefore the samples were sonicated with chloroform for 15 min, see Figure 5.32. Also, for flexibility and time efficiency, new electrodes were designed and made.

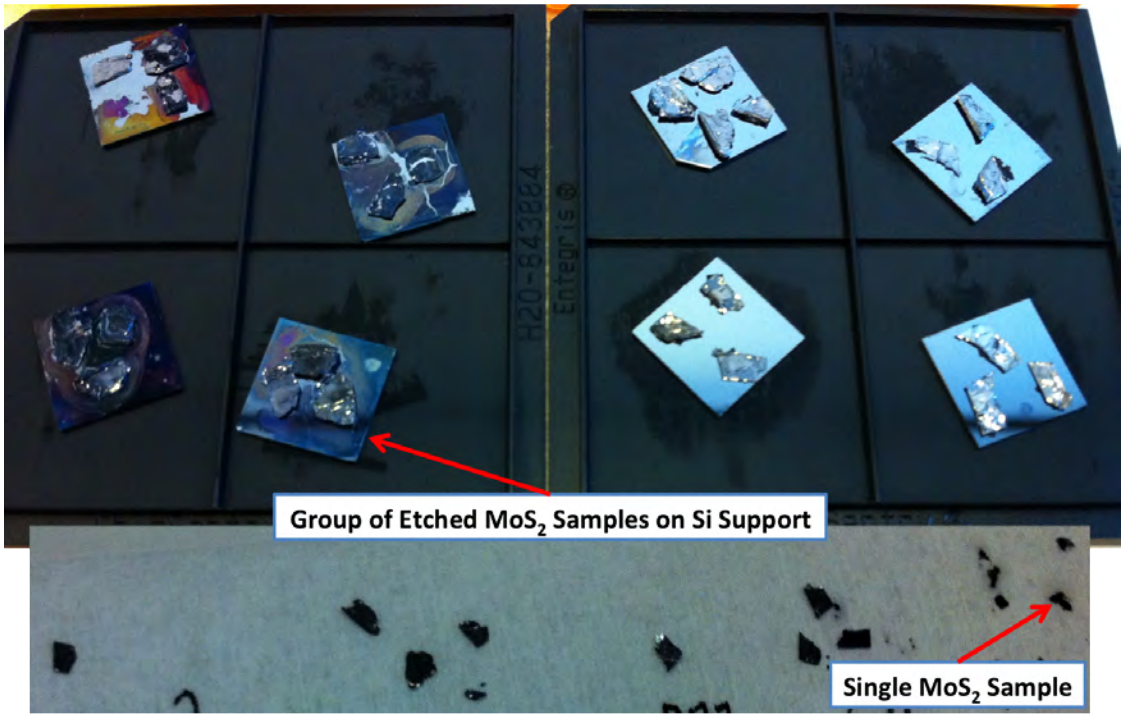

Figure 5.32: The etched MoS_2 sample groups, on silicon supports, were sonicated with chloroform for 15 min in order to remove the remaining latex polymer nano sphere etch masks. Afterwards, individual MoS_2 were ready to be attached to electrodes for CV measurements.

Electrode Construction

The final version of electrodes used in all experiments consisted of using Si supports, onto which copper tape was partly attached onto the top surface, see Figure 5.33. The MoS_2 samples (see Figure 5.32) where then placed on top of the copper tape on the Si support and liquid silver adhesive was brushed on the edge of the samples, between the top surface and the copper tape, see Figure 5.34. Small metal pipes (see Figure 5.33) with 2-3 mm diameters were used to cut out holes from teflon tape, which was used to mask off everything, except for the MoS_2 (nano structured) top surface catalyst area. Isolated copper wire was formed into a flat spiral at one end and the isolation removed with scalpel, before attached to the free end of the copper tape. The copper wire was further shielded with a thin glass pipe and the electrode was, thus, ready to be used.

The rectangular samples of electroplated MoS_2 films, on Au films deposited on quartz crystals, were directly attached to Cu tape, which were isolated with PTFE tape and connected to Cu wire extensions.

After the initial tests and setup of the electrodes, the experiments were run with the setup explained in Section 2.5 starting on page 87 in Chapter 2. The sample electrodes were inserted into the photo electrode (working electrode) compartment individually and cyclic voltammetry (CV) was run with the same parameters under the same conditions, as explained in the section, for each and every one of the sample electrodes.

Electrochemistry of Ordered MoS_2 Nano Pillar Structures

The data displayed in the figures have been corrected for by adding the potential of the reference electrode (0.244 V vs NHE) and 0.060 V·pH (from the Nernst equation), using the pH of the electrolyte (0.1 M perchloric acid) as well as normalising each current by the corresponding sample's surface area. No supporting electrolyte was used, cf. e.g.

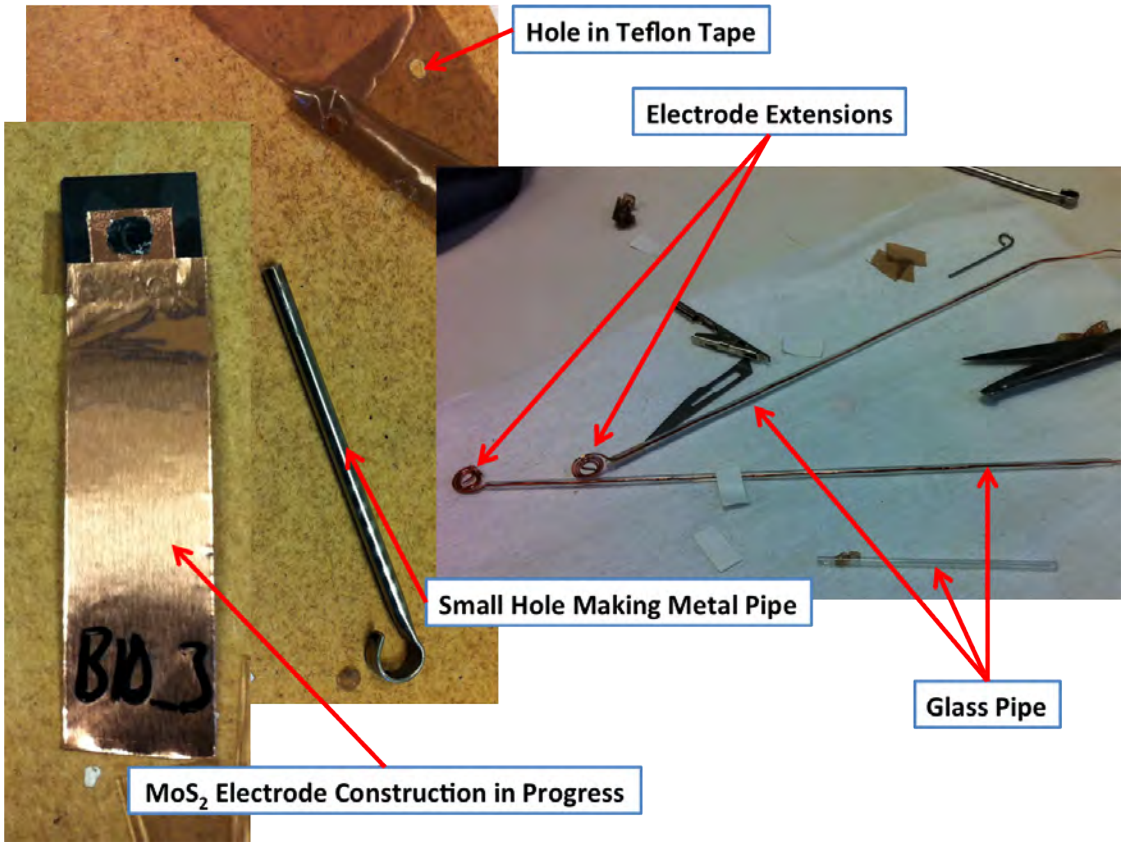

Figure 5.33: The construction of a MoS_2 electrode in progress, where the copper tape is attached to the silicon support and the MoS_2 placed on top. A small metal pipe with diameter of 2-3 mm was used to make holes in teflon tape, that masked off the sample except for the (nano structured) top surface catalyst region. Extensions of the electrodes were made from copper wires shielded with thin glass pipes.

[73, 80, 151, 152], and the voltammetry was self supported [168–170].

For clarity, only CV graphs of the best performing ordered MoS_2 pillar sample, its corresponding reference and blank reference samples are included in each figure. This makes it easier to highlight performance between pillar and reference sample within each group. For a group-by-group comparison, all graphs are added into one figure at the end. The lower the CV graph, i.e. higher currents for higher voltages, the higher HER activity the corresponding sample exhibits.

Figure 5.35 displays CVs of ordered MoS_2 nano pillar sample (A10 with NS, oxygen etched for 55 s and mixed etched for 30 s) as well as of its reference MoS_2 sample (A11

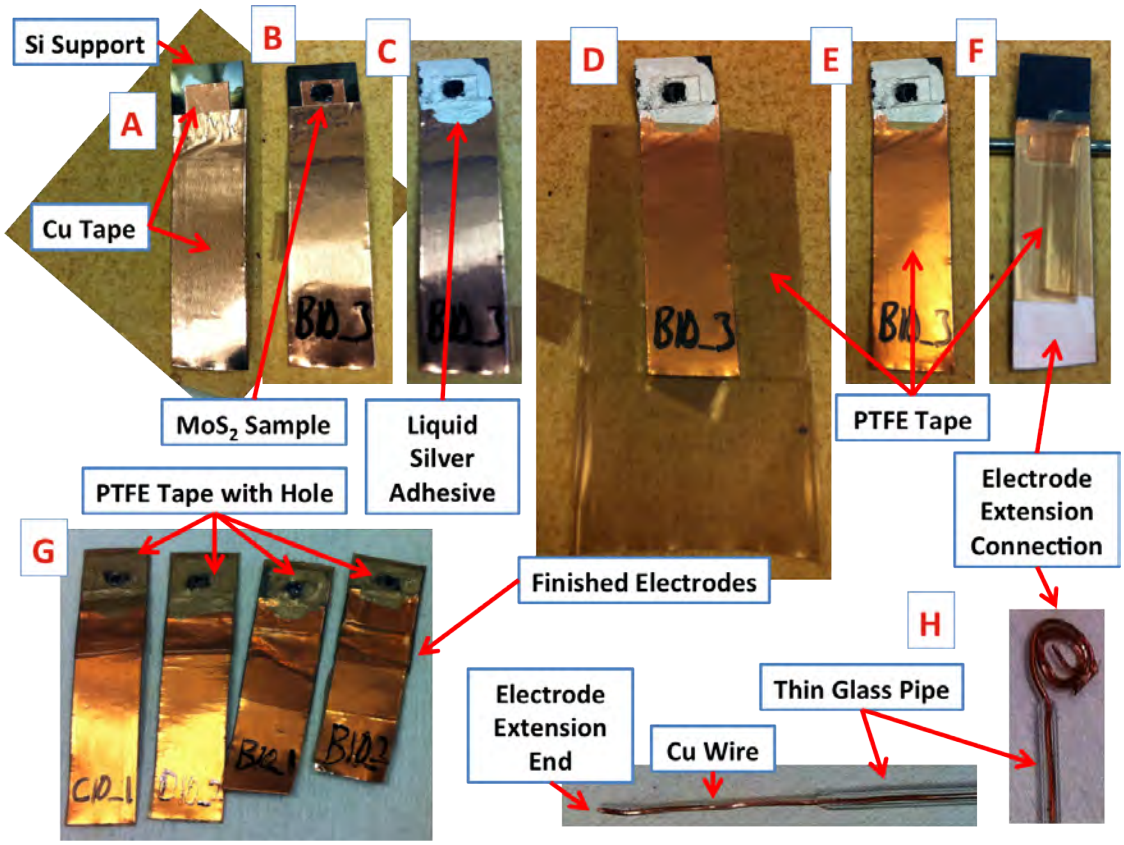

Figure 5.34: The steps in the electrode construction process are: (A) attaching copper tape to a silicon support, (B) placing a MoS_2 onto the Cu tape on top of the Si support, (C) brushing liquid silver adhesive to connect the surface layer of the MoS_2 sample to the Cu tape, (D-E) isolating the Cu tape with teflon tape, (F) leaving space on the (adhesive) backside at the end for the electrode extension connection, (G) making a small hole on PTFE tape and isolate the Si support and MoS_2 except for the (nano structured) top surface catalyst region and (H) attach glass pipe covered Cu wire extensions to the electrodes.

without NS), exposed to the same etching treatment. Blank MoS_2 has also been measured for overall reference purposes and gives a flat stable graph depicted in 'dark green' very close to the zero line. Due to initial problems with electrode construction and leakage of liquid Ag adhesive, potentially affecting the CV measurements, the whole surface of a blank MoS_2 reference sample was covered with liquid Ag adhesive and measured. The effect of the Ag adhesive is quite clear as the graph in 'dark blue', depicting the CV of the sample, shows the highest currents. The nano pillar sample (A10) shows much lower currents in the 'red' CV graph and the 'green' graph shows higher currents for the reference sample (A11).

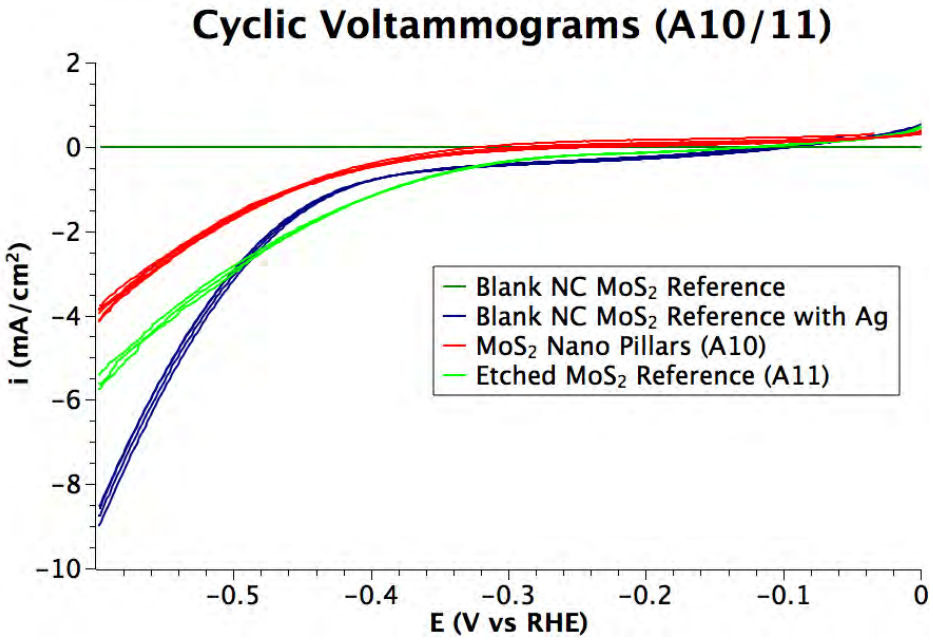

Figure 5.35: Cyclic voltammograms of blank MoS_2 samples (with and without Ag adhesive) and ordered nano pillar sample (A10 with NS, oxygen etched for 55 s and mixed etched for 30 s) as well as its etched reference (A11 without NS). 5 mV/s scan rate and -0.3 – -0.9 V vs SCE scan range.

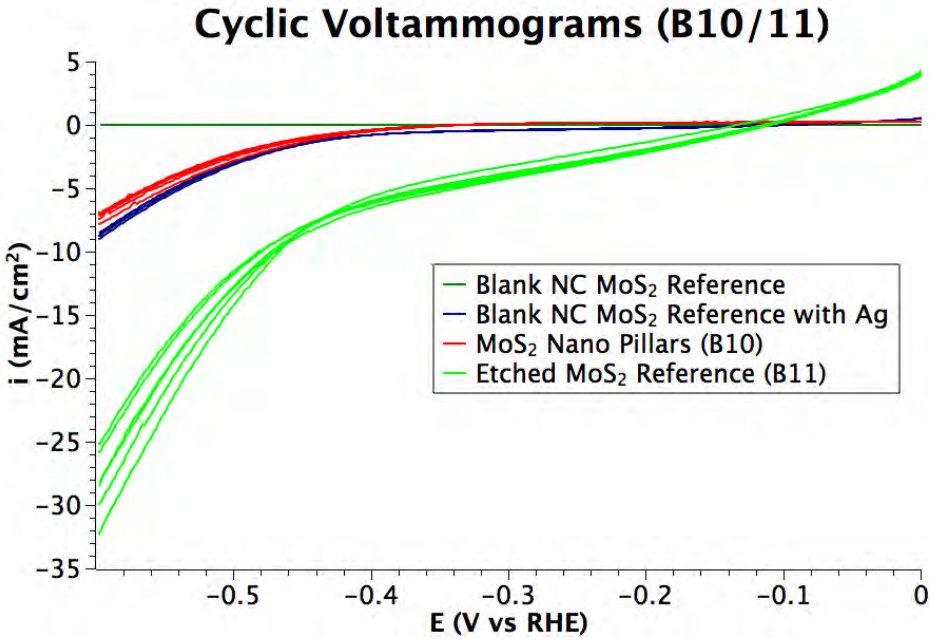

Figure 5.36: Cyclic voltammograms of blank MoS_2 samples (with and without Ag adhesive) and ordered nano pillar sample (B10 with NS, oxygen etched for 55 s and mixed etched for 10 s) as well as its etched reference (B11 without NS). 5 mV/s scan rate and -0.3 – -0.9 V vs SCE scan range.

The same CV graphs ('dark green' and 'dark blue') for the blank MoS_2 reference samples (with and without Ag adhesive), that were used in Figure 5.35, are also included in Figure 5.36 for reference purposes. The etched MoS_2 reference sample (B11 without NS, oxygen etched for 55 s and mixed etched for 10 s) shows the highest currents ('green' graph) for any of CVs depicted in the Figure. The MoS_2 nano pillar sample (B10 with NS, oxygen etched for 55 s and mixed etched for 10 s), depicted by the 'red' CV graph in Figure 5.36, has current values only slightly lower than the current values for the blank MoS_2 reference sample covered with Ag.

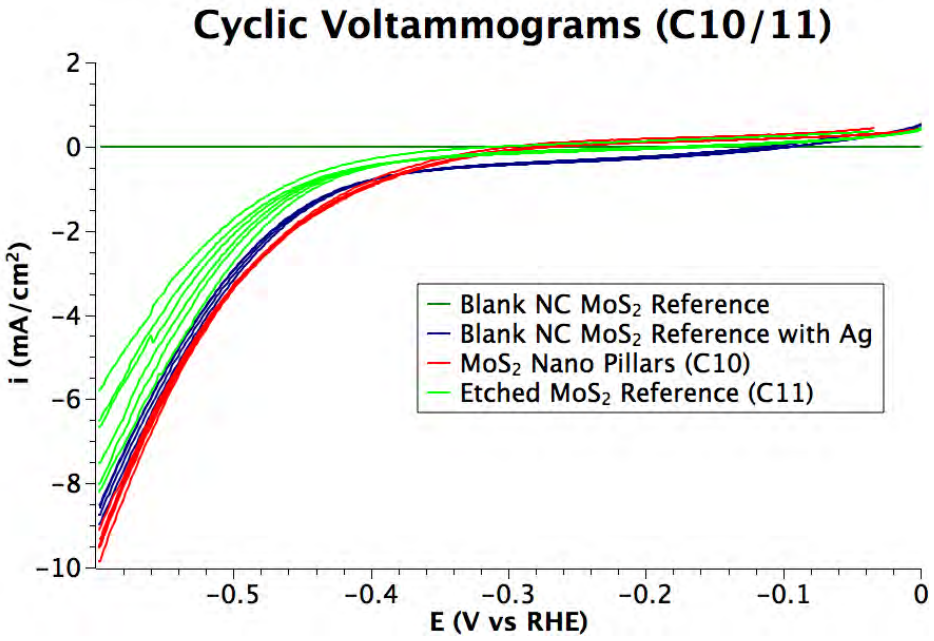

Figure 5.37: Cyclic voltammograms of blank MoS_2 samples (with and without Ag adhesive) and ordered nano pillar sample (C10 with NS, oxygen etched for 35 s and mixed etched for 30 s) as well as its etched reference (C11 without NS). 5 mV/s scan rate and -0.3 – -0.9 V vs SCE scan range.

Figure 5.37 depicts the CV graphs of MoS_2 nano pillar sample and reference samples (C10/11, oxygen etched for 35 s and mixed etched for 30 s). The 'dark green' and 'dark blue' graphs show, like before, the CV graphs of a blank MoS_2 reference sample and a silver adhesive covered blank MoS_2 reference sample, respectively. The etched MoS_2 reference sample (C11) is represented by the 'green' CV graph, which has currents lower

than the blank MoS_2 reference sample covered with Ag ('dark blue' CV graph). The MoS_2 nano pillar sample (C10) has the CV graph ('red') with the highest current values.

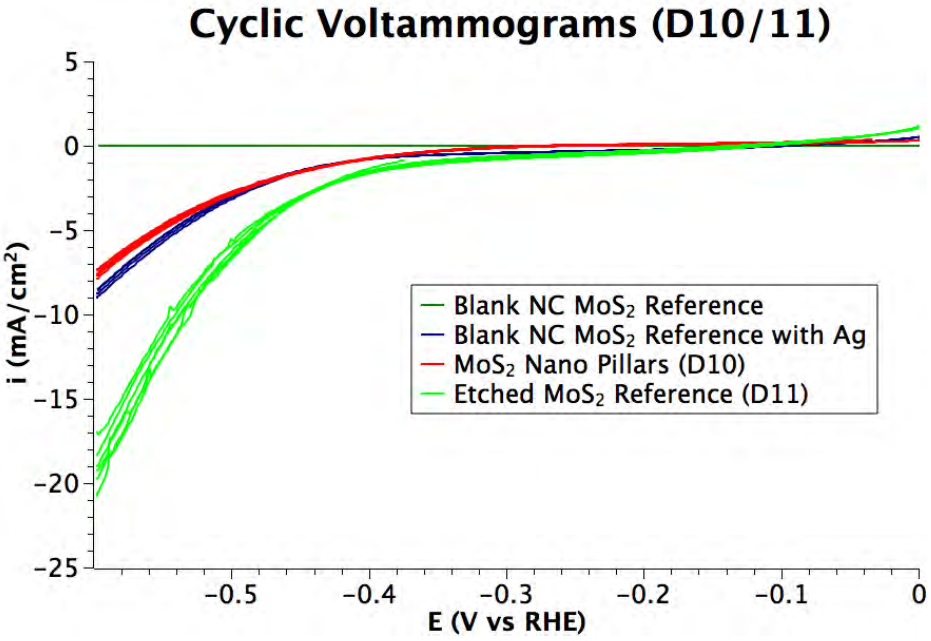

Figure 5.38: Cyclic voltammograms of blank MoS_2 samples (with and without Ag adhesive) and ordered nano pillar sample (D10 with NS, oxygen etched for 35 s and mixed etched for 10 s) as well as its etched reference (D11 without NS). 5 mV/s scan rate and -0.3 – -0.9 V vs SCE scan range.

The graphs from the CVs of ordered MoS_2 nano pillar sample and its corresponding flat reference (D10/11, oxygen etched for 35 s and mixed etched for 10 s) as well as blank MoS_2 reference samples, with and without Ag coverage, can be seen in Figure 5.38. The 'green' CV graph of etched MoS_2 reference sample (D11 without NS) shows the highest current values of all the samples. The MoS_2 nano pillar sample's (D10) CV ('red' graph) is slightly lower than the CV of the blank reference sample covered with Ag adhesive ('dark blue' graph).

Putting the CVs of the best performing samples from all the differently etched ones, gives a better overview of their overall performance. Figure 5.39 depicts the graphs of the best performing MoS_2 nano pillar samples (A10, B10, C10 and D10 with NS) and also the best performing etched reference samples related to them (A11, B11, C11 and D11 without

NS).

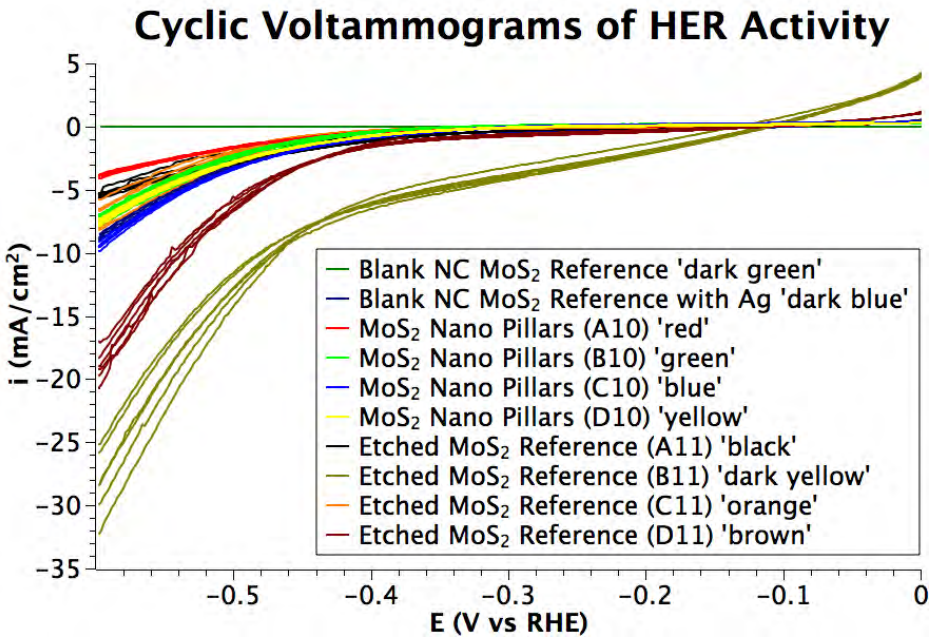

Figure 5.39: Cyclic voltammograms of blank MoS_2 samples and ordered nano pillar samples (A10, B10, C10 and D10 with NS) as well as their etched references (A11, B11, C11 and D11 without NS). 5 mV/s scan rate and -0.3 – -0.9 V vs SCE scan range.

By approximating the MoS_2 nano pillars with truncated cones, the potential number of active edge sites can be obtained for the different samples. Similarly, for the etched reference samples, the potential active sites can, e.g., be assumed to be one in every atom hexagon-ring or every surface atom site. The lateral area of a truncated cone is given by $A = \pi s(r + R)$ [171], where s is the slanted height and r & R (= 110 nm for all pillars) are the radii of the top and base of the cone, respectively. The slanted height is given by $s = \sqrt{h^2 + (R - r)^2}$, where h is the cone height. From the MoS_2 crystal (see e.g. Figure 1.5), the inter-atom separation in the plane is 0.316 nm and the inter-basal plane separation is 0.618 nm. The density of potential active edge sites for platelets is thus roughly 5/nm^2 and for the bulk surface between 2.5/nm^2 (one in every atom hexagon-ring) and 10/nm^2 (every surface atom site). Table 5.19 has the samples ordered according to highest HER activity, as observed in Figure 5.39, with values of all relevant parameters tabulated.

HER	T_{oxy} (s)	T_{mix} (s)	A_s (10^{12} nm^2)	h (nm)	r (nm)	N (10^{12})
B11	55	10	2.011	-	-	5-20
D11	35	10	1.975	-	-	5-20
C10	35	30	1.547	530	65	60
Ref+Ag	-	-	2.483	-	-	-
C11	35	30	2.402	-	-	5-25
B10	55	10	1.790	280	60	40
D10	35	10	1.897	290	75	40
A11	55	30	2.272	-	-	5-25
A10	55	30	2.218	820	30	110
Ref	-	-	2.417	-	-	5-25

Table 5.19: Samples are ordered according to highest HER activity as observed in Figure 5.39. Values of other relevant parameters are tabulated such as the oxygen and mixed etching times (T_{oxy} & T_{mix}), the sample area (A_s), average nano pillar height (h) & tip radius (r) as well as number of potential active sites (N).

Observing and comparing the CVs of the different samples in Figure 5.39 reveals a couple of things. Firstly, for the ordered MoS_2 nano pillar samples, the HER activity is lowest for A10 ('red' CV graph, highest number of possible active sites, see Table 5.19), much higher for B10 ('green' CV graph, slightly lower than half the number of possible active sites compared to A10, see Table 5.19), still a little higher for D10 ('yellow' CV graph, slightly lower than half the number of possible active sites compared to A10, see Table 5.19) and highest for C10 ('blue' CV graph, slightly higher than half the number of possible active sites compared to A10, see Table 5.19). Secondly, for the etched reference samples (with all having the number of possible active sites up to 20× lower than for A10, see Table 5.19), the HER activity is lowest for A11 ('black' CV graph), a little higher for C11 ('orange' CV graph), much higher for D11 ('brown' CV graph) and the highest for B11 ('dark yellow' CV graph). Generally, the HER activity of the etched reference samples is higher than the corresponding nano pillar samples (despite the number of possible active sites being up to 20× higher, see Table 5.19), except for C10/11 ('blue' & 'orange' CV graphs) where the opposite is true, i.e. the HER activity of the nano pillar sample is higher than the etched reference sample. The extremely high HER activity of etched samples B11 and D11 ('brown' & 'dark yellow' CV graphs), relative to the other sam-

ples, can only be explained with the fact that both samples were only mix etched for 10 s compared to the 30 s mixed etching that the other samples (A11 & C11) were exposed to.

The HER activity measurements have revealed many important insights to questions, for which answers were sought from the start of this investigation. The most important insight, is that nano pillars of MoS_2 are not better catalysts for HER than bulk MoS_2 roughened through etching. The proposed model that MoS_2 nano pillars would be like MoS_2 platelets stacked on top of each other, thus increasing the number of active edge sites by utilising three dimensions instead of being confined to two dimensions, seems to have been too simplified. More things are going on that are too important to neglect when making the overall process work. Things like the distance between pillars which affects mass transport, the electric connection between each stacked MoS_2 nano platelet making up a pillar as well as the availability of the active edge sites. The distance between pillars is very narrow (the bases touch and the tips are closer than the diameter of a base), which probably causes "shielding" (diffusion zone overlap), which depletes the same solution region. By, e.g., using a close-packed NS bilayer mask to make metal island masks to form nano pillars with larger centre-to-centre separation, maximum current density can be achieved where the diffusion of reactants is more efficient leading to higher mass transport coefficients [172, 173]. Moreover, if the pillar sides are conducting their height will affect voltammetry [173], which is interesting as the platelets stacked up to form the pillars have 1D metallic edge states [174].

Looking at the activities of the MoS_2 nano pillar samples, a further insight is that the dimensions of the pillars do somewhat fit into the explanation. For instance, A10 have the smallest pillar diameters, but because of them being tall, a truncated cone model gives the highest number of possible active edge sites, see Table 5.19. However, A10 was the least active sample, which hints towards serious issues with taller pillars, as mentioned above, rendering the large number of potential active sites unhelpful. B10, with slightly lower

than half the number of possible active sites compared to A10 (see Table 5.19), has much higher activity than A10 and its pillars also have relatively small diameters (120 nm compared to 60 nm, but still smaller than 130 nm and 150 nm of D10 and C10, respectively), but are shorter (530 nm compared to 820 nm). This leads us to speculate around the electrical connection between the stacked platelets in a pillar and the higher probability of it breaking as a function of pillar height. D10 has similar activity to B10 and its pillars are also short, but with slightly larger diameters, hence the number of possible active edge sites are comparable, see Table 5.19. C10 has the highest activity and its pillars are tall with large diameters, which translates to the highest number of possible active sites after A10 (slightly higher than half the number of possible active sites compared to A10 (see Table 5.19). There is also the factor of contamination of the active edge sites from remnants of the latex polymer nano spheres after they have been etched, with longer etch times meaning more remnants and thus more risk of contamination. This should be taken into account despite great efforts made to clean all samples thoroughly, which thus reveal that A10 (55 s + 30 s = 85 s), with the highest overall etch time (oxygen etch time + mixed etch time), has the highest risk followed by B10 (55 s + 10 s = 65 s), C10 (35 s + 30 s = 65 s) and finally D10 (35 s + 10 s = 45 s). These findings corroborate each other in somewhat explaining the results obtained, however, more experiments are necessary in order to fully grasp the mechanisms involved and the true depth of the findings themselves. Moreover, a new strategy and experiments should be drawn up in order to build on the findings and make the necessary adjustments in the fabrication of even better MoS_2 catalysts.

5.5 Summary

The use of size-selected metal clusters (Pd_{10000} & Au_{10000}) as etch masks in the formation of non-ordered nano pillars of MoS_2 has been successful. To the best of my knowledge

it is the first time this technique has been used for MoS_2 and also the first time that MoS_2 nano pillars have been fabricated. The MoS_2 nano pillars formed, after mix plasma etching process, had conically shaped bases (~20 nm heights & ~30 nm diameters) with tips cylindrically shaped (~10 nm heights & ~5 nm diameters). A very narrow (local) parameter space of the mix plasma etching process was found to enable the formation of MoS_2 nano pillars.

For ordered MoS_2 nano pillar formation, nano sphere lithography (NSL) was successfully used. The first realisation from the nano fabrication work in this thesis is that many of the NSL techniques mentioned in the literature have been presented too optimistically in relation to the needs (high-area NSL coverage) of our work. Neither different variants of drop nor spin coating could achieve high-area coverage (at least 1 cm^2) of Si, HOPG or MoS_2 with a monolayer of hexagonally close-packed latex polymer nano spheres. The best method found was immersion coating, whereby the samples to be covered were submerged under water in a basin and the close-packed nano sphere monolayer transferred to the air-water interface. By slowly siphoning the water, the water surface level, carrying the nano sphere monolayer, was lowered until the samples were covered. A slight variation of this technique was discovered, which cut down on the processing time, and allowed for hydrophobic samples to easily be covered. This adhesion coating technique utilises the presence of the close-packed nano sphere monolayer at the air-water interface, but the (hydrophobic) sample (e.g. MoS_2) to be covered is attached onto a larger (hydrophilic) substrate (e.g. Si) with graphite tape. With the surfaces of the sample(s) facing down and attached to a stand, which slowly lowers them down until the water on the surface clings onto the Si surface and wets it, the close-packed nano spheres are surrounded and pinned onto the hydrophobic sample. After the evaporation of the water, the nano sphere mask is ready to use.

Using the nano sphere masks to deposit metal island etch masks for the formation of

ordered MoS_2 nano pillars proved to be very complicated and included some quite difficult steps. At best, an ordered nano corrugated surface of MoS_2 was formed by mix etching and the use of metal (Pd) island etch masks. The egg cardboard box shaped surface had a height difference of around 15 nm between the tips and holes (up to 20 nm).

The nano sphere masks were used as etch masks and were shrunk by oxygen plasma etching to different diameters. Oxygen plasma etching was also successfully used to turn, hydrophobic samples such as, MoS_2 hydrophilic, which has improved the immersion coating technique further and currently gives it an edge over the newly developed adhesion coating technique. Ordered MoS_2 nano pillars (higher aspect ratio than above structures) with different heights and diameters were fabricated through mix etching and the use of ordered nano sphere etch masks with reduced diameters. Four different groups of samples were first oxygen etched for 55 s (group A10 & B10) and 35 s (group C10 & D10), respectively, and secondly mixed etched for 30 s (group A10 & C10) and 10 s (group B10 & D10), respectively. MoS_2 nano pillars from group A10 samples had average heights of 820 nm and tip diameters of 60 nm. Group B10 samples (55 s oxygen etch and 10 s mix etch) had nano pillars with average diameters of 120 nm and 280 nm heights. Average tip diameters of 130 nm was found for nano pillars in samples belonging to group C10 and their average heights were 530 nm. Nano pillars of MoS_2 belonging to group D10 samples had average heights of 290 nm and 150 nm tip diameters. Reference samples (A11, B11, C11 & D11) etched with same conditions, but without nano sphere etch masks, exhibited increased roughening of their surfaces (high density coverage of nano pillars with up to ~100 nm height).

The fabricated MoS_2 nano pillar samples (A10, B10, C10 & D10) and their references (A11, B11, C11 & D11) were tested through cyclic voltammetry (CV) measurements for hydrogen evolution reaction (HER) activity. A blank MoS_2 sample was also used as internal reference as well as a blank MoS_2 sample with surface fully covered with Ag

adhesive (used in the electrode construction). The HER activity of the etched samples are higher than the bulk MoS_2 sample with blank surface, clearly indicating the advantage of nano structuring of the MoS_2 catalyst for HER. The bulk MoS_2 reference sample with its surface covered in Ag adhesive has a quite high HER activity compared to many of the nano structured MoS_2 catalysts, while some of them have even higher activity still. For the ordered MoS_2 nano pillar samples, A10 (60 nm average tip diameter and average height of 820 nm) had the lowest activity followed by B10 (120 nm average tip diameter and average height of 280 nm) having a higher activity. D10 (150 nm average tip diameter and average height of 290 nm) had a slightly higher activity than B10 and was followed by C10 (130 nm average tip diameter and average height of 530 nm), which had the highest HER activity of the ordered MoS_2 nano pillar catalyst samples.

The HER activity of the etched reference samples are generally higher than the corresponding ordered MoS_2 nano pillar samples. B11 (55 s oxygen etch and 10 s mix etch) had the highest activity followed by D11 (35 s oxygen etch and 10 s mix etch). C11 (35 s oxygen etch and 30 s mix etch) had even lower HER activity followed by A11 (55 s oxygen etch and 30 s mix etch) with the overall lowest activity.

What is desired to pursue in the fabrication of catalysts, is to work with long-range flat and larger MoS_2 substrates. Despite the atomically flat nature (verified through STM) of the natural crystal MoS_2 substrates used in the thesis, it became apparent that long-range flatness would improve immersion coating of nano spheres, even etching of substrates and characterisation (imaging and HER activity measurements) of final samples. Efforts were made to make MoS_2 samples through sputter deposition and subsequent annealing as well as electroplating, but high crystal quality was never achieved. Enough time should be spent making high crystal quality MoS_2 substrates for fabrication, which is a project in and of itself.

The newly developed adhesion coating of nano spheres should be further refined in order

to achieve higher quality of the transferred close-packed nano sphere monolayer avoiding as much of the perturbation of the position of the NS, which noise and vibrations currently give rise to. An initial start would be to use a stand with a smooth ultra-fine z-direction translation for the substrates attached to a large Si base while the water basin with the close-packed NS monolayer is placed on a vibration free table (using air legs). A further step would be to computerise both the transfer of the NS to the water surface and the adhesion coating process to automate the technique and ultimately save time.

With larger flat MoS_2 substrates the etching process would be more homogenous throughout the sample and the characterisation and evaluation would also be easier. This could see, a better specific set of roughened surface of a MoS_2 sample found having the best HER activity. It would become easier to characterise different parameters for roughened surfaces and link them specifically to different catalytic activities when those are found.

For future electrochemistry experiments an in-house setup is crucial for quick turnovers when testing different catalysts samples. It will be crucial for further investigations to be more thorough and really map out the different parameters with high resolution, which will require at least a couple of samples being completely processed in a day. The processing would involve the making of the MoS_2 substrate and characterisation (could be batch processed prior), nano structuring and characterisation (could be batch processed prior), different photoelectrochemistry measurements and repeat characterisation. Different relevant characterisation methods should be applied like microscopy and spectroscopy.

CV measurements should be done to test different aspects of the catalyst samples and not only relative HER activity. Thorough photoelectrochemistry measurements should be sought using sun lamps with several similar samples being measured for reproducibility.

REFERENCES

[1] R. E. Palmer, *New Sci.* , 38 (1997).

[2] J. P. Wilcoxon and G. A. Samara, *Phys. Rev. B* **51**, 7299 (1995).

[3] H. Haberland, *Clusters of Atoms and Molecules*, Springer, 1994.

[4] I. Yamada, J. Matsuo, N. Toyoda, T. Aoki, E. Jones, and Z. Insepov, *Mat. Sci. Eng. A-Struct.* **253**, 249 (1998).

[5] I. Yamada, J. Matsuo, N. Toyoda, and A. Kirkpatrick, *Mat. Sci. Eng. R* **34**, 231 (2001).

[6] P. Milani and S. Iannotta, *Cluster Beam Synthesis of Nanostructured Materials*, Cluster Physics, Springer, 1999.

[7] V. N. Popok and E. E. B. Campbell, *Rev. Adv. Mater. Sci.* **11**, 19 (2006).

[8] L. Patrone, D. Nelson, V. I. Safarov, M. Sentis, W. Marine, and S. Giorgio, *J. Appl. Phys.* **87**, 3829 (2000).

[9] D. J. Sellmyer, M. Yu, and R. D. Kirby, *Nanostruct. Mater.* **12**, 1021 (1999).

[10] R. E. Palmer, S. Pratontep, and H. G. Boyen, *Nature* **2**, 443 (2003).

[11] C. R. Henry, *Surf. Sci. Rep.* **31**, 231 (1998).

[12] S. Gibilisco, M. D. Vece, S. Palomba, G. Faraci, and R. E. Palmer, *J. Chem. Phys.* **125**, 084704 (2006).

[13] P. Jena and A. W. Castleman Jr., *P. Natl. Acad. Sci. USA* **103**, 10560 (2006).

[14] R. L. Johnston, *Atomic and Molecular Clusters*, Taylor & Francis, 2002.

[15] T. P. Martin, *Phys. Rep.* **273**, 199 (1996).

[16] E. Roduner, *Nanoscopic Materials - Size-Dependent Phenomena*, Royal Society of Chemistry, 2006.

[17] W. Miehle, O. Kandler, T. Leisner, and O. Echt, *J. Chem. Phys.* **91**, 5940 (1989).

[18] O. Echt, K. Sattler, and E. Recknagel, *Phys. Rev. Lett.* **47**, 1121 (1981).

[19] M. K. Harbola, *P. Natl. Acad. Sci. USA* **89**, 1036 (1992).

[20] W. D. Knight, K. Clemenger, W. A. de Heer, W. A. Saunders, M. Y. Chou, and M. L. Cohen, *Phys. Rev. Lett.* **52**, 2141 (1984).

[21] W. A. de Heer, *Rev. Mod. Phys.* **65**, 611 (1993).

[22] F. Baletto and R. Ferrando, *Rev. Mod. Phys.* **77**, 371 (2005).

[23] A. W. Castleman Jr. and K. H. Bowen Jr., *J. Phys. Chem.* **100**, 12911 (1996).

[24] J. P. Bucher, D. C. Douglass, and L. A. Bloomfield, *Phys. Rev. Lett.* **66**, 3052 (1991).

[25] I. M. L. Billas, A. Châtelain, and W. A. de Heer, *J. Magn. Magn. Mater.* **168**, 64 (1997).

[26] A. L. Mackay, *Acta Crystallogr.* **15**, 916 (1962).

[27] C. Nordling and J. Sterman, *Physics Handbook - for Science and Engineering*, Studentlitteratur, 1999.

[28] W. Zhang, Q. Ge, and L. Wang, *J. Chem. Phys.* **118**, 5793 (2003).

[29] N. Watari and S. Ohnishi, *Phys. Rev. B* **58**, 1665 (1998).

[30] V. Kumar and Y. Kawazoe, *Phys. Rev. B* **66**, 144413 (2002).

[31] P. Nava, M. Sierka, and R. Ahlrichs, *Phys. Chem. Chem. Phys.* **5**, 3372 (2003).

[32] C. Barreteau, M. C. Desjonquères, and D. Spanjaard, *Eur. Phys. J. D* **11**, 395 (2000).

[33] A. P. Sutton and J. Chen, *Phil. Mag. Lett.* **61**, 139 (1990).

[34] C. Massen, T. V. Mortimer-Jones, and R. L. Johnston, *J. Chem. Soc. Dalt.* **2002**, 4375 (2002).

[35] J. M. Pénisson and A. Renou, *J. Cryst. Growth* **102**, 585 (1990).

[36] M. José-Yacamán, M. Marín-Almazo, and J. A. Ascencio, *J. Mol. Catal. A-Chem* **173**, 61 (2001).

[37] W. C. Wiley and I. H. McLaren, *Rev. Sci. Instrum.* **26**, 1150 (1955).

[38] E. W. Becker, *Z. Phys. D Atom. Mol. Cl.* **3**, 101 (1986).

[39] S. J. Carroll, S. G. Hall, R. E. Palmer, and R. Smith, *Phys. Rev. Lett.* **81**, 3715 (1998).

[40] R. Neuendorf, R. E. Palmer, and R. Smith, *Appl. Phys. Lett.* **77**, 3003 (2000).

[41] S. J. Carroll, P. D. Nellist, R. E. Palmer, S. Hobday, and R. Smith, *Phys. Rev. Lett.* **84**, 2654 (2000).

[42] R. Smith, C. Nock, S. D. Kenny, J. J. Belbruno, M. Di Vece, S. Palomba, and R. E. Palmer, *Phys. Rev. B* **73**, 125429 (2006).

[43] M. Di Vece, S. Palomba, and R. E. Palmer, *Phys. Rev. B* **72**, 073407 (2005).

[44] C. Xirouchaki and R. E. Palmer, *Vacuum* **66**, 167 (2002).

[45] S. J. Carroll, S. Pratontep, M. Streun, R. E. Palmer, S. Hobday, and R. Smith, *J. Chem. Phys.* **113**, 7723 (2000).

[46] C. Xirouchaki and R. E. Palmer, *Philos. T. Roy. Soc. A* **362**, 117 (2004).

[47] S. J. Carroll, P. Weibel, B. von Issendorff, L. Kuipers, and R. E. Palmer, *J. Phys.-Condens. Mat.* **8**, L617 (1996).

[48] R. Ferrando, J. Jellinek, and R. L. Johnston, *Chem. Rev.* **108**, 845 (2008).

[49] Z. Y. Li, J. P. Wilcoxon, F. Yin, Y. Chen, R. E. Palmer, and R. L. Johnston, *Faraday Discuss.* **138**, 363 (2008).

[50] A. N. Dobrynin, D. N. Ievlev, G. Verschoren, J. Swerts, M. J. Van Bael, K. Temst, P. Lievens, E. Piscopiello, G. Van Tendeloo, S. Q. Zhou, and A. Vantomme, *Phys. Rev. B* **73**, 104421 (2006).

[51] L. Martínez, M. Díaz, E. Román, M. Ruano, D. Llamosa P., and Y. Huttel, *Langmuir* **28**, 11241 (2012).

[52] C. Langlois, D. Alloyeau, Y. Le Bouar, A. Loiseau, T. Oikawa, C. Mottet, and C. Ricolleau, *Faraday Discuss.* **138**, 375 (2008).

[53] J. B. Park, S. F. Conner, and D. A. Chen, *J. Phys. Chem. C* **112**, 5490 (2008).

[54] N. Lidgi-Guigui, P. Mulheran, and R. E. Palmer, *Appl. Phys. Lett.* **93**, 123107 (2008).

[55] L.-M. Wang, S. Bulusu, H.-J. Zhai, X.-C. Zeng, and L.-S. Wang, *Angew. Chem. Int. Ed.* **46**, 2915 (2007).

[56] X. Li, B. Kiran, J. Li, H.-J. Zhai, and L.-S. Wang, *Angew. Chem. Int. Ed.* **41**, 4786 (2002).

[57] H.-J. Zhai, J. Li, and L.-S. Wang, *J. Chem. Phys.* **121**, 8369 (2004).

[58] W. Bouwen, P. Thoen, F. Vanhoutte, S. Bouckaert, F. Despa, H. Weidele, R. E. Silverans, and P. Lievens, *Rev. Sci. Instrum.* **71**, 54 (2000).

[59] N. Veldeman, T. Höltzl, S. Neukermans, T. Veszprémi, M. T. Nguyen, and P. Lievens, *Phys. Rev. A* **76**, 011201 (2007).

[60] S. Neukermans, E. Janssens, Z. F. Chen, R. E. Silverans, P. v. R. Schleyer, and P. Lievens, *Phys. Rev. Lett.* **92**, 163401 (2004).

[61] R. Katoh, T. Hihara, D. L. Peng, and K. Sumiyama, *Appl. Phys. Lett.* **82**, 2688 (2003).

[62] E. Pérez-Tijerina, M. Gracia Pinilla, S. Mejía-Rosales, U. Ortiz-Méndez, A. Torres, and M. José-Yacamán, *Faraday Discuss.* **138**, 353 (2008).

[63] S. Fedrigo, W. Harbich, and J. Buttet, *Phys. Rev. B* **58**, 7428 (1998).

[64] W. Harbich, S. Fedrigo, F. Meyer, D. M. Lindsay, J. Lignieres, J. C. Rivoal, and D. Kreisle, *J. Chem. Phys.* **93**, 8535 (1990).

[65] H. Jödicke, R. Schaub, A. Bhowmick, R. Monot, J. Buttet, and W. Harbich, *Rev. Sci. Instrum.* **71**, 2818 (2000).

[66] M. Ratner, W. Harbich, and S. Fedrigo, *Phys. Rev. B* **60**, 11730 (1999).

[67] S. A. Nepijko, I. Rabin, and W. Schulze, *ChemPhysChem* **6**, 235 (2005).

[68] B. L. Abrams and J. P. Wilcoxon, *Crit. Rev. Solid State* **30**, 153 (2005).

[69] Q. Li, E. C. Walter, W. E. van der Veer, B. J. Murray, J. T. Newberg, E. W. Bohannan, J. A. Switzer, J. C. Hemminger, and R. M. Penner, *J. Phys. Chem. B* **109**, 3169 (2005).

[70] J. Reyes-Gasga, S. Tehuacanero, and M. José Yacamán, *Microsc. Res. Tech.* **40**, 2 (1998).

[71] R. Tenne, *Nat. Nanotechnol.* **1**, 103 (2006).

[72] V. Varshney, S. S. Patnaik, C. Muratore, A. K. Roy, A. A. Voevodin, and B. L. Farmer, *Comp. Mater. Sci.* **48**, 101 (2010).

[73] Y. Li, H. Wang, L. Xie, Y. Liang, G. Hong, and H. Dai, *J. Am. Chem. Soc.* **133**, 7296 (2011).

[74] C. Kisielowski, Q. M. Ramasse, L. P. Hansen, M. Brorson, A. Carlsson, A. M. Molenbroek, H. Topsøe, and S. Helveg, *Angew. Chem. Int. Ed.* **49**, 2708 (2010).

[75] L. Wei, C. Jun-fang, H. Qinyu, and W. Teng, *Phys. B* **405**, 2498 (2010).

[76] E. A. Ponomarev, M. Neumann-Spallart, G. Hodes, and C. Lévy-Clément, *Thin Solid Films* **280**, 86 (1996).

[77] Y. Tomm and S. Fiechter, *J. Ceram. Process. Res.* **6**, 141 (2005).

[78] Y. Zhan, Z. Liu, S. Najmaei, P. M. Ajayan, and J. Lou, *Small* **8**, 966 (2012).

[79] A. Sobczynski, *J. Catal.* **131**, 156 (1991).

[80] T. F. Jaramillo, K. P. Jørgensen, J. Bonde, J. H. Nielsen, S. Horch, and I. Chorkendorff, *Science* **317**, 100 (2007).

[81] S. Gemming, G. Seifert, N. Bertram, T. Fischer, M. Götz, and G. Ganteför, *Chem. Phys. Lett.* **474**, 127 (2009).

[82] J. V. Lauritsen, J. Kibsgaard, S. Helveg, H. Topsøe, B. S. Clausen, E. Laegsgaard, and F. Besenbacher, *Nat. Nanotechnol.* **2**, 53 (2007).

[83] A. Enyashin, S. Gemming, and G. Seifert, *Eur. Phys. J.-Spec. Top.* **149**, 103 (2007).

[84] M. Bar Sadan, L. Houben, A. N. Enyashin, G. Seifert, and R. Tenne, *P. Natl. Acad. Sci. USA* **105**, 15643 (2008).

[85] M. Remškar, A. Mrzel, M. Viršek, and A. Jesih, *Adv. Mater.* **19**, 4276 (2007).

[86] T. R. Thurston and J. P. Wilcoxon, *J. Phys. Chem. B* **103**, 11 (1999).

[87] J. P. Wilcoxon, P. P. Newcomer, and G. A. Samara, *J. Appl. Phys.* **81**, 7934 (1997).

[88] F. Parsapour, D. F. Kelley, S. Craft, and J. P. Wilcoxon, *J. Chem. Phys.* **104**, 4978 (1996).

[89] J. P. Wilcoxon, *J. Phys. Chem. B* **104**, 7334 (2000).

[90] T. Ito and S. Okazaki, *Nature* **406**, 1027 (2000).

[91] M. Ohring, *The Materials Science of Thin Films*, Academic Press, first edition, 1992.

[92] R. C. Jäger, *Introduction to Microelectronic Fabrication*, Prentice Hall PTR, second edition, 2002.

[93] A. Biswas, I. S. Bayer, A. S. Biris, T. Wang, E. Dervishi, and F. Faupel, *Adv. Colloid Interfac.* **170**, 2 (2012).

[94] C. Vieu, F. Carcenac, A. Pépin, Y. Chen, M. Mejias, A. Lebib, L. Manin-Ferlazzo, L. Couraud, and H. Launois, *Appl. Surf. Sci.* **164**, 111 (2000).

[95] U. C. Fischer and H. P. Zingsheim, *J. Vac. Sci. Technol.* **19**, 881 (1981).

[96] H. W. Deckman and J. H. Dunsmuir, *Appl. Phys. Lett.* **41**, 377 (1982).

[97] J. C. Hulteen and R. P. Van Duyne, *J. Vac. Sci. Technol. A* **13**, 1553 (1995).

[98] K. Seeger and R. E. Palmer, *J. Phys. D Appl. Phys.* **32**, L129 (1999).

[99] M. Bale, A. J. Turner, and R. E. Palmer, *J. Phys. D Appl. Phys.* **35**, L11 (2002).

[100] N. D. Denkov, O. D. Velev, P. A. Kralchevsky, I. B. Ivanov, H. Yoshimura, and K. Nagayama, *Langmuir* **8**, 3183 (1992).

[101] M. J. Madau, *Fundamentals of Microfabrication: The Science of Miniaturization*, CRC Press, second edition, 2002.

[102] I. U. Abhulimen, S. Polamreddy, S. Burkett, L. Cai, and L. Schaper, *J. Vac. Sci. Technol. B* **25**, 1762 (2007).

[103] S. Mizuno, J. Fukuda, and H. Tochihara, *Surf. Sci.* **514**, 291 (2002).

[104] M. Y. Song, *Microfabrication of Silicon Tips for Scanning Probe Microscopy*, PhD thesis, University of Birmingham, 2009.

[105] J. Manyam, *Novel Resist Materials for Next Generation Lithography*, PhD thesis, University of Birmingham, 2010.

[106] G. Binnig, H. Rohrer, C. Gerber, and E. Weibel, *Phys. Rev. Lett.* **49**, 57 (1982).

[107] *http://www.insp.upmc.fr/axe1/Dispositifs%20quantiques/AxeI2_more/PRINCIPLE /STSprin.HTM* (2005).

[108] D. Bonnell, editor, *Scanning Probe Microscopy and Spectroscopy*, John Wiley and Sons, second edition, 2001.

[109] C. J. Chen, *Introduction to Scanning Tunneling Microscopy*, Monographs on The Physics and Chemistry of Materials, Oxford University Press, second edition, 2008.

[110] G. Binnig, C. F. Quate, and C. Gerber, *Phys. Rev. Lett.* **56**, 930 (1986).

[111] F. J. Giessibl, *Rev. Mod. Phys.* **75**, 949 (2003).

[112] P. J. Goodhew and J. Humphreys, *Electron Microscopy and Analysis*, Taylor & Francis, second edition, 1992.

[113] K. W. Urban, *Science* **321**, 506 (2008).

[114] L. D. Marks, *Rep. Prog. Phys.* **57**, 603 (1994).

[115] D. B. Williams and C. B. Carter, *Transmission Electron Microscopy*, Springer, 1996.

[116] Z. L. Wang, *Characterization of nanophase materials*, Wiley-VCH, 2000.

[117] S. C. Anderson, C. R. Birkeland, G. R. Anstis, and D. J. H. Cockayne, *Ultramicroscopy* **69**, 83 (1997).

[118] S. J. Pennycook, *Scanning Microscopy for Nanotechnology*, Springer, 2007.

[119] X. Wang, K. Maeda, A. Thomas, K. Takanabe, G. Xin, J. M. Carlsson, K. Domen, and M. Antonietti, *Nat. Mater.* **8**, 76 (2009).

[120] R. D. Adams and B. Captain, *J. Organomet. Chem.* **689**, 4521 (2004).

[121] U. Heiz and E. L. Bullock, *J. Mater. Chem.* **14**, 564 (2004).

[122] O. S. Alexeev and B. C. Gates, *Ind. Eng. Chem. Res.* **42**, 1571 (2003).

[123] I. M. Campbell, *Catalysis at Surfaces*, Chapman and Hall, 1988.

[124] M. Bowker, *The Basis and Applications of Heterogeneous Catalysis*, Oxford Univrsity Press, Oxford, 1998.

[125] H.-J. Freund, J. Libuda, M. Bäumer, T. Risse, and A. Carlsson, *Chem. Rec.* **3**, 181 (2003).

[126] W. Xu, J. S. Kong, Y.-T. E. Yeh, and P. Chen, *Nat. Mater.* **7**, 992 (2008).

[127] M. Turner, V. B. Golovko, O. P. H. Vaughan, P. Abdulkin, A. Berenguer-Murcia, M. S. Tikhov, B. F. G. Johnson, and R. M. Lambert, *Nature* **454**, 981 (2008).

[128] C. Novo, A. M. Funston, and P. Mulvaney, *Nat. Nanotechnol.* **3**, 598 (2008).

[129] S. H. Joo, J. Y. Park, C.-K. Tsung, Y. Yamada, P. Yang, and G. A. Somorjai, *Nat. Mater.* **8**, 126 (2009).

[130] P. J. Roach, W. H. Woodward, A. W. Castleman Jr., A. C. Reber, and S. N. Khanna, *Science* **323**, 492 (2009).

[131] C. Harding, V. Habibpour, S. Kunz, A. N.-S. Farnbacher, U. Heiz, B. Yoon, and U. Landman, *J. Am. Chem. Soc.* **131**, 538 (2009).

[132] M. K. Starchevsky, S. L. Hladiy, Y. A. Pazdersky, M. N. Vargaftik, and I. I. Moiseev, *J. Mol. Catal. A-Chem.* **146**, 229 (1999).

[133] B. Huber, P. Koskinen, H. Häkkinen, and M. Moseler, *Nat. Mater.* **5**, 44 (2006).

[134] B. Hvolbæk, T. V. W. Janssens, B. S. Clausen, H. Falsig, C. H. Christensen, and J. K. Nørskov, *Nano Today* **2**, 14 (2007).

[135] J. Durand, E. Teuma, and M. Gómez, *Eur. J. Inorg. Chem.* **2008**, 3577 (2008).

[136] S. Abbet, A. Sanchez, U. Heiz, W.-D. Schneider, A. M. Ferrari, G. Pacchioni, and N. Rösch, *J. Am. Chem. Soc.* **122**, 3453 (2000).

[137] A. Gniewek, J. J. Ziółkowski, A. M. Trzeciak, and L. Kępiński, *J. Catal.* **239**, 272 (2006).

[138] S. Kubota, D. Shimamoto, J. S. Park, H. Nishikiori, N. Tanaka, Y. A. Kim, T. Fujii, M. Endo, and M. S. Dresselhaus, *Chem. Commun.* **46**, 6977 (2010).

[139] Y. S. Nam, A. P. Magyar, D. Lee, J.-W. Kim, D. S. Yun, H. Park, T. S. Pollom Jr., D. A. Weitz, and A. M. Belcher, *Nat. Nanotechnol.* **5**, 340 (2010).

[140] H. I. Karunadasa, C. J. Chang, and J. R. Long, *Nature* **464**, 1329 (2010).

[141] M. Dincă, Y. Surendranath, and D. G. Nocera, *P. Natl. Acad. Sci. USA* **107**, 10337 (2010).

[142] Y. Guo, S. Chu, S. Yan, Y. Wang, and Z. Zou, *Chem. Commun.* **46**, 7325 (2010).

[143] Y. Hou, B. L. Abrams, P. C. K. Vesborg, M. E. Björketun, K. Herbst, L. Bech, A. M. Setti, C. D. Damsgaard, T. Pedersen, O. Hansen, J. Rossmeisl, S. Dahl, J. K. Nørskov, and I. Chorkendorff, *Nat. Mater.* **10**, 434 (2011).

[144] S. J. Carroll, *Deposition of size-selected atomic clusters on surfaces*, PhD thesis, University of Birmingham, 1999.

[145] S. Pratontep, *Production and Characterisation of Size-Selected Nanoclusters on Surfaces*, PhD thesis, University of Birmingham, 2002.

[146] S. Palomba, *Nanophotonics and biophysics with size-selected clusters*, PhD thesis, University of Birmingham, 2007.

[147] B. von Issendorff and R. E. Palmer, *Rev. Sci. Instrum.* **70**, 4497 (1999).

[148] S. Pratontep, S. J. Carroll, C. Xirouchaki, M. Streun, and R. E. Palmer, *Rev. Sci. Instrum.* **76**, 45103 (2005).

[149] Digital Instruments, *Nanoscope III Scanning Tunnelling Microscope Instruction Manual*, version 2 edition, 1992.

[150] D. Pearmain, *Electron Microscopy Characterisation of Size-Selected Pd Clusters and Industrial Pd Catalysts*, PhD thesis, University of Birmingham, 2011.

[151] P. C. K. Vesborg, *Photocatalysis in μ-reactors and related activities*, PhD thesis, Technical University of Denmark, 2010.

[152] A. B. Laursen, *Nanoscale design of molybdenum sulfides for more efficient electro- and photoelectrocatalytic hydrogen evolution*, PhD thesis, Technical University of Denmark, 2012.

[153] G. Grimmett and D. Stirzaker, *Probability and Random Processes*, Oxford University Press, third edition, 2001.

[154] V. Habibpour, M. Y. Song, Z. W. Wang, J. Cookson, C. M. Brown, P. T. Bishop, and R. E. Palmer, *J. Phys. Chem. C* **116**, 26295 (2012).

[155] Z. W. Wang, O. Toikkanen, F. Yin, Z. Y. Li, B. M. Quinn, and R. E. Palmer, *J. Am. Chem. Soc.* **132**, 2854 (2010).

[156] Z. W. Wang and R. E. Palmer, *Phys. Rev. Lett.* **108**, 245502 (2012).

[157] Z. W. Wang and R. E. Palmer, *Nano Lett.* **12**, 5510 (2012).

[158] Z. W. Wang and R. E. Palmer, *Nano Lett.* **12**, 91 (2012).

[159] Z. W. Wang, Z. Y. Li, S. J. Park, A. Abdela, D. Tang, and R. E. Palmer, *Phys. Rev. B* **84**, 073408 (2011).

[160] F. Yin, S. Lee, A. Abdela, S. Vajda, and R. E. Palmer, *J. Chem. Phys.* **134**, 141101 (2011).

[161] D. Pearmain, S. J. Park, Z. W. Wang, A. Abdela, R. E. Palmer, and Z. Y. Li, *Appl. Phys. Lett.* **102**, 163103 (2013).

[162] T. Seto, K. Koga, F. Takano, H. Akinaga, T. Orii, M. Hirasawa, and M. Murayama, *J. Phys. Conf. Ser.* **59**, 255 (2007).

[163] C. Allain and L. Limat, *Phys. Rev. Lett.* **74**, 2981 (1995).

[164] R. D. Deegan, *Phys. Rev. E* **61**, 475 (2000).

[165] E. R. Dufresne, E. I. Corwin, N. A. Greenblatt, J. Ashmore, D. Y. Wang, A. D. Dinsmore, J. X. Cheng, X. S. Xie, J. W. Hutchinson, and D. A. Weitz, *Phys. Rev. Lett.* **91**, 224501 (2003).

[166] L. Frastia, A. J. Archer, and U. Thiele, *Phys. Rev. Lett.* **106**, 077801 (2011).

[167] Y.-J. Chen, K. Suzuki, H. Mahara, K. Yoshikawa, and T. Yamaguchi, *Appl. Phys. Lett.* **102**, 041911 (2013).

[168] M. B. Rooney, D. C. Coomber, and A. M. Bond, *Anal. Chem.* **72**, 3486 (2000).

[169] A. M. Bond, D. C. Coomber, S. W. Feldberg, K. B. Oldham, and T. Vu, *Anal. Chem.* **73**, 352 (2001).

[170] E. J. F. Dickinson, J. G. Limon-Petersen, N. V. Rees, and R. G. Compton, *J. Phys. Chem. C* **113**, 11157 (2009).

[171] L. Råde and B. Westergren, *Mathematics Handbook - for Science and Engineering*, Studentlitteratur, Lund, 1998.

[172] T. J. Davies and R. G. Compton, *J. Electroanal. Chem.* **585**, 63 (2005).

[173] E. J. F. Dickinson, I. Streeter, and R. G. Compton, *J. Phys. Chem. C* **112**, 11637 (2008).

[174] M. Bollinger, J. Lauritsen, K. Jacobsen, J. Nørskov, S. Helveg, and F. Besenbacher, *Phys. Rev. Lett.* **87**, 3 (2001).

[175] S. Vučković, J. Samela, K. Nordlund, and V. N. Popok, *Eur. Phys. J. D* **52**, 107 (2009).

[176] B. Radisavljevic, A. Radenovic, J. Brivio, V. Giacometti, and A. Kis, *Nat. Nanotechnol.* **6**, 147 (2011).

[177] F. Yin, Z. W. Wang, and R. E. Palmer, *J. Am. Chem. Soc.* **133**, 10325 (2011).

[178] D. J. Masiel, B. W. Reed, T. B. LaGrange, G. H. Campbell, T. Guo, and N. D. Browning, *ChemPhysChem* **11**, 2088 (2010).

[179] K. I. Schiffmann, M. Fryda, G. Goerigk, R. Lauer, and P. Hinze, *Fresen. J. Anal. Chem.* **358**, 341 (1997).

[180] T. Tada, T. Kanayama, K. Koga, K. Seeger, S. J. Carroll, P. Weibel, and R. E. Palmer, *Microelectron. Eng.* **41-42**, 539 (1998).

[181] T. Tada, T. Kanayama, K. Koga, P. Weibel, S. J. Carroll, K. Seeger, and R. E. Palmer, *J. Phys. D Appl. Phys.* **31**, L21 (1998).

[182] J. Tersoff and D. R. Hamann, *Phys. Rev. B* **31**, 805 (1985).

[183] T. J. Konno, S. Yamamuro, and K. Sumiyama, *J. Appl. Phys.* **90**, 3079 (2001).

[184] C. Langlois, Z. W. Wang, D. Pearmain, C. Ricolleau, and Z. Y. Li, *J. Phys Conf. Ser.* **241**, 012043 (2010).

[185] F. Yin, C. Xirouchaki, Q. Guo, and R. E. Palmer, *Adv. Mater.* **17**, 731 (2005).

[186] H. Park, S. Choi, S. Lee, and K. H. Koh, *J. Vac. Sci. Technol. B* **22**, 1290 (2004).

[187] J. Deng, C. Troadec, and C. Joachim, *IOP C. Ser. Mater. Sci. Eng.* **6**, 012033 (2009).

[188] S. J. C. Cleghorn and D. Pletcher, *Electrochim. Acta* **38**, 2683 (1993).

[189] J. R. Maiolo III, H. A. Atwater, and N. S. Lewis, *J. Phys. Chem. C* **112**, 6194 (2008).

[190] A. Frommhold, *Nanotexturisation of Gold Surfaces and its Application to Neural Implants*, PhD thesis, University of Birmingham, 2010.